

C.A. Willbold ED33

567750

150p<sub>35</sub>



**UNITED  
TECHNOLOGIES  
RESEARCH  
CENTER**

East Hartford, Connecticut 06108

**ORIGINAL CONTAINS  
COLOR ILLUSTRATIONS**

R89-957852-24

The Effects of Reynolds Number, Rotor  
Incidence Angle and Surface Roughness  
on the Heat Transfer Distribution in  
a Large-Scale Turbine Rotor Passage

REPORTED BY

M. F. Blair

M. F. Blair

O. L. Anderson

O. L. Anderson

APPROVED BY

R. W. Paterson

R. W. Paterson

DATE November 1989

NO. OF PAGES \_\_\_\_\_

COPY NO. \_\_\_\_\_

*The Effects of Reynolds Number, Rotor Incidence  
Angle and Surface Roughness on the Heat Transfer  
Distribution in a Large-Scale Turbine Rotor Passage*

**TABLE OF CONTENTS**

	<u>Page</u>
LIST OF SYMBOLS .....	iv
SUMMARY .....	1
INTRODUCTION .....	2
EXPERIMENTAL EQUIPMENT .....	5
1. Turbine Facility .....	5
2. Turbine Airfoil Coordinates .....	6
3. Rotor Passage Heat Transfer Model .....	6
Description of the Heat Transfer Technique .....	6
Instrumented Airfoil Construction Technique .....	7
Rotor Hub Endwall Heat Transfer Model .....	8
Rotor Passage Test Configurations .....	10
4. Rig and Turbine Model Assembly .....	10
Slipring-Rotary Union Assembly .....	10
Hardware and Model Assembly .....	11
5. Thermocouple Instrumentation Coordinates .....	11
6. Liquid Crystal Temperature Measurements .....	12
TEST CONDITIONS .....	13
1. Flowpath Aerodynamic Documentation .....	13
2. Compendium of Available LSRR Aerodynamic Data .....	15
3. Test Matrix for Present Program .....	16

	<u>Page</u>
EXPERIMENTAL RESULTS .....	17
1. Sample Liquid–Crystal Data .....	17
2. Data Format .....	20
3. Heat Transfer Contours for the Smooth–Wall Model .....	21
4. Heat Transfer Contours for the Rough–Wall Model .....	23
5. Midspan Heat Transfer Distributions .....	24
COMPUTATIONAL PROGRAM .....	25
1. Analysis .....	25
Generalized Potential Flow Coordinates .....	25
Construction of Duct Passage and Coordinates .....	26
Equations of Motion .....	26
Auxiliary Equations .....	28
Stationary/Rotating Coordinates .....	28
Global Conditions and Boundary Conditions .....	29
Algebraic Turbulence Modeling .....	31
2. Results and Discussion .....	32
Turbulent Flow in a Square Curved Duct .....	32
LSRR Gas Turbine Cascade .....	33
Construction of Duct Passage & Computational Grid .....	33
Verification of Aerodynamic Predictions .....	34
Verification of the Turbulence Model .....	34
Development of the Passage Vortex .....	35
Evaluation of the Heat Transfer Predictions .....	36
LSRR Gas Turbine Rotor .....	36
Construction of Duct Passage & Computational Grid .....	36
Evaluation of Heat Transfer Predictions .....	37
Comparison of Stator/Rotor Coriolis Effects .....	37
CONCLUSIONS .....	37
REFERENCES .....	40
TABLES	
FIGURES	

## LIST OF SYMBOLS

$\vec{A}_i$	Area on coordinate surfaces
$\vec{b} \vec{b}^i \vec{b}_i$	Base vectors for potential flow coordinates
Bx	Airfoil axial chord
Cx	Axial flow speed
$C_p$	Specific heat at constant pressure
Cp	Pressure coefficient, $CP = (PTOA-P)/Q_U$
$e^{ijk} e_{ijk}$	Permutation symbol
g	Determinate of metric tensor
$Gg^{ij} g_{ij}$	Metric tensor
$h_i$	Metric scale coefficients
$H_T$	Total enthalpy
$\vec{K}$	Principal curvature of potential flow streamlines
$\vec{n}$	Inward facing vector at boundary on $Y_1$ plane
N	Rotor RPM
P P <sub>T</sub>	Static pressure – total pressure
$\bar{P}$	Mass flow weighted average total pressure
PTOA	Turbine inlet absolute total pressure
PrPr <sub>t</sub>	Prandtl number – molecular/turbulent
Q <sub>U</sub>	Dynamic pressure based on U
$\vec{r}$	Position vector
$\vec{R}_m$	Relaxation parameters
R	Gas constant
Re	Reynolds number (based on airfoil axial chord and exit flow conditions)
Re <sub>θ</sub>	Reynolds number (based on momentum thickness)

## LIST OF SYMBOLS (Cont'd)

$S$	Surface arc length
$\dot{s}$	Source term in continuity equation
$\vec{\tau}$	Tangent vector at boundary on $Y_1$ plane
$T_r$	Mass flow weighted average total temperature
$U$	Rotor wheel speed at midspan
$\vec{U}_s$	Secondary flow velocity vector
$U_n U_t$	Normal and tangential secondary boundary velocities
$U_1 U_2 U_3$	Contravariant velocity components
$\vec{v}$	Potential flow velocity
$W$	Mass flow rate
$W_O$	Inlet mass flow rate
$W_t$	Relative tangential flow speed
$\vec{x}x_i$	Cartesian coordinates
$\vec{x}_o$	Initial Cartesian coordinates of streamlines
$\vec{y}y_i$	Arc length along potential flow coordinate
$\vec{Y}Y_i$	Potential flow coordinates
$\alpha_1$	Absolute flow angle from tangential at first stator exit
$\vec{a}a_i$	Unit vectors in Cartesian coordinates
$\beta_1$	Relative flow angle from tangential at the rotor inlet
$\vec{\beta}\beta_i$	Unit vectors in potential flow coordinates
$\gamma$	Ratio of specific heats
$\mu\mu_t$	Viscosity – molecular/turbulent
$\rho$	Density

## LIST OF SYMBOLS (Cont'd)

- $\Omega$  Secondary vorticity
- $\tilde{\Omega}$  Source term in vorticity equation

# **THE EFFECTS OF REYNOLDS NUMBER, ROTOR INCIDENCE ANGLE AND SURFACE ROUGHNESS ON THE HEAT TRANSFER DISTRIBUTION IN A LARGE-SCALE TURBINE ROTOR PASSAGE**

**Michael F. Blair  
Olof L. Anderson**

## **SUMMARY**

A combined experimental and computational program was conducted to examine the heat transfer distribution in a turbine rotor passage geometrically similar to the SSME HPFTP. Heat transfer was measured and computed for both the full-span suction and pressure surfaces of the rotor airfoil as well as for the hub endwall surface. The primary objective of the program was to provide a benchmark-quality data base for the assessment of rotor passage heat transfer computational procedures.

The experimental portion of the study was conducted in a large-scale, ambient temperature, rotating turbine model. Heat transfer data were obtained using thermocouple and liquid-crystal techniques to measure temperature distributions on the thin, electrically-heated skin of the rotor passage model. Test data were obtained for various combinations of Reynolds number, rotor incidence angle and model surface roughness. The data are reported in the form of contour maps of Stanton number. These heat transfer distribution maps revealed numerous local effects produced by the three-dimensional flows within the rotor passage. Of particular importance were regions of local enhancement produced on the airfoil suction surface by the main-passage and tip-leakage vortices and on the hub endwall by the leading-edge horseshoe vortex system. Comparisons between the present results and midspan results from a previous NASA-HOST funded study are included.

The computational portion consisted of the application of a well-posed parabolized Navier-Stokes analysis to the calculation of the three dimensional viscous flow through ducts simulating a gas turbine passage. These cases include a 90° turning duct, a gas turbine cascade simulating a stator passage, and a gas turbine rotor passage including Coriolis forces. The calculated results have been evaluated using experimental data of the three dimensional velocity fields, wall static pressures, and wall heat transfer on the suction surface of the turbine airfoil and on the end wall. Particular attention has been paid to an accurate modeling of the passage vortex and to the development of the wall boundary layers including the crossflow. The results of this assessment indicate that the procedure has the potential to predict the aerodynamics and the heat transfer in a gas turbine passage and can be used to develop detailed three dimensional turbulence models for the prediction of skin friction and heat transfer in complex three dimensional flow passages.

## INTRODUCTION

The aerodynamics and heat transfer occurring in the airfoil-to-airfoil passages of a turbine are strongly three dimensional in nature. This complexity of the flow is due to both viscous and inviscid flow mechanisms that come into play. Viscous effects in a turbine passage are present on the airfoil surfaces in the form of boundary layers and wakes, with the major contribution to three dimensionality occurring near the endwalls. An idea of the complexity of the three dimensional endwall boundary layers can be obtained by considering the observations of Langston, Nice and Hooper (1977) and/or Sieverding (1985) for large-scale cascades. These studies demonstrated that viscous effects completely dominated the endwall flow. They showed that near the leading edge stagnation point the endwall boundary layer flow was in the upstream direction and that before the flow had reached the passage exit all of the incoming endwall boundary layer had been swept across the endwall from the pressure surface to the suction surface. This cross-passage endwall flow rolled up into a secondary flow vortex leaving an extremely thin endwall boundary layer behind. In addition, their results showed that as the cross-passage flow moved onto the suction surface it radically altered the flow near the airfoil hub and tip.

Inviscid effects are also important in turbine passage flows not only because of the three dimensional nature of the airfoil geometry but also because of the vorticity present in the flow and because of the rotating frame of reference of the rotor. The "relative eddy," an inviscid mechanism produced by the vorticity in the rotating frame of reference, can create significant secondary flow effects on rotor pressure surfaces (Dring and Joslyn, 1983).

Considering the highly three dimensional nature of turbine passage aerodynamics it is not surprising that these flows have a powerful impact on the associated heat transfer distributions. As an example, Graziani et al. (1980) presented contours of the airfoil and endwall heat transfer for the same two dimensional cascade used for the aerodynamic study of Langston, Nice and Hooper (1977). These results demonstrated that the flow across the endwall from the pressure to the suction surface had an important impact on both the endwall and suction surface heat transfer distributions. An interesting fact to keep in mind is that the complex three dimensional aerodynamics and heat transfer in this cascade had their origins in the aerodynamics and not in the geometry. The cascade geometry was purely two dimensional.

From the computational perspective, progress toward modeling these flows has been dramatic. This is partly due to more efficient algorithms and partly due to the expansion of computer capabilities and the introduction of supercomputers. As an example, the inviscid aspects of the three dimensional flow in the LSRR rotor have been predicted remarkably well by Holmes and Tong (1984). Not only were the airfoil pressure distributions predicted quite accurately but so also was the effect of the rotating frame of reference in producing the relative eddy.

For at least three reasons, progress in computing the viscous aspects of these flows has been less dramatic. First, the computational modeling of the diffusion terms adds complexity. Second, the calculations are in general far more time consuming. Finally, and perhaps most importantly, the physical models for the turbulent transport processes (for shear and heat flux) are neither very

reliable, nor general, nor accurate. Some relatively recent examples of the calculation of three dimensional viscous flows in turbine airfoil passages can be found in Anderson and Hankins (1981), Anderson (1985), Hah (1983), Kreskovsky, Briley and McDonald (1979) and Moore and Moore (1979). Each of these calculations is based on an elegant formulation of the discretized governing equations and each is based on relatively efficient and accurate computational algorithms. However, all of them suffer from inaccuracy in modelling the turbulent transport. The impact of this shortcoming is frequently inconsequential to the prediction of the global inviscid aspects of the flow, i.e. the pressure distributions. Its impact on the local aerodynamics may be serious but the general qualitative trends can frequently be predicted. The impact of this shortcoming on predicting the heat transfer, however, can be much more serious. The reason for this is that the aerodynamic aspects involve the global flow field and local inaccuracies can be either compensated for or averaged out. Heat transfer, on the other hand, is a local effect and even local inaccuracies in a prediction may obscure strong local gradients and regions with high local heat loads.

Accurate physical models for turbulent heat transfer in the extremely hostile environment of the gas turbine airfoil, e.g. high levels of freestream unsteadiness (both periodic and random), local separations and strong surface curvature still need to be developed for two dimensional flows. It is not unreasonable to expect that even more turbulence-model-development problems will be encountered in the computation of the three dimensional flows of the full-span turbine airfoil and endwall.

Considering the complexity of the aerodynamics and heat transfer present in the full span flow in a turbine passage, it is essential that any computational procedure aimed at predicting these flows be assessed against a benchmark data base. Such a data base would need to satisfy the following requirements:

- (1) The turbine model used in the experiment must be relevant to the turbines for which the computational procedure is intended, having geometric similarity and basically good performance.
- (2) The data base should contain a sufficiently detailed description of the turbine and its airfoils so as to provide all the geometry input required by the computation.
- (3) All of the conditions upstream of the rotor should be documented and available.
- (4) Sufficiently detailed flow visualization data should be available to provide a description of the flow on the airfoil surfaces.
- (5) Aerodynamic data downstream of the airfoil sufficient to provide a detailed description of the flow from hub to tip should be available.
- (6) Detailed heat transfer data should be provided on the airfoil suction and pressure surfaces as well as on the hub endwall.

As will be discussed in detail in EXPERIMENTAL EQUIPMENT, the turbine model employed in this study was directly relevant to the Space Shuttle Main Engine (SSME) drive turbine (item 1). Items (2) and (3) will provide all the information required to set up and carry out a prediction of the flow and heat transfer. Items (4), (5) and (6) will provide the aerodynamics and

heat transfer data required to assess the accuracy of the prediction and to isolate where and why the prediction might fail. The geometric description of the test model is included in EXPERIMENTAL EQUIPMENT (item 2). Items 3, 4 and 5 are available for the model design flow coefficient ( $C_x/U = 0.78$ ) in Joslyn and Dring (1989). Item 4 is available for  $C_x/U = 0.56$  in Joslyn and Dring (1983). The primary objective of the present program has been to provide the associated comprehensive set of full-span heat transfer data (item 6) thus fulfilling all requirements for a benchmark-quality data set.

A secondary objective of the program has been to examine the ability of a relatively simplified analysis to capture the major features of a rotating, viscous turbine passage flow. The need for this new analysis arises because of the excessively large computational resource requirements involved if the full Navier-Stokes equations are employed for solution of this problem. Use of the full Navier-Stokes equations results in a problem so large that even modern supercomputers cannot resolve all scales involved in the flow field and currently requires that the problem be solved on a much reduced computational mesh.

Generally this means that one is forced to make a number of approximations concerning the nature of the boundary layer so that the problem is tractable. Unfortunately this means that one can not now completely resolve the scales involved in calculating the flow in the boundary layer. In addition, these approximations are based on our knowledge of two dimensional boundary layers and may be inadequate for three dimensional boundary layers which are different in some important respects. Finally we should note that while there is an established paradigm for the prediction of the forces in the flow field, there is no comparable paradigm for the prediction of the turbulence in the flow field although many models have been suggested. This is particularly important for the prediction of the heat transfer on the turbine airfoils where unsteadiness and transition are important factors. Therefore it would be useful to solve a subset of the Navier-Stokes equations, namely the parabolized Navier-Stokes (PNS) equations. Although one would be limited in the class of problems one can consider, it does have the advantage of speed so that a detailed mesh can be used to resolve all the scales in the three dimensional flow field and so that the boundary layer can be treated in a more direct manner. Such an algorithm could be used to develop detailed models of turbulence and could also be used to provide a quick assessment of the flow field for such quantities as heat transfer in the design stage of building a gas turbine. The present study describes one such PNS solution algorithm, applies it to the gas turbine problem, and evaluates the procedure against experimental data for both a rotor and a stator.

The development of the PNS equations and a solution algorithm has two requirements. First it must be shown that the equations are parabolic, and second it must be shown the the problem is well posed. In addition one must face the problem that the solution of a parabolic problem is a function only of the initial conditions and the boundary conditions. It is not a function of the downstream conditions. Therefore some information about the elliptic properties of the flow field must be included in the solution algorithm. Generally speaking, three methods have been used to resolve these problems: 1. parabolized fully viscous methods, 2. reduced Navier-Stokes methods, and 3. fully parabolized Navier-Stokes methods. In the first method, pioneered by Patanker and

Spalding (1973), Curreto, Curr, and Spalding (1973), and Briley (1974), these problems are resolved by neglecting the second derivatives in the streamwise direction to parabolize the equations, and using the inviscid streamwise static pressure gradient with some corrections to make the problem well posed and to include the elliptic effects in the algorithm. This unfortunately results in a solution in which the streamwise and crosswise pressure are split and not the same. The second method, developed by Schiff and Steger (1979), Vigneron et al. (1978), and Barnett (1982), again neglects the streamwise second derivatives to parabolize the Navier–Stokes equations but uses a special treatment of the static pressure in the boundary layer to make the problem well posed. This method appears to work well for supersonic flow but it is not clear at the present time that it would work with subsonic flow. The third method, developed by Anderson et al. (1981) involves writing the equations of motion in a potential flow coordinate system in which stream surfaces and potential surfaces are the coordinates. Then Navier–Stokes equations are parabolized by assuming that the crossflow velocities are small following a procedure similar to that used in deriving the boundary layer equations. This procedure results in a set of equations which are parabolic and the problem is well posed. In addition, the elliptic properties of the flow field are contained in the coordinate system. The price one pays for using this procedure is that one may be limited in the magnitude of the cross flow velocities which may be treated. The detailed procedure is given by Anderson (1989) and is the method contained in the UTRC PATH code which will be evaluated in this report.

The scope of the computational portion of this report is to: 1. describe this analytical procedure, 2. calculate the three dimensional flow fields for a 90° turning duct, a low speed cascade simulating a gas turbine stator, and a gas turbine rotor, and 3. evaluate and assess the method by comparison with experimental data for the three dimensional velocity fields, wall static pressure distributions, and, wall heat transfer.

## EXPERIMENTAL EQUIPMENT

### 1. Turbine Facility

All experimental work for this program was conducted in the United Technologies Research Center Large Scale Rotating Rig (LSRR). This test facility was designed for conducting detailed experimental investigations of flow within turbine and compressor blading. The LSRR facility is of the open circuit type with flow entering through a 12-ft. diameter inlet. A 6 in. thick section of honeycomb is mounted at the inlet face to remove any cross flow effects. The inlet smoothly contracts the cross section to 5 ft. diameter. The flow is then passed through a series of fine mesh screens to reduce the turbulence level. Immediately downstream of the screens is a 7-foot long section which slides axially and permits access to the test section. The test section consists of a series of constant diameter casings enclosing the turbine, compressor, or fan model assemblies. The casings are wholly or partially transparent which facilitates flow visualization and laser–Doppler–velocimeter studies. The rotor shaft is cantilevered from two downstream bearings, thus providing a clean flow path at the model inlet. Axial length of the test section is 36 inches. The

rotor is driven or braked by a hydraulic pump and motor system which is capable of maintaining shaft speeds up to 890 rpm. Downstream of the test section flow passes through an annular diffuser into a centrifugal fan and is subsequently exhausted from the rig. A vortex valve is mounted at the fan inlet face for flow rate control.

The general features of the turbine test section geometry are shown in figures 1 through 3. Figure 1 presents a sketch of the test section arranged in the 1 1/2 stage (stator1/rotor/stator2) configuration. As indicated in Fig. 1, the turbine model has 22 first stage stator airfoils, 28 first stage rotor airfoils and 28 second stage stator airfoils. Figure 2 shows a radial view of the first stage airfoils at midspan. A photograph of the facility showing the rotor and second stator rows installed in the test section is presented in Fig. 3.

The turbine model simulates a relatively heavily loaded machine with a hub/tip radius ratio of 0.8. All three airfoil rows have solidities and aspect ratios very near unity. When operating at design conditions the turbine (at midspan) has a flow coefficient ( $C_x/U$ ) of 0.78, a stage loading coefficient of 2.8 and 34% static pressure reaction. The axial spacing between the first stator and the rotor was 50% of the average of the first stage stator and rotor axial chords ( $B_x$ ). The axial spacing between the rotor and the second stator was 63%  $B_x$ . The rotor tip clearance was 0.060 inches or 1% span which is typical for current aircraft engine design.

The LSRR turbine model is shown schematically in Fig. 4 along with the SSME/HPFTP drive turbine. Comparisons of the flow paths and turbine design parameters for the LSRR and the HPFTP are given in Fig. 4 and Table 1. These comparisons indicate that the LSRR and HPFTP are highly similar, even in the approach duct and the center body upstream of the turbine. The hub/tip ratios are quite close (0.83 vs 0.80) while the airfoil aspect ratios (span/axial chord) are within about 15%. Table 1 indicates that the airfoil exit angles ( $\alpha_2$ ) for the LSRR and the HPFTP are within 1/2 deg. while the inlet flow angles ( $\beta_1$ ) can also be brought within 1 deg. by operating the turbine at a flow coefficient ( $C_x/U$ ) of 0.57 instead of its nominal design value of 0.78. The LSRR has a gap/chord ratio which is about 40% greater than that of the HPFTP. This higher loading is typical of aircraft turbines and is achieved while maintaining good airfoil aerodynamics. Extensive flow visualization tests conducted in the LSRR have confirmed that there is no boundary layer separation on any of the airfoils at  $C_x/U = 0.78$ .

## 2. Turbine Airfoil Coordinates

The surface coordinates ( $x, y$ ) of the three airfoil rows (stator1/rotor/stator2) are given in Tables 2, 3 and 4, respectively, for the hub, midspan and tip sections.

## 3. Rotor Passage Heat Transfer Model

Description of the Heat Transfer Technique. Of the numerous phenomena that influence turbine convective heat transfer rates the most important effects (first order effects) are a consequence of local flow conditions. Examples of aerodynamic phenomenon which have

extremely large effects on turbine convective heat transfer rates are the transition of a boundary layer from laminar to turbulent flow, separation or reattachment, velocity gradients, and strong secondary flows such as the leading edge horseshoe and main passage vortices. These "first order" heat transfer effects can be experimentally simulated without reproducing the large temperature differences present in the gas turbine environment but by employing only very small levels of surface heat flux. These small heat flux levels generate proportionally small fluid temperature gradients and result in flows of near constant density. For such near-constant density flows the absolute direction of convective heat flux, whether to or from the solid surface, is immaterial. In numerous earlier experiments (e.g. Reynolds, Kay, and Kline, 1958; Ota and Kon, 1974; and Subramanian and Antonia, 1981) electrical resistive heating of surface metal foils has proved to be a highly practical method for generating low levels of uniform surface heat flux. Recently this basic experimental method has been significantly improved through a series of technique development programs at UTRC. Of primary importance has been the development of techniques for using rigid cast urethane foam as the construction material for test aerodynamic models. Rigid urethane has an extremely low thermal conductivity ( $8 \times 10^{-5}$  gm-cl/cm-s K) which nearly eliminates errors in heat transfer measurements due to conduction in the airfoil. Techniques have also been developed for attaching metal foil to the urethane foam models using extremely thin layers of adhesive. Use of these new construction techniques results in uniform heat flux test models with negligible (less than 1 percent) back-losses and minimal transverse "smearing" through conduction. Calculations indicate that, even in a region with a lateral gradient of heat transfer coefficient of 100 percent per inch, local heat transfer coefficients can be measured within an accuracy of 5 percent using these construction materials and techniques. Graziani et al., 1980; Blair, 1983; and Blair, 1984, present examples of the use of these heat transfer measurement techniques.

Instrumented Airfoil Construction Technique. As described in the preceding section, heat transfer measurements were obtained in this study using low conductivity rigid foam castings of the test airfoils. A uniform heat flux was generated on the surface of the foam test airfoils using an electrically heated metal foil skin attached to the model surface. Local heat transfer coefficients around the airfoils were determined using thermocouples and liquid crystal techniques to measure the temperature difference between the heated metal skin and the free stream.

Photographs of the first stage rotor airfoil model at various steps of fabrication are presented in Fig. 5, 6 and 7. The first stage of the fabrication process consisted of developing a metal "master airfoil." An aluminum rotor blade, chosen at random from the LSRR rotor, was carefully inspected to determine locations with surface waviness. These slight deviations from a perfectly "developable" surface (a surface with no compound curvature) are an inherent characteristic of the "multiple radial station contour tracing" machining process used to manufacture the aluminum airfoils. Despite the fact that this surface waviness only consists of depressions a few thousandths of an inch deep at their maximum, they do present a problem unique to this method of instrumentation. The metal foil which is to be glued to the exterior surface of the airfoil is extremely intolerant of surface waviness. Even miniscule depressions on the airfoil translate to "wrinkles" or "lumps" on the finished, assembled airfoil surface. For this reason it was necessary that any

depressions be filled to produce as nearly a "developable" surface as possible. This filling procedure consisted of a trial-and-error/inspection iteration towards the finished airfoil. An airfoil was accepted as a "master" only after a completely wrinkle-free "test" metal foil could be glued to its entire surface. An inviscid flow computation of the velocity distribution around the finished "master" airfoil indicated that the maximum change in local velocity produced by the surface filling (measured maximum filling thickness) was only 1/4 percent.

A steel skeleton (Fig. 5) was fabricated for each of the test airfoils to ensure adequate strength to endure both the aerodynamic and centrifugal forces of the test environment. The skeleton also provided a secure location to attach the foam airfoil to the rotor hub. The photograph of the steel skeletons presented in Fig. 5 shows the "button" for precisely positioning the steel skeletons. The "button" duplicates the mandril used to position the metal "master airfoil" in the rotor hub. The remaining photographs of Fig. 5 show one of the steel skeletons mounted in a special fixture designed to ensure precise alignment of the steel skeleton in the mold. The curved base plate shown in these photographs duplicates the 24-inch hub radius of the turbine test model and serves as the hub wall of the airfoil mold. The bracket below the curved base plate precisely fits both the mandril "button" on the "metal master" airfoil and the "button" which slides over the mounting post on the steel skeletons.

The next step in the model fabrication process consisted of casting a concrete mold of the master airfoil. Special low shrinkage gypsum cement (USG Hydrocal) was used to produce a smooth airfoil surface and a precise geometrical reproduction. A photograph of the completed mold is presented in Fig. 6. The final assembly of the steel skeleton, alignment bracket and concrete mold is also shown in Fig. 6 with one wall removed. Photographs of the completed cast foam airfoils showing both the pressure and suction surfaces are also presented in Fig. 6.

Heat transfer measurements were obtained over the entire surface of a rotor passage (rotor endwall and the pressure and suction surfaces of a pair of adjacent rotor airfoils). The rotor airfoil with instrumentation along its pressure surface will henceforth be referred to as the Pressure Surface Airfoil, its adjacent twin as the Suction Surface Airfoil.

Photographs of the Pressure Surface Airfoil at various stages of assembly are given in Fig. 7. The two upper photographs show the airfoil following the attachment of the stainless steel foil to the pressure surface. Miniature thermocouples have been welded to the "backside" of the foil through holes in the airfoil. Thermocouple leads coming from the instrumentation sites were routed in grooves along the airfoil suction surface. The lower-left photograph shows the model with the instrumentation grooves filled to restore the original airfoil contour. Also shown in this photograph are the full span buss bars to which the foil would be attached. The lower right-hand photograph shows the airfoil after the foil was attached to the suction surface and connected to the buss bars. After the groove between the buss bars was filled the airfoil was ready for installation on the rotor hub.

Rotor Hub Endwall Heat Transfer Model. The rotor airfoils in the (LSRR) are mounted on a 48-inch diameter ring (the rotor hub). This hub serves to rigidly support the rotor airfoils and to ensure their precise circumferential and axial locations. Because of the large centrifugal forces

associated with the rotating airfoils the rotor hub is, of necessity, a massive device (total weight is approximately 250 pounds).

In order to facilitate the measurement of the hub-endwall heat transfer distributions a new LSRR rotor hub was designed and fabricated. This new hub differs from earlier models in two ways. First, a deep relief (spanning almost two airfoil pitches) to accommodate the endwall heat transfer model had to be incorporated into the hub. Second, the axial length was greatly increased so that endwall heat transfer data could be obtained upstream and downstream of the airfoil leading and trailing edges. New support rib structures were designed into this hub to prevent out-of-round distortion during rotation.

A photograph of the endwall-heat-transfer hub is presented in Fig. 8. The relieved region in which the hub endwall heat transfer model will be installed can be seen in the upper right of the photo. Also shown in the photo are the radial holes around the circumference of the hub to be used for mounting the airfoils.

As with the airfoil heat transfer models, the hub-endwall model consisted of a block of rigid urethane foam with an electrically heated thin metal foil skin. The endwall foam block was cast to fit into the hub relief region with its exterior surface precisely matching the hub outside diameter. In other words, the endwall casting replaced the relief region cut into the hub.

The heated endwall surface extended axially from 1.50 in. (0.24 Bx) upstream of the rotor leading edge to 1.30 in. (0.21 Bx) downstream of the rotor trailing edge (total axial heated length of 9.15 in.). Circumferentially the heated surface covered the entire endwall between the instrumented airfoils and extended to approximately midway across the endwalls of the two adjacent passages (total circumferential extent of approximately 2 rotor airfoil pitches). Three parallel, 3.05 in wide, circumferentially running metal foil strips were used to generate the uniform heat flux boundary condition on the endwall surface. These three strips were wired in series to assure that precisely the same current passed through each.

With this arrangement the endwall heating foil passed beneath the bases of the two instrumented heat transfer airfoils. Since there would be no gap at the bases of the airfoils and hence no airflow across the bases there would be no exterior convective mechanism to remove the locally generated heat. To alleviate this problem cooled copper plates, shaped to conform to the airfoil profile at the hub, were incorporated into the endwall model. These cooled plates removed the heat generated by the endwall heating foil beneath the base of the heat transfer airfoils.

Photographs showing various views of the endwall model hardware are presented in figure 9. The upper photograph shows the disassembled components including the copper blade root cooling inserts, the power buss bars, and the support frame by which the endwall model is attached to the rotor hub. Note that the copper base plates have cooling tubes soldered to their bottom surfaces. The amount of cooling air passing through the tubes on the backside of the plates was adjusted during operation to achieve the correct thermal boundary conditions. The lower left photograph shows the assembled endwall components viewed from the bottom of the support frame. This view shows the cooling lines, the buss bar power lines, and the access holes for the instrumentation from the rotor

blades. The lower right hand photograph shows the assembled endwall model as viewed from the top. Note the instrumentation holes through the copper cooling plates for the rotor blade instrumentation.

Two photographs of the rotor hub/endwall model assembly are presented in Figure 10. The left hand photograph shows the cutout region of the hub, the support bushings for the rotor airfoils and the routing holes for the various power, cooling, and instrumentation lines. The right hand photograph of figure 10 shows the assembled endwall model installed in the hub cutout and ready for the casting of the rigid urethane foam endwall surface.

Rotor Passage Test Configurations. Rotor passage heat transfer data were obtained for two model surface conditions; for an aerodynamically smooth wall and with wall roughness simulating actual SSME hardware. A photograph of the completely assembled rotor passage model in the smooth-wall condition is shown in Fig. 11. For these smooth-wall tests the airfoil and endwall surfaces were prepared for obtaining liquid-crystal data, i.e. they were covered with a black base paint and then coated with encapsulated liquid crystals. The grid lines on the airfoils and endwall were required for interpretation of the photographs of the liquid-crystal temperature patterns. These grid lines were created by masking the unpainted model and provide a very smooth, trip-free finished surface.

The target characteristics of the rough-wall test-model surface were determined by measuring the roughness of a sample SSME rotor airfoil with a surface profilometer. These measurements for actual engine hardware indicated a maximum roughness height of 0.0033 inches which scales to 0.026 inches for the LSRR model. A screened grit of 0.026 inches was applied uniformly over the entire rotor model test surface for these rough-wall tests. A photograph of the completed rough-wall model is presented in Figure 12.

#### 4. Rig and Turbine Model Assembly

Slipring-Rotary Union Assembly. Thermocouple and electrical power leads for the rotor airfoils and endwall model were all connected through a Wendon Co. 212 slipring unit. Leads from the rotating models passed through a hollow arbor which also served to support the slipring unit. Photographs of the slipring unit and arbor are presented in Figure 13. These photographs show an important feature of this slipring unit, the stationary and rotating connection points are in close proximity in an effort to minimize any secondary voltages generated at these connections.

Coolant air for the copper baseplates (mounted beneath the rotor airfoils) is also passed through this hollow arbor. The stationary/rotating connection for this coolant air is made through a rotary union mounted on the extreme end of the arbor. The rotary union can be seen in the upper photograph of Figure 13 in which the components are shown disassembled. The high pressure flexible hoses shown in this disassembled view were connected to the rotating face of the union, passed through the arbor and were connected to a bank of 6 remotely controlled needle valves (not shown). The coolant flowrates in the passages in the copper baseplates were controlled by these needle valves. The assembled slip ring/rotary union is shown in the lower photograph of Figure 13.

**Hardware and Model Assembly.** As part of the installation of the new rotor hub into the rig it was necessary to fabricate and fit a pneumatic seal between the first-stage stator and the rotor hub. This seal consists of an abradable ring on the forward face of the rotor hub which was custom-fit to a set of knife-edges aft of the stator support ring. This custom-fitting process consisted of a series of step-by-step engagements of the stator knife edges into the abradable rotor seal with the LSRR operating at very low speed. With each successive step the knife edges wear grooves of increasing depth into the abradable material. The end result of this procedure is a precision-fit rotating seal which prevents leakage of air from the inner rig cavity to the gas path.

Installation of the test hardware into the LSRR consisted of the following tasks: (1) The 28 rotor airfoils (2 heat transfer airfoils and 26 solid aluminum airfoils) were installed into the rotor hub. (2) The first stator and rotor passage throats were set precisely to assure uniform, periodic blade-to-blade flow through the stage. (3) The blade tip gaps were adjusted to assure equal tip/rotor-casing clearance for all airfoils. (4) All power and instrumentation wiring and all cooling lines were routed to the sliping/rotary union. (5) The completed hub-assembly was dynamically balanced at 320 RPM.

A photograph of the partially completed assembly is presented in Figure 14. Shown in the photo are the 6 remote controlled needle valves, the cooling lines running to the rotor blade baseplates, and the instrumentation wiring routed to the rig centerline. Figure 15 shows the rotor at the next stage of assembly. In this photograph the instrumentation wiring has been routed through the sliping. Note the completed heat transfer model mounted on the rotor hub.

## 5. Thermocouple Instrumentation Coordinates

For the present program, detailed heat transfer distribution data were obtained over the hub endwall and on both the suction and pressure surfaces of the rotor airfoil. A special rotor surface instrumentation coordinate system was developed to accommodate the complex three dimensional geometry of the rotor airfoil. This instrumentation coordinate system fulfilled two purposes: (1) it provided a technique to accurately position heat transfer measurement sites (thermocouples), and (2) it provided a system for transmittal of the experimentally measured heat transfer distributions. The coordinate system uniquely identifies a position on the rotor airfoil surface (1) radially in terms of percent span, and (2) chordwise in terms of percent distance along the respective (pressure or suction) surface. Surface distances along the airfoil were measured between reference  $S=0\%$  and  $100\%$  locii, the definitions of which are illustrated in Fig. 16. The geometric "zero" at a given spanwise location was defined as the point on the leading edge circle tangent to a straight line which was also tangent to the trailing edge circle ( $S=100\%$ ). The tip, midspan and hub tangencies are illustrated in Fig. 16. The locii of the tangency points at all spanwise locations formed the  $S=0\%$  and  $S=100\%$  lines. As shown in Fig. 16, the distance "S" is defined as increasing positive along the suction surface and increasing negative along the pressure surface.

A full-scale coordinate-system rotor airfoil model was constructed to facilitate the production of a template in the above % span vs. % S coordinates. This template was later employed for locating

thermocouples during the instrumentation of the heat transfer models. First, the span on one of the original 28 metal airfoils from the LSRR rotor was extended by 1% (the tip clearance for the rotor model) to provide a "100%—span" geometric model. Second, the entire airfoil surface was covered with a sheet of Vellum drafting paper. Third, the  $S=0\%$  and  $100\%$  locii as well as locii of constant % span (in 5% increments) were drawn onto the Vellum. Finally, straight lines were generated, from hub to tip, connecting points of equal % (in 5% increments) surface arc length. The resulting pattern on the Vellum sheet, then, consisted of lines of constant % span and % S in 5% increments.

Four views of the assembled coordinate system model are presented in Fig. 17. Also shown in Fig. 17 are the locations of the adjacent airfoils on the rotor stage. It should be pointed out that the locii of constant % span correspond to surfaces of constant radius from the turbine axis of rotation but that the locii of constant % S are not radial and do not correspond to lines of constant axial position.

The thermocouple instrumentation arrays for the pressure and suction surface heat transfer airfoils are presented in Figures 18 and 19 respectively. Note that each airfoil thermocouple site is located at the juncture of a grid line of fixed % span and a grid line of constant % surface distance. The lines marked LE in Figs. 18 and 19 correspond to the airfoil leading edge ( $S=0$ ). Both the spanwise and surface length grid lines are in increments of 5%. For both Figs. 18 and 19, the airfoil root is located at the bottom. Following is an example of determining a thermocouple location: for Fig. 19, thermocouple number 24 is located 8 grid increments from the root (40% span) and 2 grid increments from the leading edge (10% S).

For the pressure surface airfoil there were 89 thermocouples installed on the test (pressure) surface and 7 thermocouples on the reverse side. For the suction surface airfoil there were 124 test (suction) surface thermocouples and 6 on the backside. The locations of the power buss bars are also shown in each figure.

A diagram of the thermocouple pattern for the endwall model is presented in Figure 20. The endwall instrumentation extends from 0.12 Bx upstream of the leading edge plane to 0.14 Bx downstream of the trailing edge plane. As indicated in Fig. 20, there were 101 thermocouples installed on the endwall surface.

## 6. Liquid Crystal Temperature Measurements

Liquid-crystal techniques were used in conjunction with data from the model thermocouple arrays to determine the heat transfer distributions on the airfoil and endwall surfaces. The objective of employing liquid-crystals in addition to the thermocouple arrays was to obtain more detailed information in regions of strong spatial variations of the passage heat transfer distributions. All liquid crystals employed in this investigation consisted of a mixture of Hallcrest encapsulated Chiralnematic slurries. The mixture contained 8 slurries, each with a different color-band temperature. The width of each color band, however, was 2 deg. F for all of the individual slurries. The nominal color-change (begin-red) temperatures for the 8 slurries were 50, 60, 70, 80, 90, 100, 106 and 116 deg. F. The accuracy of each color band was within 1 deg. F as determined in water

calibration tests. Application of the liquid-crystal mixture on the passage surface was accomplished by spraying over a Hallcrest-supplied black base coat (see Fig. 14).

The liquid-crystal illumination was accomplished with a General Radio Model 1540 Strobolume synchronized to the passing of the rotor model. A Xenon bulb with a flash duration of 12  $\mu$ sec. and a power of 1.8 Joules/flash was employed. Photographs were obtained with a Cannon 35 mm. SLR with a 35-105 mm zoom lens and 200 ASA color print film. Typical exposure settings were approximately f5.6. The camera viewed the rotor passage through a plexiglass window at the rotor axial station. The arrangement provided near-normal viewing angles to most of the rotor airfoil and endwall surfaces.

## TEST CONDITIONS

### 1. Flowpath Aerodynamic Documentation

The aerodynamic characteristics of the LSRR 1 1/2 stage turbine model have been thoroughly documented in previous investigations, most of which were conducted at the design flow coefficient ( $C_x/U = 0.78$ ). All of these aerodynamic data are available either in the form of UTRC reports, Government Contract reports or as open literature publications.

The most exhaustive documentation of the aerodynamics of the turbine model is presented by Joslyn and Dring (1989). Some of the most important results from this document will be presented here as an indication of the nature of the aerodynamic data available for this model.

Joslyn and Dring (1989) present a comprehensive set of rotor airfoil aerodynamic data including measurements of the total pressure, static pressure, flow velocity and flow direction both upstream and downstream of the rotor. These measurements were obtained through the use of inter-airfoil-row traversing instrumentation. Both stationary and rotating instrumentation were employed. All of the traverse and rake probes utilized in this study were standard United Sensor products. Ammonia-Ozalid paper surface flow visualization techniques were employed on the turbine airfoil surfaces.

The highly three-dimensional nature of the flow through the rotor is demonstrated by the flow visualization results of Fig. 21. The suction surface results clearly show the flow convergence produced by the hub and tip passage vortices (endwall cross-passage flow moving onto the suction surface). The suction surface view also shows how the path taken by the tip leakage flow varied along the chord. The dominant feature on the rotor pressure surface was the radial flow toward the tip due to the relative eddy. This is an inviscid mechanism due to the vorticity in the rotating frame of reference. Its effect was strongest on the forward portion of the pressure surface because the surface flow speed was lowest there (Dring and Joslyn, 1983). The surface streamlines turned away from the radial direction as the flow accelerated toward the trailing edge. The hub end wall flow visualization (not shown) revealed strong over-turning due to secondary flow.

Comparisons of the measured and computed static pressure distributions for the first stage stator and rotor are shown in Fig. 22 for the 2%, 50% and 98% span locations. The curves are the time-averaged computed results and the symbols are the measured results.

The measured rotor pressure distribution data are shown as pairs of symbols at the 2% and 50% locations. These two symbols represent the range of the measurements that have been taken on the rotor during the various experiments that have been conducted between 1977 and 1988. A similar comparison for the first stator showed that the range of measurements for this airfoil was within the size of the symbols.

The computed results for the stator and rotor are by Rai (1987). This comparison was made in spite of the fact that the rotor aspect ratio in the computation was low (by the factor 11/14) and in spite of the fact that the tip clearance was too small (0.4% vs. 1% span). The results by Madavan et al. (1989), however, showed that the impact of the rotor aspect ratio on the rotor pressure distribution was relatively small. The same can not necessarily be said for the effect of the rotor tip clearance, especially at the 98% span location. This question remains to be answered (Rai, 1989a).

In general, the agreement between the measured and computed pressure distribution results was excellent. For the stator the agreement was excellent from hub to tip. For the rotor the agreement at the hub was reasonably good and the results of Madavan et al. (1989) show that the suction surface agreement gets better when the correct aspect ratio (and a finer computational grid) were used. At the rotor midspan agreement was excellent. At the tip, however, there was a difference between the measured and computed results on the aft portion of the rotor suction surface. This discrepancy may well have been due to the small tip clearance used in the Rai (1987) calculation.

Total pressure contours in the flow downstream of the first stator are shown in Fig. 23a. These data were obtained over a plane located 17% aft of the stator trailing edge. The contours show the migration toward the hub of the low total pressure hub and tip secondary flows. The maximum local losses for the tip secondary flow (near 65% span) and hub secondary flow (near 13% span) were about 1.5 and 2.5 respectively. These results indicate a thicker endwall boundary layer at the tip than at the hub, a result due to the thicker tip boundary layer at the stator inlet.

The measured secondary flow vectors downstream of the first stator are shown in Fig. 23b. The radial component of each vector is proportional to the radial velocity component. The tangential component of each vector was proportional to the difference between the actual tangential velocity component and the tangential velocity component corresponding to the actual axial velocity component and the area averaged yaw angle at midspan. This corresponds to looking upstream at the velocity vectors from the direction of the averaged yaw angle at midspan.

Each vector in Fig. 23b represents a measurement location. It can be seen that the data density was highest in the airfoil wakes and near the end walls. These results demonstrate the radial transport (toward the hub) in the stator wake due to the strong radial static pressure gradient at this plane. This was the mechanism that moved the tip and hub secondary flows toward the hub (Fig. 23a). Note the vortical motion in the hub secondary flow.

The spanwise distribution of the measured relative yaw angles aft of the first stator are shown in Fig. 24. As for Fig. 23 these data were obtained at a station 17% aft of the trailing edge. The two outermost measured points demonstrate the problem of under-turning near the tip.

Contours of rotary total pressure aft of the rotor are shown in Fig. 25a. Here, as with Fig. 23, the traverse data were acquired over two pitches. Since there were 22 first stator airfoils and 28 rotor airfoils the circumferential width of Fig. 25 was reduced by a factor of 11/14 relative to Fig. 23. The contours of Fig. 25a indicate that there was a large low total pressure region downstream of the rotor centered at about 60% span. This was produced by the hub and tip endwall flows impacting the rotor suction surface and then moving toward the midspan region. Note that at this station the hub and tip secondary flows had merged into a single low total pressure region. The effect of the rotor tip leakage flow can be seen in the regions of low rotary total pressure between 80% span and the tip. Recall that the rotor tip clearance was 1% span.

The secondary flow velocity vectors in the flow aft of the rotor are shown in Fig. 25b. This plot was generated in the same manner as Fig. 23b for the flow aft of the first stator. Here also the viewing angle was the averaged relative yaw angle at midspan. Two distinct counter-rotating vortices are clearly evident in the flow downstream of each rotor airfoil passage. These are the hub and tip secondary flow vortices. The region of low rotary total pressure for Fig 25a was coincident with the tip secondary flow vortex at about 60% span.

The final figure demonstrating aerodynamic documentation of the LSRR turbine model presents the spanwise distribution of the rotor relative exit flow angle (Fig. 26). These results can be employed to demonstrate the relationship between turning and axial velocity. A comparison of these turning angle distributions with their respective axial velocity distribution measurements revealed that regions of high angle (over-turning) correspond to regions of low axial velocity, and vice-versa.

## 2. Compendium of Available LSRR Aerodynamic Data

The results presented in Figs. 21 through 26 represent only a small fraction of the total volume of aerodynamic data available for the LSRR turbine model. This facility has been in operation since 1974 and, since that time, a large number of experimental programs have been conducted in it. Following is a list of these programs in chronological order.

(1) The turbine model was operated in the LSRR with the intent to examine endwall and other secondary flows occurring in the stationary vane and rotor passages (Joslyn, Dring and Camarata, 1976). Several experiments were conducted to improve and expand the capability to obtain meaningful measurements on board a moving rotor (Joslyn, Dring and Camarata, 1977).

(2) A study of film cooling on a turbine rotor blade was conducted under contract to AFAPL, Contract No. F33615-77-C-2068 (Dring, 1977 and Dring, Blair and Joslyn, 1980). This study demonstrated the insensitivity of film effectiveness to centrifugal effects and also demonstrated that the coolant trajectory had an unexpectedly strong radial component on the blade pressure surface.

(3) A study of the three-dimensional nature of the flow over an axial turbine rotor blade was documented by Dring and Joslyn (1981). This study examined a wide variety of flow features and, particularly, the radial flow on the rotor pressure surface and the effects of secondary flow and the tip leakage flow on the nature of the rotor exit flow field.

(4) The turbine model was used to study unsteady and three dimensional effects. This program utilized multi-element hot-film probes and the on-line phase-lock-averaging capabilities of the LSRR data system. Complete radial-circumferential arrays of the instantaneous and phase-lock-averaged velocity vector were acquired downstream of each of the three airfoil rows. A very small portion of the  $10^9$  measurements in this program were presented by Joslyn, Dring and Sharma (1982).

(5) A study of turbine rotor-stator interaction and turbine negative incidence stall was conducted under AFWAL Contract No.F33615-80-C-2008 (Dring et al., 1981 and Dring et al. 1982). This work demonstrated that extremely large fluctuations of the rotor and stator pressure distributions occur at typical rotor-stator axial gaps. As part of this study it was also demonstrated that the relative eddy present in the rotor passage was responsible for the strong radial flows on the rotor pressure surface (Dring and Joslyn, 1983). The impact of rotor negative incidence stall on the rotor fullspan pressure distribution and surface flow visualization was also investigated. The onset of the pressure surface stall separation bubble, its impact on the pressure distribution and the radial flow within it were all demonstrated (Joslyn and Dring, 1983).

(6) A study of the effects of inlet turbulence and rotor-stator interactions on the aerodynamics (and heat transfer) of the turbine model was conducted under NASA Contract NAS3-23717. Aerodynamic measurements obtained in the program include distributions of the mean and fluctuating velocities at the turbine inlet and, for each airfoil row, midspan airfoil surface pressures and circumferential distributions of the downstream steady state pressures and fluctuating velocities. (Dring et al., 1986 and Blair, Dring and Joslyn, 1989).

(7) In addition to the above experimental studies conducted in the LSRR, the following analytical programs have dealt with the prediction of the flow through this same turbine geometry: (a) Rai, 1987, (b) Rai and Dring, 1987, (c) Rai and Madavan, 1988, and (d) Madavan, Rai and Gavali, 1989.

### 3. Test Matrix for Present Program

Rotor passage heat transfer distributions were obtained over a range of Reynolds numbers and rotor inlet flow angles, the variations produced by changing rotor rotational speed and turbine throughflow velocity. A map of the various operating conditions for which heat transfer data were obtained is presented in Fig. 27. An examination of Fig. 27 reveals that sets A, C, E, H, and I correspond to  $\beta_1 = 40^\circ$  ( $C_x/U = 0.78$ ), set G corresponds to  $\beta_1 = 45^\circ$  ( $C_x/U = 0.68$ ) and sets B, D, and F correspond to  $\beta_1 = 54^\circ$  ( $C_x/U = 0.57$ ). Heat transfer data were obtained for all nine conditions with both the smooth-wall model and the rough-wall model for a total of eighteen (18) data sets.

The total number of heat transfer data sets (18) recorded under this contract exceeded the requirements of the statement of work by a factor of three. Due to cost limitations, it was not possible to complete the reduction, tabulation, presentation and analysis of all these heat transfer data under the present funding. For this reason eight (8) of the data sets were selected for reduction and presentation in this report. The eight (8) sets were selected such that data could be presented for two

(2) Reynolds numbers and two (2) flow coefficients (0.78 & 0.57) for both smooth and rough wall conditions, thus fulfilling the statement of work. Referring to Fig. 27, the data sets presented in this report were recorded at conditions B, E, F and G (both smooth and rough wall conditions for each of the four cases). The data recorded for the remaining ten (10) sets of data will be reduced, analyzed, and reported, assuming a separate follow-on contract effort is approved by NASA. UTRC anticipates submitting a formal proposal for this effort in the near future.

## EXPERIMENTAL RESULTS

As previously discussed, heat transfer data were obtained using both liquid-crystal thermography techniques and with arrays of surface thermocouples. The data will be presented in the following order: (1) Samples of the liquid-crystal data will be presented and discussed. The purpose of introducing these particular data first is that they provide a convenient method to discuss a number of general, qualitative features of the passage heat transfer distributions. (2) Next, the quantitative measurements of the passage heat transfer distributions (determined using both the thermocouple and liquid-crystal data) will be presented in the form of contour maps of Stanton number on the airfoil and hub endwall surfaces. (3) Finally, the streamwise distributions of the airfoil midspan heat transfer will be compared to the other test cases and to similar midspan data obtained previously under NASA-HOST funding.

### 1. Sample Liquid Crystal Data

Photographs of rotor-passage liquid-crystal temperature patterns were recorded for all nine (9) combinations of incidence and Reynolds number (see Fig. 27). These liquid-crystal data were obtained for the smooth-wall model only since color-temperature patterns were not discernable on the roughened surfaces. The liquid-crystal data acquisition procedure consisted of setting the LSRR to a particular incidence and Reynolds number combination and then adjusting the rotor-model power to produce a multi-color-band system of temperature contours. After allowing the heated model to reach thermal equilibrium, photographs of the temperature contours and scans of the model thermocouple array were simultaneously recorded.

Multiple photographs covering a range of film exposures and camera viewing angles were obtained for each test condition. In total, there were approximately 200 print-film and 100 slide-film photographs recorded for this program. Fourteen (14) print photographs have been selected from this array for presentation in this report. These fourteen (14) photographs were selected to demonstrate all the important qualitative features of the passage heat transfer distributions revealed in these liquid-crystal tests. The slide-film records will be employed to produce graphics for presentations.

Color-temperature contours recorded on the rotor pressure surface for a range of Reynolds numbers (from 2.3 to  $5.8 \times 10^5$ ) but a fixed incidence angle of  $\beta_1 = 40^\circ$  ( $C_x/U=0.78$ ) are presented in Fig. 28. Figure 28a was obtained for the highest test Reynolds number ( $Re = 5.8 \times 10^5$ ) and illustrates two important features of the pressure surface heat transfer. First, near the leading edge,

for the outer 60% of the span, the heat transfer pattern was nearly two-dimensional. There were three closely-spaced, monotonically increasing in temperature, isotherms roughly parallel to the leading edge line. These lines are marked by the (A) in Fig. 28a. This pattern indicates that, for  $\beta_1 = 40^\circ$ , the leading edge flow was attached (no separation bubble). Second, near the endwall, Fig. 28a shows a wedge-shaped region of relatively high heat transfer ((B) marker). One isotherm of this wedge pattern extended out to about 25% span. The next-higher-temperature isotherm, though showing a less distinct wedge shape, extended to nearly midspan. This phenomenon is thought to be produced by the secondary flows emerging from the first-stage stator. The first stator generates passage vortices near the hub and tip which enter the blade row as regions of intense turbulence and secondary flow (see Fig. 23). It is reasonable to expect that an enhancement of the heat transfer near the hub and tip would be produced as the rotor cuts through these regions of intense secondary flows. The tip region was not visible through the viewing window so it was not possible to determine if a similar effect occurred at the outer part of the span.

Figure 28b shows the liquid-crystal data for the next lower Reynolds number ( $Re = 5.2 \times 10^5$ ). Although the general features of this photograph are similar to those of Fig. 28a, there are two additional effects shown here that merit discussion. First, there was a small region of relatively high temperature (low heat transfer) indicated by the (C) marker. This max-temperature isotherm delineates the region of minimum heat transfer for the entire pressure surface at this inlet flow angle. As expected, this minimum heat transfer occurred near the end of the region of minimum flow speed on the pressure surface. It is interesting to note, however, that because of secondary flow effects the absolute-minimum heat transfer only existed in a small patch near midspan.

The photograph of the rotor passage model presented in Fig 28b captured a relatively clear view of the hub and revealed a feature of the hub-endwall heat transfer pattern. An endwall isotherm can be seen running from the pressure-surface/hub intersection at about 25% Bx, and across the hub at about 25% gap ((D) marker). The region enclosed by this isotherm corresponded to the zone of minimum hub endwall heat transfer. This region of relatively low hub heat transfer near the hub/pressure-surface intersection was common to all the  $\beta_1 = 40^\circ$  cases.

Figure 28c also shows an important feature of the endwall heat transfer. A zone of significantly increased heat transfer can be clearly seen near the hub/leading-edge intersection ((E) marker). This region of enhanced heat transfer is a product of the leading-edge (horseshoe) vortex system. Interactions between the horseshoe vortex system, the near-hub secondary flows from the upstream stator and the airfoil surface boundary layer may also be involved in the "wedge-shaped" pattern on the pressure surface near the endwall.

Notice that all four photographs of Fig. 28 show a local cold spot on the endwall near the pressure-surface junction and about 1/2 inch downstream of the first spanwise running grid line ((F) marker on Fig. 28c for example). This cold spot is not associated with the flow in the passage but arose solely because of a nearby hole through the heater foil. This hole was beneath the airfoil and was required to allow the main support rod for the airfoil to attach to the hub (see Figs. 6 and 9). Corrections for the localized non-uniformity in heater-foil current which arose from this hole were incorporated into the reduction of the endwall data.

Finally, Figure 28d also shows the small patch of minimum heat transfer near midspan similar to that indicated by the (C) marker of Fig. 28b.

Liquid-crystal temperature patterns for the airfoil pressure surface are also presented in Fig. 29. For this figure color-temperature patterns are shown for a range of both inlet flow angles and Reynolds numbers. Figure 29a shows the temperature distribution for  $Re = 5.1 \times 10^5$  and  $\beta_1 = 45^\circ$ . The temperature pattern near the leading edge was significantly different at this inlet flow angle than for all the cases of  $\beta_1 = 40^\circ$  shown in Fig. 28. At midspan the color pattern shows, moving downstream from the leading edge, that the temperature first increased then decreased and then increased again. This pattern indicates that there was a separation bubble near the leading edge overspeed site for this incidence angle. The local separation produced low heat transfer beneath the bubble followed by higher heat transfer at reattachment. The location and extent of the separation bubble probably coincide quite accurately with the fully closed isotherm indicated by the (G) marker.

Changing inlet flow angle from  $\beta_1 = 40^\circ$  also had an impact on the previously discussed "wedge-shaped" region of enhancement near the pressure-surface/endwall intersection. At  $\beta_1 = 45^\circ$  the near-endwall enhancement region merged with the midspan-region of enhancement associated with the reattachment of the separation bubble. For this incidence, then, a band of relatively high heat transfer, indicated by the (H) marker, extended across the entire span.

The remaining three photographs of Fig. 29 show color patterns recorded for  $\beta_1 = 54^\circ$  for a range of Reynolds numbers from 2.4 to  $4.2 \times 10^5$ . All three photographs show a narrow band of low heat transfer near the leading edge corresponding to a leading-edge-overspeed separation bubble. All three photographs also show that downstream of the separation bubble a band of relatively high heat transfer extended across the entire span.

To review, the effects of changing incidence on the leading-edge region heat transfer distribution can be seen by comparing Figs. 28b, 29a and 29d which were all recorded for roughly equal Reynolds numbers. For Fig 28a ( $\beta_1 = 40^\circ$ ) the flow was attached, but as the inlet flow angle was increased to  $\beta_1 = 45^\circ$  (Fig. 29a) and then to  $\beta_1 = 54^\circ$  (Fig. 29d) the leading-edge overspeed produced a local separation bubble. The strength and streamwise extent of the bubble reattachment zone increased with increasing  $\beta_1$ .

Notice, also, that Figs. 29a, b and c all show the enhancement of heat transfer produced by the horseshoe vortex system at the leading-edge/endwall junction. This effect is shown particularly clearly in Figs. 29b and c where two color bands (the second band is indicated by the (I) marker in Fig. 29c) were photographed in the leading edge region.

Suction-surface color-temperature patterns, obtained for a range of Reynolds numbers and inlet flow angles, are presented in Fig. 30. The effects on the temperature patterns produced by changing flow conditions ( $Re$  and  $\beta_1$ ) were much less on the suction surface than for the pressure surface. In fact, the general characteristics of the various temperature patterns for the suction-surface were so similar that they can be discussed most easily as a group. All four photographs of Fig. 30 show a pattern of isotherms originating near the front of the suction surface at either the hub or tip and converging near midspan at around 70%  $Bx$  (e.g. the isotherms marked

(J) for Fig. 30a). The order of the color bands indicates that the heat transfer was progressively higher moving from midspan towards the hub or tip. This temperature pattern, which was common to all the smooth-wall, suction surface test conditions, was almost certainly produced by the passage secondary flows (see Figs 21a and 25b).

The endwall boundary layers, having been swept across the endwall towards the suction surface by the cross-passage static pressure gradient, roll up into a pair of vortices located near the suction-surface-tip/endwall and the suction-surface-hub/endwall corners. This pair of passage secondary flows has the effect of producing a streamwise-converging flow pattern in the suction-surface boundary layer. Flow visualization data of Langston et al., 1977 and Joslyn and Dring, 1989 showed that this converging pattern corresponded to a pair of suction-surface separation lines. These separation lines divide the streamwise flow in the midspan region from the hub and tip regions which are dominated by the secondary passage flows. The effect on the suction-surface heat transfer produced by these secondary flows is to enhance the local Stanton number. The shape of the color-temperature patterns correspond directly with the shape of the lines of separation deduced from the flow visualization results presented in Fig. 21a.

All four photographs of Fig. 30 also show a region of intense heat transfer near the tip for the downstream 70% of the chord (e.g. (K) marker, Fig. 30a). This local enhancement was produced by the tip-leakage flow which rolls into a tip-leakage vortex in that region (see Fig. 21). Also, all four photographs of Fig. 30 show a region of enhanced heat transfer on the endwall just downstream of the airfoil leading edge (e.g. (L) marker, Fig. 30b). This enhancement is probably produced by the suction-surface leg of the leading-edge horseshoe vortex.

Finally, Fig. 31 presents close-up views of the color-temperature patterns on the airfoil trailing edge. Both photographs are for the same flow condition and merely give different views of the same color pattern. Apparently the trailing-edge heat transfer rates were much higher near the tip than for the remainder of the span. The (M) marker of Fig. 31a indicates three color lines between the midspan and tip regions.

## 2. Data Format

The heat transfer distributions measured on the airfoil and hub endwall surfaces will be presented in the form of contour maps of equal Stanton number. These contour maps were created in a three-step process. First, a commercially available topographical plotting routine (SURFER-Golden Software, Inc.) was employed to create contour maps from the thermocouple-array data. Second, these thermocouple-based contour maps were compared with the liquid-crystal temperature contours to assure compatibility with these supportive measurements. And finally, the liquid-crystal results were used to supplement the thermocouple data in regions where extremely localized effects were beyond the resolution of the thermocouple array, e.g. the leading-edge separation bubbles fell between rows of thermocouples.

The shape of the rotor airfoil surface, unwrapped and flattened on a plane, is complex (see Figs. 18 and 19). In order to alleviate the complexities involved with generating contours in this form a

coordinate system, illustrated in Fig. 32, was developed to project the complex airfoil-surface shape onto rectangles with the same span/arc-length ratio. The left-hand portion of Fig. 32 compares a number of coordinate scales on a rectangle. The horizontal axis is straightforward with the span percentage equal to the radial distance from the hub divided by the total airfoil span of 6.0 inches. The vertical scale running up the center of the rectangle shows the surface arc length, measured at midspan, with  $S = 0$  defined as in Fig. 16. The central-vertical and the horizontal scales are consistent in that 1 inch of span = 1 inch of arc-length. The right-hand vertical scale was constructed by non-dimensionalizing the surface distance by the total-arc-length for the respective (suction or pressure) surface. Although this scale has the advantage of ending at  $\pm 100\%$  (the trailing edge line) the inequality between the suction and pressure scales was considered to be cumbersome. To eliminate this problem it was decided to non-dimensionalize all arc-length distances by the span, thus making grid increments equal for the horizontal and for both the pressure and suction portions of the vertical scale. The disadvantage of this, of course, is that the trailing-edge lines coincide with values  $\neq 100\%$ . For the suction surface the trailing-edge line falls at 185% while for the pressure surface it falls at 132%.

The airfoil surface, though having a constant span, was not rectangular when unwrapped because the total surface-arc-length (on both surfaces) was a function of span. Rectangular projections were achieved by plotting off-midspan data at surface distances proportionally scaled by the ratio of midspan/local arc length. The mathematical definition of  $S^*$  is given at the top of Fig. 32.

The right-hand portion of Fig. 32 shows a sample set of airfoil surface heat transfer contours plotted in these % span vs. %  $S^*$  coordinates.

### 3. Heat Transfer Contours for the Smooth-Wall Model

Contour maps of the rotor passage heat transfer distributions (smooth-wall model) are presented in Figs. 33 through 36 for the various combinations of Reynolds number and inlet flow angle. Each data set is presented in three forms: a. - an overall view of both the endwall and airfoil heat transfer distributions, b. - expanded, separate views of the airfoil suction and pressure surface distributions and, c. - an expanded view of the hub endwall distribution .

For all of the contour map figures the inlet flow angle ( $\beta_1$ ), rotor RPM (N) and the test Reynolds number (Re) are given at the top. Contour keys indicate that the solid contours were constructed from the thermocouple data, the dash-dot contours were inferred from the liquid-crystal data and the dashed contours show finer increments of Stanton number (0.0001) for the pressure surface. The physical scales of the airfoil surface and hub endwall plots are identical for figures in which both appear (a-type figures) That is, spanwise, surface-arc-length, and the chordwise and gapwise dimensions are all consistent.

The first data set presented (Figs. 33a, b, and c) was obtained at  $\beta_1 = 40^\circ$  and  $Re = 4.4 \times 10^5$ . The airfoil surface views (a and b), consistent with the previously discussed liquid-crystal results, indicate that three-dimensional flow effects had a much stronger influence on the suction than on

the pressure surface. The influence of the passage vortices on the suction-surface heat transfer are apparent for  $S^* > 50\%$  at both the hub and tip. Note that the shape of the lines of constant suction-surface Stanton number shown on Figs. 33a and b agree with the shape of the lines of constant temperature for the suction-surface liquid-crystal photographs of Fig. 30. The absolute level of the Stanton number contours within the zones dominated by secondary flow (outboard of the suction-surface separation lines) was higher than observed at any streamwise station at midspan. In addition, two-dimensional boundary layer computations for the midspan flow, to be discussed in a later section, indicate that the midspan heat transfer reached equilibrium fully turbulent levels for the last 30% of chord. Based on these two facts it has been concluded that the passage-vortex secondary flows not only drove the suction-surface boundary layer through transition but also increased the heat transfer in the secondary-flow-dominated region above two-dimensional turbulent boundary layer rates.

The highest heat transfer rates on the suction surface were recorded near the tip for  $70\% < S^* < 130\%$ . This local enhancement, as discussed in the previous section, was produced by the tip-leakage vortex.

The pressure-surface results can be discussed most easily using Fig. 33b which shows contours of Stanton number with finer increments than used for the other figures. This figure shows the "wedge-shaped" enhancement region near the hub at  $S^* = 20\%$  and the minimum-heat-transfer patch at about 60% span and 30%  $S^*$ . Both of these features, as previously discussed, can be seen in the liquid-crystal photographs of Fig. 28. Note, also, that in the trailing-edge region the heat transfer rates were slightly higher near the tip than at the hub. This was probably a result of the tip-leakage flow. Because of the flow across the tip from the pressure surface the near-tip pressure-surface boundary layer is thinned relative the rest of the span. Somewhat higher heat transfer rates result for this near-tip region of reduced  $Re_\theta$  boundary layers.

The final observation regarding the rotor surface heat transfer can be seen in Fig. 33a. This figure shows that the peak heat transfer on the rotor was recorded at  $S^* = 0$  at midspan but at positive  $S^*$  (onto the suction surface) near the hub-leading edge intersection.

The hub endwall heat transfer distribution is presented in expanded scale in Fig. 33c. This figure clearly shows the regions of intense heat transfer near the rotor-leading-edge/endwall junction. This effect, a product of the leading-edge horseshoe vortex system, was also visible in the photographs of Figs. 28 and 29. The heat transfer beneath these leading-edge vortices was the maximum observed anywhere on the endwall. Notice that the region of enhanced heat transfer near the leading edge is not symmetrical about the stagnation line but extends considerably further towards the suction surface. This result supports the observation of the (towards-suction-surface) movement of the maximum-stagnation-line heat transfer on the rotor airfoil. The lowest heat transfer on the endwall occurred near the pressure-surface corner. Again, this effect was demonstrated in a liquid-crystal photograph in Fig. 28b.

The data set presented in Figs. 34 a, b, and c was obtained at the same inlet flow angle as the previous set but at a higher Reynolds number ( $Re = 5.8 \times 10^5$ ). The general characteristics of Figs. 34 were the same as for Figs. 33 with only minor changes of heat transfer level. As expected with

an increase in Reynolds number, all the fully-turbulent regions (the entire pressure surface, the aft portion of the suction surface and the entire endwall) showed slightly lower Stanton numbers compared to those of Fig. 33. The data trend in the fore-chord region of the suction surface was also as expected. In this region the boundary layer was passing through transition from laminar to turbulent, a process which was hastened by increasing the Reynolds number. Observe that for Fig. 33b there was a small patch of low (transitional) heat transfer at 70% span and 50%  $S^*$ . This transitional patch had disappeared for the higher test Reynolds number of Fig. 34.

The heat transfer distributions presented in Figs. 33 and 34 were for  $\beta_1 = 40^\circ$  while Figs. 35 and 36 present heat transfer distributions measured for two Reynolds numbers,  $2.4$  and  $4.2 \times 10^5$ , at  $\beta_1 = 54^\circ$ . The impact of changing the inlet flow angle can be readily seen by comparing the data of Figs. 33b and 36b which were obtained at nearly the same Reynolds number but at  $\beta_1 = 40^\circ$  and  $54^\circ$  respectively. Increasing the inlet flow angle produced the expected effects, increasing and decreasing the heat transfer rates on the pressure and suction surfaces respectively. The effects of changing Reynolds number at this incidence can be seen by comparing Figs. 35 and 36. Again, the trends were as expected with Stanton number decreasing everywhere with increased Reynolds number.

In the region of the airfoil leading edge, for both cases at  $\beta_1 = 54^\circ$ , a narrow band of reduced heat transfer (the region between the pairs of  $St = 0.0025$  contours of Figs. 35b and 36b) was observed at  $S^* = -5\%$ . Downstream of this narrow band of low heat transfer, the Stanton number increased rapidly and then gradually decreased for  $S^* > -20\%$ . In order to illustrate this effect in another format, plots of the streamwise distributions of the Stanton number at midspan are given in Figs. 35b and 36b. These plots show the rapid fall, the subsequent rise and then the gradual fall of Stanton number with increasing  $S$ . This heat transfer pattern indicates that, for  $\beta_1 = 54^\circ$ , a short separation bubble resulted at the pressure-surface leading-edge overspeed. The low heat transfer resulted directly beneath the bubble while the rapid rise to a much higher level was associated with reattachment. The gradual decline of the Stanton number downstream of reattachment coincided with the streamwise growth of the pressure-surface boundary layer.

The effects of the change in incidence on the hub endwall heat transfer distribution were not large. A comparison of Figs. 33c and 36c indicates that the most important effect was a slight ( $\approx 10\%$ ) drop in the Stanton number in the fore-chord region for the higher inlet flow angle. This decrease in the fore-chord region heat transfer with increased  $\beta_1$  was almost certainly due to the associated decrease in relative inlet velocity.

#### 4. Heat Transfer Contours for the Rough-Wall Model

Contour maps of the rotor passage heat transfer distributions for the rough-wall model are presented in Figs. 37 through 40 for the same combinations of Reynolds numbers and inlet flow angles as given for the smooth-wall cases. Again, each data set is presented in three forms: a. – an overall view of both the endwall and airfoil heat transfer distributions, b. – expanded, separate views of the airfoil suction and pressure surface distributions and, c. – an expanded view of the hub endwall

distribution. As previously discussed, no liquid-crystal data are incorporated into these rough-wall data sets.

Comparisons of any of the rough-wall and smooth-wall data sets obtained at similar operating conditions reveals that the surface roughness significantly increased the heat transfer rates at all locations. The largest relative changes ( $> 100\%$ ) occurred in the fore-chord, suction-surface region for the two cases at  $\beta_1 = 40^\circ$ . For the smooth-wall tests the boundary layer in this region was laminar/transitional while for the rough-wall cases it was apparently fully turbulent. The heat transfer data indicates that the surface roughness tripped the suction-surface boundary layer very near the stagnation line. This produced a low  $Re_\theta$  turbulent boundary layer with very high levels of heat transfer.

It is interesting to note that the local regions of augmented heat transfer, e.g. the leading-edge/endwall junction and the mid-chord, near-tip region of the suction surface, were still present on the rough-wall model. This result indicates that surface roughness had important augmentation effects even in regions with extremely thin, skewed, non-equilibrium boundary layers.

## 5. Midspan Heat Transfer Distributions

In the previous two sections rotor-passage heat transfer contour maps were presented for various inlet flow angles ( flow coefficients) and Reynolds numbers. These maps displayed the streamwise and spanwise variations in heat transfer on the airfoil surfaces as well as revealing highly localized heat transfer effects on the endwall.

Another useful format for the presentation of these heat transfer data consists of plots of the streamwise variation of the Stanton number at the airfoil midspan. In this form the present rough-wall and smooth-wall data can be compared to midspan heat transfer data obtained previously for this same turbine airfoil under NASA-HOST Contract NAS3-23717 (Dring et al., 1986). Midspan heat transfer distributions for  $Re = 4.2$  and  $5.6 \times 10^5$  at  $\beta_1 = 40^\circ$  are given in Figure 41. Data from the present tests are presented for both the smooth and rough wall cases, compared with NASA-HOST data for the same conditions. Also included are predictions from a two-dimensional, fully turbulent boundary layer computational procedure. For both Reynolds numbers the suction-surface smooth-wall and NASA-HOST data were in extremely good agreement. Agreement between these same data sets on the pressure surface was excellent for the entire surface at the lower Reynolds number and for the upstream half of the surface for the higher Reynolds number.

For the downstream half of the pressure surface at the higher Reynolds number the present heat transfer rates were as much as 25% less than those recorded for the NASA-HOST program. This discrepancy is thought to be a result of the difference in surface roughnesses for the NASA-HOST and the present models. Profilometer measurements of these surfaces indicates that the roughness of the NASA-HOST model was considerably more than for the present-test smooth-wall model and considerably less than for the present-test rough-wall model. The increments in surface

roughness separating the models were very nearly equal to factors of ten, i.e. the NASA-HOST model was approximately 10 times rougher than the present-test smooth-wall model while the present-test rough-wall model was 10 times rougher still than the NASA-HOST model.

By far the most dramatic effect shown in Figure 41 is the impact of the surface roughness. Its effect was to increase the heat transfer everywhere on the airfoil surface with the largest increase (approximately 100%) in the fore-chord regions of the suction surfaces. Note that the furthest-downstream point on the (rough wall) pressure surface registered a local decrease in Stanton number for both Reynolds numbers. This effect may be the result of one of the roughness grains sitting directly on the thermocouple site and is probably not a "real" phenomenon.

Midspan heat transfer distributions for  $Re = 2.3$  and  $4.2 \times 10^5$  at  $\beta_1 = 54^\circ$  are given in Figure 42. Although there were data obtained at this  $\beta_1$  under the NASA-HOST program none were obtained at these Reynolds numbers. For this reason Fig. 42 shows only a comparison of the respective rough and smooth wall cases. As with the data of Figure 41, these results indicate that the surface roughness produced a very significant increase in the heat transfer. Again, increases were particularly large in the fore-chord of the suction surface. The data points of Figure 42 are shown connected with straight-line segments for ease of interpretation.

Figure 43 shows comparisons of the smooth (upper figure) and rough (lower figure) wall data obtained at the same Reynolds number  $Re = 4.2 \times 10^5$  but different inlet flow angles. The effects were well behaved for the smooth-wall cases. Lowering the flow coefficient (increasing the inlet flow angle) increased and decreased heat transfer in the fore-chord regions of the pressure and suction surfaces respectively. Note that for the smooth-wall cases the trailing-edge-region heat transfer for the two flow coefficients were equal for both the suction and pressure surfaces. This is the expected result because the passage exit velocity (Reynolds number) was nearly identical for these two cases.

Results for the rough wall cases were less clear. Flow coefficient had little effect on either the pressure or suction surface heat transfer. This was probably because any leading-edge-overspeed/separation-bubble effects associated with off-design operation were overwhelmed by the extreme surface roughness.

## COMPUTATIONAL PROGRAM

### 1. Analysis

#### Generalized Potential Flow Coordinates

The basic equations of motion are derived in a potential flow coordinate system  $Y_1, Y_2, Y_3$  using the general vector relations derived by Owczarek (1964). This potential flow coordinate system can be constructed from any potential flow solution using the potential surfaces as one coordinate (streamwise coordinate  $Y_1$ ) and two mutually independent sets of stream surfaces ( $Y_2,$

$Y_3$ ) satisfying the Pfaffian differential equations described by Karamcheti (1980). This coordinate system has the particular advantages that it is body conforming and that the  $Y_1$  surfaces are orthogonal to the  $Y_2$  and  $Y_3$  surfaces reducing the number of metrics that must be stored. The general procedure for constructing a coordinate system is described by Anderson (1989).

### Construction of Duct Passage and Coordinates

The first step is to construct a duct passage simulating the gas turbine passage. With the blades and inlet conditions given, the UTRC CASPOF code was used to obtain the potential flow solution of the mid plane blade section yielding the upstream and downstream stagnation streamlines. In using the CASPOF code the downstream flow angle was adjusted until the pressure distribution matched the experimental pressure distribution. Then using the stagnation streamlines and the blade shape, a duct was constructed using these as boundaries. A two dimensional grid was then obtained using the UTRC CODUCT code which is an analysis based on the Schwarz–Christoffel transformation (Anderson et al., 1982). This grid is a potential flow solution for the flow through the simulated turbine passage in which the streamlines and potential lines form the coordinate grid. The UTRC Path code (Anderson, 1989) then constructs a three dimensional grid by extension in the radial direction calculating all the metrics as well as the transformation tensor from Cartesian coordinates to the calculation coordinates.

### Equations of Motion

The basic equations of motion are derived in the potential flow coordinate system using the general vector equations derived by Owczarek (1964). Since it is intended to use the secondary vorticity  $\Omega_1$  as a dependent variable, the two transverse momentum equations are replaced by the corresponding  $Y_2$  and  $Y_3$  components of Poisson's dynamical equations (see Owczarek, 1964) and the  $Y_1$  component of the vorticity transport equation. These equations are first derived in a general coordinate system using the metric coefficients of Warsi (1981). Then using the properties of the potential flow coordinate system, it is assumed that the cross flow velocities  $U_2$  and  $U_3$  are small compared the the streamwise velocity  $U_1$  and the secondary vorticity  $\Omega_1$  is small compared to the primary vorticities  $\Omega_2$  and  $\Omega_3$ .

$$\frac{\Omega_1}{\Omega_2} = \frac{\Omega_1}{\Omega_3} = O(\epsilon) \quad (1.1)$$

The equations of motion are then parabolized by neglecting terms of  $O(\epsilon^2)$ . It is noted that in in equations listed below, the distinction between covariant and contravariant vectors is dropped except for the metric coefficients.

### Continuity Equation

$$\frac{\partial}{\partial Y_1} \left[ \frac{\sqrt{g}}{h_1} \rho U_1 \right] + \frac{\partial}{\partial Y_2} \left[ \frac{\sqrt{g}}{h_2} \rho U_2 \right] + \frac{\partial}{\partial Y_3} \left[ \frac{\sqrt{g}}{h_3} \rho U_3 \right] = 0.0 \quad (1.2)$$

Reynolds, W. C., Kays, W. M. and Kline, S. J., 1958, "Heat Transfer in the Turbulent Incompressible Boundary Layer, III Arbitrary Wall Temperature and Heat Flux, NASA Memo 12-3-58w.

Schiff, L. B. and Steger, J. L., 1979, "Numerical Simulation of Steady Supersonic Viscous Flows", 17th Aerospace Sciences Meeting, AIAA paper 79-0130.

Sharma, O. P. and Graziani, R. A., 1983, "Influence of End Wall Flow on Airfoil Suction Surface Midheight Boundary Layer Development in a Turbine Cascade", ASME J. Engr. for Power, Vol. 105, pp. 147-155.

Sieverding, C. H., 1985, "Recent Progress in the Understanding of Basic Aspects of Secondary Flows in Turbine Blade Passages", ASME Journal of Engr. for Gas Turbines and Power, Vol. 107, No. 2, pp. 248-257.

Subramanian, C. S. and Antonia, R. A., 1981, "Effect of Reynolds Number on a Slightly Heated Turbulent Boundary Layer", Int. Journal of Heat and Mass Transfer, Vol. 24, No. 11, pp. 1833-1846.

Taylor, A. M. K. P., Whitelaw, J. H. and Yianneskis, M., 1981, "Measurements of Laminar and Turbulent Flow in a Curved Duct With Thin Inlet Boundary Layers", NASA Contractor Report 3367.

Vermeulen, A. J., 1971, "Measurements of Three Dimensional Turbulent Boundary Layers", Phd. Dissertation, University College, Cambridge.

Vigneron, Y. C., Rakich, J. V. and Tannehill, J. C., 1978, "Calculation of Supersonic Viscous Flows Over Delta Wings with Sharp Supersonic Leading Edges", NASA TM-78500.

Warsi, Z. U. A., Tensors and Differential Geometry Applied to Analytic and Numerical Coordinate Generation, Mississippi State University, MSSU-EIRS-81-1.

### Streamwise Momentum Equation

$$\begin{aligned}
 & \frac{\partial}{\partial Y_1} \left[ \frac{\sqrt{g}}{h_1} \rho U_1 U_1 \right] + \frac{\partial}{\partial Y_2} \left[ \frac{\sqrt{g}}{h_2} \rho U_2 U_1 \right] + \frac{\partial}{\partial Y_3} \left[ \frac{\sqrt{g}}{h_3} \rho U_3 U_1 \right] + \frac{\sqrt{g}}{h_1} \frac{\partial P}{\partial Y_1} \\
 & - \sqrt{g} g^{22} \frac{\partial}{\partial Y_2} \left[ \mu_t \frac{\partial U_1}{\partial Y_2} \right] - \sqrt{g} g^{23} \frac{\partial}{\partial Y_2} \left[ \mu_t \frac{\partial U_1}{\partial Y_3} \right] \\
 & - \sqrt{g} g^{32} \frac{\partial}{\partial Y_3} \left[ \mu_t \frac{\partial U_1}{\partial Y_2} \right] - \sqrt{g} g^{33} \frac{\partial}{\partial Y_3} \left[ \mu_t \frac{\partial U_1}{\partial Y_3} \right] = 0.0
 \end{aligned} \tag{1.3}$$

### Transverse Pressure Equation

$$\begin{aligned}
 & \frac{\partial}{\partial Y_2} \left[ \sqrt{g} (g^{22} \frac{\partial P}{\partial Y_2} + g^{23} \frac{\partial P}{\partial Y_3}) \right] + \frac{\partial}{\partial Y_3} \left[ \sqrt{g} (g^{23} \frac{\partial P}{\partial Y_2} + g^{33} \frac{\partial P}{\partial Y_3}) \right] \\
 & + \frac{\partial}{\partial Y_2} \left[ \frac{\sqrt{g}}{h_2} K_2 \rho U_1^2 \right] + \frac{\partial}{\partial Y_3} \left[ \frac{\sqrt{g}}{h_3} K_3 \rho U_1^2 \right] + C_r \frac{\partial}{\partial Y_3} \left[ \frac{\sqrt{g}}{h_3} \rho \frac{U_1^2}{r} \right] = 0.0
 \end{aligned} \tag{1.4}$$

### Energy Equation

$$\begin{aligned}
 & \frac{\partial}{\partial Y_1} \left[ \frac{\sqrt{g}}{h_1} \rho U_1 H_T \right] + \frac{\partial}{\partial Y_2} \left[ \frac{\sqrt{g}}{h_2} \rho U_2 H_T \right] + \frac{\partial}{\partial Y_3} \left[ \frac{\sqrt{g}}{h_3} \rho U_3 H_T \right] + \\
 & - \frac{1}{Pr_t} \sqrt{g} g^{22} \frac{\partial}{\partial Y_2} \left[ \mu_t \frac{\partial H_T}{\partial Y_2} \right] - \frac{1}{Pr_t} \sqrt{g} g^{23} \frac{\partial}{\partial Y_2} \left[ \mu_t \frac{\partial H_T}{\partial Y_3} \right] \\
 & - \frac{1}{Pr_t} \sqrt{g} g^{32} \frac{\partial}{\partial Y_3} \left[ \mu_t \frac{\partial H_T}{\partial Y_2} \right] - \frac{1}{Pr_t} \sqrt{g} g^{33} \frac{\partial}{\partial Y_3} \left[ \mu_t \frac{\partial H_T}{\partial Y_3} \right] \\
 & - \frac{Pr_t - 1}{2Pr_t} \sqrt{g} g^{22} \frac{\partial}{\partial Y_2} \left[ \mu_t \frac{\partial U_1^2}{\partial Y_2} \right] - \frac{Pr_t - 1}{2Pr_t} \sqrt{g} g^{23} \frac{\partial}{\partial Y_2} \left[ \mu_t \frac{\partial U_1^2}{\partial Y_3} \right] \\
 & - \frac{Pr_t - 1}{2Pr_t} \sqrt{g} g^{32} \frac{\partial}{\partial Y_3} \left[ \mu_t \frac{\partial U_1^2}{\partial Y_2} \right] - \frac{Pr_t - 1}{2Pr_t} \sqrt{g} g^{33} \frac{\partial}{\partial Y_3} \left[ \mu_t \frac{\partial U_1^2}{\partial Y_3} \right] = 0.0
 \end{aligned} \tag{1.5}$$

### Vorticity Equation

$$\frac{\partial}{\partial Y_2} \left[ \frac{g_{23}}{h_2} U_2 + h_3 U_3 \right] - \frac{\partial}{\partial Y_3} \left[ h_2 U_2 + \frac{g_{23}}{h_3} U_3 \right] - \frac{\sqrt{g}}{h_1} \Omega = 0.0 \tag{1.6}$$

## Vorticity Transport Equation

$$\begin{aligned}
 & \frac{\partial}{\partial Y_1} \left[ \frac{\sqrt{g}}{h_1} \rho U_1 \Omega \right] + \frac{\partial}{\partial Y_2} \left[ \frac{\sqrt{g}}{h_2} \rho U_2 \Omega \right] + \frac{\partial}{\partial Y_3} \left[ \frac{\sqrt{g}}{h_3} \rho U_3 \Omega \right] - \frac{\sqrt{g}}{h_1} \Omega \frac{\partial}{\partial Y_1} [\rho U_1] \\
 & - (h_1 h_2 K_2) \frac{\partial}{\partial Y_3} [\rho U_1^2] + (h_1 h_3 K_3) \frac{\partial}{\partial Y_2} [\rho U_1^2] \\
 & - \sqrt{g} g^{22} \frac{\partial^2}{\partial Y_2^2} [\mu_t \Omega] - 2\sqrt{g} g^{23} \frac{\partial^2}{\partial Y_2 \partial Y_3} [\mu_t \Omega] - \sqrt{g} g^{33} \frac{\partial^2}{\partial Y_3^2} [\mu_t \Omega] + C_r 2V_2 \frac{1}{h_1} \frac{\partial}{\partial Y_1} \left[ \frac{\sqrt{g}}{h_1} \rho U_1 \right] = 0.0 \quad (1.7)
 \end{aligned}$$

In these equations, the two first order momentum equations have been replaced by the vorticity transport equation and a transverse pressure equation. The vorticity transport equation is used in the manner of Briley and McDonald (1974) to explicitly calculate the secondary vorticity. The transverse pressure equation is obtained by differentiating the first order momentum equations (Poisson's dynamical equations) and adding together in the manner of Ghia (1979). It should be noted that some curvature terms (derivatives of the metrics in the stress tensor) have been neglected based on the experience of Anderson (1980) in that streamline curvature is much more important in the turbulence modeling than in the momentum equations. It is also noted that there is a significant residual benefit to using the potential flow coordinate system. The pressure gradient may be separated into two components; the streamwise pressure gradient determined by duct area and flow blockage, and the transverse pressure gradient determined by the principal streamline curvature. As can be seen by the transverse pressure equation, (Eq. 1.4), the transverse pressure is determined exclusively by the principal curvature components  $K_2$  and  $K_3$ .

## Auxiliary Equations

These equations of motion are closed using the following auxiliary relations.

$$P = \rho RT \quad (1.8)$$

$$H_T = C_p T + \frac{U^2}{2} - C_r \frac{V^2}{2} \quad (1.9)$$

In addition it is noted that the magnitude of the velocity is given by

$$U^2 = U_1^2 + U_2^2 + U_3^2 + \frac{2g_{23}}{h_2 h_3} U_2 U_3 \quad (1.10)$$

## Stationary/Rotating Coordinates

The Constant  $C_r$  takes on the value of 0.0 for stationary coordinates and the value of 1.0 for rotating coordinates. In rotating coordinates, the terms having  $C_r$  as a coefficient are the Coriolis

terms. All the dependent variables  $U_1, U_2, U_3, H, \Omega$  are the values in the rotating coordinating system.  $H_T$  becomes the rothalpy in the rotating coordinate system, but  $U_\phi$  remains the tangential velocity in the stationary coordinate system. These Coriolis forces are assumed to be written in a coordinate system where the coordinate  $Y_3$  is assumed to be aligned with the radial direction. These Coriolis forces are easily identified. In the transverse pressure equation Eq. 1.4, the term is essentially the centrifugal force. In the vorticity transport Eq. 1.7, it is the component of coordinate rotation added to the relative vorticity after the manner of (Dring and Joslyn, 1983).

### Global Conditions and Boundary Conditions

The solution to these equations requires boundary conditions for six equations and six unknowns. These boundary conditions are

$$U_1 = 0 \quad (1.11)$$

$$U_2 = 0 \quad (1.12)$$

$$U_3 = 0 \quad (1.13)$$

for the no slip boundary condition. For adiabatic walls we have,

$$\frac{\partial H_T}{\partial Y_2} = 0.0 \quad (1.14)$$

$$\frac{\partial H_T}{\partial Y_3} = 0.0 \quad (1.15)$$

and for prescribed wall temperature (heat transfer) we have,

$$H_T = H_{TW} \quad (1.16)$$

On the vorticity we have,

$$\begin{aligned} \frac{\sqrt{g}}{h_1} \Omega &= \frac{\partial}{\partial Y_2} \left[ \frac{g_{23}}{h_2} U_2 + h_3 U_3 \right] \\ \frac{\sqrt{g}}{h_1} \Omega &= -\frac{\partial}{\partial Y_3} \left[ h_2 U_2 + \frac{g_{23}}{h_3} U_3 \right] \end{aligned} \quad (1.17)$$

Finally for the transverse static pressure equation we may have either of two boundary conditions.

$$\begin{aligned} \frac{\partial P}{\partial Y_2} &= 0.0 \\ \frac{\partial P}{\partial Y_3} &= 0.0 \end{aligned} \quad (1.18)$$

$$\frac{\partial P}{\partial Y_2} = -\frac{\sqrt{g}}{h_1 h_3^2} \frac{\partial(\mu_t \Omega)}{\partial Y_3}$$

$$\frac{\partial P}{\partial Y_3} = \frac{\sqrt{g}}{h_1 h_2^2} \frac{\partial(\mu_t \Omega)}{\partial Y_2} \quad (1.19)$$

depending on the wall. The first boundary condition 1.18 is consistent with the approximations used to simplify the equations of motion namely that the cross flow is small. The second set of boundary conditions (1.19) is required when the cross flow is moderately large. Substitution of the definition of vorticity into this equation results in

$$\frac{\partial P}{\partial Y_2} = -\frac{\sqrt{g}}{h_1 h_3^2} \frac{\partial}{\partial Y_3} \left( \mu_t \frac{\partial U_2}{\partial Y_3} \right) \quad (1.20)$$

which is easily recognized from the boundary layer equations as the pressure gradient in the crossflow direction. The second boundary conditions is implemented by integrating Eqs. 1.19 around the boundary to obtain the static pressure to within an additive constant. These conditions on the pressure and their consequence will be discussed in more detail later in the discussion section.

In addition we note according to Brandt that two global conditions must be satisfied.

$$\int \dot{S} dY_2 dY_3 = \oint h_1 \rho \vec{U} \circ \vec{n} dy \quad (1.21)$$

and

$$\int \dot{\Omega} dY_2 dY_3 = \oint \vec{U} \circ d\vec{y} = \Gamma \quad (1.22)$$

where

$$\dot{S} = -\frac{\partial}{\partial Y_1} \left[ \frac{\sqrt{g}}{h_1} \rho U_1 \right] \quad (1.23)$$

$$\dot{\Omega} = \frac{\sqrt{g}}{h_1} \Omega \quad (1.24)$$

Eq. 1.21 states that the rate of change of mass flow crossing the computational area is equal to the net mass flow entering at the boundaries. Eq. 1.22 is recognized as Stokes theorem which states that the integral of the secondary vorticity over the crosssectional area is equal to the circulation. We note that either Eq. 1.18 or Eq. 1.19 satisfies the boundary condition only to within an additive constant. This additive constant is obtained by satisfying the global mass flow constraint Eq. 1.21. The second constraint, Eq. 1.22, is necessary to insure convergence of the secondary flow field (i.e.,  $U_2, U_3$ ). It can be seen from Stokes theorem that for flows in ducts, the circulation over a crosssection is always zero. The algorithm for solving these equations with the given boundary conditions is given in Anderson (1989).

## Algebraic Turbulence Modeling

The problem associated with implementing an algebraic turbulence model for a turbulent boundary layer is the determination of a turbulent length scale such as the boundary layer thickness, boundary layer displacement thickness, or as with the Baldwin–Lomax model a length scale based on vorticity. In complex three dimensional flows such as occur in turbine vane passages, this length scale is often ambiguous and difficult to determine. Thus as an example, three dimensional flows have no region in the free stream where the vorticity is zero so that the Baldwin–Lomax vorticity function which was fitted to a simple flat plate boundary may lose some of its meaning. However although boundary layer displacement thickness is ambiguous in passage flows, blockage is not. Therefore an algebraic eddy viscosity model based on blockage, which is an extension of the model used in Anderson (1980), was developed.

This model is a two layer model where the outer portion of the boundary and the free stream is described with a constant eddy viscosity based on the blockage and the inner layer near the wall is described by the Van Driest's model. In the outer region we have an effective displacement thickness  $\delta^*$  given by,

$$\delta^* = \frac{A}{l} \left[ 1 - \frac{W}{A(\rho U_1)_{max}} \right] \quad (1.25)$$

where  $A$  is the passage area,  $W$  is the mass flow,  $l$  is the wall perimeter, and  $\rho U_1$  is the mass flux. As can be seen from the definition,  $\delta^*$  is defined by global parameters which are unambiguous. The eddy viscosity in the outer layer is then given by,

$$\mu_t = \mu + \chi_e (\rho U_1)_{max} \delta^* \quad (1.26)$$

The Van Driest eddy viscosity distribution is given by;

$$\mu_t = \mu + \frac{2\mu_w (\kappa D Y^+)^2}{1 + \sqrt{1 + 4(\kappa D Y^+)^2}} \quad (1.27)$$

where the Van Driest damping is given by,

$$D = 1 - \exp\left(\frac{-Y^+}{A^+}\right) \quad (1.28)$$

In a corner two walls affect the mixing length  $Y^+$ . Therefore it was assumed that

$$\frac{1}{(Y^+)^2} = \frac{1}{(Y_1^+)^2} + \frac{1}{(Y_2^+)^2} \quad (1.29)$$

where the subscripts refer to the closest and next closest walls. It may be observed that far from the second wall, the mixing length reduces to that for a two dimensional boundary layer.

## 2. Results and Discussion

### Turbulent Flow in a Square Curved Duct

The laminar and turbulent flow in a square curved duct with small radius of curvature was measured by Taylor et al. (1981) and a solution for the turbulent flow field was first given by Kreskovsky et al. (1979) using an approximate solution for the turbulent sublayer. This flow field presents a particularly difficult test for the analysis because of the large secondary flows which are generated in the plane normal to the mean flow direction. Thus the assumption of small secondary flow velocities, which was used to derive the equations of motion, is severely tested.

The potential flow solution used for the coordinate system was calculated using the analysis given by Anderson et al. (1982) where the computational grid consists of 100 streamwise stations with a crossplane grid of 49 x 49 mesh points. Figure 44 shows, for clarity, the coordinate grid with only 17 uniformly spaced streamlines and 50 streamwise stations (potential planes). The actual grid consists of 49 streamlines nonuniformly spaced to resolve the boundary layer flow accurately. The inlet conditions were measured at approximately streamwise station  $I = 20$  (i.e.  $I = 10$  on Fig. 44) which is just upstream of the turn. The measured conditions were used to start the calculation at this station. The exit station just downstream from the turn occurs at approximately  $I = 72$  (i.e.  $I = 36$  on Fig. 44).

The flow conditions given in Taylor et al. (1981) indicate a Reynolds number based on hydraulic diameter as 40,000 in water which is turbulent and incompressible. Thus the mean inlet flow velocity was chosen at 100 ft/sec to eliminate compressibility effects and the molecular viscosity adjusted to match the Reynolds number. Initial conditions specified uniform flow with a boundary layer thickness about 10 per cent of the height of the duct corresponding to a Reynolds number based on momentum thickness of about 400 which is quite low.

Data was obtained at angular distances of  $\theta = 30.$ ,  $60.$ , and  $90.$  degs. At  $\theta = 90.$  degs, the secondary flow field is shown on Fig. 45. The center of the passage vortex is clearly seen centered near the ID wall. Maximum velocities in the end wall boundary layer reach 40 ft/sec which is a significant fraction of the free stream velocity (100 ft/sec) and which severely test the assumptions made in the analysis. The streamwise velocity profile in the boundary layer in universal coordinates is shown on Fig. 46 where it is compared to the law of the wall and a laminar sublayer curve of  $U^+ = Y^+$ . This profile was taken at  $\theta = 90.$  degs on the end wall and in the mid channel. It can be seen from this figure that the law of the wall is satisfied using the algebraic turbulence model developed for this analysis. Details of the boundary layer at this same location are shown in Fig. 47. The  $U_1$  and  $U_2$  components were resolved into the free stream direction  $U_s$ , and the cross flow direction  $U_c$ . However since the boundary layer Reynolds number is so low, power law curve fits such as the empirical correlation of Mager (1952) are not useful.

Figs. 48 through 53 show a comparison of the calculated streamwise and cross flow velocities with the measurements for planes at  $\theta = 30.$ ,  $60.$  and  $90.$  degs. It can be seen from these figures that the results are quite good indicating that the analysis can provide a quite accurate calculation even

when the cross flow velocity is quite large. A closer inspection indicates that the secondary  $U_2$  is predicted very well. At  $r^* = .1$  and  $.9$ , the traverses are within the side wall boundary layers large velocity gradients and so are quite sensitive to location of the traverse relative to the boundary layer thickness. In the core flow region, the predictions are also good. The overall boundary layer thickness is also predicted very well. In addition one notes that the flow ( $U_1$  velocity) at  $\theta = 60$ . and  $90$ . degs has a significant depression on the ID wall near the mid span. This phenomena is also predicted, but the extent of the region is under predicted. It is also interesting that the analysis correctly predicts that the  $U_1$  velocity peaks on the OD (pressure) side of the duct. This peaking of the velocity on the pressure side of the duct is a consequence of the secondary flow mixing which appears to be reasonably well modeled by the analysis.

### LSRR Gas Turbine Cascade

The UTRC Low Speed Rotating Rig (LSRR) tests used a rotor mid plane section identical to earlier tests performed in a cascade by Graziani et al. (1980). These tests included static pressure distributions at several spanwise sections, and heat transfer measurements on the blade surfaces and the end wall. Since these tests are in stationary coordinates, they may be thought of as representative of heat transfer on a gas turbine stator, and can be used to verify the analysis and the computational procedure.

### **Construction of Duct Passage & Computational Grid**

The coordinate system for the gas turbine cascade was constructed using the procedure described in the analysis section. The grid obtained in this manner is shown on Fig. 54 with the turbine blades superimposed. It has  $100 \times 49 \times 49$  mesh ( $Y_1, Y_2, Y_3$  directions respectively) points and will be used as a reference grid for all the figures which follow. The actual calculation was made on a  $200 \times 49 \times 49$  where the intermediate streamwise grid planes were interpolated.

As was noted in the analysis section, this grid is obtained from the potential flow solution for the flow through the simulated gas turbine passage. Thus the computational coordinates are the potential lines  $Y_1$  coordinate and the streamlines  $Y_2$  coordinate. Therefor the potential flow static pressure distribution can be obtained from the metric  $h_1$  of the coordinates. In terms of the metrics, the pressure coefficient  $C_p$  is given by,

$$C_p = 1 - \left(\frac{h_1^0}{h_1}\right)^2 \quad (2.30)$$

By comparing the calculated inviscid static pressure distribution with the measured static pressure distribution, one can evaluate how well the simulated gas turbine passage represents the the blade. This comparison is shown on Fig. 55 and indicates that the coordinates are a reasonable approximation of the turbine cascade passage.

In addition to constructing the mesh, one must consider the distribution of mesh points. Thus in order to clearly resolve the boundary layers down into the sublayer rather than using wall function or other approximations near the wall a large number of mesh points must be devoted to defining the boundary layer. This may be done by distorting the mesh and crowding mesh points near the wall.

The distribution of mesh points was determined by requiring at least fifteen to twenty mesh points to define the boundary layer as shown in the detail of the boundary layer shown on Fig. 56.

### Verification of Aerodynamic Predictions

Since the LSRR gas turbine cascade is simulated by a duct passage, it is very important that the duct passage produce a static pressure distribution which closely approximates the pressure distribution on the cascade blades. Measurements of the static pressure distributions at three locations on the cascade blade were taken by Camarata et al. (1975) which can be used as a baseline comparison with the calculated pressure distributions. The calculations were made with the pressure boundary condition Eq. 1.18 which specifies a zero normal pressure at the walls. The comparisons between the calculated and measured wall pressure distributions are shown on Figs. 57, 58 and 59. As can be seen on these figures, the predictions are quite good for the mid span and quarter span pressure distributions but fail to predict the unloading of the blade near the hub. When one examines the equations of motion, it is seen that a pressure gradient can only be produced by the streamline curvature of the potential flow as expressed by Eq. 1.4. For this case, the potential flow has no spanwise pressure distribution and therefore there is no spanwise pressure distribution calculated. However if one uses the boundary condition given by Eq. 1.19, a spanwise pressure distribution will be created by the secondary flow. Attempts to implement this second boundary condition have not been successful.

### Verification of the Turbulence Model

The algebraic eddy viscosity model was used for this calculation is an extension to three dimensions of the model used by Anderson (1980) and is described in the analysis section. It is a two layer model satisfying the law of the wake and the law of the wall. Since detailed boundary layer profile data are not available for this case, verification consists of making sure that the law of the wall is satisfied. Figures 60 and 61 show the developing streamwise velocity profiles in universal turbulent coordinates compared to the law of the wall and laminar sublayer along the end wall and along the suction surface of the duct. As can be seen from these comparisons, the law of the wall is accurately captured. Note also the number of points in the sublayer which is accurately captured as well. Near the inlet ( $i = 10$ ), the wake region of the boundary layer is much like any two dimensional boundary layer. However as the flow progresses downstream, the wake region changes considerably. At the present time, this effect can not be evaluated without detailed boundary layer data.

Detailed boundary layer data is not available for this case. However detailed boundary layer data was obtained by Vermeulen (1971) for a rectangular duct turning 60 deg. If one compares two stations on the end wall with the same amount of turning, the principal features of the boundary layer should be similar. At the selected point in the flow field, the the edge of the boundary, the magnitude of the free stream velocity  $U_e$ , and the flow direction were determined. Then the velocity components were resolved into the streamwise direction  $U_s$  and the normal (crosswise) direction  $U_c$ . Using the friction velocity  $U_\tau$ , the two components of velocity can be calculated in universal

coordinates. Fig. 62 shows the boundary layer profiles in universal coordinates calculated for the LSRR turbine cascade passage, and Fig. 63 shows the results measured by Vermuelen (1971). Although a one on one comparison can not be made, the principal features of the boundary layer flow are similar. The  $U_s^+$  velocity component closely follows the law of the wall in both cases. The cross flow component  $U_c^+$  reaches a maximum at about  $Y^+ = 30$  for the calculated flow and at about  $Y^+ = 50$  for the measured flow. The calculated flow shows a slightly higher maximum crossflow velocity. Overall it may be concluded that the principal features of the boundary layer flow on the end wall are captured.

### Development of the Passage Vortex

It is well known that gas turbine passages develop a passage vortex which generally ends up near the suction surface at the exit. This passage vortex plays an important role in the heat transfer. Thus an accurate capturing of the passage vortex is essential for the prediction of the heat transfer. The development of this vortex is shown on Fig. 64. As shown on this figure, the secondary flow on the end wall is just starting at ( $i = 20$ ) which is near the leading edge of the blades. Near the mid chord ( $i = 30$ ), a clear vortex pattern has developed which appears centered on the end wall. The center of this vortex moves along the end wall from the pressure to the suction side of the passage until near the trailing edge at ( $i = 60$ ) it is in the corner of the passage. Then the vortex moves up the suction surface at the trailing edge as shown at ( $i = 80$ ). The location of this vortex is close to where it is observed experimentally in turbine passages. The mechanism by which the vorticity generated by the end wall boundary layer is swept up into a vortex is clearly captured. In addition we note that the vortex follows streamlines as the vorticity transport theorem predicts.

A detail of the flow in the suction surface/end wall corner is shown on Fig. 65 where the gapwise velocity ( $U_2$ ) distribution is clearly plotted. This velocity decreases as it approaches the suction surface and turns the corner. Then on the suction surface, the spanwise velocity increases as it leaves the end wall. One can see clearly that the peak crossflow is very close to the wall. The development of the crossflow velocity along the end wall on a coordinate line midway along the gap ( $j = 25$ ) is shown on Fig. 66. Peak gapwise velocities reach a value of 89.0 ft/sec at about ( $i = 42$ ) and then decrease slowly. This peak velocity thus approaches the inlet streamwise velocity which is 93.0 ft/sec. Some interesting observations may be made about the secondary vorticity distribution (streamwise component of vorticity) which drives the secondary flow. Since the derivative ( $dU_2/dY_3$ ) is the vorticity near the end wall, the vorticity must change sign at the peak velocity. Hence we see from Fig. 66 that the vorticity distribution consists of a very large region of small vorticity in the middle of the duct and a very thin region of very large vorticity along the walls. In fact these two regions must just cancel since by Stokes theorem the circulation on a crossplane must be zero. The vorticity in the core flow is the classical (inviscid) secondary vorticity, while the vorticity near the wall is that generated by the boundary layer and which slowly diffuses inward.

The passage vortex has a profound effect on the wall streamlines. Since the limiting streamlines are tangent to the skin friction vectors, a plot of these vectors shows the direction of these streamlines. These vectors are shown on Figs. 67 and 68. On the end wall one observes very large

crossflow from the pressure side to the suction side of the passage. This crossflow, as observed above, approaches the inlet streamwise velocity of 93.0 ft/sec. On the suction surface, one observes the flow moving from the end walls in towards the midspan. These spanwise velocities are not quite as large as the gapwise velocities, but do approach approximately 60.0 ft/sec compared to the 93.0 ft/sec of the inlet streamwise velocity. The effect of the passage vortex is to sweep flow from the end wall up on to the suction surface.

### **Evaluation of Heat Transfer Predictions**

A comparison of the calculated heat transfer with experimental data Graziani et al. (1980) for the end wall and suction surfaces is shown on Figs. 69 through 74. It should be noted that since the cascade passage is treated as a duct, the complex flow on the end wall surrounding the leading edge can not be rigorously treated as well as the flow on the leading edge of the blade. However, in spite of this, the general features and level of the heat transfer on the end wall are captured. Thus we note that a small peak in heat transfer near the leading edge ( $S_t = 3.0 \times 10^3$ ) is predicted. The heat transfer then drops off especially near the pressure surface (note  $S_t = 1.0 \times 10^3$  contour). Finally the heat transfer reaches a peak near the trailing edge of ( $S_t = 4.0 \times 10^3$ ) compared to the maximum measured heat transfer of ( $S_t = 4.0 \times 10^3$ ). The comparison of the suction surface heat transfer shown on Figs. 71 and 72 is not quite as good. The calculation shows peak heat transfer near the midspan (note  $S_t = 3.5 \times 10^3$  contour) where the measured peak heat transfer is close to the end walls. However, it should be noted that the boundary layer on the suction surface was a transitional boundary layer (Sharma and Graziani, 1983) and transition was not modeled. These observations are also seen in Figs. 73 and 74 which compare the calculated  $S_t$  on the end wall and suction surface with the measurements of Graziani et al. (1980). In both cases it appears that the general level of the heat transfer is predicted as well as the high and low points although the location of these points are not that well predicted.

### **LSRR Gas Turbine Rotor**

#### **Construction of Duct Passage & Computational Grid**

The gas turbine blade sections designed for the LSRR tests are shown stacked on Fig. 75. It has a constant axial chord with a slight twist and a considerable change in the thickness distribution. The gap to chord and span to chord are approximately 1.0. At the present time, the PATH code does not have the capability of constructing a coordinate system for this blade passage. Therefore an approximate blade passage was constructed using the mid span blade section and assuming a constant blade section. The mid span section is the same as that used in the cascade tests by Graziani et al. (1980) and Langston et al. (1977). The procedure for obtaining the coordinate system is described in the analysis section and leads to a coordinate system shown on Fig. 54. The calculations then will not show any effects due to blade twist or blade thickness distribution.

## Evaluation of Heat Transfer Predictions

A comparison between the calculated and measured heat transfer is shown on Figs. 76 through 79 for the end wall and suction surfaces. The comparison for the end wall Figs. 76 and 77 generally shows lower predicted heat transfer than was measured although the code does predict a qualitative increase in heat transfer near the trailing edge of the blade similar to that which was measured and a low rate of heat transfer near the pressure surface. The distribution of end wall heat transfer is qualitatively similar to that predicted for the cascade (stator) passage. The comparison for the suction surface is shown on Figs. 78 and 79. Again we note higher rates of measured heat transfer than was calculated and in addition we note that the distribution of heat transfer is quite different. The calculated heat transfer is again more similar to that calculated for cascade (stator). A major difference can of course be attributed to the fact that the twist a thickness distribution effects were not simulated although a final conclusion can not be made until the calculation is repeated with these effects included. Since the calculations used the mid span blade shape to construct the coordinate system, heat transfer on the mid span may be better predicted. A comparison of the calculated and measured mid span heat transfer on the suction surface is shown on Fig. 80. One can see that the predictions are quite good accept near the leading edge where one may expect differences since a duct passage was used to simulate the turbine passage so that the leading edge effects were neglected.

## Comparison of Stator/Rotor Coriolis Effects

The calculations for both the cascade (stator) and the rotor were run on the same coordinates and with the same inlet conditions. The only difference being that the rotor had the Coriolis forces included whereas the stator did not. Therefore these calculations can be used to estimate the effect of Coriolis forces alone on the heat transfer. Figure 81 shows the effect of Coriolis forces on the behavior of the passage vortex by comparing the location of the passage vortex for the stator and rotor at the same location in the turbine passage. This figure appears to indicate that the Coriolis effect alone on the location of the vortex is quite small. Figures 82 and 83 show the effect of Coriolis forces on the endwall and suction heat transfer. It appears that the Coriolis forces have very little effect on the mid span suction surface heat transfer and a significant effect on the end wall heat transfer. A second observation may also be made in that the blade thickness distribution and twist have a major effect on the suction surface heat transfer as indicated by Figs. 78 and 79.

## CONCLUSIONS

A combined experimental and computational program has been conducted to examine the heat transfer distribution in a turbine rotor passage. Heat transfer was measured and computed for both the full-span suction and pressure surfaces of the rotor airfoil as well as for the hub endwall surface. The effects of the following variables on the rotor passage heat transfer were documented:

- \* Reynolds number
- \* Rotor inlet flow angle (flow coefficient)

\* Surface roughness

Conclusions reached from an examination of these results are as follows:

### Design-Incidence Test Cases

- (1) The heat transfer data indicate that the flow was everywhere attached at design incidence; there was no evidence of separation bubbles on either the airfoil or endwall surfaces (e.g. Figs. 33 and 34).
- (2) Three-dimensional flow effects associated with the main passage vortices had a much stronger influence on the suction than on the pressure surface (e.g. Fig. 33b). In the aft-chord region, near both the hub and tip, these secondary flows not only drove the suction-surface boundary layer through transition but also increased the local heat transfer above two-dimensional turbulent rates.
- (3) Increasing the Reynolds number produced the expected reduction of local Stanton number for all locations in the rotor passage where the boundary layers were turbulent. Increasing the Reynolds number also hastened the transition process in regions where the boundary layer was laminar/transitional (Fig. 41).
- (4) The highest heat transfer rates on the suction surface were observed in the mid-chord region near the tip. This local enhancement was produced by tip-leakage flow which rolls up into a tip-leakage vortex near the tip/casing corner (e.g. Fig. 33b).
- (5) The secondary flows produced by the first stage stator increased the heat transfer near the hub and tip of the forechord region of the rotor airfoil (e.g. Fig. 28a-marker B and Fig. 33b).
- (6) The minimum heat transfer on the pressure surface occurred near the downstream end of the minimum-speed region. This area of minimum heat transfer occurred near midspan, away from the effects of the hub and tip secondary flow effects (e.g. Fig. 28b-marker C and Fig. 33b).
- (7) Heat transfer rates in the aft-chord region of the pressure surface were slightly higher near the tip than for the remainder of the span (e.g. Fig. 33b). This resulted because the tip-leakage flow reduced the pressure-surface boundary layer thickness near the tip.
- (8) Comparisons of the present smooth-wall midspan heat transfer distributions with midspan data previously obtained for this same airfoil section (NASA-HOST) show very good agreement (Fig. 41).
- (9) The leading edge horseshoe vortex system produced a region of greatly enhanced heat transfer on the endwall at the leading-edge/endwall junction (e.g. Fig. 28c-marker E and Fig. 33c). The maximum endwall heat transfer rates were observed in this region.
- (10) The minimum heat transfer on the hub endwall occurred in the mid-chord region near the endwall/pressure-surface corner (e.g. Fig. 28b-marker D and Fig. 33c).

## Off-Design-Incidence Test Cases

(1) Increasing the rotor inlet flow angle from  $\beta_1 = 40^\circ$  to  $54^\circ$  produced a full-span separation bubble near the streamwise location of the pressure-surface leading edge overspeed. Reattachment downstream of this bubble produced a narrow, full-span band of relatively high heat transfer (e.g. Figs. 29d and 36a).

(2) Increasing the rotor inlet flow angle increased the heat transfer in the fore-chord region of the pressure surface and simultaneously decreased the heat transfer in the fore-chord region of the suction surface. As expected, trailing-edge region heat transfer rates for both the pressure and suction surfaces were unchanged by changing incidence (Fig. 43).

(3) The fore-chord region of the endwall showed a decrease in heat transfer with increased inlet flow angle, an effect produced directly by the decrease in relative inlet velocity (compare Fig. 33c with 36c.).

## Rough-Wall Test Cases

(1) Increased surface roughness significantly increased heat transfer rates relative to the smooth-wall test cases for all locations within the rotor passage (compare Fig. 33a with 37a).

(2) The largest relative changes produced by the wall roughness ( $> 100\%$ ) occurred in the fore-chord, suction-surface region for  $\beta_1 = 40^\circ$  (Fig. 41). For the smooth-wall test cases the boundary layer in this region was laminar/transitional while for the rough-wall test cases it was apparently fully turbulent.

(3) Local regions of augmented heat transfer that were observed for the smooth-wall test cases were also present for the rough-wall cases, e.g. the leading-edge/endwall junction and the tip-leakage vortex site (compare Fig. 33a with 37a). This result indicates that surface roughness had important augmentation effects even in regions with extremely thin, skewed, nonequilibrium boundary layers.

## Computational Program

(1) An assessment of the analytical and computational procedure indicates that the PATH code can predict reasonably well the aerodynamic properties of the three dimensional flow field, the wall skin friction, and the wall heat transfer in a gas turbine passage as indicated by comparisons of the three dimensional velocity fields, wall static pressure distributions, and wall heat transfer.

(2) Use of the vorticity equation and vorticity transport equation rather than the two transverse momentum equations insures that the passage vortex is accurately captured with little numerical diffusion as indicated by the results shown of the development of the passage vortex. At the present time Navier-Stokes solution algorithms using the transverse momentum equations show considerable numerical diffusion of the passage vortex.

(3) The results indicate that the development of the three dimensional boundary layers on the end wall and airfoil surfaces conform accurately to the law of the wall and that the sublayer and crossflow can be accurately captured with an appropriate computational mesh and that the small length scales in the boundary layer can be resolved.

(4) The present analysis can be improved significantly if the alternative boundary condition on the static pressure can be used since it would account for crosswise pressure gradients on surfaces where there is no pressure gradients in the potential flow solution.

(5) Although the equations of motion are quite general in that they can account for more general duct passages than were treated in this report, there is now no coordinate generator to set up a computational mesh for the more general problem such as the turbine passage with twist and varying thickness distributions. Development of such a coordinate generator would be very useful.

(6) Although not explicitly examined in this report, it is possible to significantly improve the computational time by adding a multi-grid capability to part of the algorithm. For the rotor case, as an example, it took 9854 iterations to converge the primary flow solution but 35979 iterations to resolve the secondary flow solution. Since the solution of the secondary flow involves the classical generalized Cauchy-Rieman problem, it is possible that a multi-grid procedure may significantly improve the computational time.

## REFERENCES

Anderson, O. L., 1980, "Calculation of Internal Viscous Flows in Axisymmetric Ducts at Moderate to High Reynolds Numbers", Intl. J. Computers and Fluids, Vol. 8, No. 4, pp. 391-411.

Anderson, O. L. and Hankins, G. B., 1981, "Development of a Parabolic Finite Difference Method for 3-D Viscous Internal Flows", ASME Winter Meeting - Computers in Flow Predictions and Fluid Dynamic Experiments.

Anderson, O. L., Davis, R. T., Hankins, G. B. and Edwards, D. E., 1982, "Solution of Viscous Internal Flows on Curvilinear Grids Generated by the Schwarz-Christoffel Transformation", Numerical Grid Generation, J. F. Thompson editor, Elsevier Science Publishing Co., Inc.

Anderson, O. L., 1985, "Assessment of a 3-D Boundary Layer Code to Predict Heat Transfer and Flow Field in a Turbine Passage", UTRC Report R85-956834-2.

Anderson, O. L., 1989, "A Parabolic Analysis of a Three Dimensional Compressible Viscous Flow Solution Based on Potential Flow Coordinates", UTRC Report, December 1989.

Barnett, M., 1982, "The Solution of the Parabolized Navier-Stokes Equations by a Fully Implicit Method", AIAA 20th Aerospace Sciences Meeting, AIAA-82-0415.

Blair, M. F., 1983, "Influence of Free-Stream Turbulence on Turbulent Boundary Layer Heat Transfer and Mean Profile Development", ASME Journal of Heat Transfer, Vol. 105, pp. 33-47.

Blair, M. F., 1985, "Heat Transfer in the Vicinity of a LargeScale Obstruction in a Turbulent Boundary Layer", AIAA Journal of Propulsion and Power, Vol. 1, No. 2, pp. 158-160.

Blair, M. F., Dring, R. P. and Joslyn, H. D., 1989, "The Effects of Turbulence and Stator/Rotor Interactions on Turbine Heat Transfer, Part-I, Design Operating Conditions, Part-II, Effects of Reynolds Number and Incidence", ASME Journal of Turbomachinery, Vol. 111, No. 1, pp. 87-103.

Brandt, A., "Multi-Grid Solutions to Elliptic Flow Problems", Dept. of Applied Mathematics, The Weizmann Institute of Science, Rehovot, Israel.

Briley, W. R., 1974, "Numerical Methods for Predicting ThreeDimensional Steady Viscous Flow in Ducts", J. Comp. Physics, Vol. 14, pp. 8-28.

Briley, W. R. and McDonald, H., 1979, "Analysis and Computation of Viscous Subsonic Primary and Secondary Flows", AIAA Computational Fluid Dynamics Conference, AIAA paper No. 79-1453.

Camarata, F. J., Hooper, R. M. and Nice, M. L., 1975, "Experimental Investigation of Passage Flow in a Baseline Build of a Large Scale Turbine Cascade", UTRC Report R75-212632.

Caretto, L. B., Curr, R.M. and Spalding, D. B., 1973, "Two Numerical Methods for Three Dimensional Boundary Layers", Comp. Methods in Applied Mechanics and Engineering, Vol. 1, pp. 1.

Dring, R. P., Blair, M. F. and Joslyn, H. D., 1980, "An Experimental Investigation of Film Cooling on a Turbine Rotor Blade", ASME Journal of Engr. for Power, Vol. 102, No. 1, pp. 81-87.

Dring, R. P. and Joslyn, H. D., 1981, "Measurement of Turbine Rotor Blade Flows", ASME Journal of Engr. for Power, Vol. 103, No. 2, pp. 400-405.

Dring, R. P., Joslyn, H. D., Hardin, L. W. and Wagner, J. H., 1982, "Turbine Rotor-Stator Interaction", ASME Journal of Engr. for Power, Vol. 104, No. 4, pp. 729-742.

Dring, R. P. and Joslyn, H. D., 1983, "The Relative Eddy in Axial Turbine Rotor Passages", ASME paper number 83-GT-22.

Dring, R. P., Blair, M. F., Joslyn, H. D., Power, G. D. and Verdon, J. M., 1986, "The Effects of Inlet Turbulence and Rotor/Stator Interactions on the Aerodynamics and Heat Transfer of a LargeScale Rotating Turbine Model", Vol. I, Final Report, NASA Contractor Report 4079.

Ghia, K. N. and Sokhey, J. S., 1979, "Laminar Incompressible Viscous Flow in Curved Ducts of Regular Crosssection", ASME J. of Fluids Engr., Vol. 99, pp. 640-648.

Graziani, R. A., Blair, M. F., Taylor, J. R. and Mayle, R. E., 1980, "An Experimental Study of Endwall and Airfoil Surface Heat Transfer in a Large Scale Turbine Blade Cascade", ASME Journal of Engr. for Power, Vol. 102, pp. 257-267.

Hah, C., 1983, "A Navier-Stokes Analysis of Three-Dimensional Turbulent Flows Inside Turbine Blade Rows at Design and Off Design Conditions", ASME paper number 83-GT-40.

Holmes, D. G. and Tong, J. S., 1984, "A Three-Dimensional Euler Solver for Turbomachinery Blade Rows", ASME paper number 84-GT-69.

Joslyn, H. D., Dring, R. P. and Camarata, F. J., 1977, "Some Experiments Pertinent to Relative Frame Data Acquisition in the UTRC Large Scale Rotating Rig" UTRC Report UTRC77-12.

Joslyn, H. D. and Dring, R. P., 1977, "Final Results of the 1976 PWA Turbine Program in the UTRC Large Scale Rotating Rig", UTRC Report R77-217020.

Joslyn, H. D., Dring, R. P. and Sharma, O. P., 1983, "Unsteady Three-Dimensional Turbine Aerodynamics", ASME Journal of Engr. for Power, Vol. 105, pp. 322-331.

Joslyn H. D. and Dring, R. P., 1983, "Turbine Rotor Negative Incidence Stall", ASME paper number 83-GT-23.

Joslyn, H. D. and Dring, R. P., 1989, "Three Dimensional Flow and Temperature Profile Attenuation in an Axial Flow Turbine", Final Report under AFOSR Contract F49620-86-C-0020, UTRC Report R89-957334-1.

Karamcheti, K., 1980, Principals of Ideal Fluid Mechanics, Robert E. Krieger Publishing Company, Malabar, Florida.

Kreskovsky, J. P., Briley, W. R., and McDonald, H., 1979, "Analysis and Computation of Three-Dimensional Flow in Strongly Curved Ducts, ASME Annual Winter Meeting-Flow in Primary, Non-Rotating Passages in Turbomachines.

Langston, L.S., Nice, M. S. and Hooper, R. M., 1977, "ThreeDimensional Flow Within a Turbine Cascade Passage", ASME Journal of Engr. for Power, Vol. 99.

Madavan, N. K., Rai, M. M. and Gavali, S., 1989, "Grid Refinement Studies of Turbine Rotor-Stator Interaction", AIAA paper AIAA-89-0325.

Mager, A., Mahoney, J. J. and Budinger, R. E., 1952, "Discussion of Boundary Layer Characteristics Near the Wall of an Axial Flow Compressor", NACA Report 1085.

Moore, J. and Moore, J. G., 1979, "A Calculation Procedure for Three-Dimensional, Viscous, Compressible Duct Flow", ASME Winter Annual Meeting-Flow in Primary, Non-Rotating Passages in Turbomachines.

Owczarek, J. A., 1964, Fundamentals of Gas Dynamics, International Textbook Co., Scranton, Pennsylvania.

Patankar, S. V. and Spalding, D. B., 1972, "A Calculation Procedure for Heat, Mass, and Momentum Transfer in Three Dimensional Parabolic Flows", Int. J. Heat and Mass Transfer, Vol. 15, pp. 1787-1805.

Rai, M. M., 1987, "Unsteady Three-Dimensional Navier-Stokes Simulations of Turbine Rotor-Stator Interaction Including Tip Effects", AIAA paper number AIAA-87-2058.

Rai, M. M. and Dring, R. P., 1987, "Navier-Stokes Analysis of the Redistribution of Inlet Temperature Distortions in a Turbine", AIAA paper number AIAA-87-2146.

Rai, M. M. and Madavan, N. K., 1988, "Multi-Airfoil Navier-Stokes Simulations of Turbine Rotor-Stator Interaction", AIAA paper number AIAA-88-0361.

Rai, M. M., 1989, Private communication regarding a turbine stage calculation at NASA/Ames with the same rotor aspect ratio and tip clearance as in the experiment. January 12, 1989.

**Table 4b  
Airfoil Geometry**

AIRFOIL: SECOND STATOR (MIDSPAN)  
PITCH (ins.): 6.05879

	LEADING EDGE	TRAILING EDGE
RADIUS (ins.)	0.34999	0.19000
METAL ANGLE (degr.)	45.66800	25.00000
WEDGE ANGLE (degr.)	27.50000	6.50000

	X(ins.)	Y <sub>L</sub> (ins.)	Y <sub>U</sub> (ins.)
1	0.00000	4.10291	4.10291
2	0.06452	3.47786	4.30650
3	0.12904	3.52885	4.40610
4	0.19356	3.57793	4.50013
5	0.25808	3.62510	4.58895
6	0.32260	3.67035	4.67285
7	0.38712	3.71368	4.75210
8	0.45164	3.75508	4.82695
9	0.51616	3.79454	4.89760
10	0.58068	3.83206	4.96425
11	0.64520	3.86762	5.02707
12	0.80650	3.94796	5.16834
13	0.96780	4.01599	5.28865
14	1.12910	4.07162	5.38963
15	1.29040	4.11482	5.47259
16	1.45170	4.14552	5.53859
17	1.61300	4.16371	5.58849
18	1.77430	4.16934	5.62296
19	1.93560	4.16244	5.64258
20	2.09690	4.14298	5.64778
21	2.25820	4.11101	5.63888
22	2.41950	4.06655	5.61615
23	2.58080	4.00965	5.57973
24	2.74210	3.94037	5.52972
25	2.90340	3.85879	5.46611
26	3.06470	3.76498	5.38882
27	3.22600	3.65906	5.29771
28	3.38730	3.54111	5.19255
29	3.54860	3.41127	5.07300
30	3.70990	3.26967	4.93863
31	3.87120	3.11644	4.78891
32	4.03250	2.95172	4.62316
33	4.19380	2.77568	4.44053
34	4.35510	2.58849	4.24001
35	4.51640	2.39030	4.02052
36	4.67770	2.18130	3.78134
37	4.83900	1.96166	3.52218
38	5.00030	1.73160	3.24330
39	5.16160	1.49128	2.94535
40	5.32290	1.24090	2.62941
41	5.48420	0.98064	2.29682
42	5.64550	0.71074	1.94914
43	5.80680	0.43141	1.58790
44	5.87132	0.31707	1.43996
45	5.93584	0.20126	1.29018
46	6.00036	0.08400	1.13867
47	6.06488	-0.03471	0.98552
48	6.12940	-0.15484	0.83080
49	6.19392	-0.27639	0.67459
50	6.25844	-0.39934	0.51699
51	6.32296	-0.52368	0.35805
52	6.38748	-0.64939	0.19786
53	6.45200	0.00000	0.00000

**Table 4c**  
**Airfoil Geometry**

**AIRFOIL: SECOND STATOR (TIP)**  
**PITCH (ins.): 6.70506**

	LEADING EDGE	TRAILING EDGE
RADIUS (ins.)	0.35006	0.19000
METAL ANGLE (degr.)	50.49115	24.98778
WEDGE ANGLE (degr.)	25.12000	4.09000

	X(ins.)	Y <sub>L</sub> (ins.)	Y <sub>U</sub> (ins.)
1	0.00000	4.53429	4.53429
2	0.06452	4.33178	4.73679
3	0.12904	4.26282	4.81836
4	0.19356	4.22116	4.89463
5	0.25808	4.19652	4.96641
6	0.32260	4.18530	5.03396
7	0.38712	4.18619	5.09751
8	0.45164	4.19929	5.15728
9	0.51616	4.22602	5.21343
10	0.58068	4.25762	5.26613
11	0.64520	4.28729	5.31552
12	0.80650	4.35297	5.42538
13	0.96780	4.40647	5.51708
14	1.12910	4.44777	5.59199
15	1.29040	4.47683	5.65117
16	1.45170	4.49364	5.69551
17	1.61300	4.49819	5.72567
18	1.77430	4.49045	5.74219
19	1.93560	4.47047	5.74550
20	2.09690	4.43822	5.73590
21	2.25820	4.39375	5.71360
22	2.41950	4.33706	5.67874
23	2.58080	4.26823	5.63135
24	2.74210	4.18728	5.57140
25	2.90340	4.09426	5.49876
26	3.06470	3.98924	5.41323
27	3.22600	3.87229	5.31449
28	3.38730	3.74348	5.20215
29	3.54860	3.60289	5.07566
30	3.70990	3.45062	4.93435
31	3.87120	3.28675	4.77738
32	4.03250	3.11139	4.60366
33	4.19380	2.92465	4.41196
34	4.35510	2.72666	4.20118
35	4.51640	2.51749	3.97077
36	4.67770	2.29731	3.72077
37	4.83900	2.06620	3.45177
38	5.00030	1.82436	3.16495
39	5.16160	1.57187	2.86176
40	5.32290	1.30889	2.54389
41	5.48420	1.03553	2.21304
42	5.64550	0.75199	1.87091
43	5.80680	0.45841	1.51902
44	5.87132	0.33818	1.37585
45	5.93584	0.21639	1.23140
46	6.00036	0.09302	1.08577
47	6.06488	-0.03190	0.93902
48	6.12940	-0.13607	0.79122
49	6.19392	-0.17738	0.64244
50	6.25844	-0.18996	0.49272
51	6.32296	-0.17995	0.34214
52	6.38748	-0.14267	0.19073
53	6.45200	0.00000	0.00000

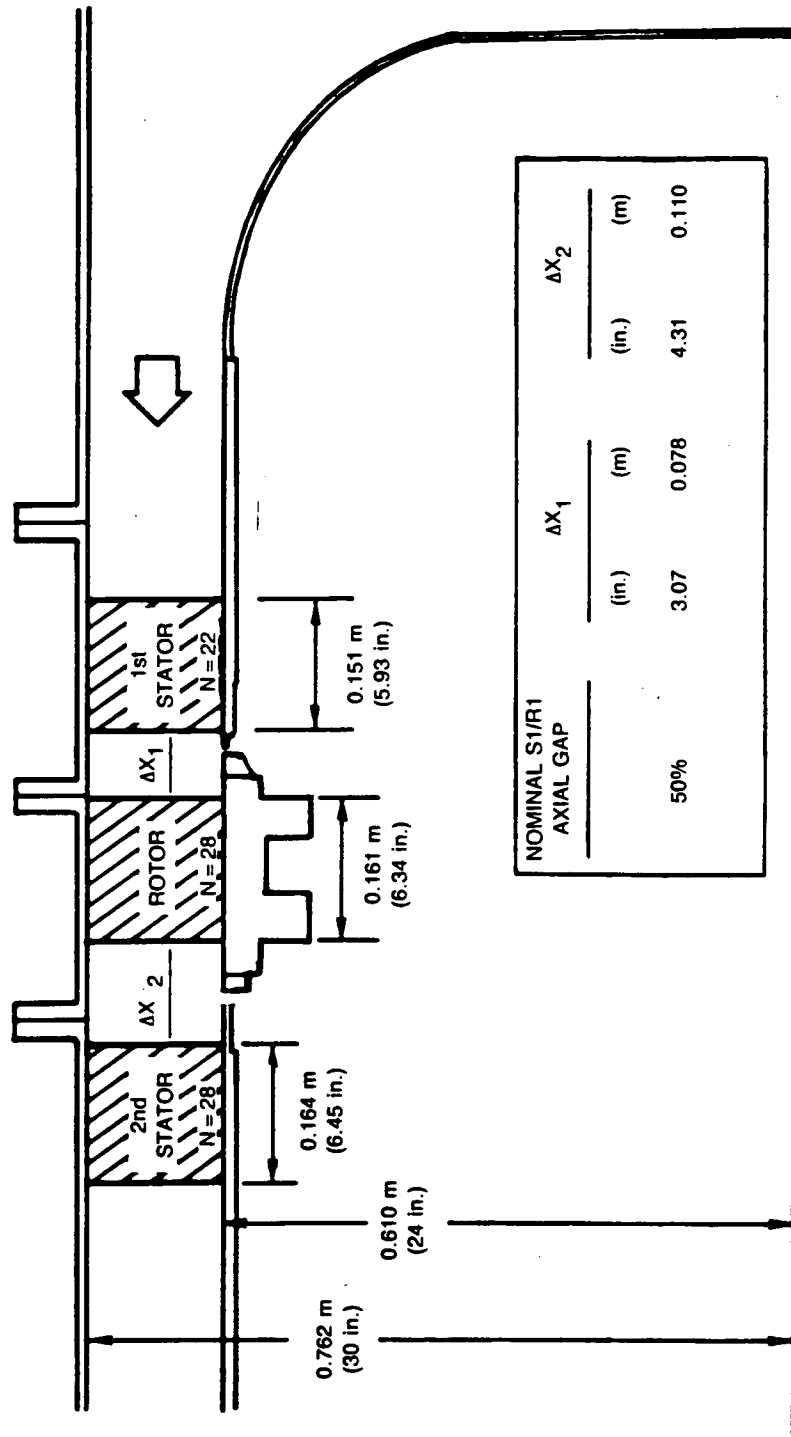
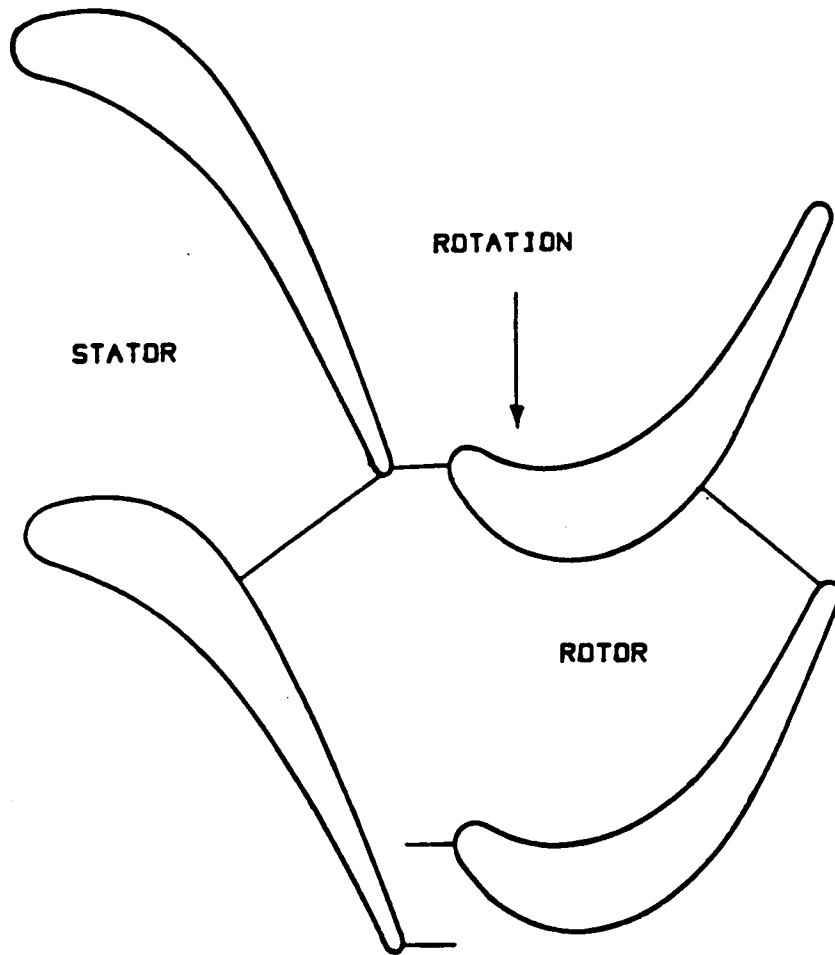


Figure 1 United Technologies Research Center  
Large Scale Rotating Rig



**Figure 2 Turbine Stage at Mid Span**

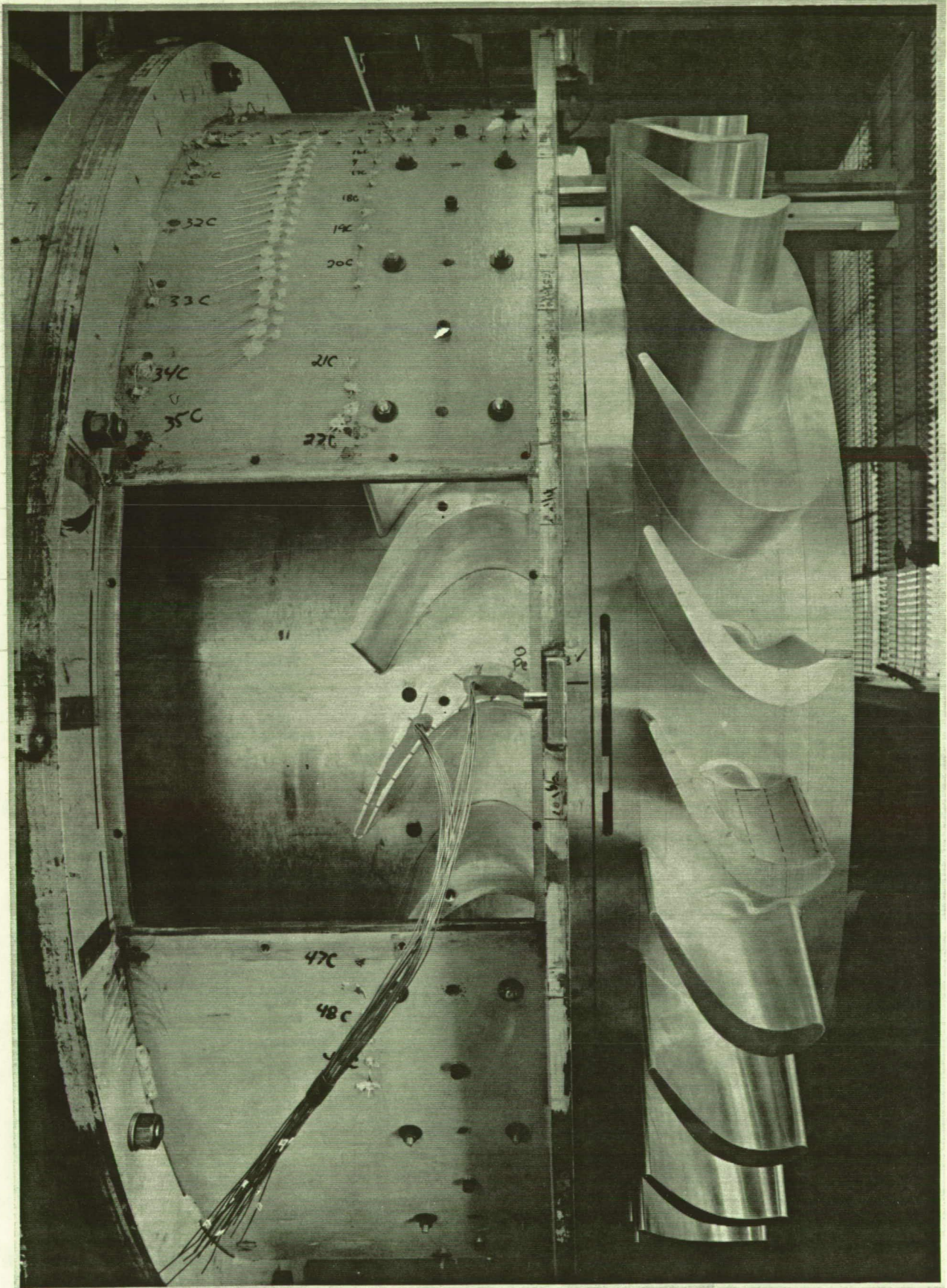


Figure 3 Large Scale Rotating Rig 1 1/2 Stage Turbine Configuration

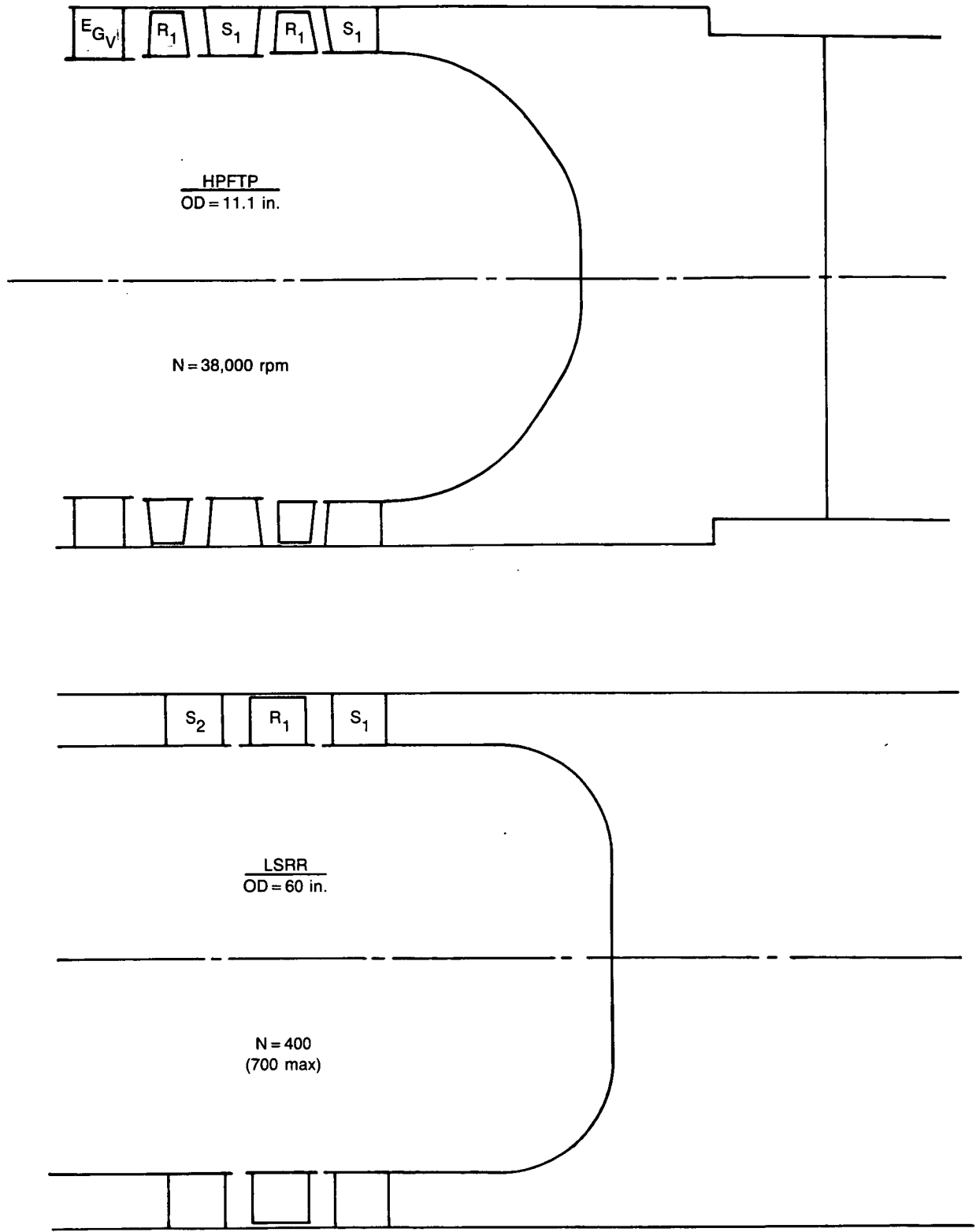
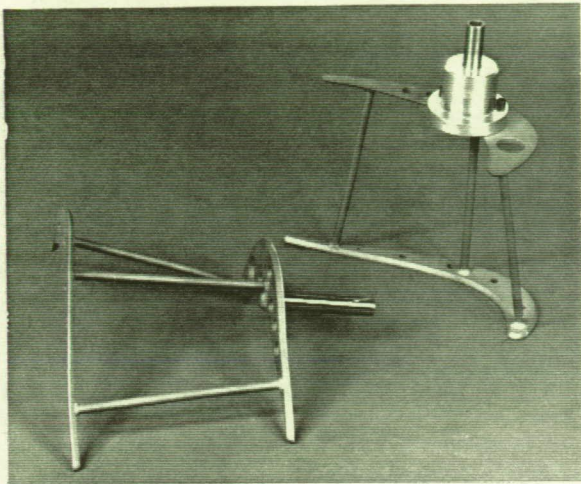
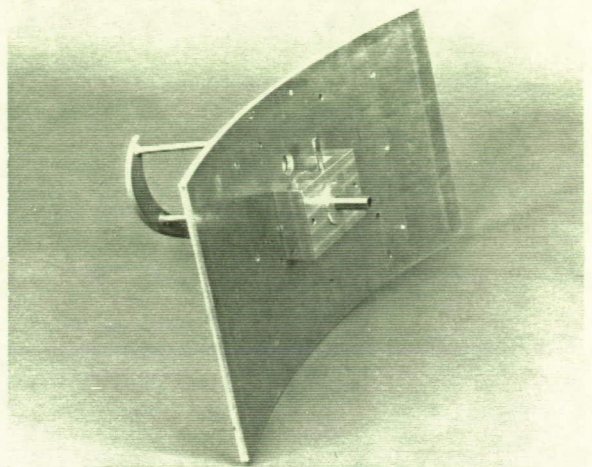


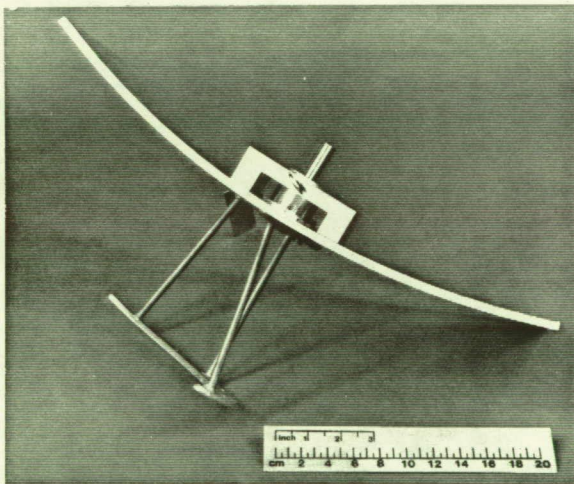
Figure 4 Comparison of the UTRC/LSRR and the SSME/HPFTP Drive Turbine



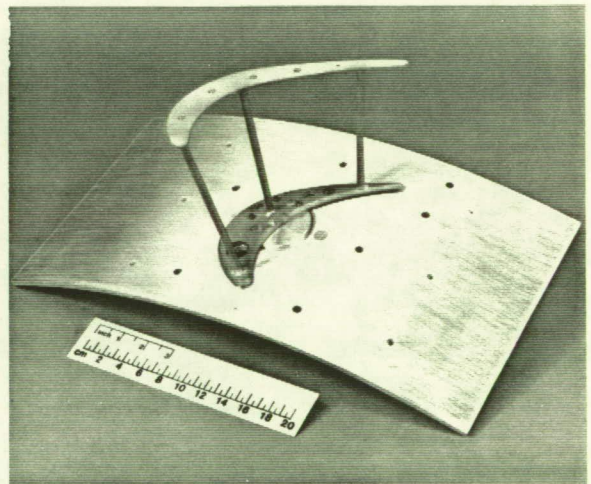
STEEL SKELETONS



SKELETON MOUNTED IN ALIGNMENT BRACKET (VIEW FROM ROOT)

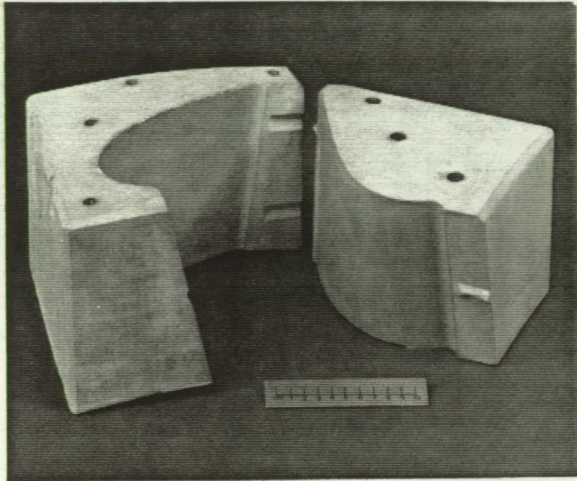


SKELETON MOUNTED IN ALIGNMENT BRACKET (VIEW FROM LEADING EDGE)

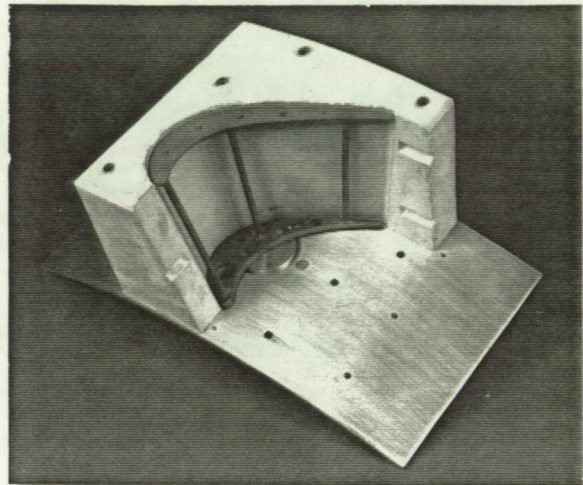


SKELETON MOUNTED IN ALIGNMENT BRACKET (VIEW FROM TIP)

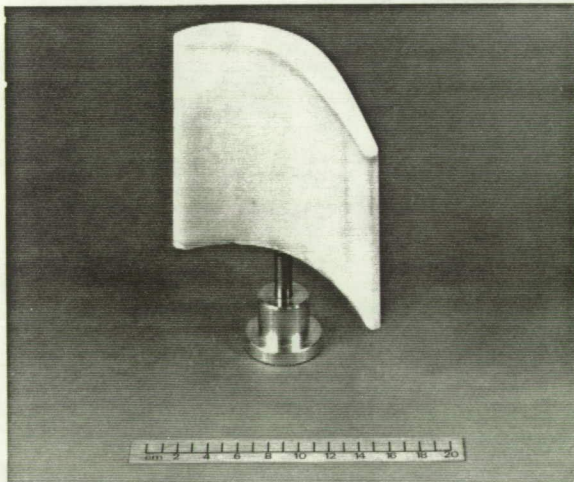
Figure 5 Stages of Rotor Airfoil Fabrication



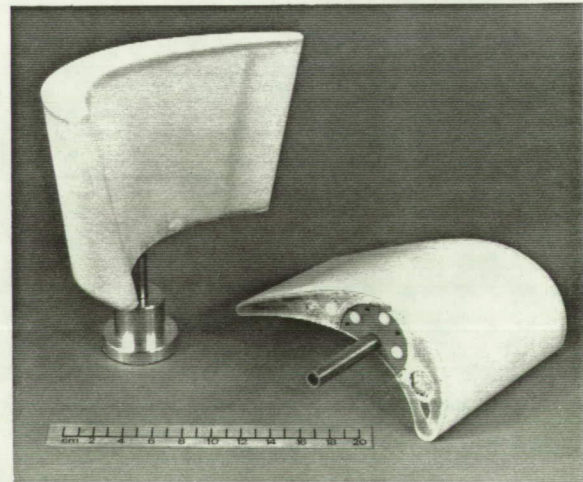
ROTOR AIRFOIL MOLD



STEEL SKELETON - MOLD ASSEMBLY



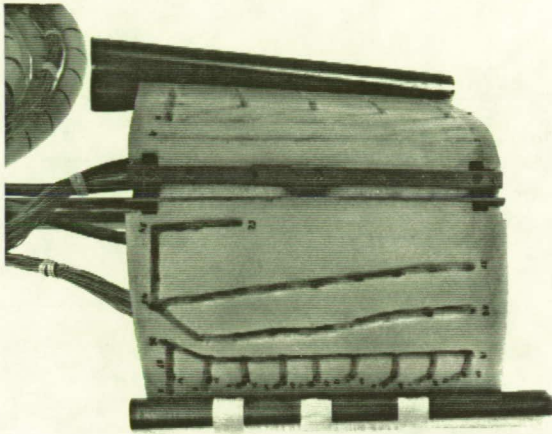
CAST FOAM AIRFOIL (VIEW FROM PRESSURE SURFACE)



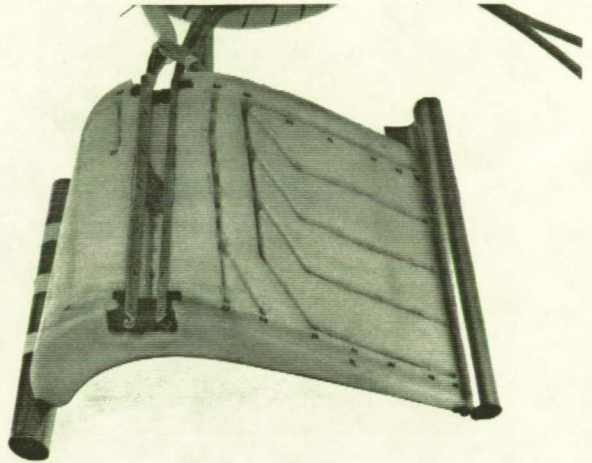
CAST FOAM AIRFOILS

Figure 6 Stages of Rotor Airfoil Fabrication

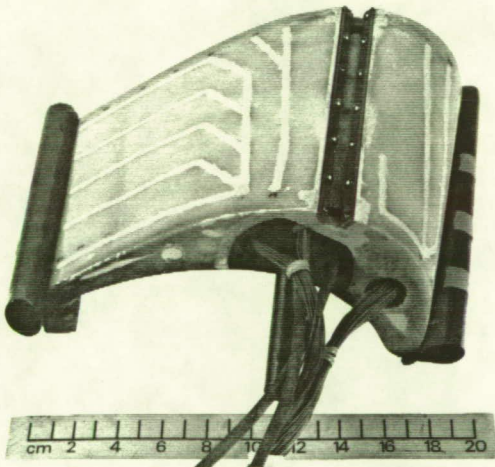
ORIGINAL PAGE  
BLACK AND WHITE PHOTOGRAPH



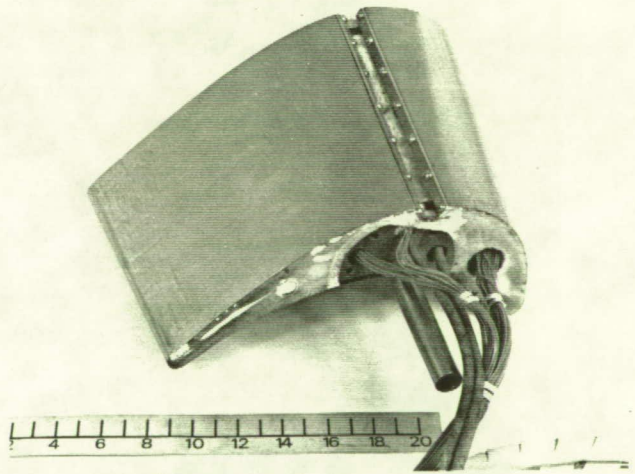
VIEW OF FORE-CHORD  
INSTRUMENTATION ROUTING



VIEW OF AFT-CHORD  
INSTRUMENTATION ROUTING



AIRFOIL MODEL WITH INSTRUMENTATION  
ROUTING FILLED



AIRFOIL MODEL WITH COMPLETED  
FOIL INSTALLATION

**Figure 7 Stages of Pressure Surface Airfoil Instrumentation**

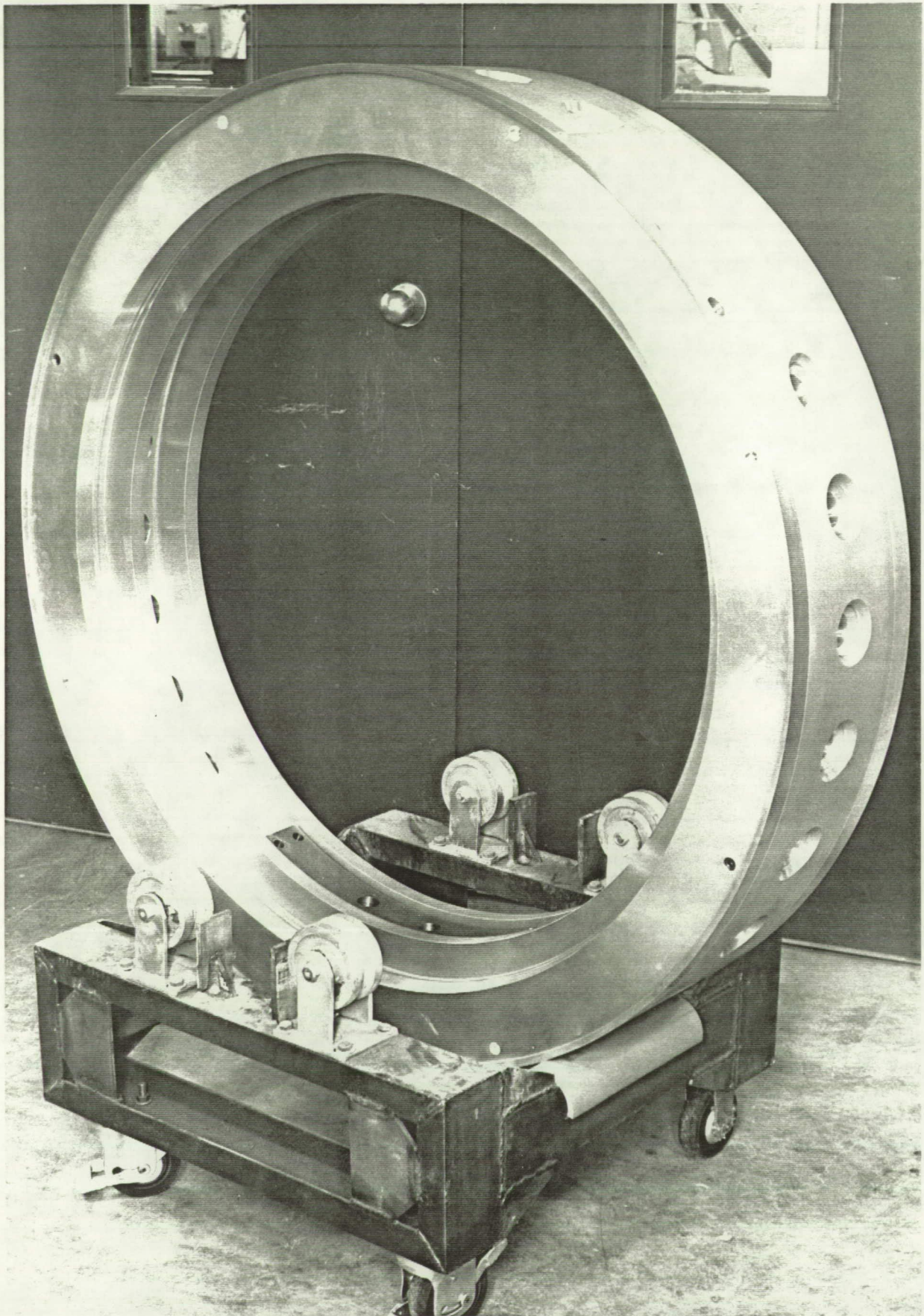
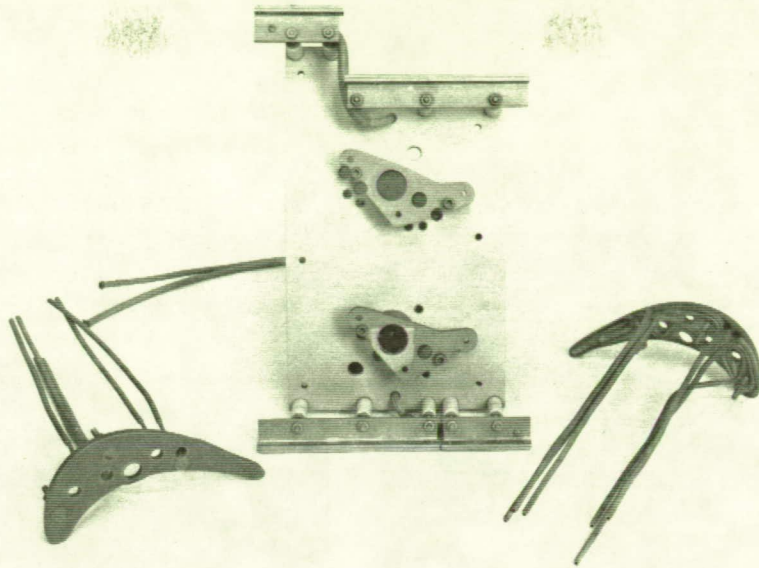
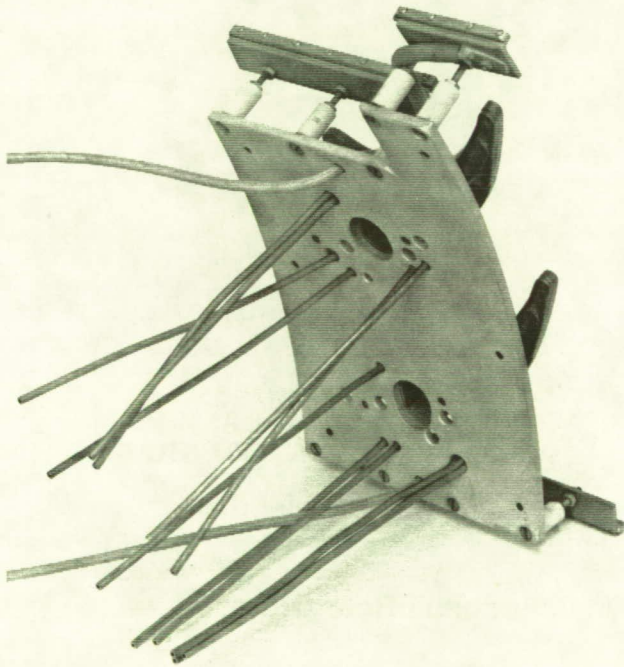


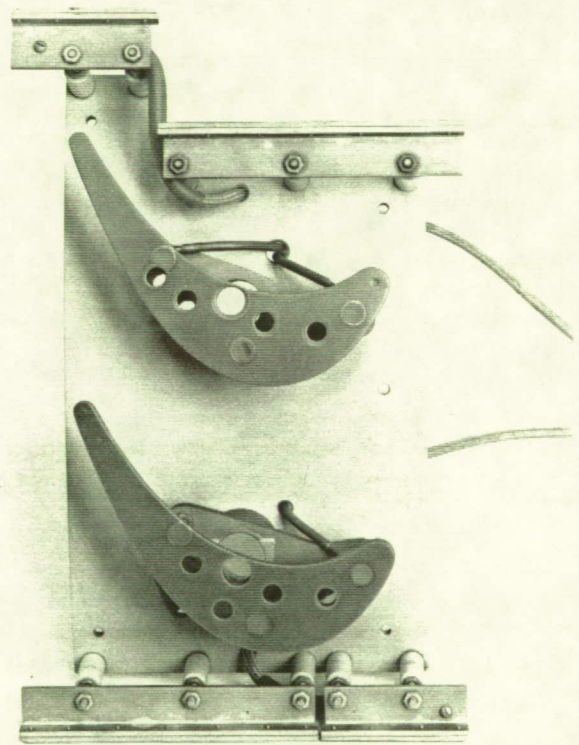
Figure 8 Rotor Hub Showing Endwall Heat Transfer Region



ENDWALL MODEL COMPONENTS



ENDWALL MODEL ASSEMBLY  
BOTTOM VIEW



ENDWALL MODEL ASSEMBLY  
TOP VIEW

Figure 9 Endwall Model Assembly Prior to Casting

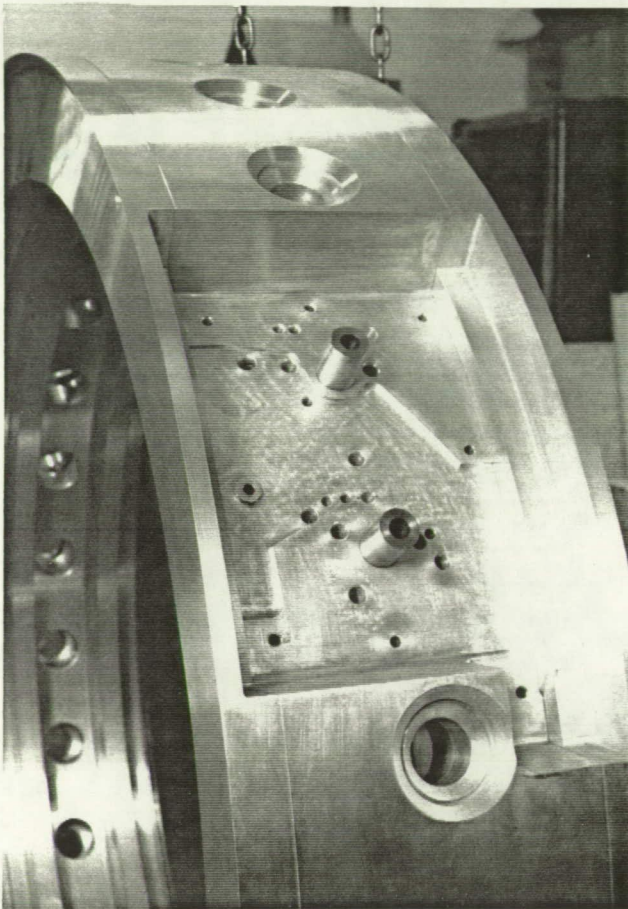
88-268B

88-268C

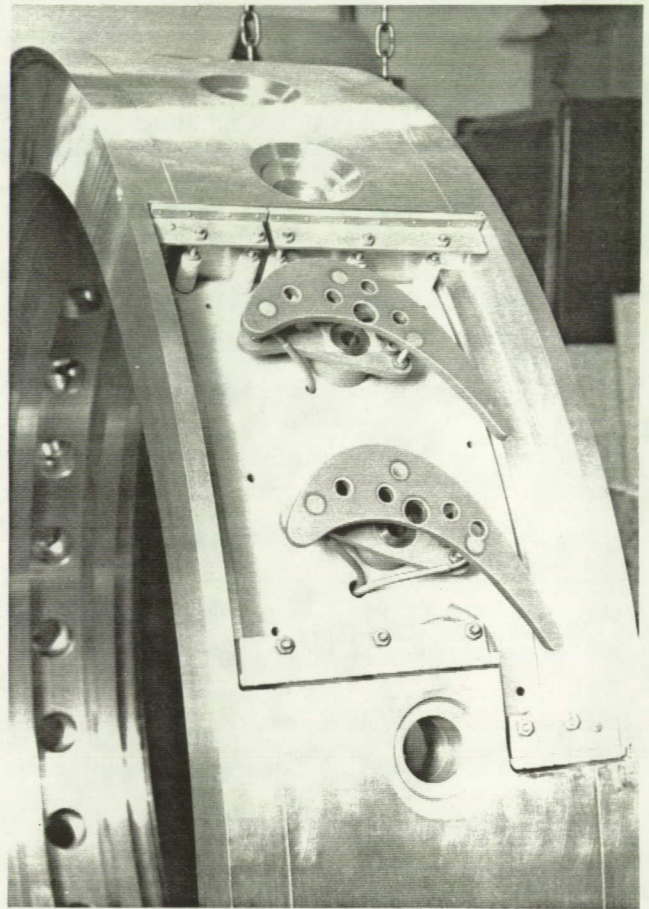
88-268A

ORIGINAL PAGE  
BLACK AND WHITE PHOTOGRAPH

88-7-14-1



CUTOUT REGION OF ROTOR HUB



ENDWALL MODEL ASSEMBLY  
INSTALLED IN HUB CUTOUT

**Figure 10 Endwall Model Installation in Rotor Hub**

ORIGINAL PAGE  
BLACK AND WHITE PHOTOGRAPH

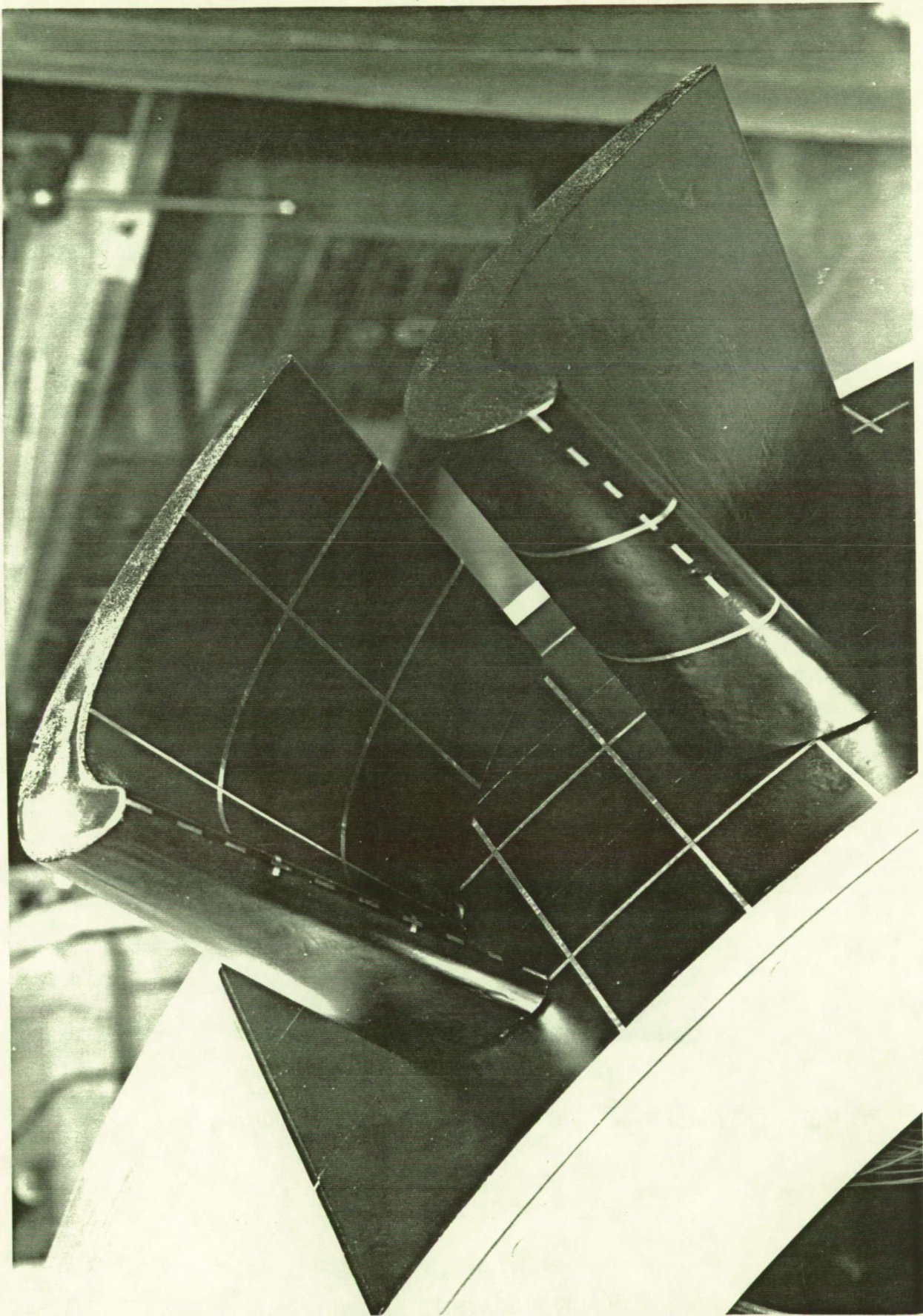


**Figure 11** Airfoil and Endwall Heat Transfer Models Installed in Rotor Hub — the Bench-Test Model for Evaluating Liquid-Crystal Techniques

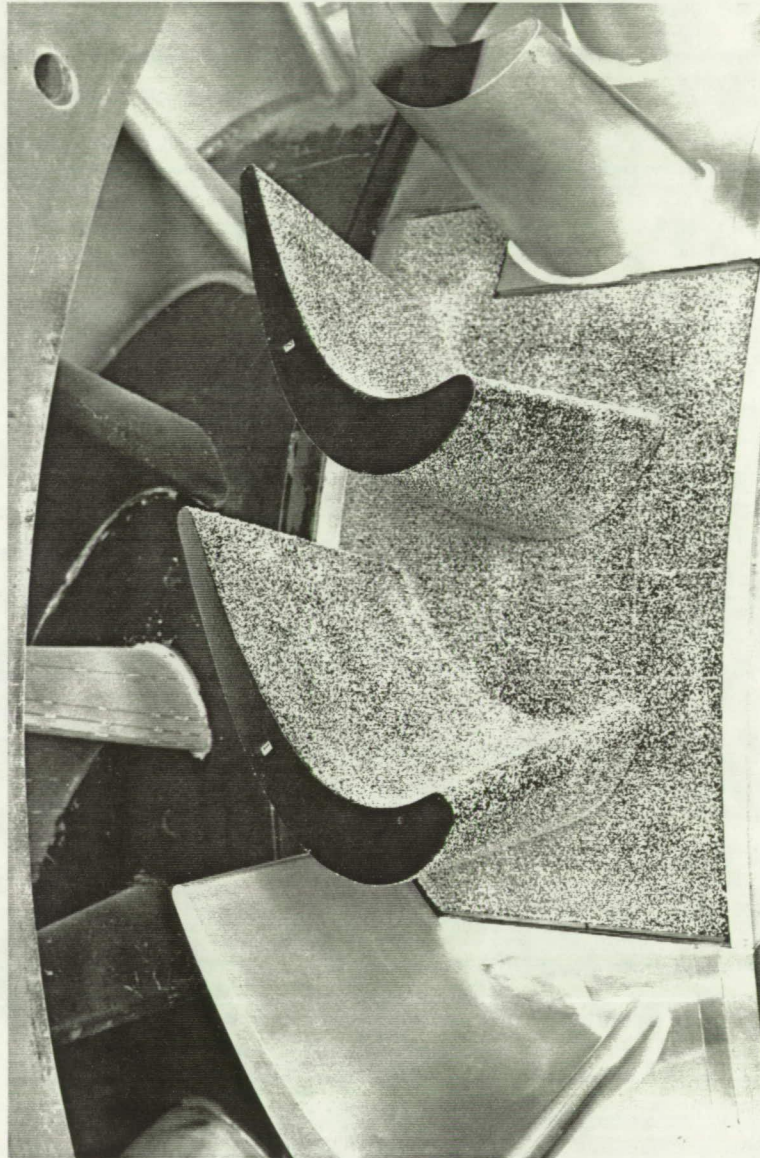
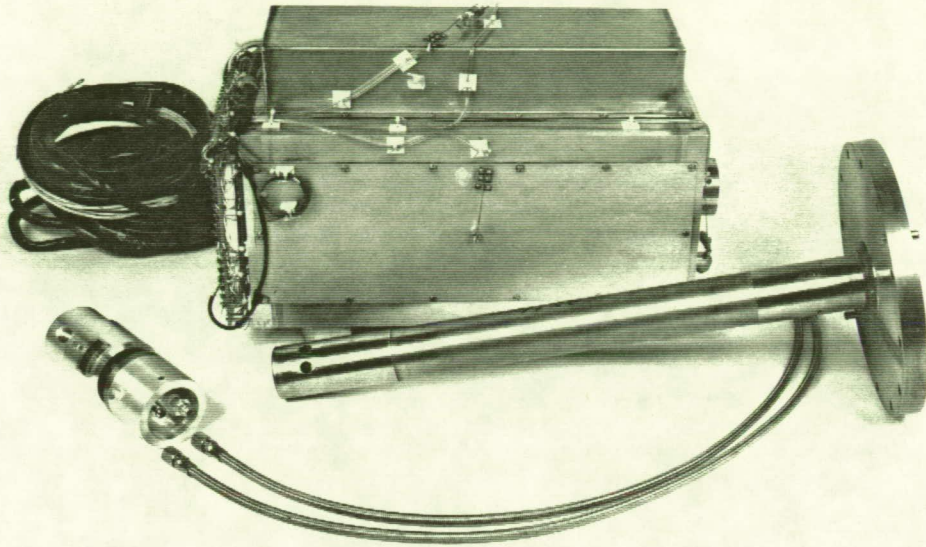
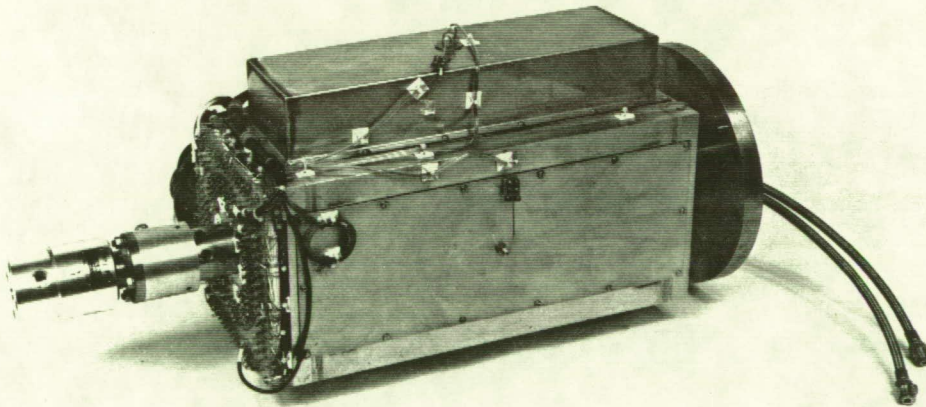


**Figure 12 Rotor Passage Heat Transfer Model with Surface Roughness Grit**

ORIGINAL PAGE  
BLACK AND WHITE PHOTOGRAPH



SLIP RING, MOUNTING ARBOR AND ROTARY UNION



ASSEMBLED UNIT READY FOR INSTALLATION INTO LSRR

**Figure 13 Slip Ring — Rotary Union Assembly**

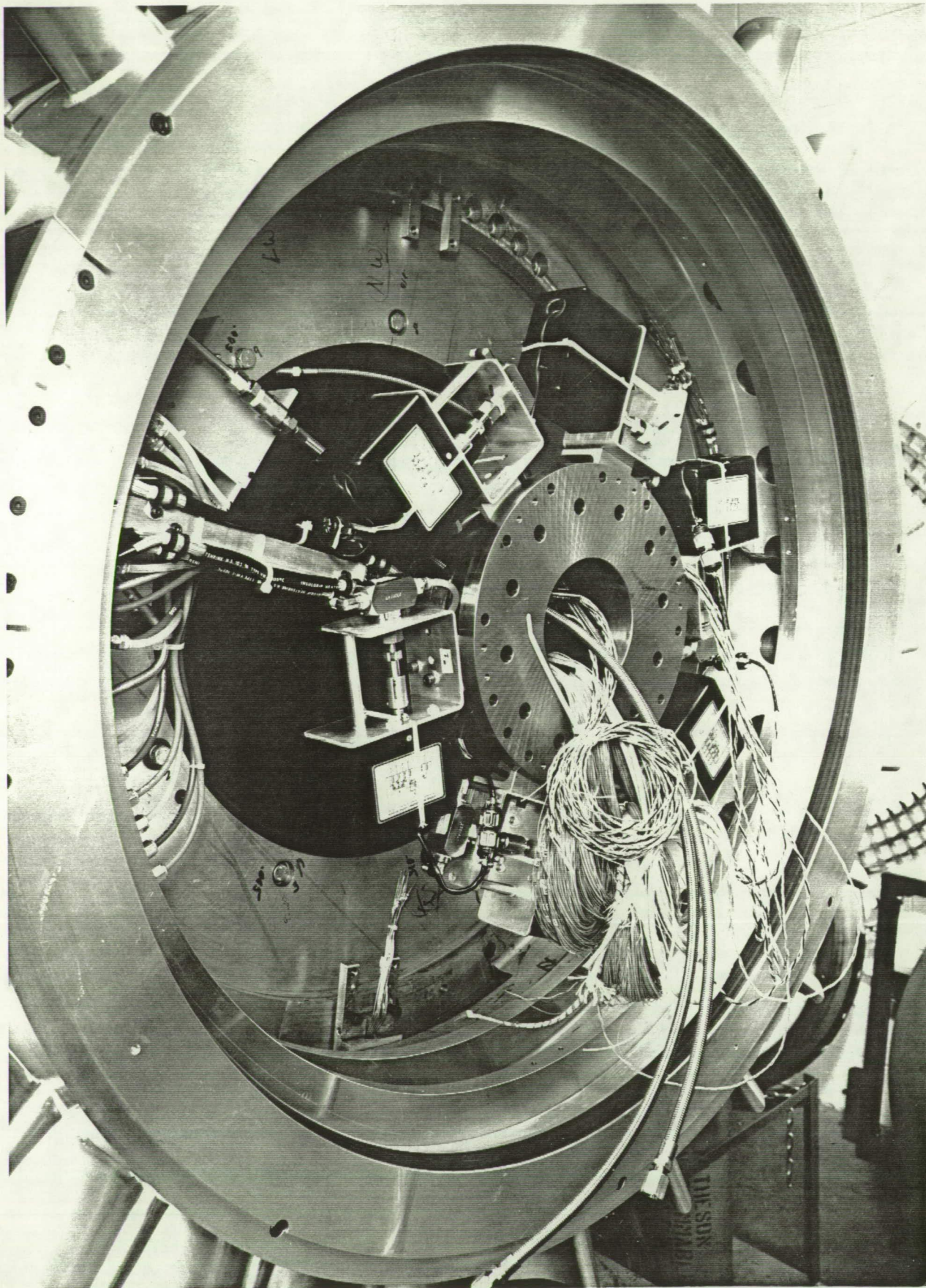


**Figure 14 Rotor Instrumentation Prior to Installation of Slip-ring - Note Remote Control Valves and Heat Transfer Model Wiring**

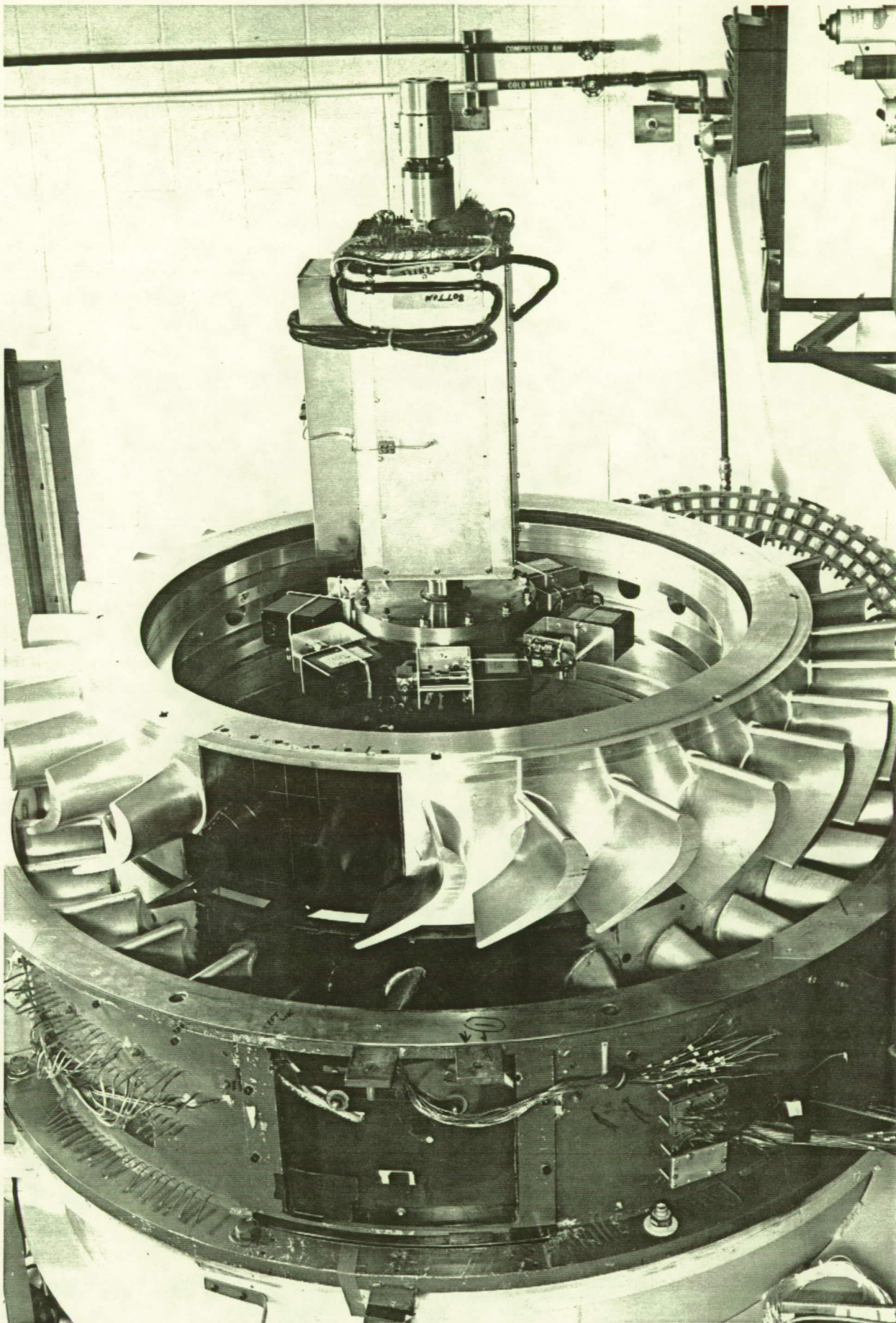


Figure 15 LSRR Rotor with Case Removed -- Slip-ring Installed - Note Heat Transfer Model Installed

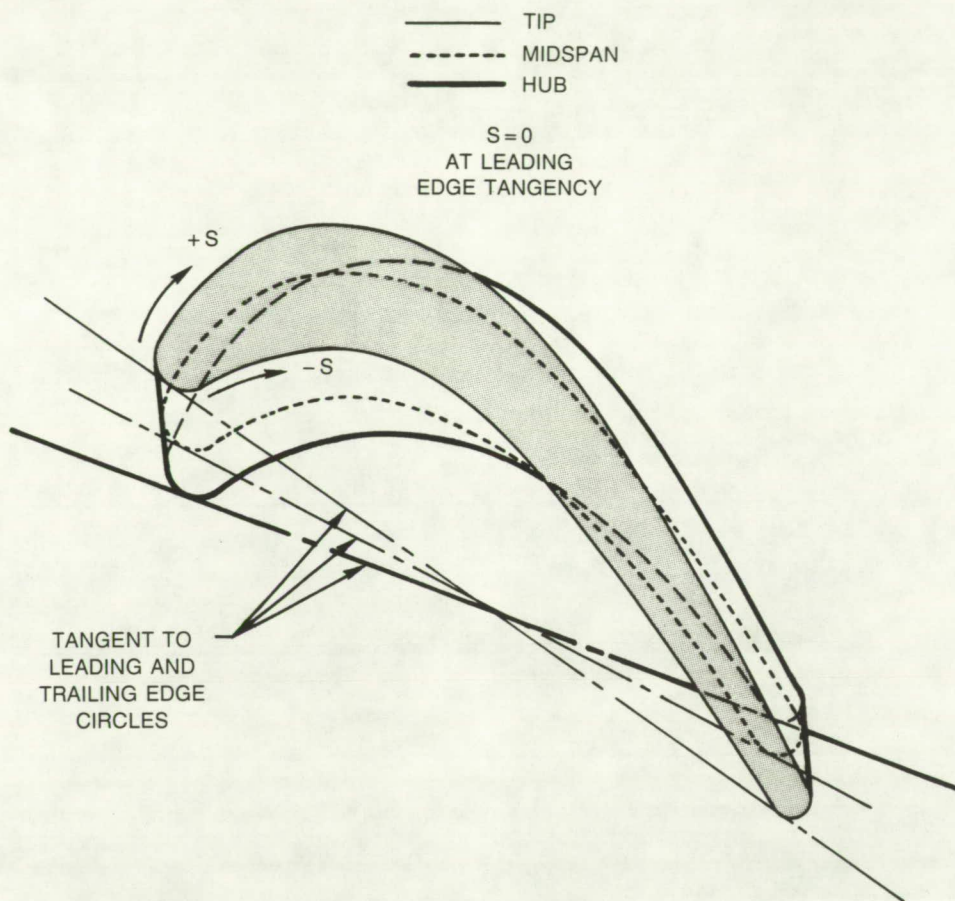
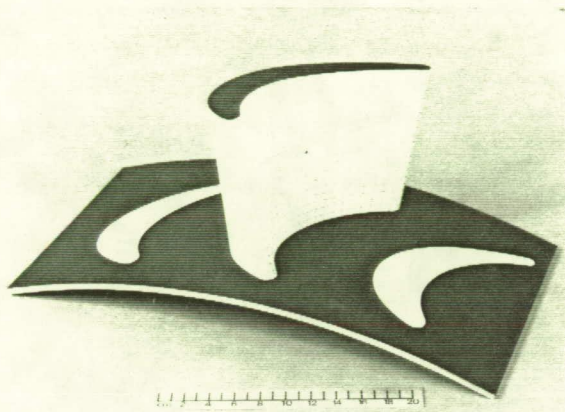
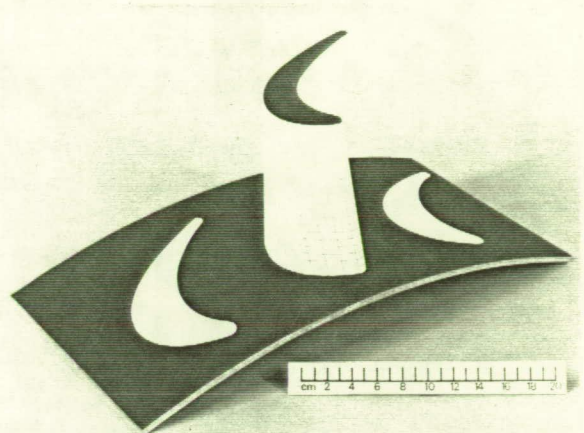


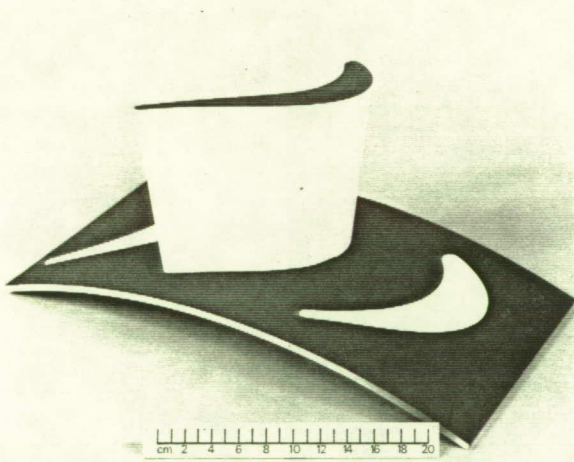
Figure 16 Diagram of Surface Distance (s) Nomenclature



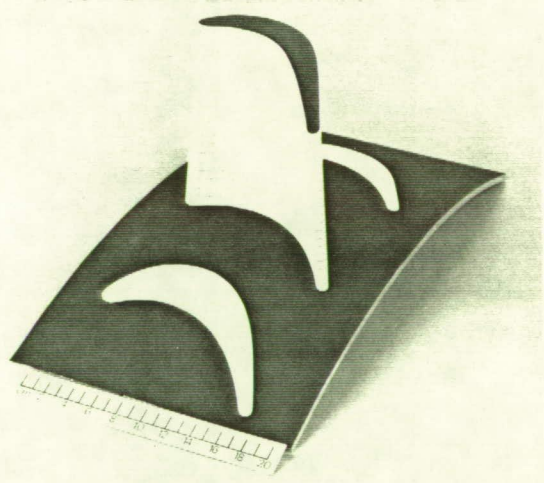
LEADING EDGE-PRESSURE  
SURFACE VIEW



LEADING EDGE-SUCTION  
SURFACE VIEW



TRAILING EDGE-SUCTION  
SURFACE VIEW



TRAILING EDGE-PRESSURE  
SURFACE VIEW

Figure 17 Rotor Airfoil Instrumentation Coordinate System

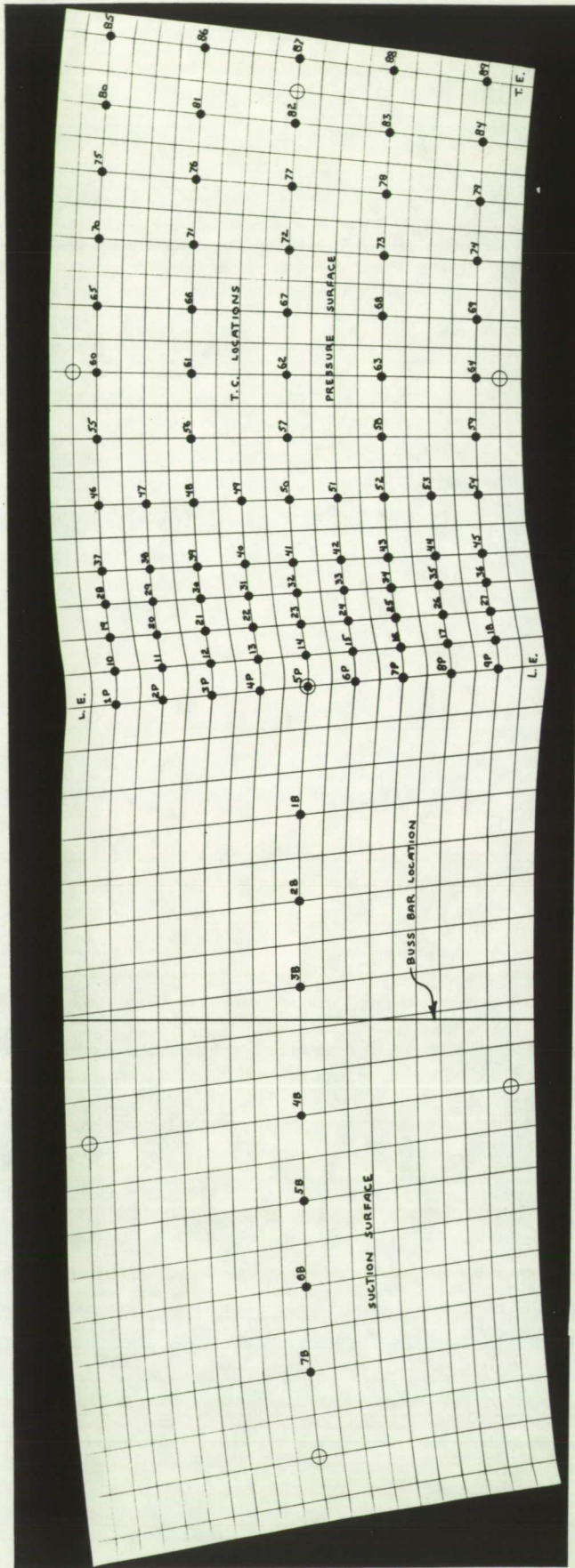


Figure 18 Pressure Surface Thermocouple Instrumentation Array

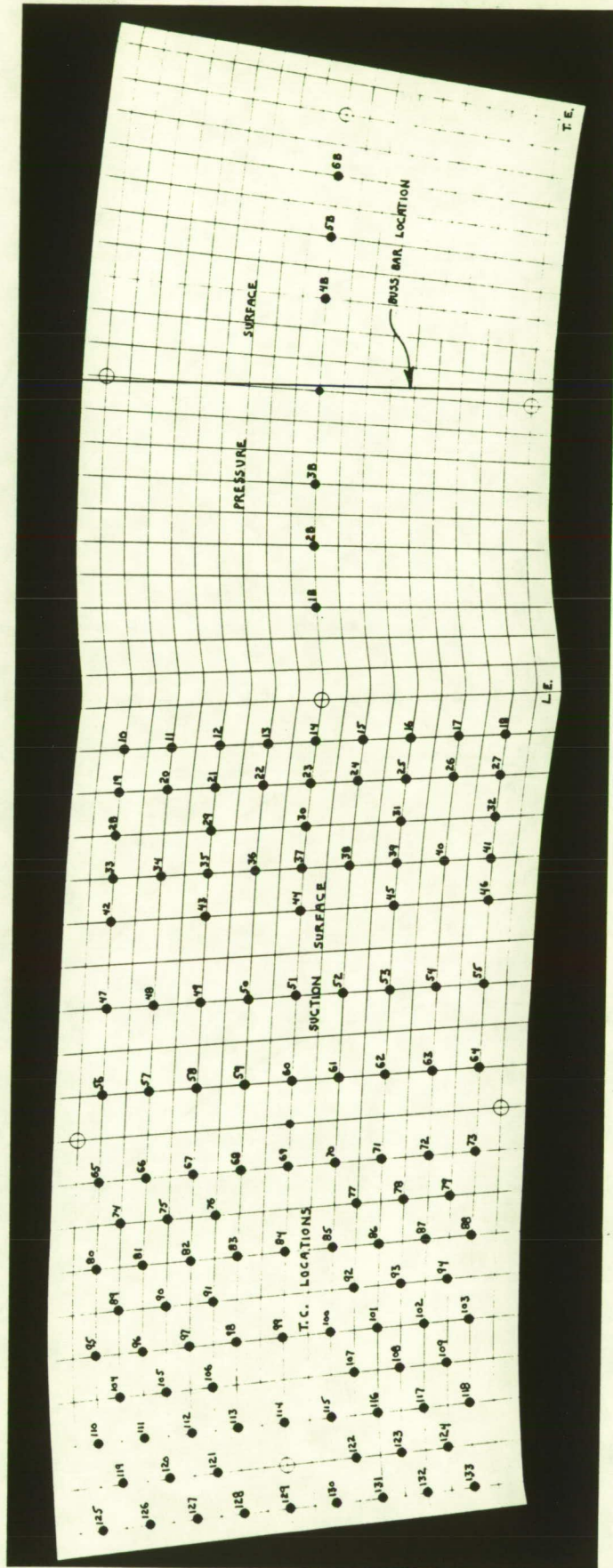


Figure 19 Suction Surface Thermocouple Instrumentation Array

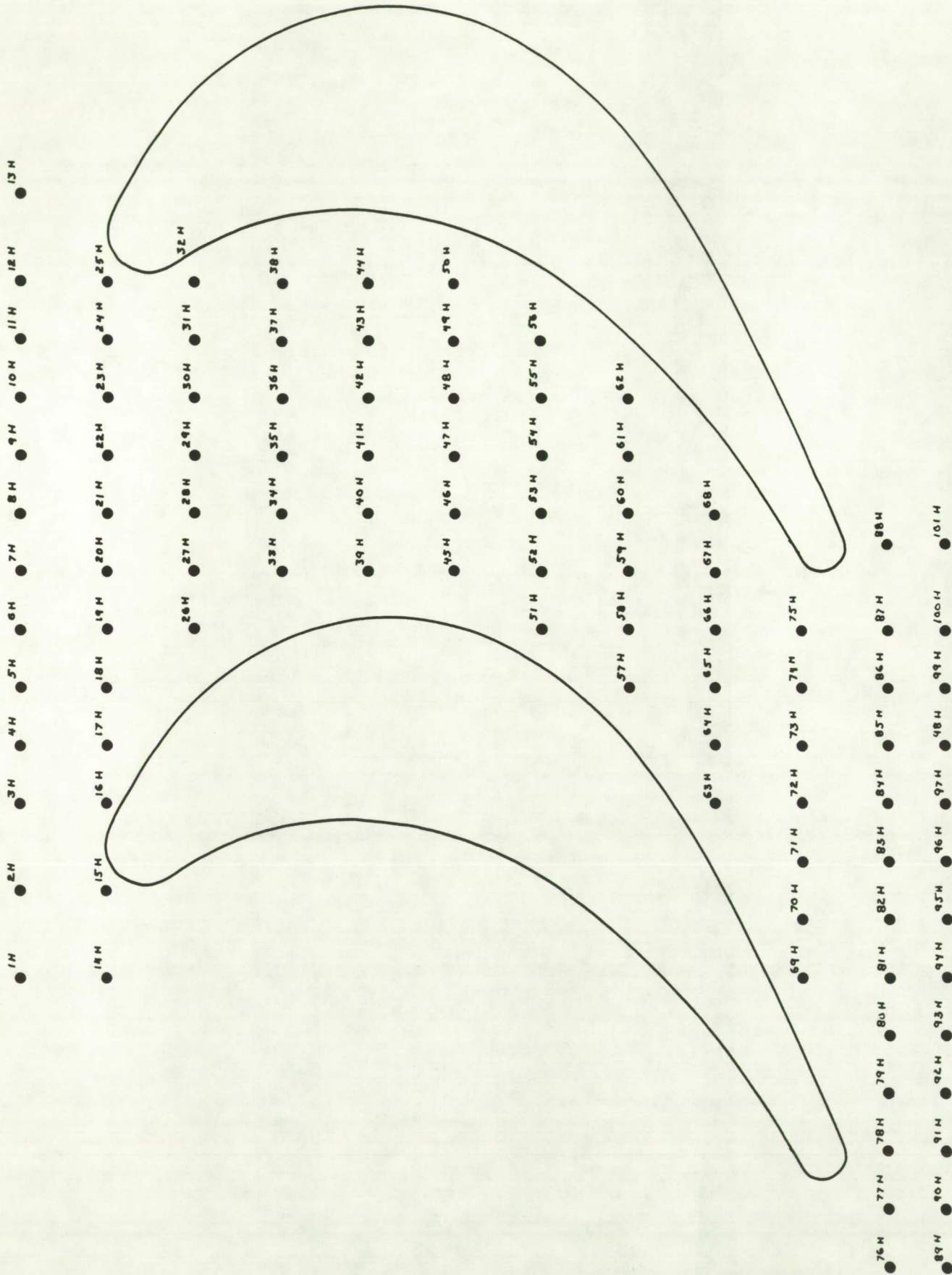
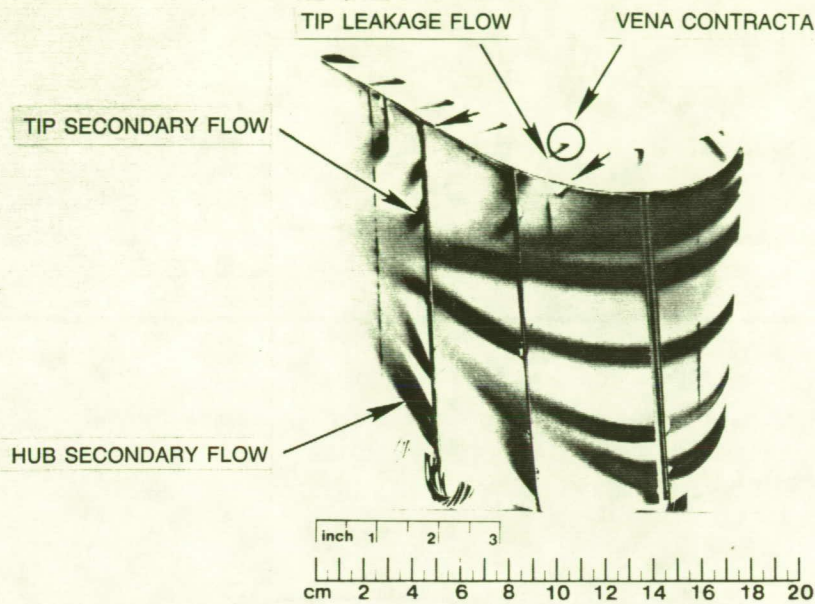
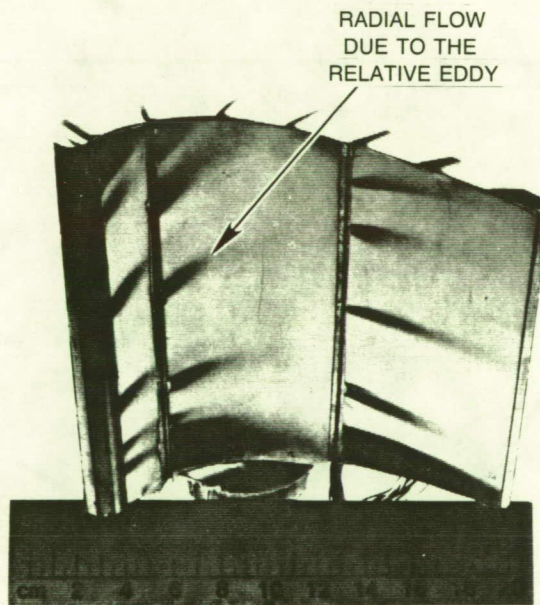


Figure 20 Endwall Thermocouple Instrumentation Array



a) SUCTION SURFACE AND TIP



b) PRESSURE SURFACE AND TIP

Fig. 21 Rotor Surface Flow Visualization, Showing Hub and Tip Secondary Flow, Tip Leakage and Effect of Relative Eddy

ORIGINAL PAGE IS  
OF POOR QUALITY

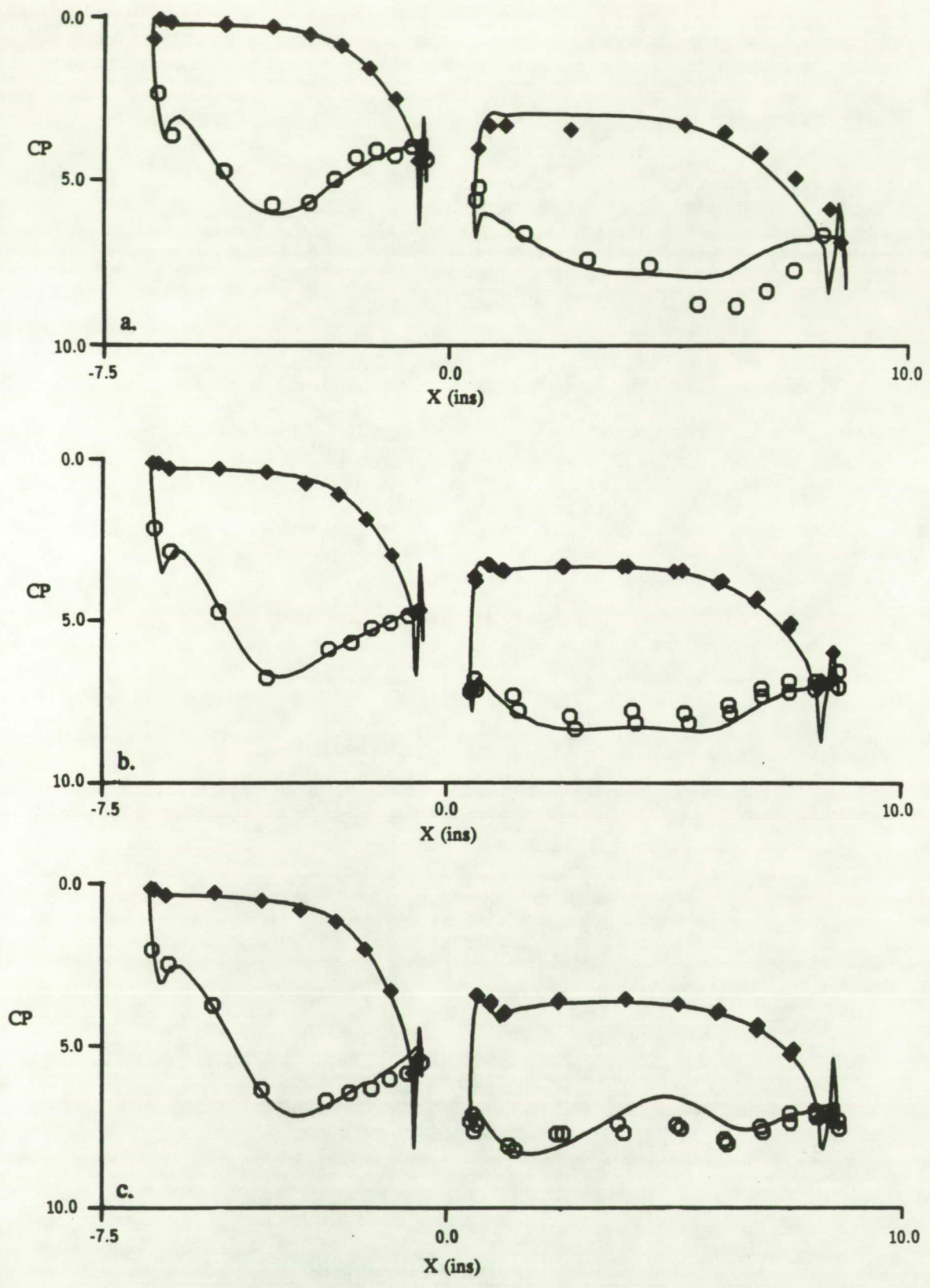


**Figure 22 First Stator and Rotor Fullspan Pressure Distributions**  
 a. 98% Span  
 b. 50% Span  
 c. 2% Span

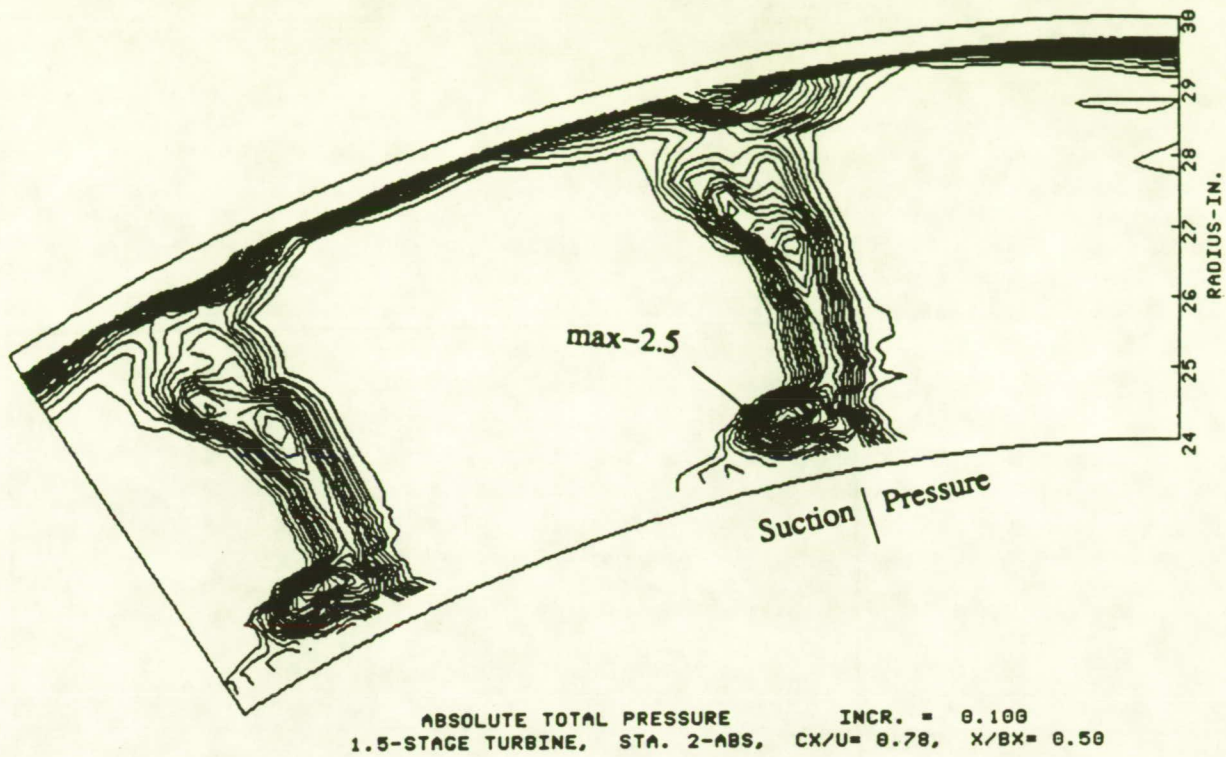


Figure 23a First Stator Exit Results, Plane 2-Absolute, Measured 17% Aft, Absolute Total Pressure Contours,  $\Delta CPTABS=0.10$

$\langle V/UM \rangle = 0.100$

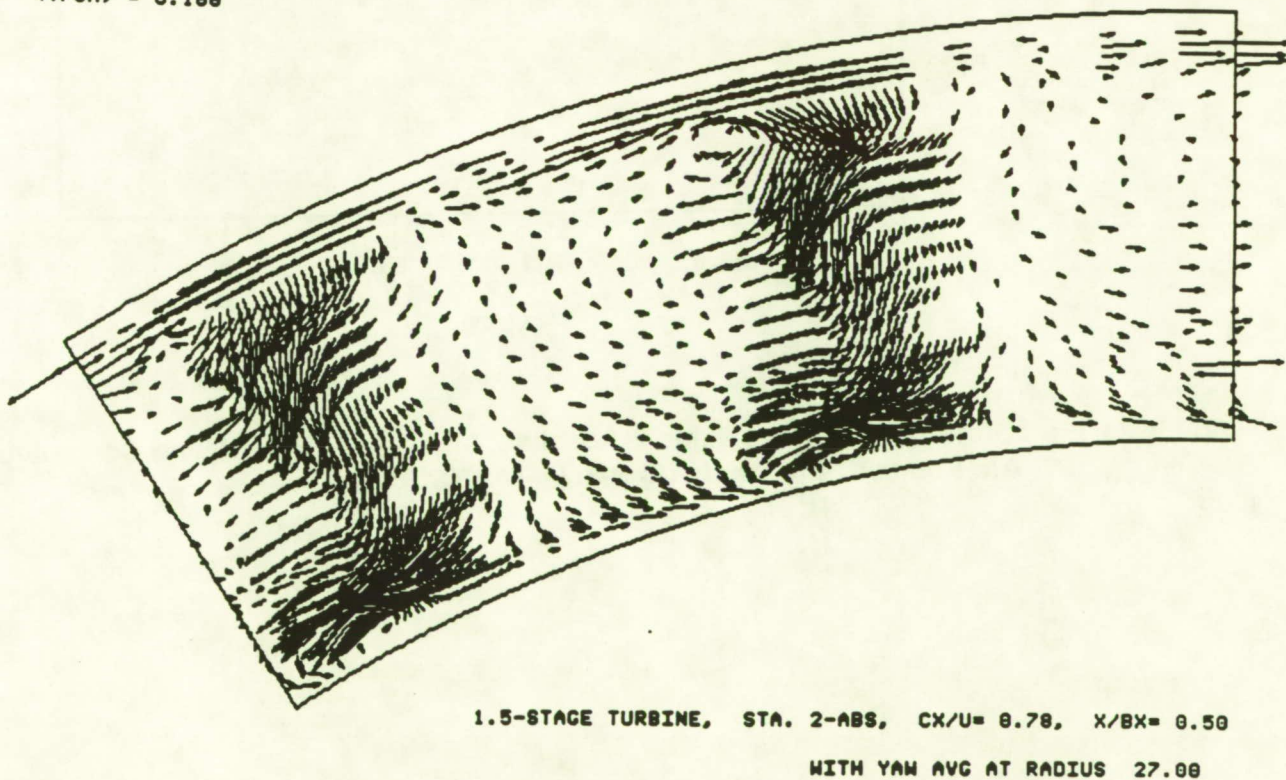
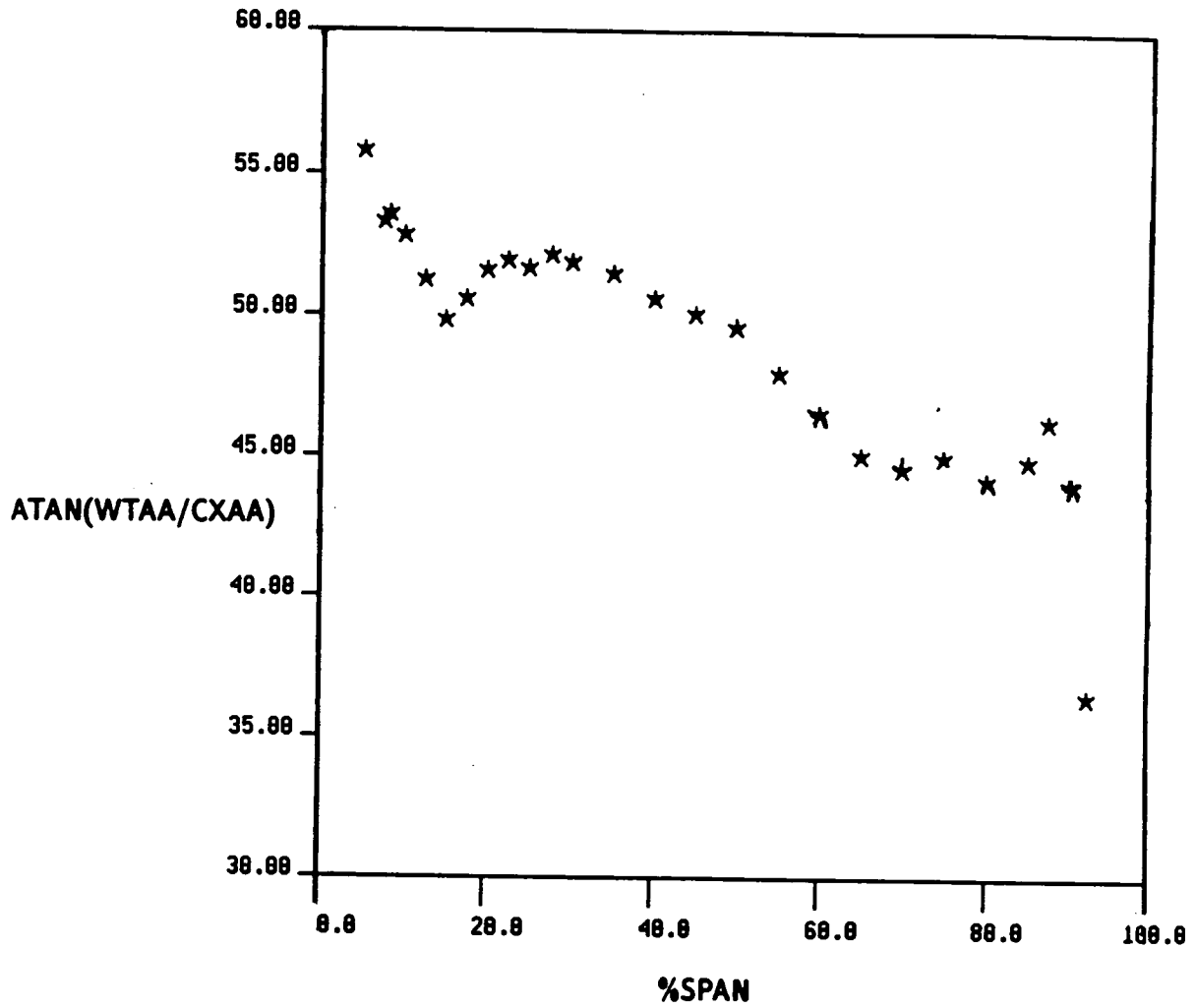
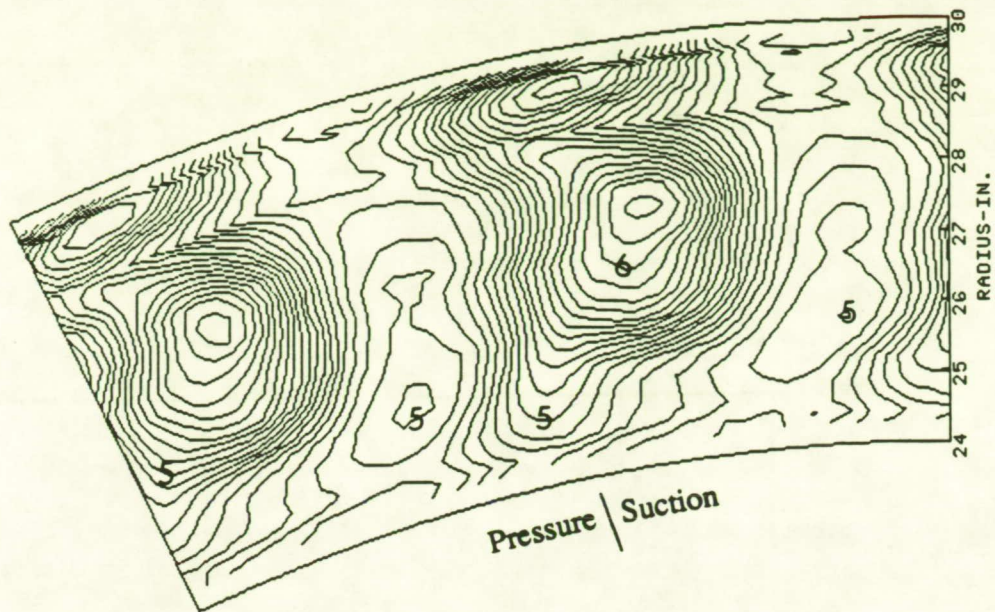


Figure 23b First Stator Exit Results, Plane 2-Absolute, Measured 17% Aft, Secondary Flow with Average Yaw (Absolute) at 50% Span

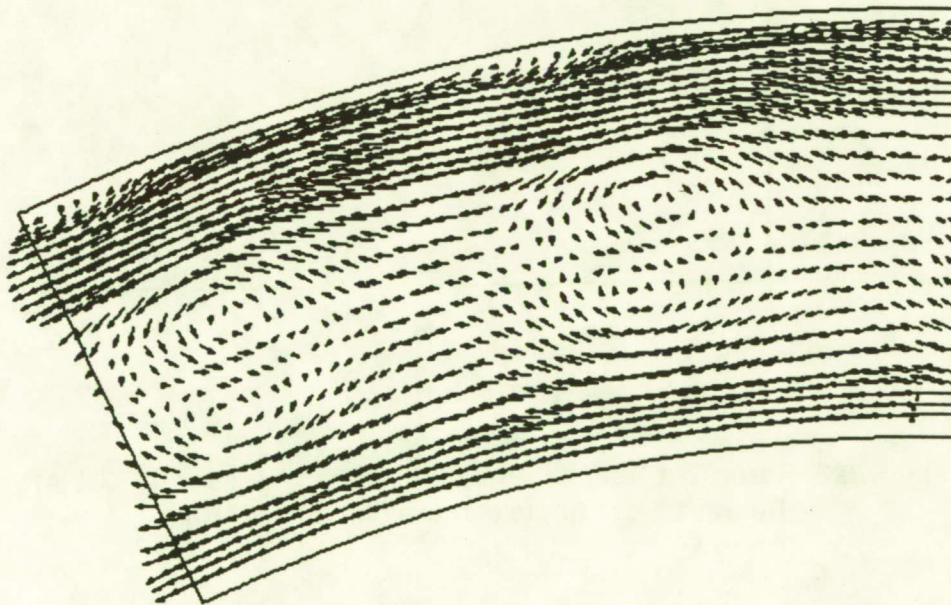


**Figure 24 First Stator Exit Results, Plane 2-Absolute, Measured 17% Aft, and Computed 9% Aft, Relative Flow Angle (Arctan [WTAA/CXAA])**



ROTARY TOTAL PRESSURE                      INCR. = 0.100  
 1.5-STAGE TURBINE, STA. 3-REL,    CX/U= 0.78, X/BX= 0.50

**Figure 25a Rotor Exit Results, Plane 3-Relative, Measured 36% Aft,  
 Rotary Total Pressure Contours,  $\Delta C_{PTROT}=0.10$**



1.5-STAGE TURBINE, STA. 3-REL, CX/U= 0.78, X/BX= 0.50  
 WITH YAW AVG AT RADIUS 27.00

**Figure 25b Rotor Exit Results, 3-Relative, Measured 36% Aft,  
 Secondary Flow with Average Yaw (Relative) at 50% Span**

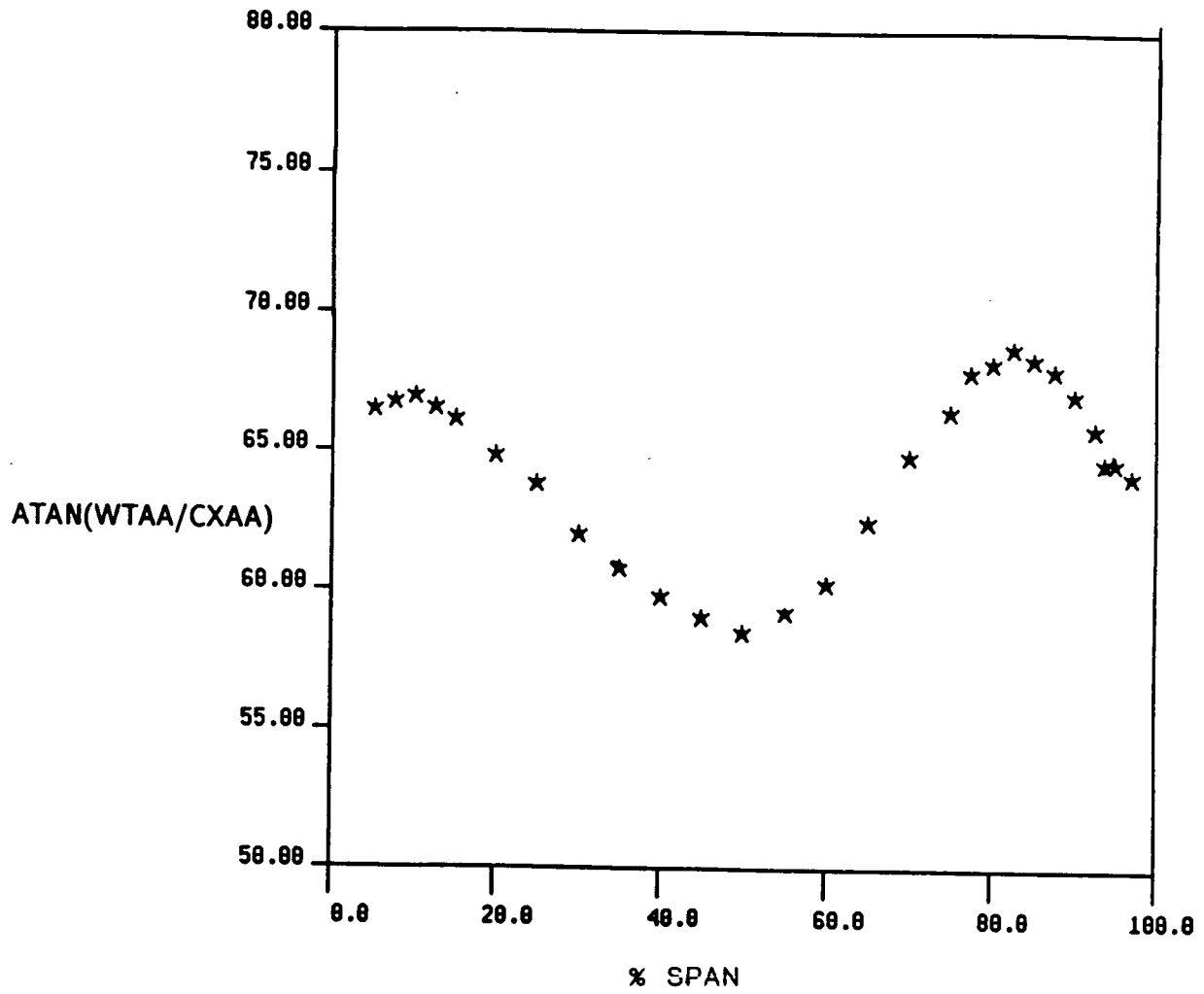


**Figure 26 Rotor Exit Results, Plane 3-Relative, Measured 36% Aft,  
Relative Flow Angle (Arctan [WTAA/CXAA])**

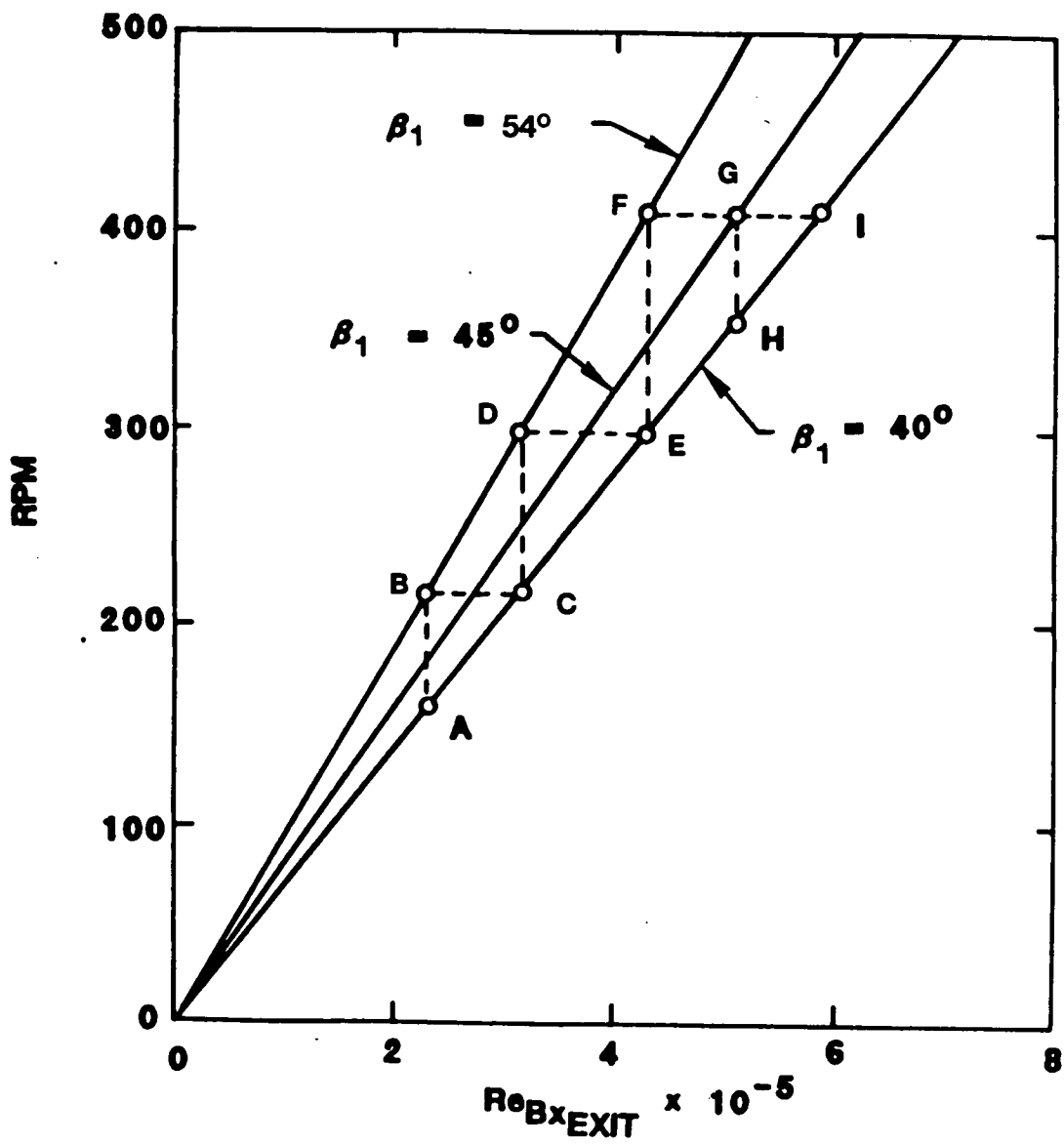
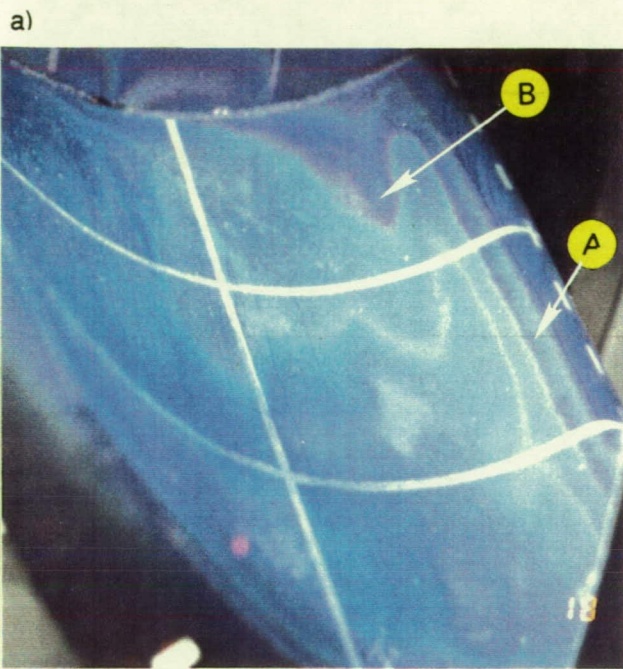
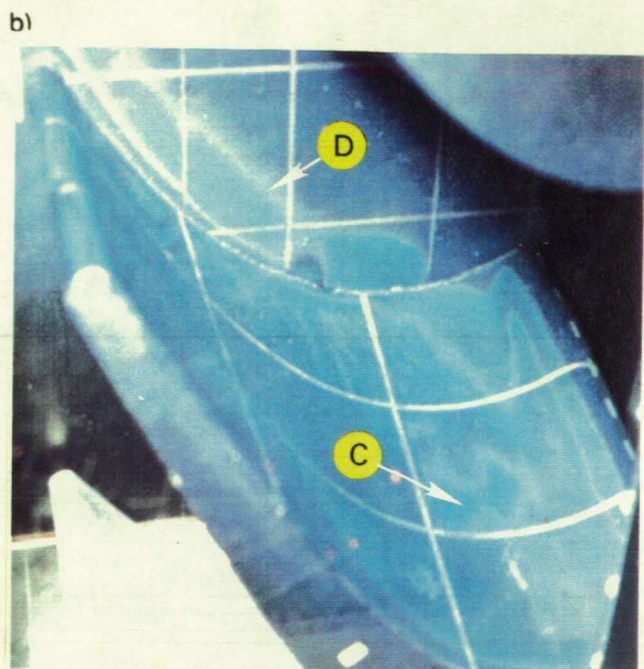


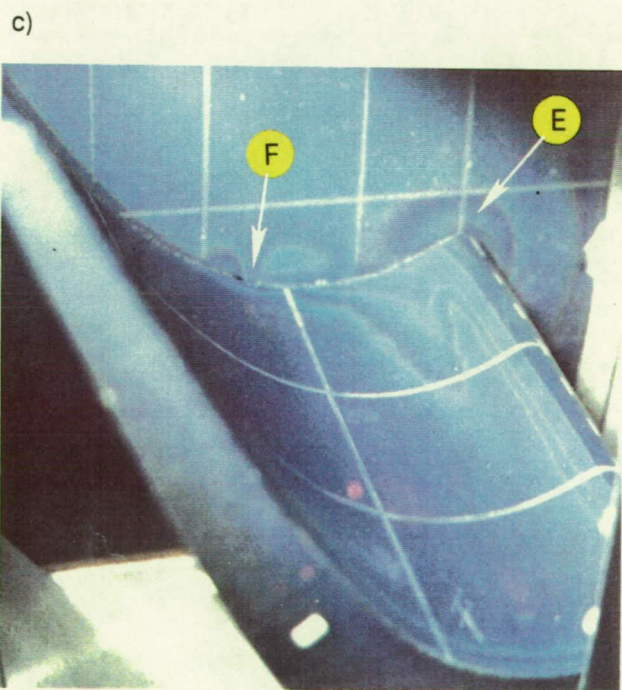
Figure 27 Matrix of Test Data Obtained for the Present Program



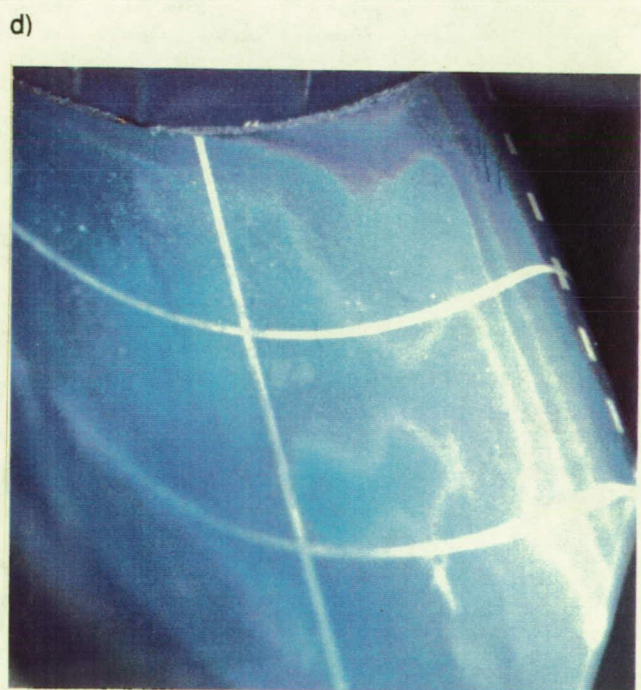
$\beta_1 = 40^\circ$        $Re = 5.8 \times 10^5$



$\beta_1 = 40^\circ$        $Re = 5.2 \times 10^5$



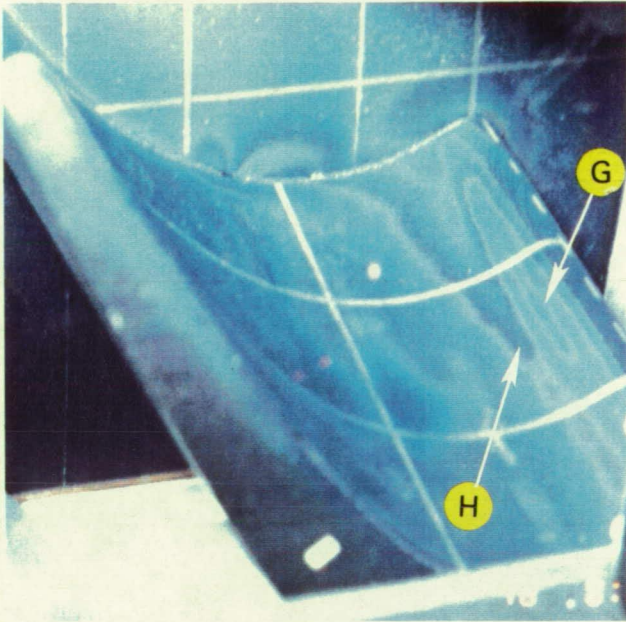
$\beta_1 = 40^\circ$        $Re = 3.2 \times 10^5$



$\beta_1 = 40^\circ$        $Re = 2.3 \times 10^5$

Figure 28 Liquid-Crystal Temperature Contours on the Rotor Pressure Surface for a Range of Reynolds Numbers at  $\beta_1=40^\circ$

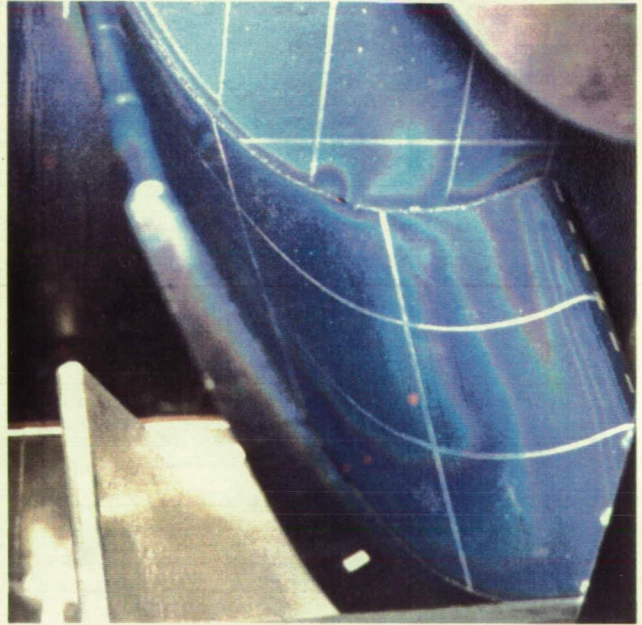
a)



$\beta_1 = 45^\circ$

$Re = 5.1 \times 10^5$

b)



$\beta_1 = 54^\circ$

$Re = 2.4 \times 10^5$

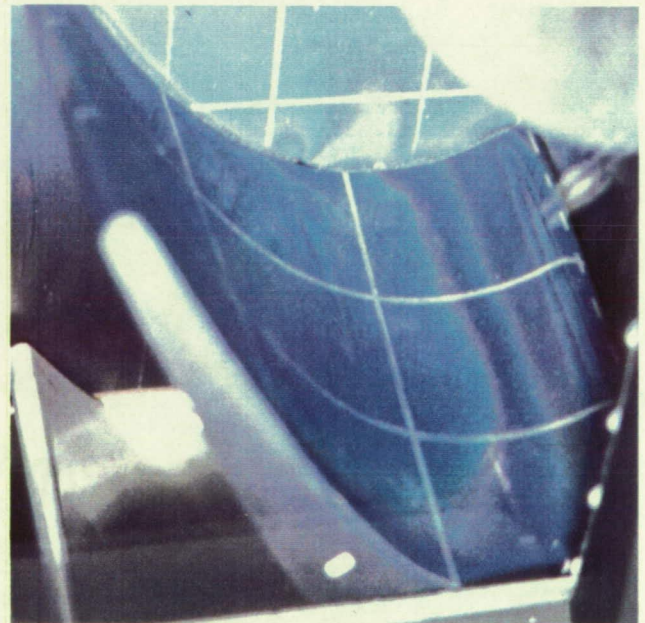
c)



$\beta_1 = 54^\circ$

$Re = 3.2 \times 10^5$

d)

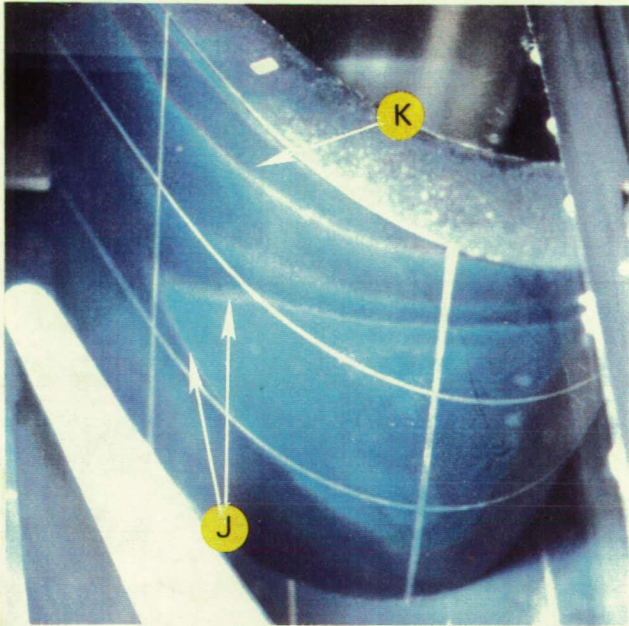


$\beta_1 = 54^\circ$

$Re = 4.2 \times 10^5$

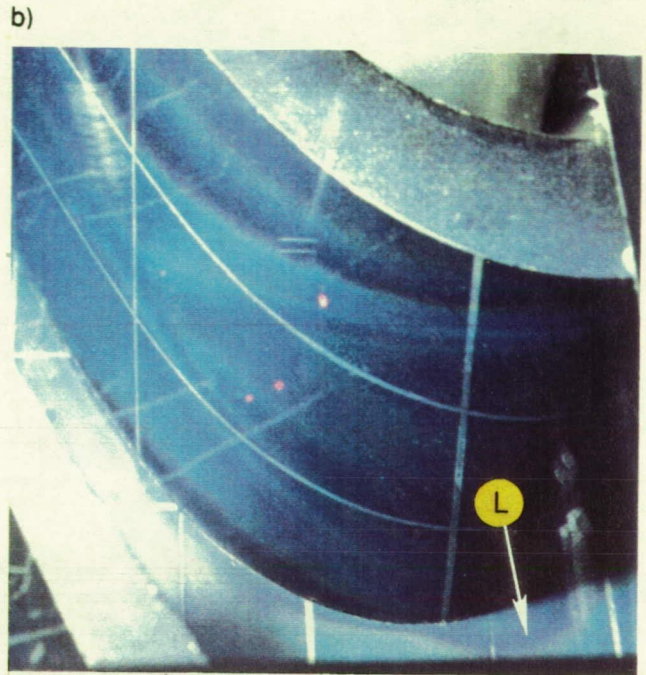
**Figure 29 Liquid-Crystal Temperature Contours on the Rotor Pressure Surface for a Range of Incidence Angles and Reynolds Numbers**

ORIGINAL PAGE  
COLOR PHOTOGRAPH



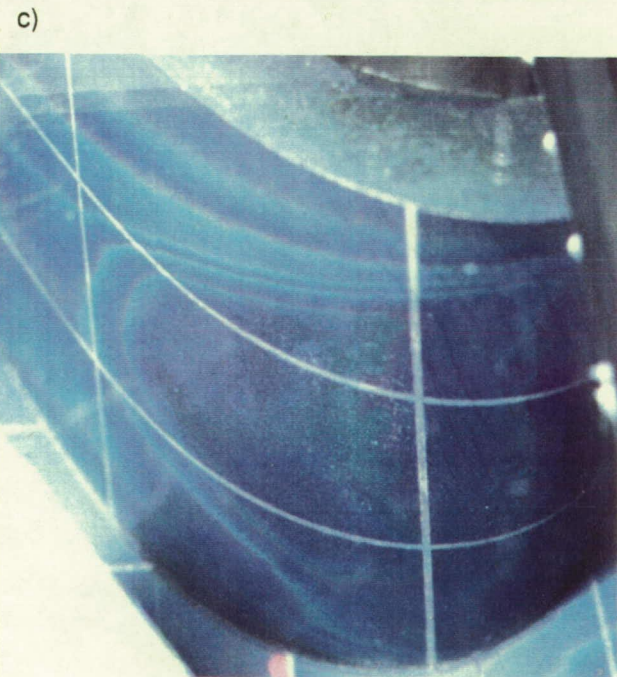
$\beta_1 = 40^\circ$

$Re = 2.3 \times 10^5$



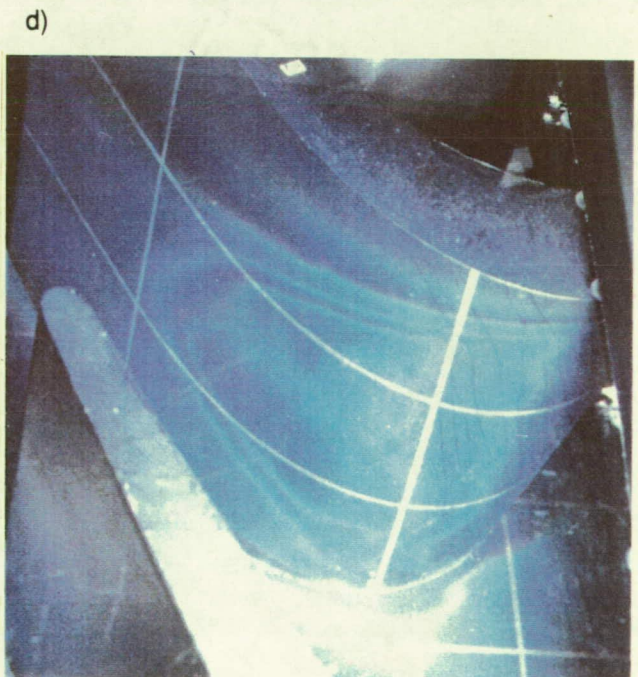
$\beta_1 = 40^\circ$

$Re = 3.2 \times 10^5$



$\beta_1 = 54^\circ$

$Re = 2.4 \times 10^5$



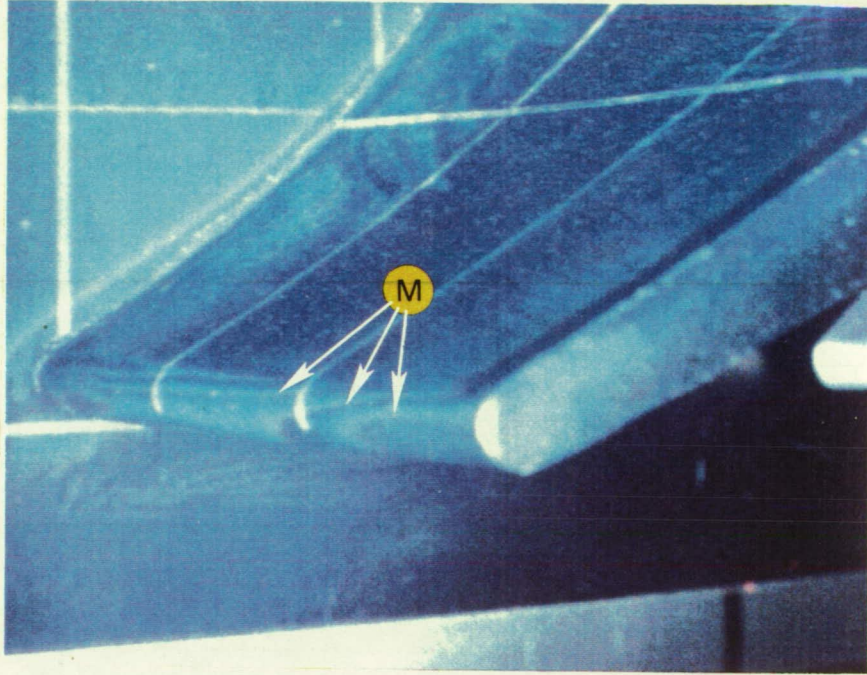
$\beta_1 = 54^\circ$

$Re = 3.2 \times 10^5$

**Figure 30 Liquid-Crystal Temperature Contours on the Rotor Suction Angle Surface for a Range of Incidence Angles and Reynolds Numbers**

ORIGINAL PAGE  
COLOR PHOTOGRAPH

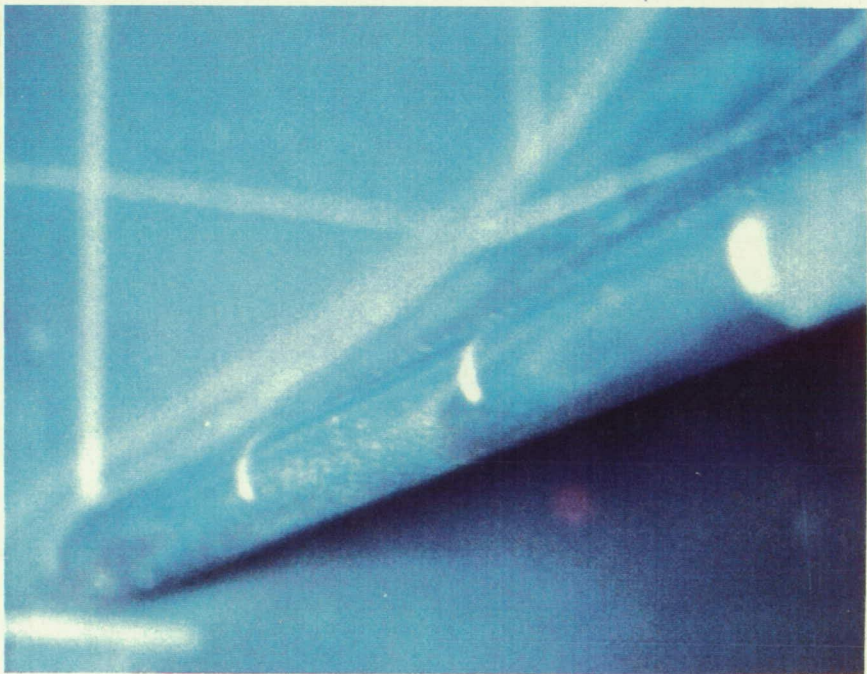
a)



$$\beta_1 = 54^\circ$$

$$Re = 4.2 \times 10^5$$

b)



$$\beta_1 = 54^\circ$$

$$Re = 4.2 \times 10^5$$

Figure 31 Close-up Photographs of the Liquid-Crystal Temperature Contours on the Airfoil Trailing Edge for  $\beta_1=54^\circ$  and  $Re=4.2 \times 10^5$

$$S^* = \frac{S}{S_{tot}(r)} \frac{S_{tot}(\text{midspan})}{SPAN}$$

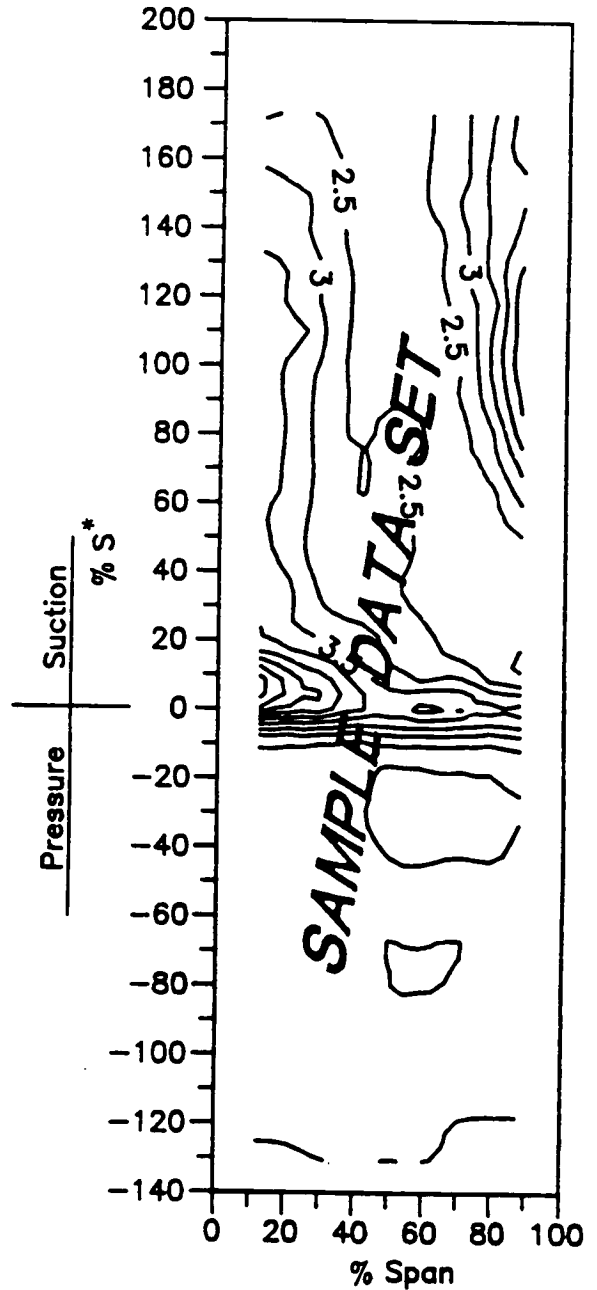
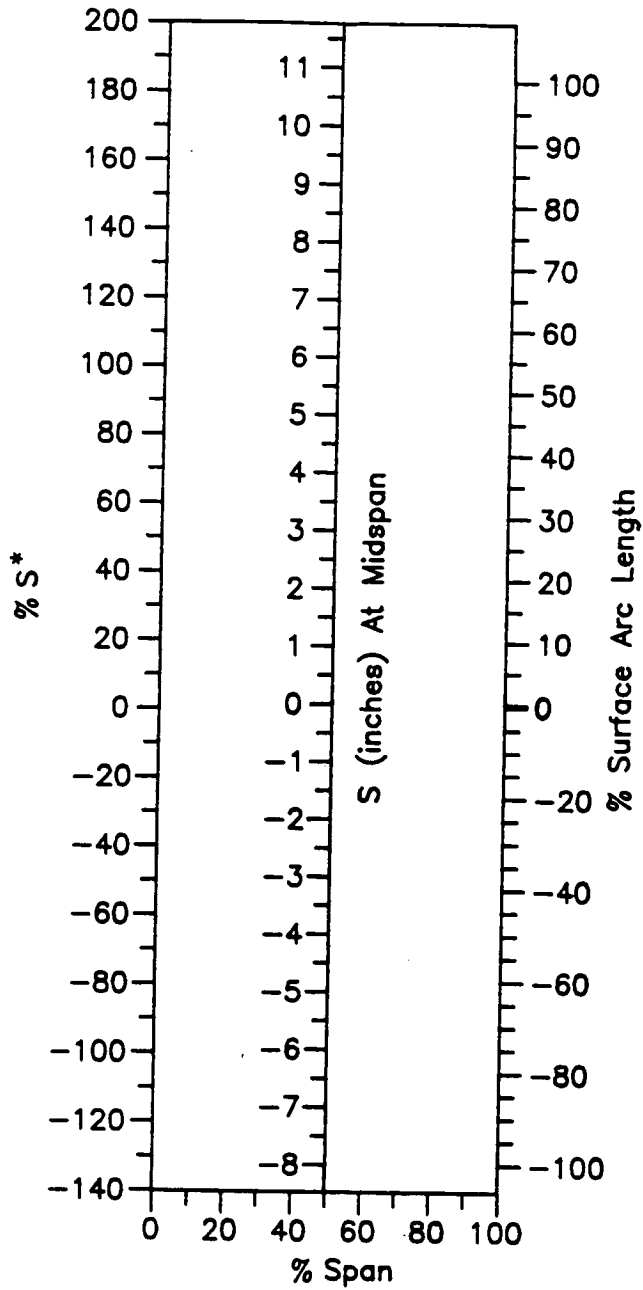


Figure 32 Coordinates for Presentation of the Airfoil Surface Contours of Stanton Number

SMOOTH-WALL MODEL

$\beta_1 = 40^\circ$

$N = 300$

$Re = 4.370 \times 10^5$

CONTOUR KEY ( $St \times 10^3$ )	
—	Thermocouple Data
- · -	Liquid Crystal Data

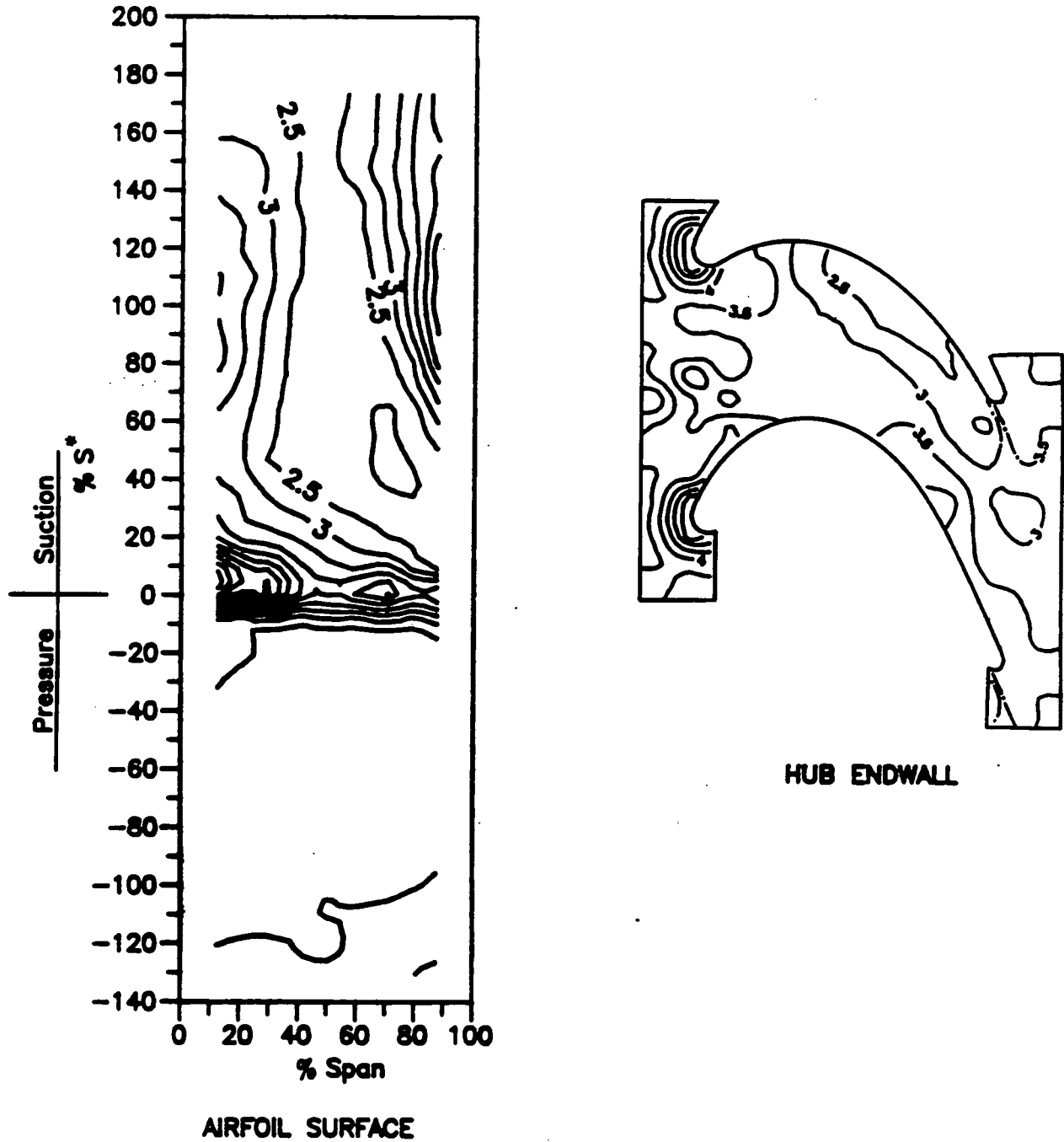


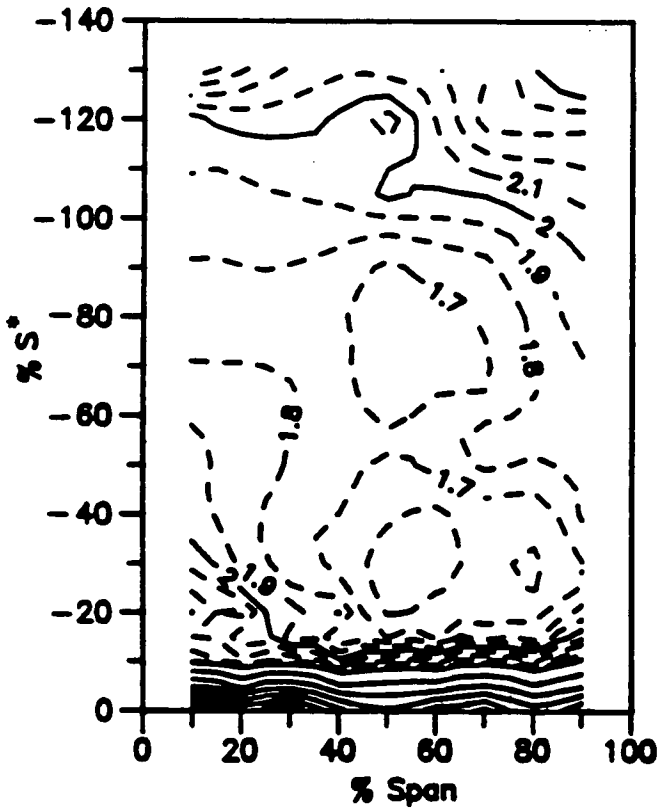
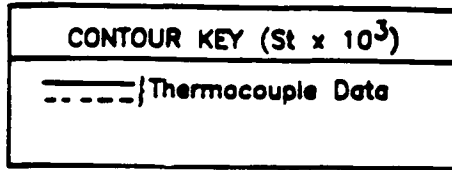
Figure 33a Stanton Number Contours on the Airfoil and Hub Endwall Surfaces

SMOOTH-WALL MODEL

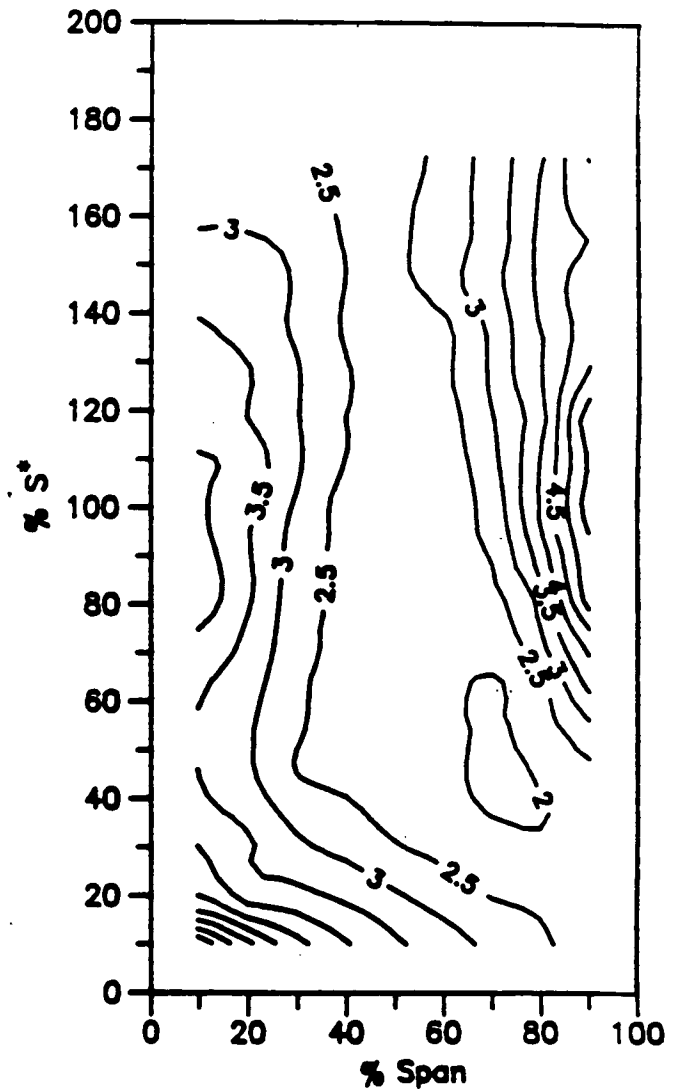
$$\beta_1 = 40^\circ$$

$$N = 300$$

$$Re = 4.370 \times 10^5$$



PRESSURE SURFACE



SUCTION SURFACE

Figure 33b Details of the Stanton Number Contours on the Airfoil Suction and Pressure Surfaces

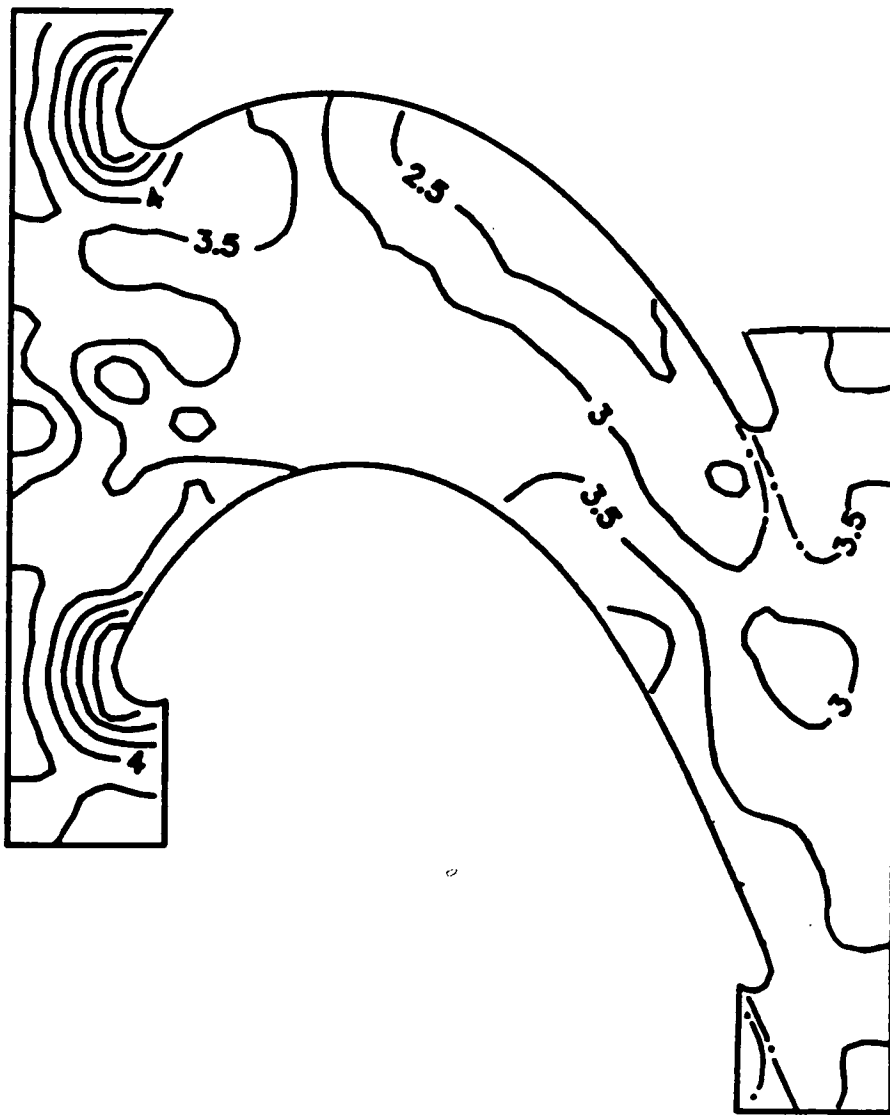
SMOOTH-WALL MODEL

$$\beta_1 = 40^\circ$$

$$N = 300$$

$$Re = 4.370 \times 10^5$$

CONTOUR KEY ( $St \times 10^3$ )	
—	Thermocouple Data
- · -	Liquid Crystal Data



HUB ENDWALL

Figure 33c Details of the Stanton Number Contours on the Hub Endwall Surface

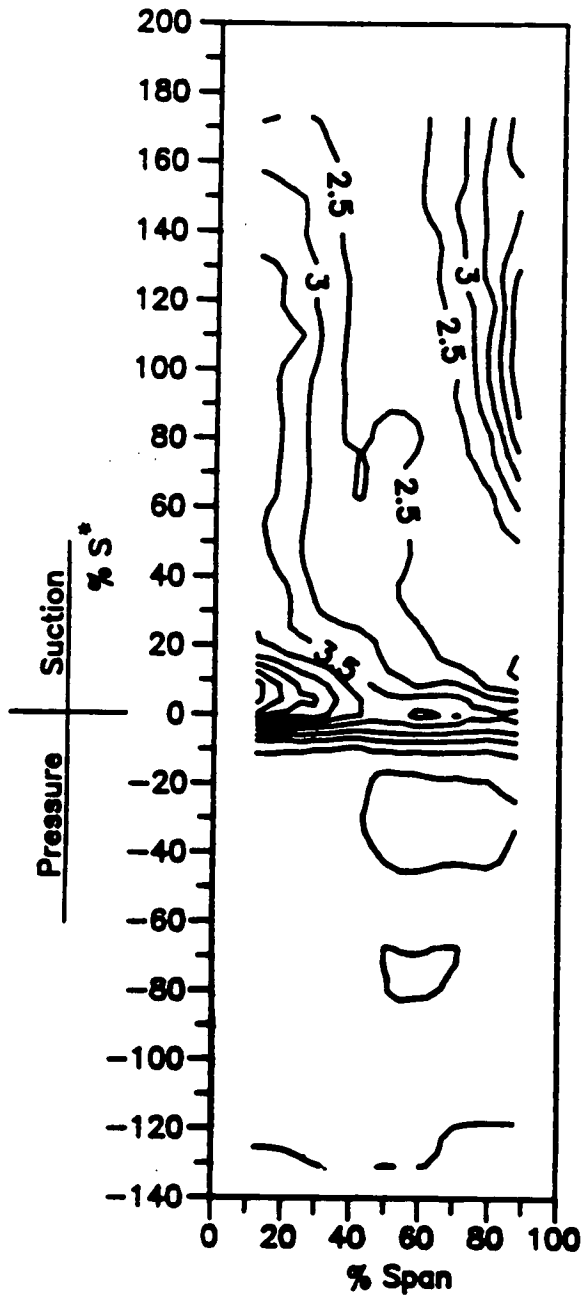
SMOOTH-WALL MODEL

$\beta_1 = 40^\circ$

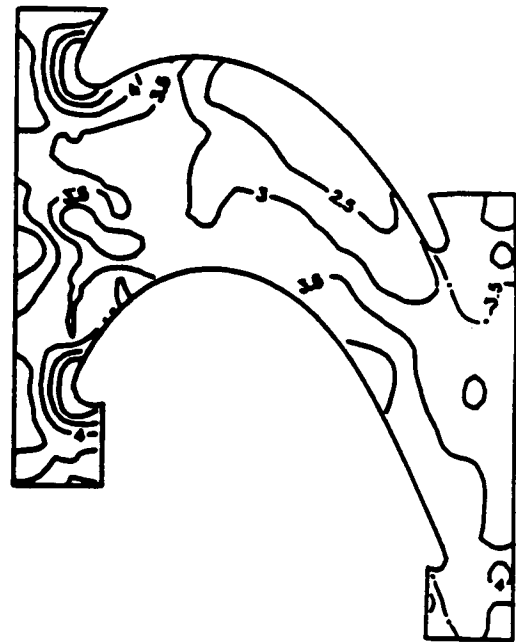
$N = 410$

$Re = 5.838 \times 10^5$

CONTOUR KEY ( $St \times 10^3$ )	
—	Thermocouple Data
- · -	Liquid Crystal Data



AIRFOIL SURFACE



HUB ENDWALL

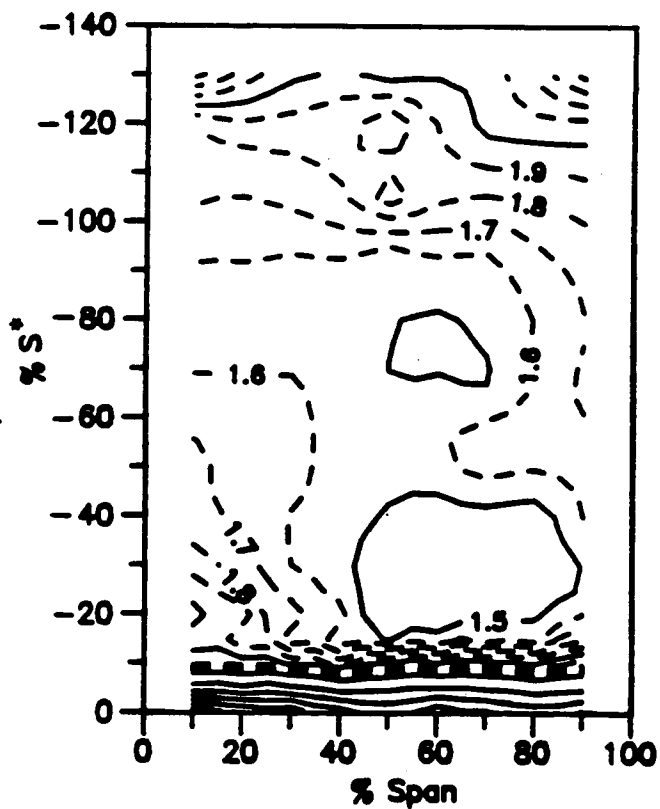
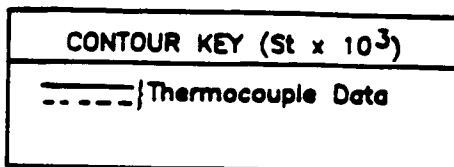
Figure 34a Stanton Number Contours on the Airfoil and Hub Endwall Surfaces

SMOOTH-WALL MODEL

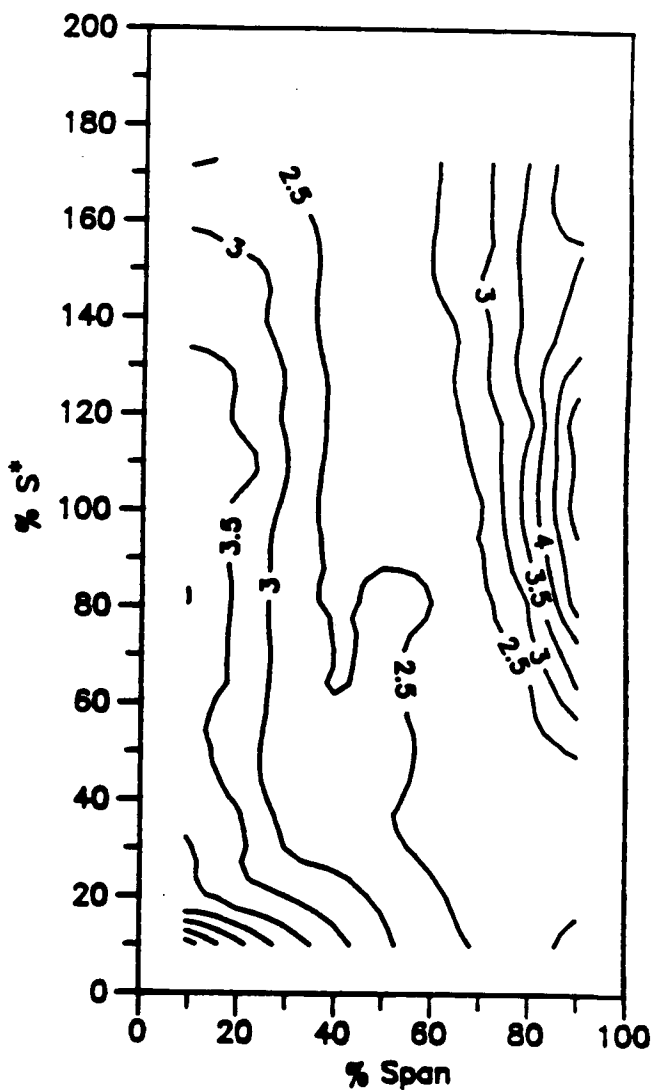
$$\beta_1 = 40^\circ$$

$$N = 410$$

$$Re = 5.838 \times 10^5$$



PRESSURE SURFACE



SUCTION SURFACE

Figure 34b Details of the Stanton Number Contours on the Airfoil Suction and Pressure Surfaces

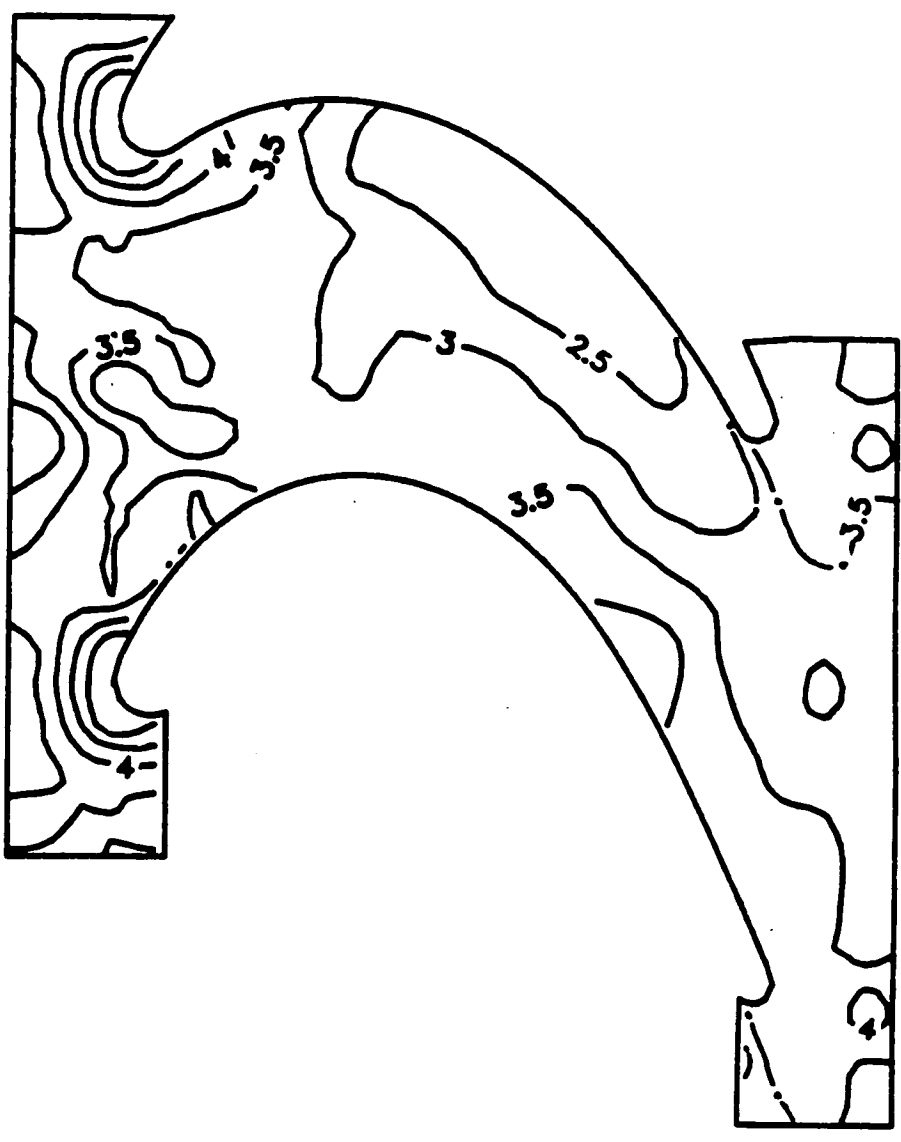
SMOOTH-WALL MODEL

$\beta_1 = 40^\circ$

$N = 410$

$Re = 5.838 \times 10^5$

CONTOUR KEY ( $St \times 10^3$ )	
—	Thermocouple Data
-.-	Liquid Crystal Data



HUB ENDWALL

Figure 34c Details of the Stanton Number Contours on the Hub Endwall Surface

SMOOTH-WALL MODEL

$\beta_1 = 54^\circ$

$N = 219$

$Re = 2.366 \times 10^5$

CONTOUR KEY ( $St \times 10^3$ )	
—	Thermocouple Data
- · -	Liquid Crystal Data

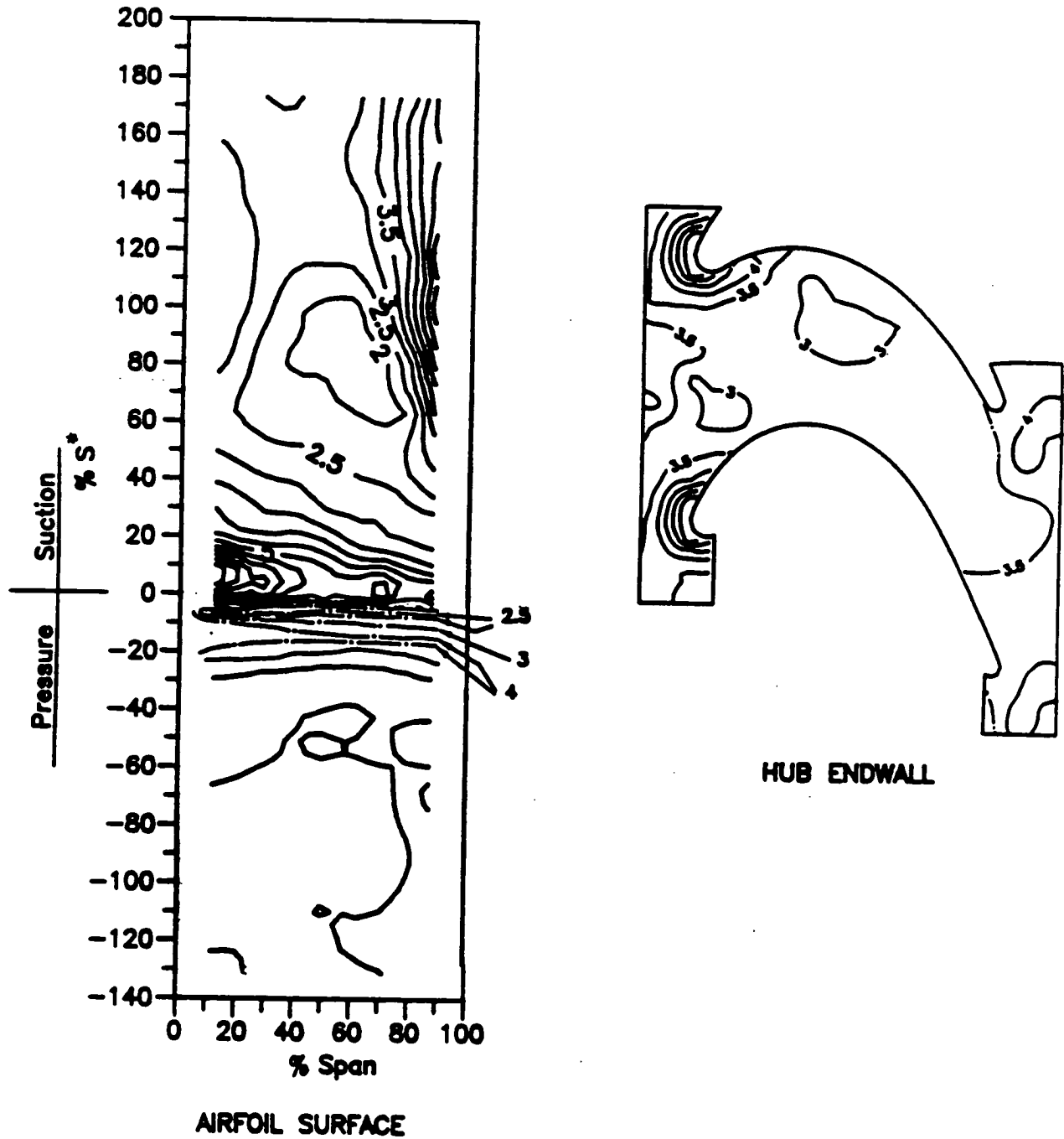


Figure 35a Stanton Number Contours on the Airfoil and Hub Endwall Surfaces

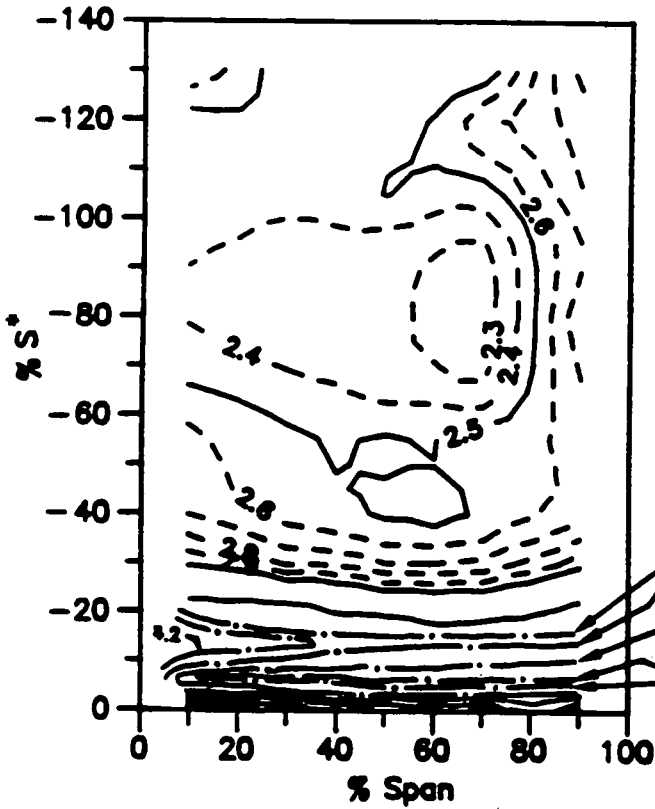
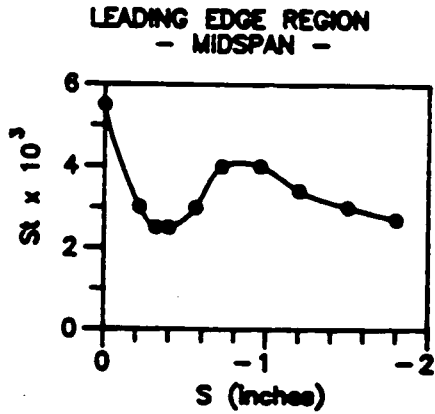
$\beta_1 = 54^\circ$

SMOOTH-WALL MODEL

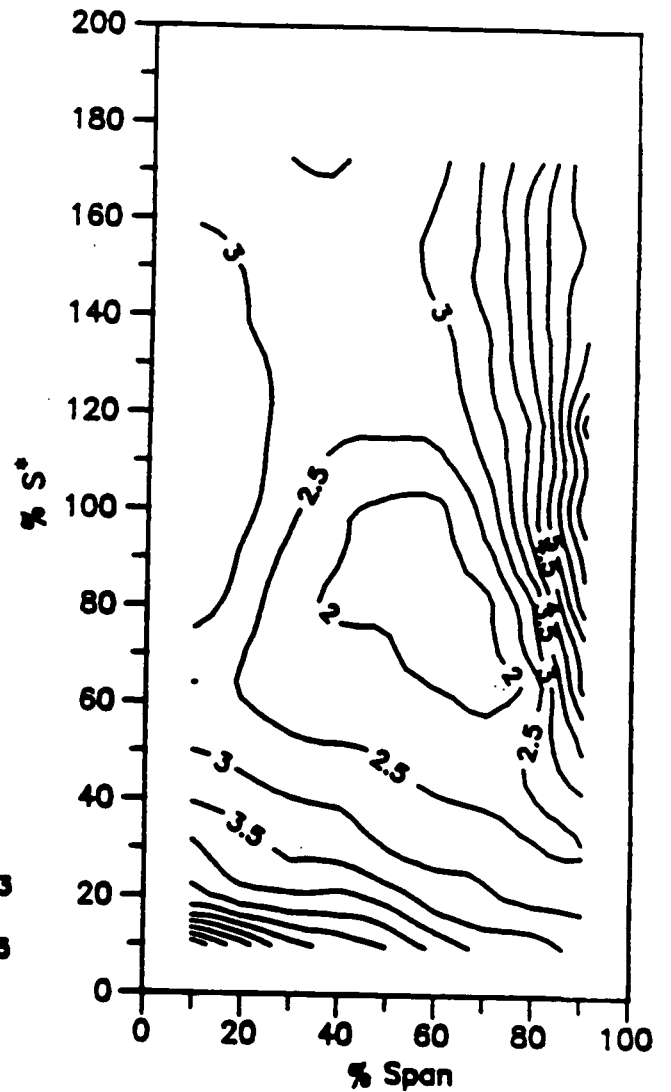
$N = 219$

$Re = 2.366 \times 10^5$

CONTOUR KEY ( $St \times 10^3$ )	
-----	Thermocouple Data
- - - - -	Liquid Crystal Data



PRESSURE SURFACE



SUCTION SURFACE

Figure 35b Details of the Stanton Number Contours on the Airfoil Suction and Pressure Surfaces

SMOOTH-WALL MODEL

$$\beta_1 = 54^\circ$$

$$N = 219$$

$$Re = 2.366 \times 10^5$$

CONTOUR KEY ( $St \times 10^3$ )	
—	Thermocouple Data
- · -	Liquid Crystal Data



HUB ENDWALL

Figure 35c Details of the Stanton Number Contours on the Hub Endwall Surface

SMOOTH-WALL MODEL

$$\beta_1 = 54^\circ$$

$$N = 397$$

$$Re = 4.235 \times 10^5$$

CONTOUR KEY ( $St \times 10^3$ )	
—	Thermocouple Data
- - -	Liquid Crystal Data

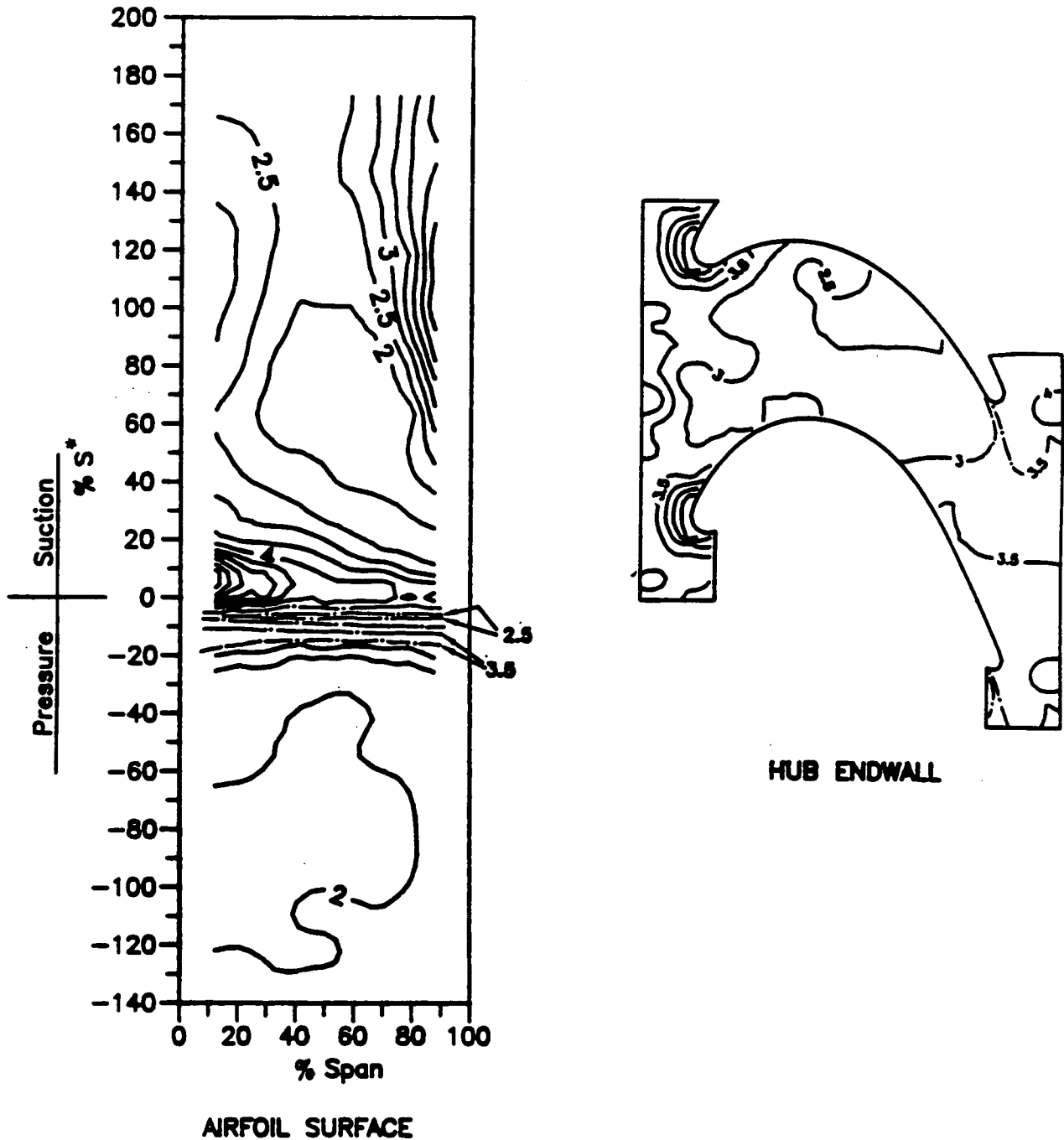


Figure 36a Stanton Number Contours on the Airfoil and Hub Endwall Surfaces

SMOOTH-WALL MODEL

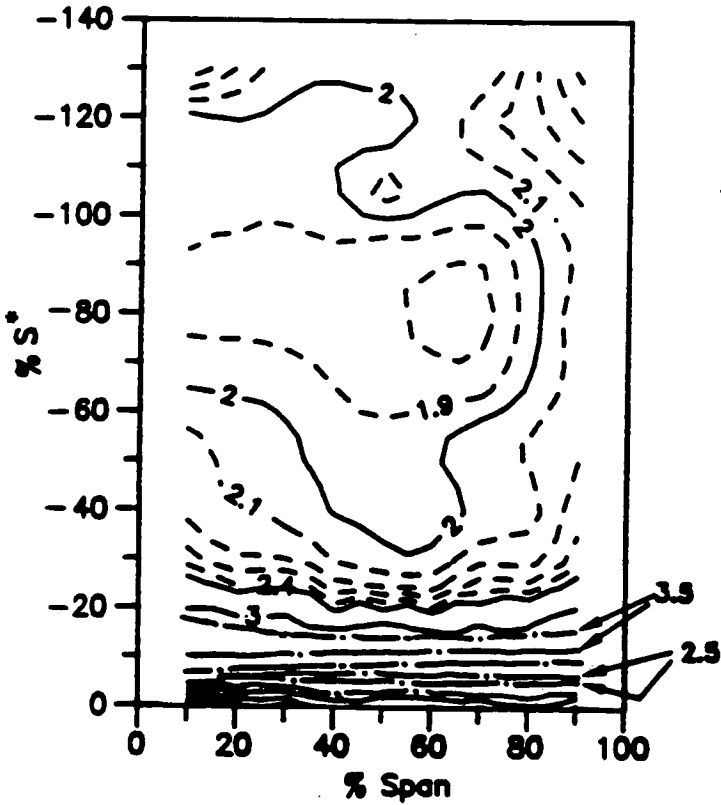
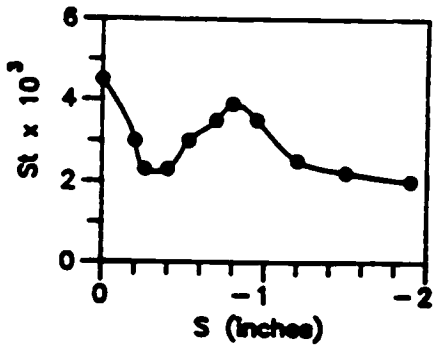
$\beta_1 = 54^\circ$

$N = 397$

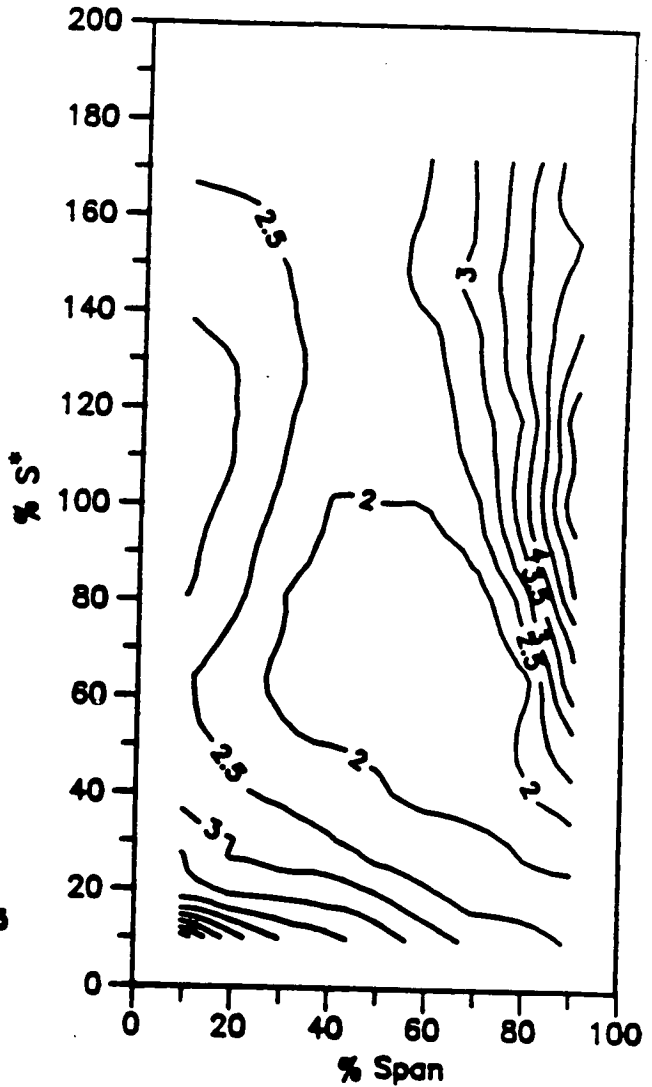
$Re = 4.235 \times 10^5$

CONTOUR KEY ( $St \times 10^3$ )	
-----	Thermocouple Data
- · - -	Liquid Crystal Data

LEADING EDGE REGION  
- MIDSPAN -



PRESSURE SURFACE



SUCTION SURFACE

Figure 36b Details of the Stanton Number Contours on the Airfoil Suction and Pressure Surfaces

SMOOTH-WALL MODEL

$$\beta_1 = 54^\circ$$

$$N = 397$$

$$Re = 4.235 \times 10^5$$

CONTOUR KEY ( $St \times 10^3$ )	
—	Thermocouple Data
- · -	Liquid Crystal Data

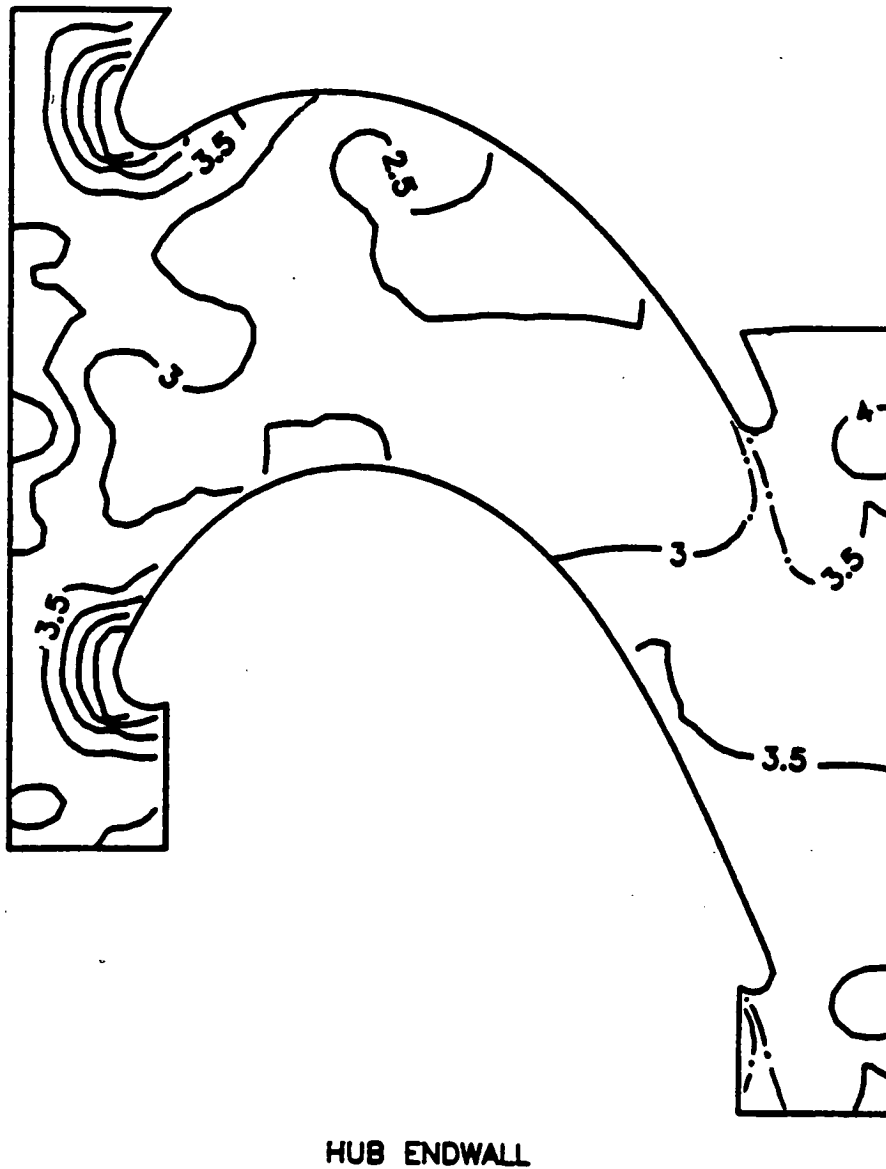


Figure 36c Details of the Stanton Number Contours on the Hub Endwall Surface

ROUGH-WALL MODEL

$\beta_1 = 40^\circ$

$N = 300$

$Re = 4.122 \times 10^5$

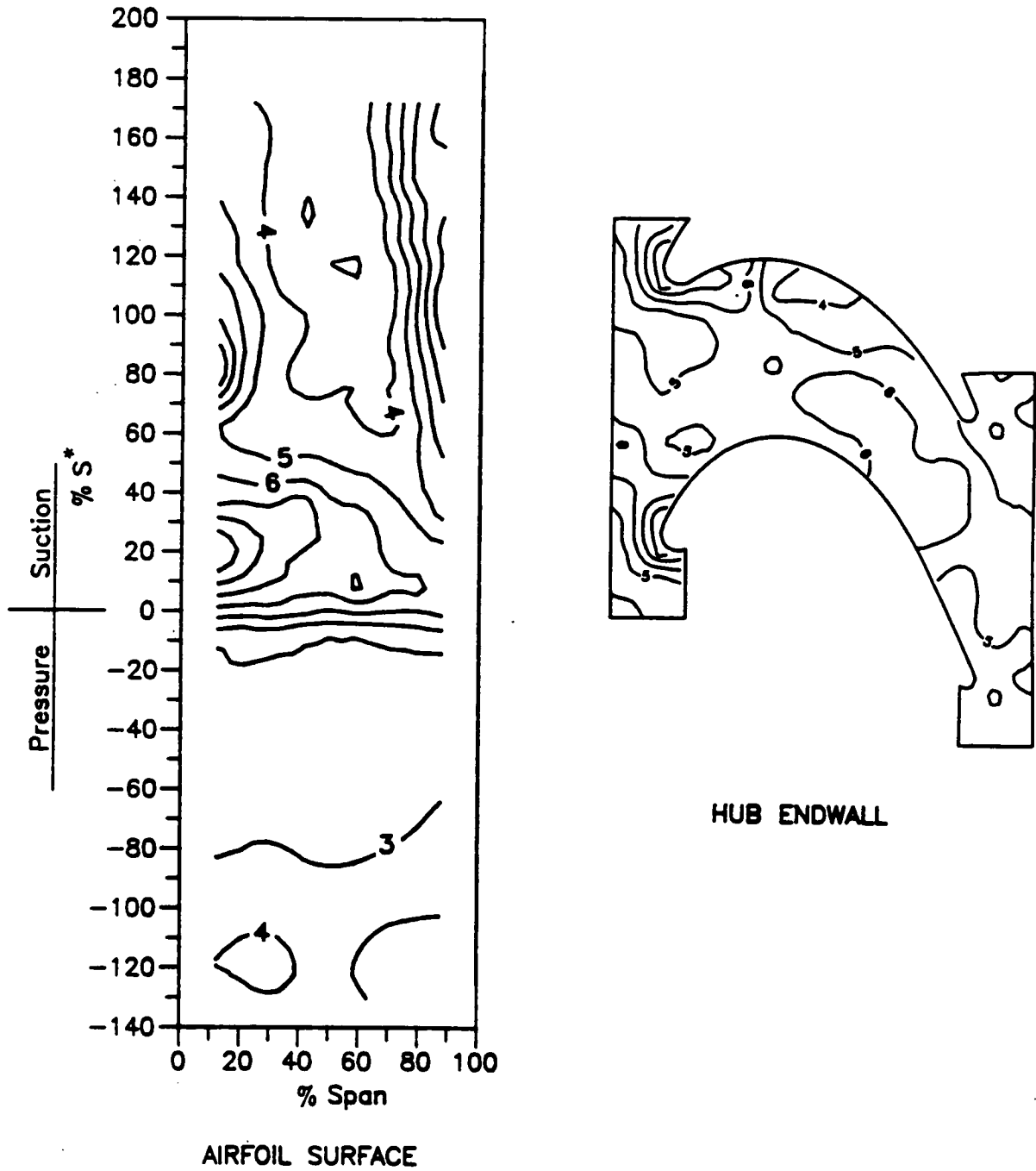
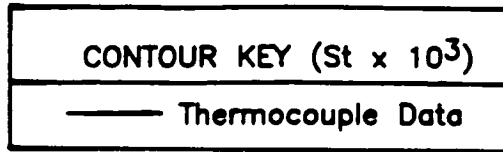


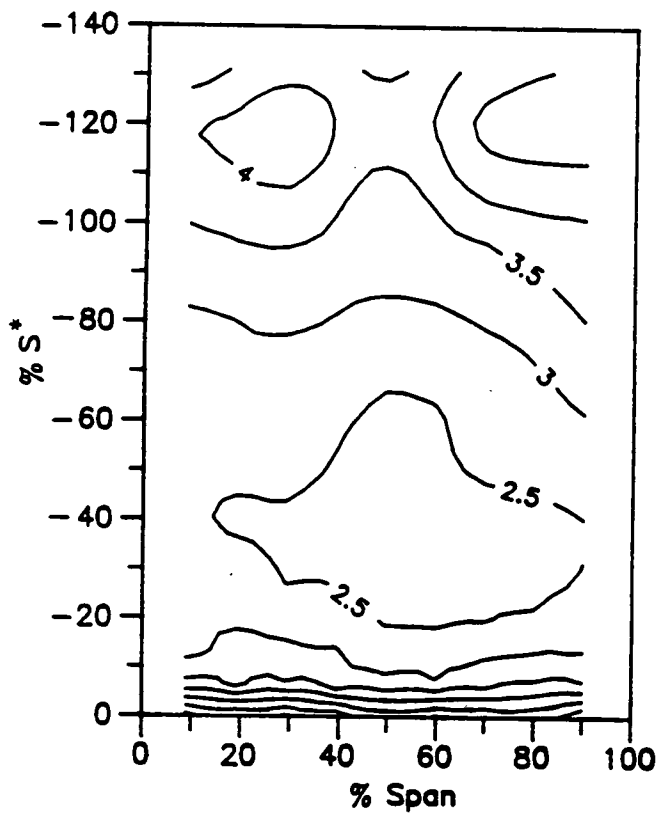
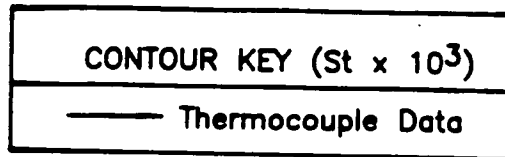
Figure 37a Stanton Number Contours on the Airfoil and Hub Endwall Surfaces

$\beta_1 = 40^\circ$

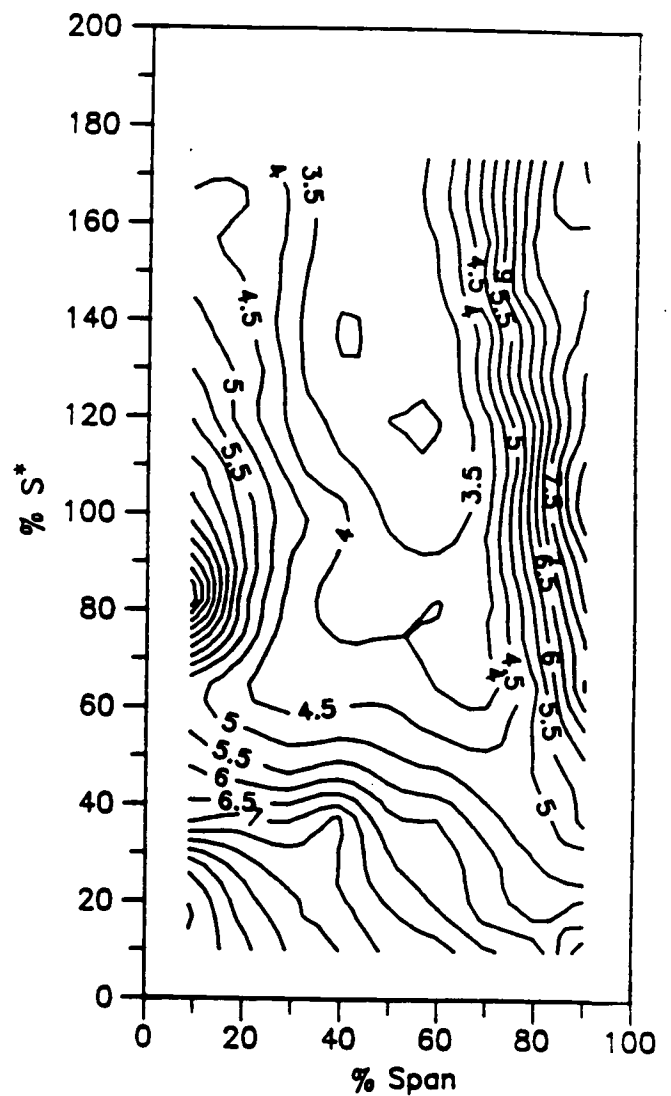
ROUGH-WALL MODEL

$N = 300$

$Re = 4.122 \times 10^5$



PRESSURE SURFACE



SUCTION SURFACE

Figure 37b Details of the Stanton Number Contours on the Airfoil Suction and Pressure Surfaces

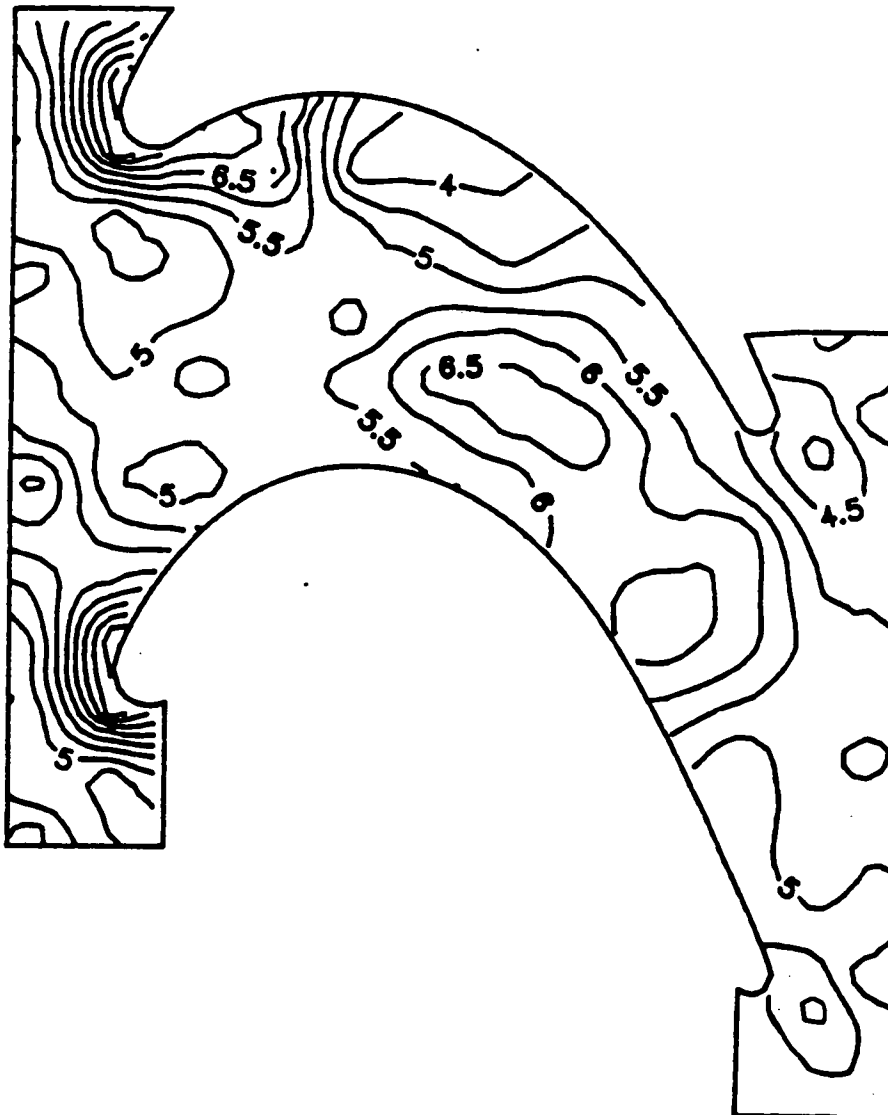
ROUGH-WALL MODEL

$$\beta_1 = 40^\circ$$

$$N = 300$$

$$Re = 4.122 \times 10^5$$

CONTOUR KEY ( $St \times 10^3$ )
— Thermocouple Data



HUB ENDWALL

Figure 37c Details of the Stanton Number Contours on the Hub Endwall Surface

ROUGH-WALL MODEL

$$\beta_1 = 40^\circ$$

$$N = 410$$

$$Re = 5.533 \times 10^5$$

CONTOUR KEY ( $St \times 10^3$ )
— Thermocouple Data

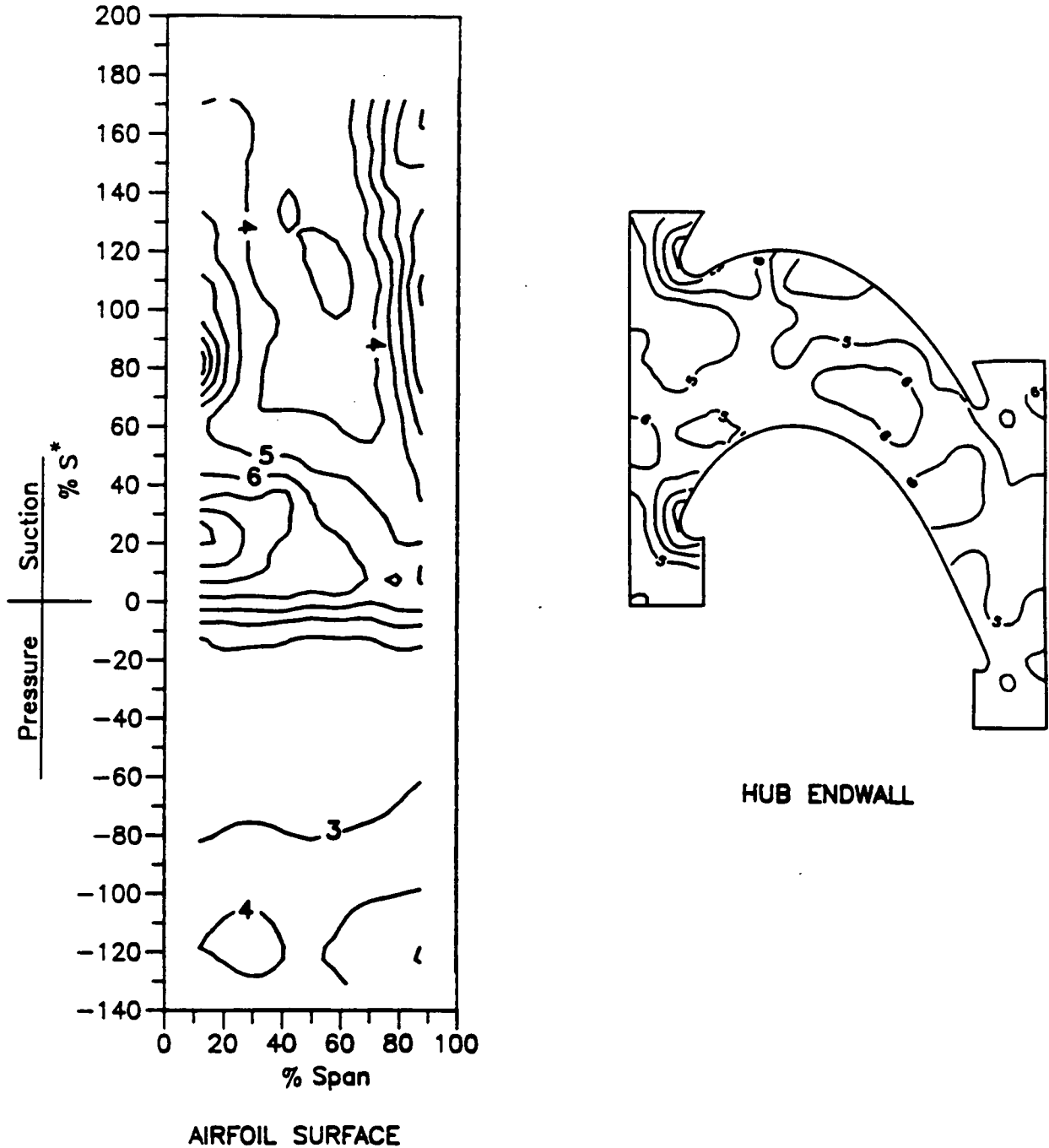


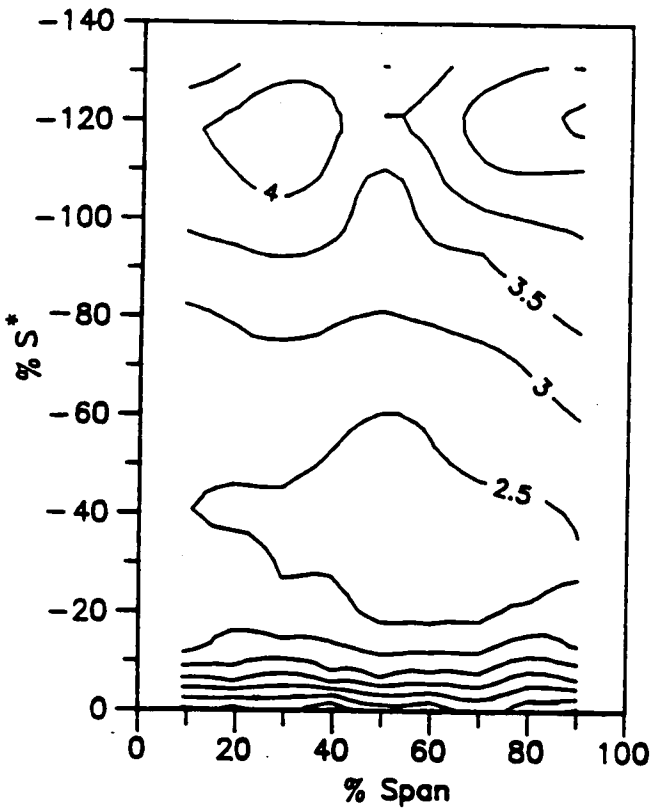
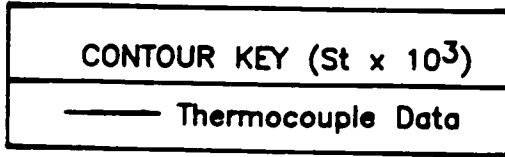
Figure 38a Stanton Number Contours on the Airfoil and Hub Endwall Surfaces

$\beta_1 = 40^\circ$

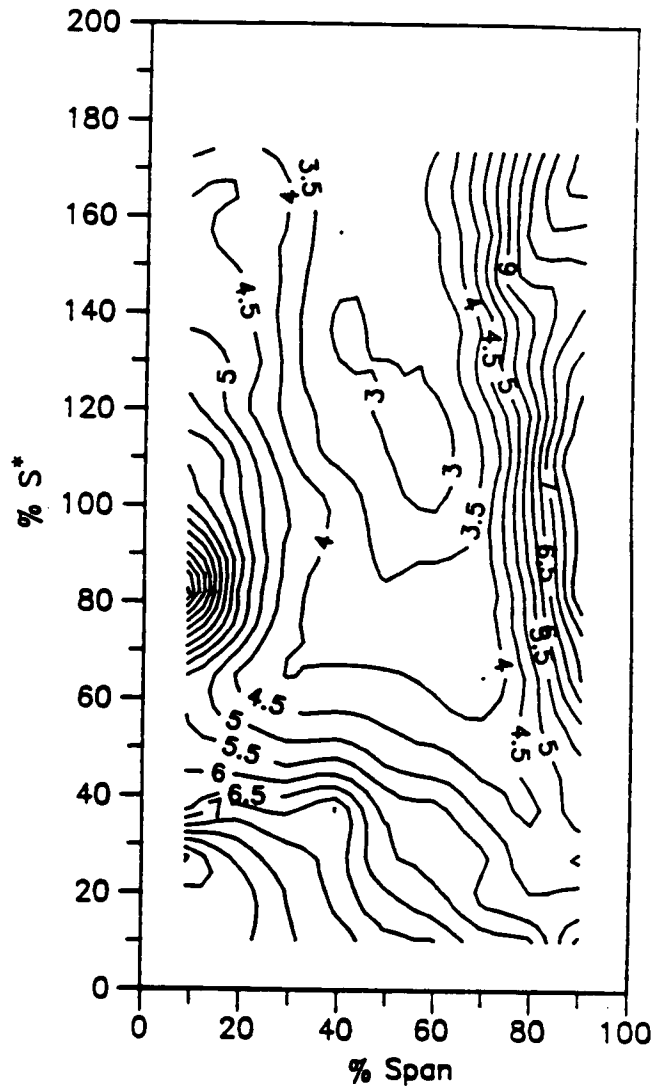
ROUGH-WALL MODEL

$N = 410$

$Re = 5.533 \times 10^5$



PRESSURE SURFACE



SUCTION SURFACE

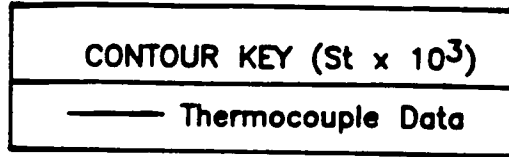
Figure 38b Details of the Stanton Number Contours on the Airfoil Suction and Pressure Surfaces

ROUGH-WALL MODEL

$$\beta_1 = 40^\circ$$

$$N = 410$$

$$Re = 5.533 \times 10^5$$



HUB ENDWALL

Figure 38c Details of the Stanton Number Contours on the Hub Endwall Surface

ROUGH-WALL MODEL

$$\beta_1 = 54^\circ$$

$$N = 219$$

$$Re = 2.230 \times 10^5$$

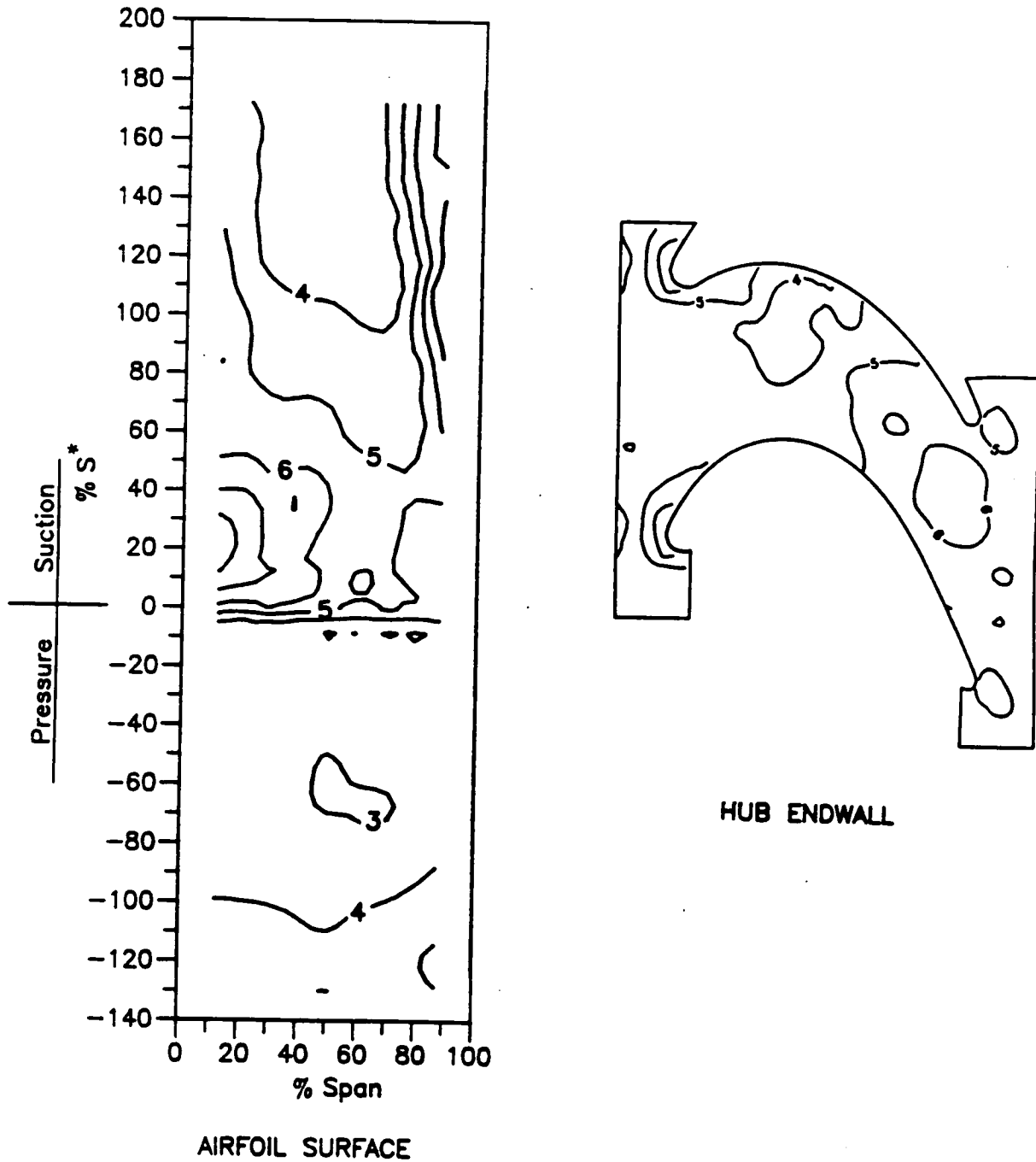
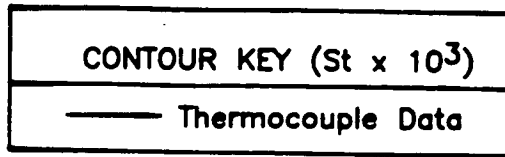


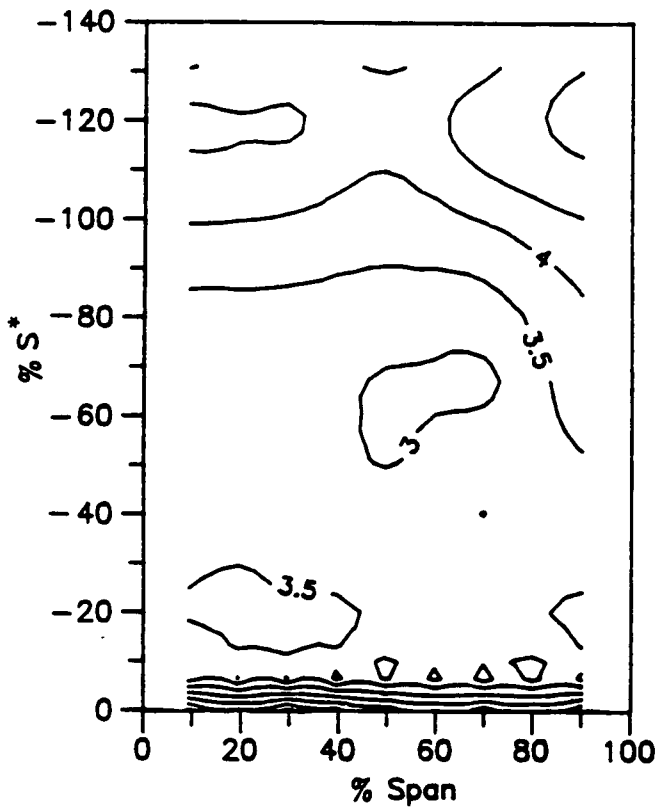
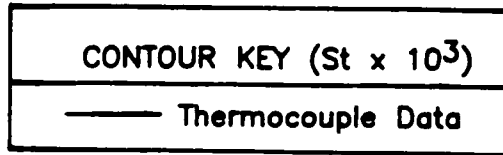
Figure 39a Stanton Number Contours on the Airfoil and Hub Endwall Surfaces

ROUGH-WALL MODEL

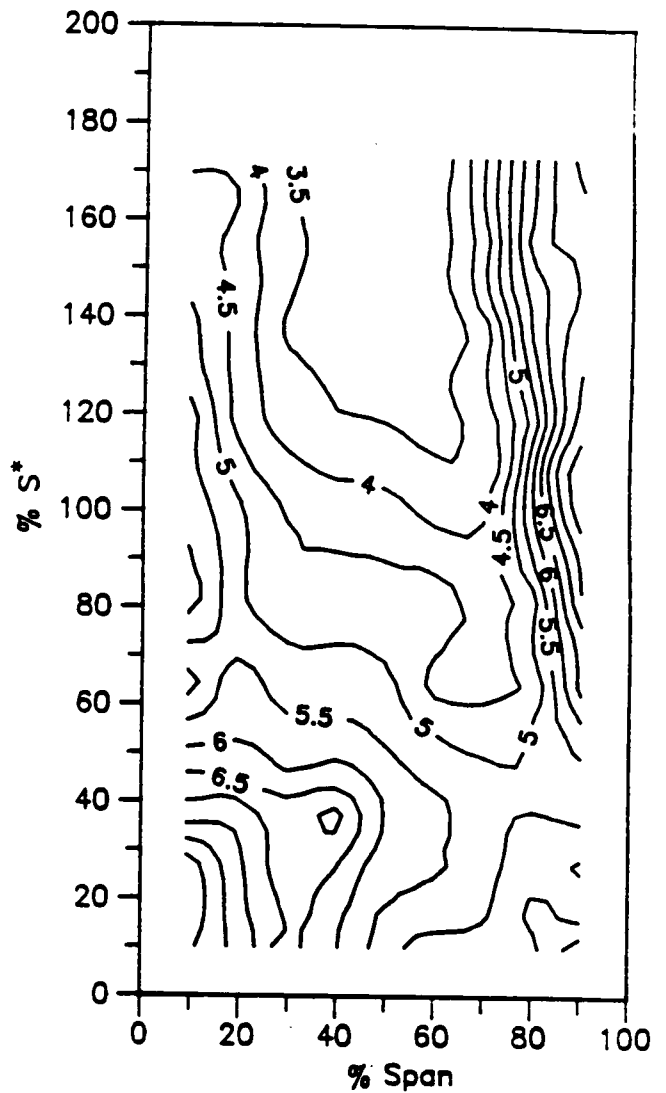
$$\beta_1 = 54^\circ$$

$$N = 219$$

$$Re = 2.230 \times 10^5$$



PRESSURE SURFACE



SUCTION SURFACE

Figure 39b Details of the Stanton Number Contours on the Airfoil Suction and Pressure Surfaces

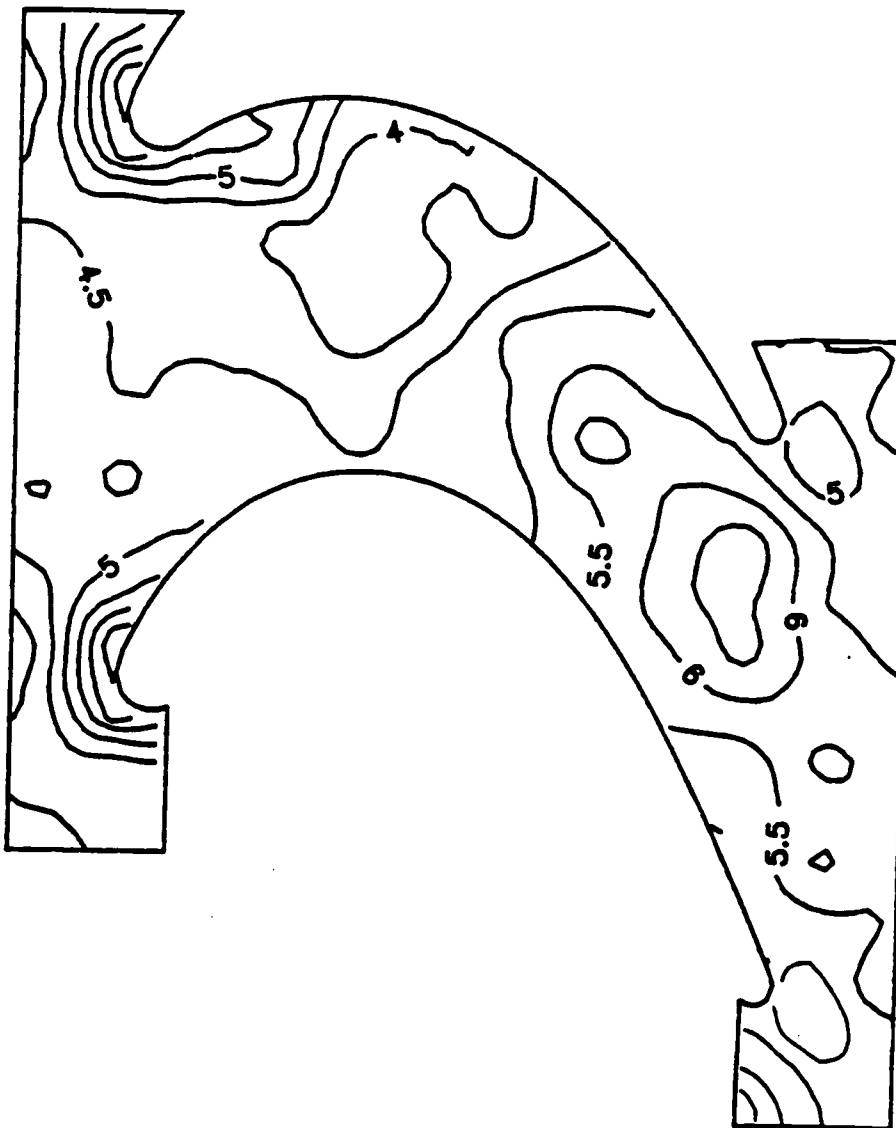
ROUGH-WALL MODEL

$$\beta_1 = 54^\circ$$

$$N = 219$$

$$Re = 2.230 \times 10^5$$

CONTOUR KEY ( $St \times 10^3$ )
— Thermocouple Data



HUB ENDWALL

Figure 39c Details of the Stanton Number Contours on the Hub Endwall Surface

ROUGH-WALL MODEL

$\beta_1 = 54^\circ$

$N = 397$

$Re = 4.027 \times 10^5$

CONTOUR KEY ( $St \times 10^3$ )  
— Thermocouple Data

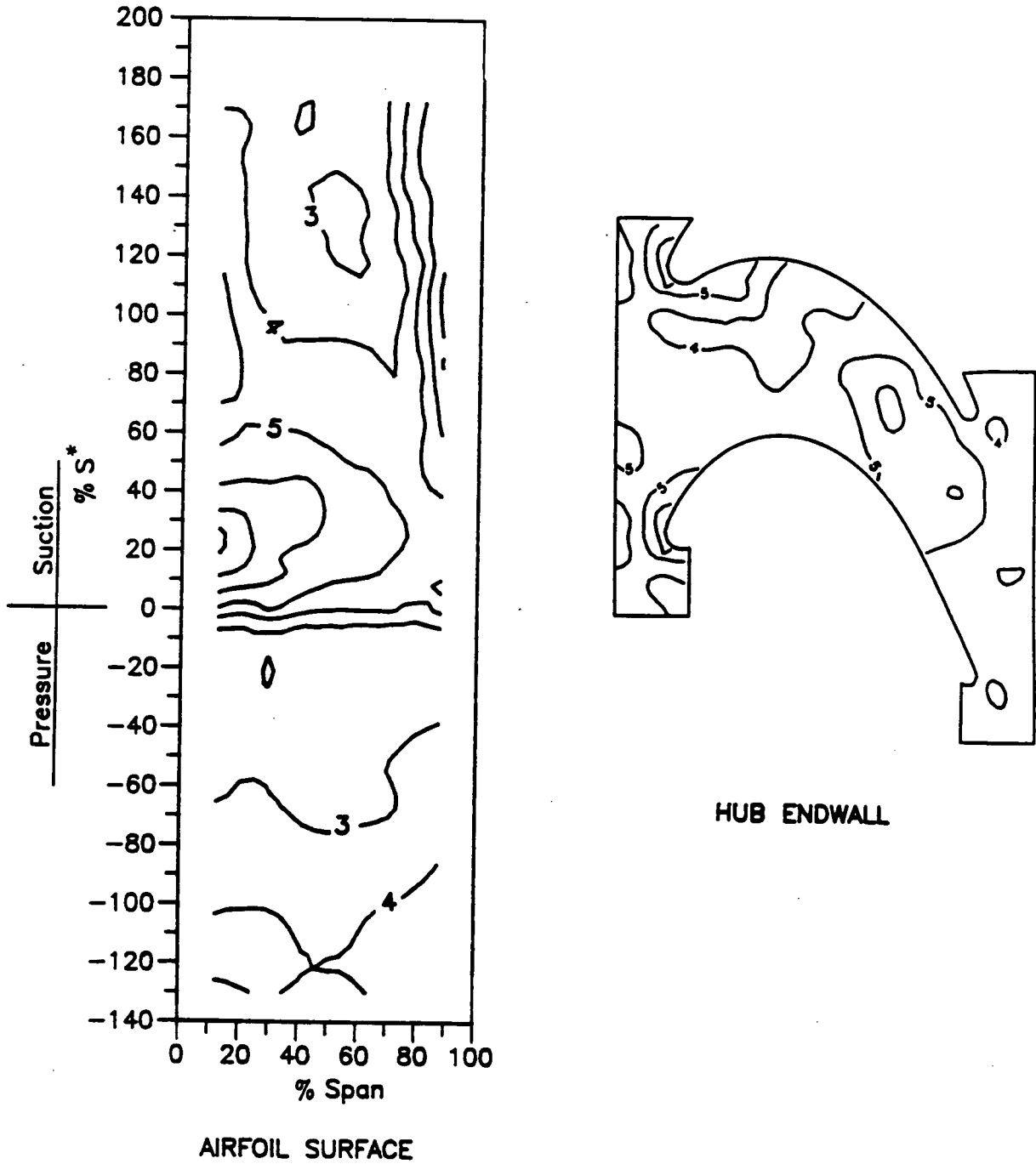


Figure 40a Stanton Number Contours on the Airfoil and Hub Endwall Surfaces

Table 1  
Comparison of the UTRC/LSRR with the SSME Turbopump Drive Turbines

<u>Parameter</u>	<u>HPFTP</u>	<u>LSRR</u>	<u>HPOTP</u>
$D_T$ (ins)	11.1	60.0	
$N$ (rpm)	38000	410 (520)	
Hub/Tip	0.83	0.80	0.88
Stator 1			
$(S/B_x)$ avg	0.84	1.01	
$(\tau/B_x)$ avg	0.75	1.30	
$\alpha_1$	90.0°	90.0°	90.0°
$\alpha_2$	22.5°	22.0°	16.0°
Rotor 1			
$(S/B_x)$	1.20	0.95	
$(\tau/B_x)$	0.69	0.96	
$\beta_1$	53.4°	40.0° (54.2°)	25.8°
$\beta_2$	25.5°	25.0°	24.0°
Stator 2			
$(S/B_x)$	0.94	0.93	
$(\tau/B_x)$	0.79	0.94	
$\alpha_1$	69.0°	50.0° (68.7°)	32.4°
$\alpha_2$	23.5°	25.0°	24.0°
Rotor 2			
$(S/B_x)$	1.29		
$(\tau/B_x)$	0.71		
$\alpha_1$	54.4°		32.4°
$\alpha_2$	29.5°		24.0°
$\phi = (C_x/U_m)$	0.61	0.78 (0.57)	

$B_x$  - Airfoil axial chord  
 $C_x$  - Axial flow speed  
 $D_T$  - Tip diameter  
 $N$  - Rotor speed  
 $S$  - Airfoil span  
 $U_m$  - Midspan wheel speed  
 $\alpha_1$  - Stator inlet flow angle  
 $\alpha_2$  - Stator exit flow angle  
 $\beta_1$  - Rotor inlet flow angle  
 $\beta_2$  - Rotor exit flow angle  
 $\tau$  - Airfoil pitch

**Table 2a**  
**Airfoil Geometry**

**AIRFOIL: FIRST STATOR (HUB)**  
**PITCH (ins.): 6.88865**

	LEADING EDGE	TRAILING EDGE
RADIUS (ins.)	0.44485	0.10988
METAL ANGLE (degr.)	90.00395	22.44246
WEDGE ANGLE (degr.)	31.79000	6.85000

	X(ins.)	Y <sub>L</sub> (ins.)	Y <sub>U</sub> (ins.)
1	0.00000	5.98844	5.98844
2	0.05932	5.76650	6.21038
3	0.11864	5.68598	6.29089
4	0.17796	5.63254	6.34433
5	0.23728	5.59498	6.38189
6	0.29660	5.56902	6.40786
7	0.35592	5.55114	6.42556
8	0.41524	5.53364	6.44182
9	0.47456	5.51555	6.45743
10	0.53388	5.49688	6.47239
11	0.59320	5.47760	6.48668
12	0.74150	5.42681	6.51919
13	0.88980	5.37219	6.54678
14	1.03810	5.31366	6.56894
15	1.18640	5.25111	6.58508
16	1.33470	5.18440	6.59454
17	1.48300	5.11341	6.59667
18	1.63130	5.03800	6.59063
19	1.77960	4.95798	6.57559
20	1.92790	4.87318	6.55065
21	2.07620	4.78339	6.51481
22	2.22450	4.68839	6.46704
23	2.37280	4.58791	6.40627
24	2.52110	4.48160	6.33143
25	2.66940	4.36922	6.24143
26	2.81770	4.25033	6.13530
27	2.96600	4.12450	6.01210
28	3.11430	3.99119	5.87111
29	3.26260	3.84973	5.71175
30	3.41090	3.69938	5.53366
31	3.55920	3.53930	5.33677
32	3.70750	3.36863	5.12118
33	3.85580	3.18656	4.88723
34	4.00410	2.99229	4.63534
35	4.15240	2.78525	4.36603
36	4.30070	2.56517	4.07986
37	4.44900	2.33245	3.77749
38	4.59730	2.08792	3.45958
39	4.74560	1.83271	3.12684
40	4.89390	1.56797	2.78000
41	5.04220	1.29464	2.41981
42	5.19050	1.01365	2.04697
43	5.33880	0.72592	1.66229
44	5.39812	0.60905	1.50524
45	5.45744	0.49120	1.34645
46	5.51676	0.37243	1.18596
47	5.57608	0.25271	1.02380
48	5.63540	0.13213	0.86004
49	5.69472	0.01077	0.69471
50	5.75404	-0.08624	0.52783
51	5.81336	-0.10952	0.35947
52	5.87268	-0.09755	0.18966
53	5.93200	0.00001	0.00001

**Table 2b**  
**Airfoil Geometry**

AIRFOIL: FIRST STATOR (MIDSPAN)

PITCH (ins.): 7.71118

	LEADING EDGE	TRAILING EDGE
RADIUS (ins.)	0.44484	0.10987
METAL ANGLE (degr.)	90.00000	21.42000
WEDGE ANGLE (degr.)	31.80000	6.84000

	X(ins.)	Y <sub>L</sub> (ins.)	Y <sub>U</sub> (ins.)
1	0.00000	6.80766	6.80766
2	0.05932	6.44830	7.15365
3	0.11864	6.43405	7.17319
4	0.17796	6.41912	7.19210
5	0.23728	6.40354	7.21034
6	0.29660	6.38729	7.22791
7	0.35592	6.37035	7.24476
8	0.41524	6.35273	7.26089
9	0.47456	6.33441	7.27624
10	0.53388	6.31540	7.29080
11	0.59320	6.29568	7.30453
12	0.74150	6.24325	7.33502
13	0.88980	6.18623	7.35957
14	1.03810	6.12447	7.37758
15	1.18640	6.05781	7.38835
16	1.33470	5.98603	7.39114
17	1.48300	5.90896	7.38513
18	1.63130	5.82633	7.36940
19	1.77960	5.73787	7.34300
20	1.92790	5.64326	7.30490
21	2.07620	5.54212	7.25403
22	2.22450	5.43404	7.18927
23	2.37280	5.31852	7.10949
24	2.52110	5.19498	7.01363
25	2.66940	5.06273	6.90066
26	2.81770	4.92096	6.76967
27	2.96600	4.76873	6.61989
28	3.11430	4.60490	6.45078
29	3.26260	4.42825	6.26202
30	3.41090	4.23771	6.05354
31	3.55920	4.03254	5.82550
32	3.70750	3.81279	5.57826
33	3.85580	3.57948	5.31230
34	4.00410	3.33397	5.02816
35	4.15240	3.07798	4.72650
36	4.30070	2.81269	4.40803
37	4.44900	2.53937	4.07350
38	4.59730	2.25873	3.72369
39	4.74560	1.97172	3.35942
40	4.89390	1.67884	2.98147
41	5.04220	1.38062	2.59066
42	5.19050	1.07737	2.18773
43	5.33880	0.76951	1.77352
44	5.39812	0.64517	1.60482
45	5.45744	0.52020	1.43448
46	5.51676	0.39451	1.26252
47	5.57608	0.26816	1.08901
48	5.63540	0.14117	0.91397
49	5.69472	0.01364	0.73745
50	5.75404	-0.11456	0.55950
51	5.81336	-0.24329	0.38014
52	5.87268	-0.37263	0.19943
53	5.93200	0.00000	0.00000

**Table 2c**  
**Airfoil Geometry**

AIRFOIL: FIRST STATOR (TIP)  
PITCH (ins.): 8.53371

	LEADING EDGE	TRAILING EDGE
RADIUS (ins.)	0.44487	0.10986
METAL ANGLE (degr.)	90.00401	20.25751
WEDGE ANGLE (degr.)	31.79000	6.79000

	X(ins.)	Y <sub>L</sub> (ins.)	Y <sub>U</sub> (ins.)
1	0.00000	7.57702	7.57702
2	0.05932	7.35507	7.79897
3	0.11864	7.27456	7.87949
4	0.17796	7.22112	7.93293
5	0.23728	7.18355	7.97049
6	0.29660	7.15759	7.99646
7	0.35592	7.13967	8.01409
8	0.41524	7.12193	8.02987
9	0.47456	7.10338	8.04449
10	0.53388	7.08402	8.05803
11	0.59320	7.06383	8.07044
12	0.74150	7.00967	8.09615
13	0.88980	6.95010	8.11406
14	1.03810	6.88487	8.12374
15	1.18640	6.81377	8.12465
16	1.33470	6.73650	8.11627
17	1.48300	6.65274	8.09803
18	1.63130	6.56207	8.06935
19	1.77960	6.46407	8.02955
20	1.92790	6.35817	7.97793
21	2.07620	6.24376	7.91381
22	2.22450	6.12004	7.83635
23	2.37280	5.98609	7.74477
24	2.52110	5.84072	7.63818
25	2.66940	5.68263	7.51566
26	2.81770	5.51023	7.37624
27	2.96600	5.32200	7.21892
28	3.11430	5.11693	7.04264
29	3.26260	4.89526	6.84631
30	3.41090	4.65850	6.62883
31	3.55920	4.40859	6.38910
32	3.70750	4.14741	6.12648
33	3.85580	3.87650	5.84072
34	4.00410	3.59714	5.53208
35	4.15240	3.31031	5.20125
36	4.30070	3.01688	4.84935
37	4.44900	2.71730	4.47775
38	4.59730	2.41223	4.08802
39	4.74560	2.10214	3.68183
40	4.89390	1.78726	3.26080
41	5.04220	1.46798	2.82654
42	5.19050	1.14458	2.38047
43	5.33880	0.81723	1.92403
44	5.39812	0.68529	1.73880
45	5.45744	0.55272	1.55219
46	5.51676	0.41958	1.36422
47	5.57608	0.28587	1.17502
48	5.63540	0.15177	0.98458
49	5.69472	0.01698	0.79299
50	5.75404	-0.08620	0.60033
51	5.81336	-0.10950	0.40661
52	5.87268	-0.09754	0.21192
53	5.93200	0.00001	0.00001

**Table 3b  
Airfoil Geometry**

AIRFOIL: FIRST ROTOR (MIDSPAN)  
PITCH (ins.): 6.05879

	LEADING EDGE	TRAILING EDGE
RADIUS (ins.)	0.34872	0.19000
METAL ANGLE (degr.)	42.18646	25.97093
WEDGE ANGLE (degr.)	31.24000	5.31000

	X(ins.)	Y <sub>L</sub> (ins.)	Y <sub>U</sub> (ins.)
1	0.00000	3.41970	3.41970
2	0.06341	3.21919	3.62774
3	0.12682	3.15069	3.74347
4	0.19023	3.10908	3.84906
5	0.25364	3.08419	3.94593
6	0.31705	3.07242	4.03518
7	0.38046	3.07243	4.11769
8	0.44387	3.08422	4.19414
9	0.50728	3.10912	4.26511
10	0.57069	3.14694	4.33106
11	0.63410	3.18401	4.39238
12	0.79262	3.26583	4.52752
13	0.95115	3.33349	4.63984
14	1.10967	3.38822	4.73220
15	1.26820	3.43094	4.80674
16	1.42672	3.46228	4.86506
17	1.58525	3.48271	4.90837
18	1.74377	3.49248	4.93760
19	1.90230	3.49176	4.95347
20	2.06082	3.48053	4.95652
21	2.21935	3.45868	4.94712
22	2.37787	3.42596	4.92555
23	2.53640	3.38201	4.89193
24	2.69492	3.32633	4.84632
25	2.85345	3.25830	4.78863
26	3.01197	3.17735	4.71868
27	3.17050	3.08283	4.63616
28	3.32902	2.97433	4.54063
29	3.48755	2.85162	4.43151
30	3.64607	2.71488	4.30799
31	3.80460	2.56463	4.16905
32	3.96312	2.40136	4.01334
33	4.12165	2.22577	3.83912
34	4.28017	2.03852	3.64406
35	4.43870	1.84022	3.42595
36	4.59722	1.63139	3.18387
37	4.75575	1.41252	2.91861
38	4.91427	1.18402	2.63221
39	5.07280	0.94623	2.32774
40	5.23132	0.69955	2.00832
41	5.38985	0.44403	1.67680
42	5.54837	0.18008	1.33571
43	5.70690	-0.09214	0.98699
44	5.77031	-0.20337	0.84573
45	5.83372	-0.31578	0.70359
46	5.89713	-0.42949	0.56065
47	5.96054	-0.54448	0.41698
48	6.02395	-0.63800	0.27261
49	6.08736	-0.67575	0.12765
50	6.15077	-0.68673	-0.01791
51	6.21418	-0.67591	-0.16397
52	6.27759	-0.63841	-0.31052
53	6.34100	-0.49672	-0.49672

**Table 4a  
Airfoil Geometry**

**AIRFOIL: SECOND STATOR (HUB)  
PITCH (ins.): 5.41251**

	LEADING EDGE	TRAILING EDGE
<b>RADIUS (ins.)</b>	<b>0.34999</b>	<b>0.19000</b>
<b>METAL ANGLE (degr.)</b>	<b>41.01068</b>	<b>4.98619</b>
<b>WEDGE ANGLE (degr.)</b>	<b>29.91000</b>	<b>8.91000</b>

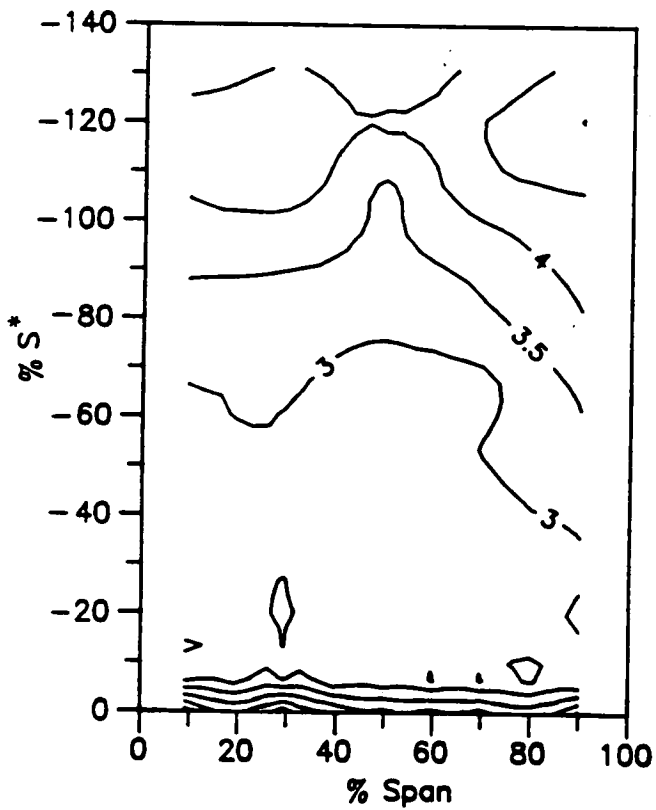
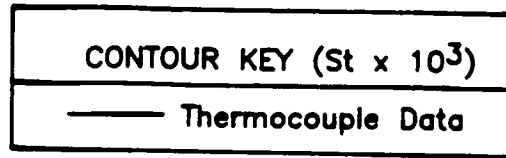
	X(ins.)	Y <sub>L</sub> (ins.)	Y <sub>U</sub> (ins.)
1	0.00000	3.68263	3.68263
2	0.06452	3.48015	3.89472
3	0.12904	3.41120	4.01869
4	0.19356	3.36955	4.13494
5	0.25808	3.34493	4.24410
6	0.32260	3.33372	4.34672
7	0.38712	3.33462	4.44324
8	0.45164	3.34773	4.53408
9	0.51616	3.37461	4.61958
10	0.58068	3.41583	4.70006
11	0.64520	3.45739	4.77578
12	0.80650	3.55269	4.94580
13	0.96780	3.63560	5.09069
14	1.12910	3.70599	5.21287
15	1.29040	3.76376	5.31424
16	1.45170	3.80880	5.39634
17	1.61300	3.84106	5.46037
18	1.77430	3.86048	5.50735
19	1.93560	3.86704	5.53806
20	2.09690	3.86072	5.55317
21	2.25820	3.84153	5.55319
22	2.41950	3.80950	5.53852
23	2.58080	3.76468	5.50948
24	2.74210	3.70714	5.46629
25	2.90340	3.63698	5.40908
26	3.06470	3.55430	5.33790
27	3.22600	3.45921	5.25273
28	3.38730	3.35188	5.15348
29	3.54860	3.23245	5.03995
30	3.70990	3.10111	4.91189
31	3.87120	2.95802	4.76892
32	4.03250	2.80339	4.61058
33	4.19380	2.63745	4.43628
34	4.35510	2.46037	4.24527
35	4.51640	2.27244	4.03662
36	4.67770	2.07384	3.80928
37	4.83900	1.86483	3.56222
38	5.00030	1.64569	3.29479
39	5.16160	1.41663	3.00662
40	5.32290	1.17789	2.69784
41	5.48420	0.92975	2.36890
42	5.64550	0.67246	2.02068
43	5.80680	0.40629	1.65431
44	5.87132	0.29738	1.50296
45	5.93584	0.18710	1.34900
46	6.00036	0.07548	1.19252
47	6.06488	-0.03748	1.03361
48	6.12940	-0.13608	0.87238
49	6.19392	-0.17738	0.70890
50	6.25844	-0.18997	0.54327
51	6.32296	-0.17996	0.37560
52	6.38748	-0.14267	0.20595
53	6.45200	0.00000	0.00000

$\beta_1 = 54^\circ$

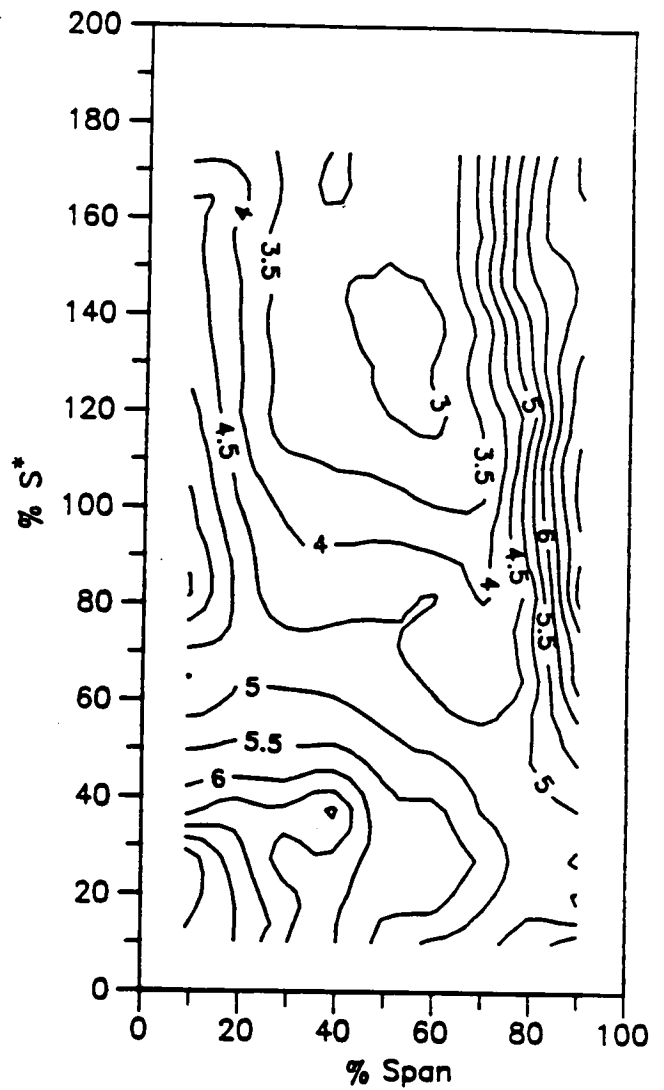
ROUGH-WALL MODEL

$N = 397$

$Re = 4.027 \times 10^5$



PRESSURE SURFACE



SUCTION SURFACE

Figure 40b Details of the Stanton Number Contours on the Airfoil Suction and Pressure Surfaces

ROUGH-WALL MODEL

$$\beta_1 = 54^\circ$$

$$N = 397$$

$$Re = 4.027 \times 10^5$$

CONTOUR KEY ( $St \times 10^3$ )
— Thermocouple Data



HUB ENDWALL

Figure 40c Details of the Stanton Number Contours on the Hub Endwall Surface

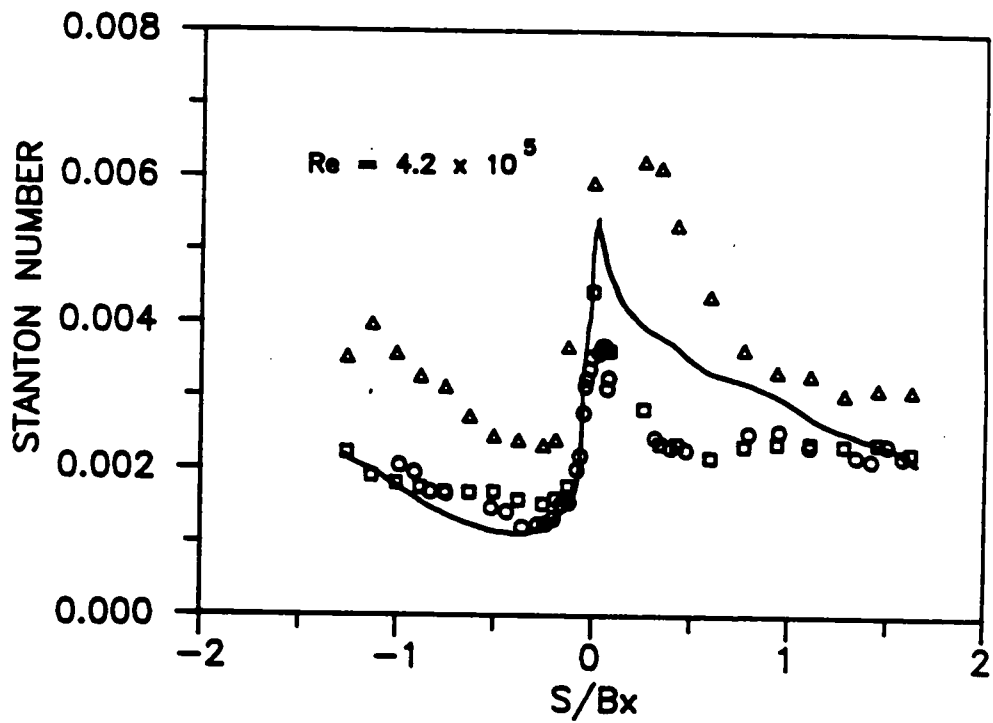
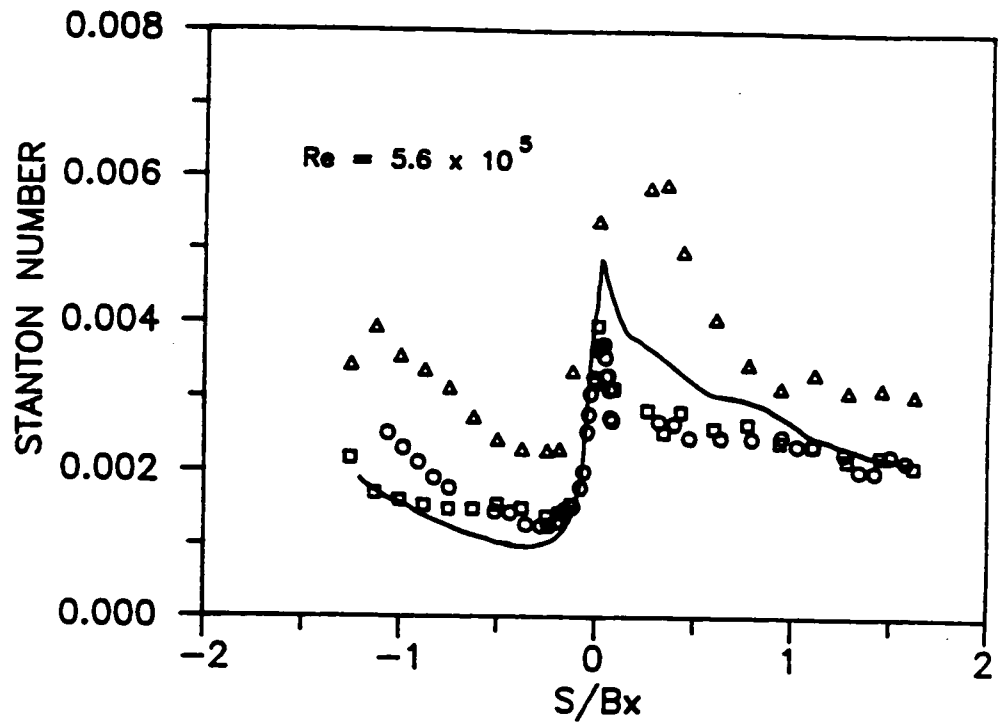


Figure 41. Comparison of Midspan Rotor Airfoil Heat Transfer Distributions Obtained for Two Reynolds Numbers at  $Cx/U=0.78$ ;  $\square$ , Smooth-Wall, Data,  $\Delta$ , Rough-Wall Data,  $\circ$ , 1986 NASA-Host Data

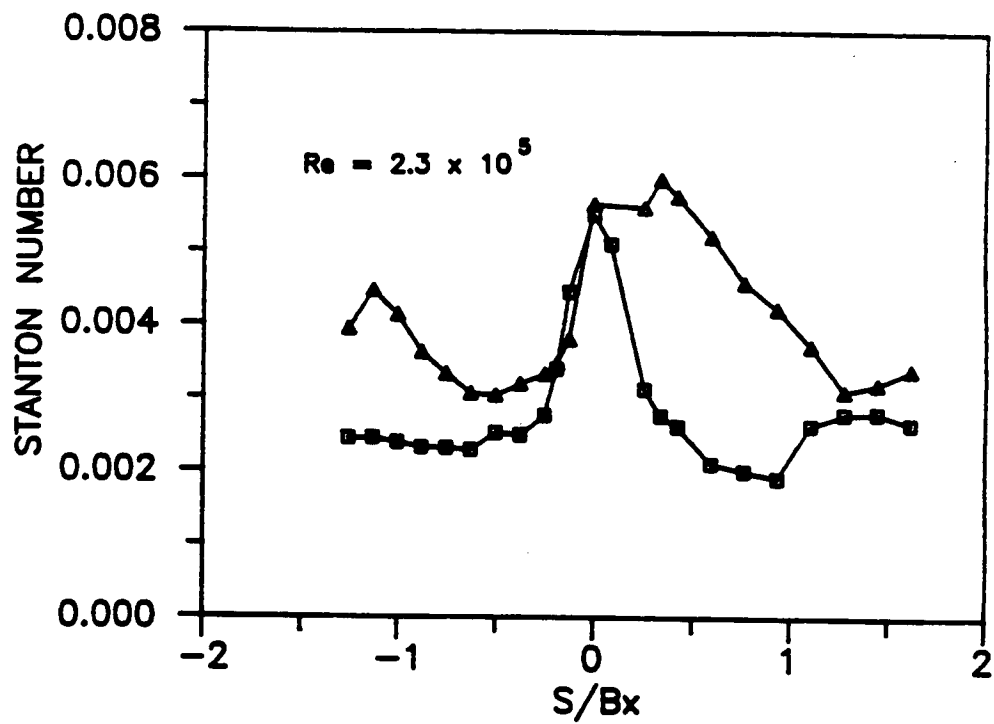
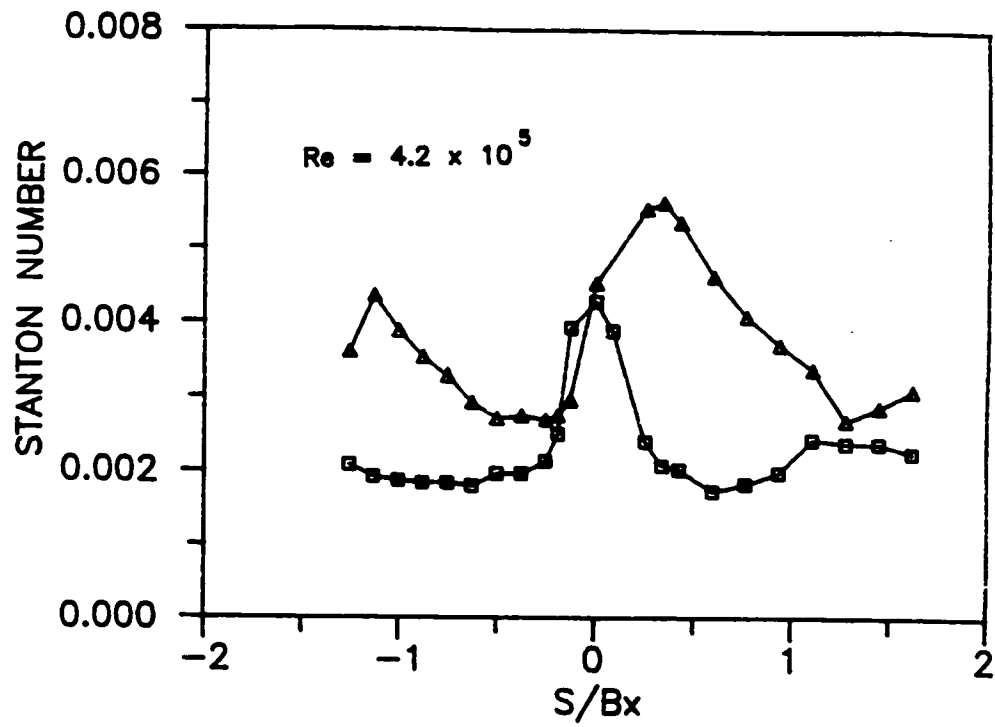


Figure 42. Comparison of Midspan Rotor Airfoil Heat Transfer Distributions Obtained for Two Reynolds Numbers at  $C_x/U=0.57$ ; □, Smooth-Wall Data, △, Rough-Wall Data

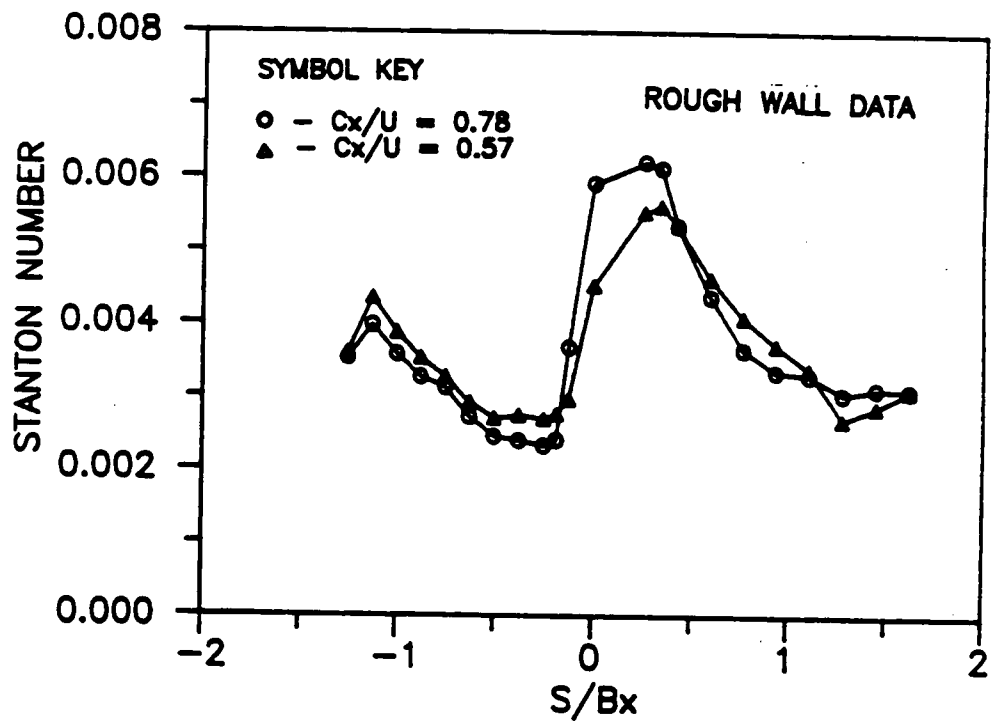
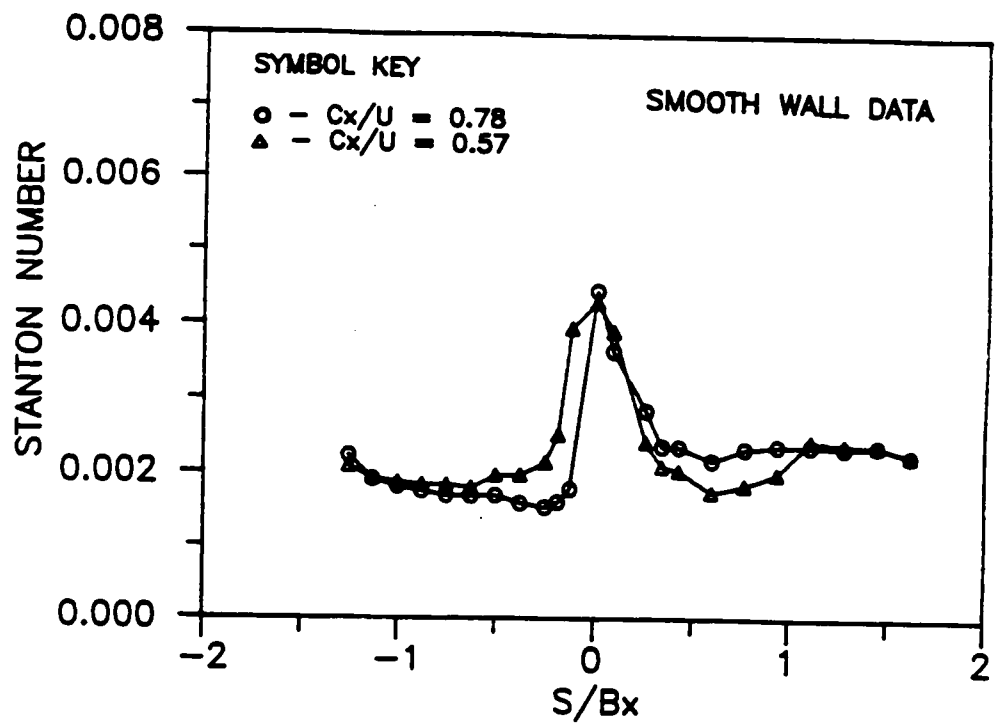


Figure 43. Comparison of Midspan Rotor Airfoil Heat Transfer Distributions Obtained for Two Flow Coefficients at  $Re=4.2 \times 10^5$

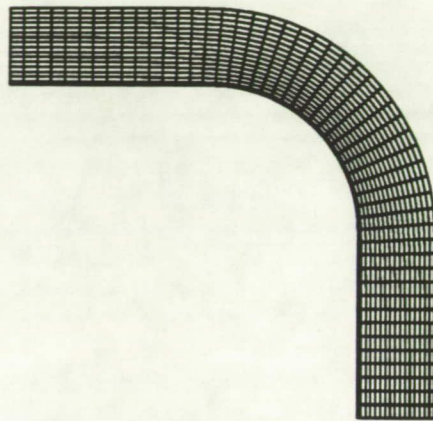


Figure 44 Coordinates for the Square Curved Duct

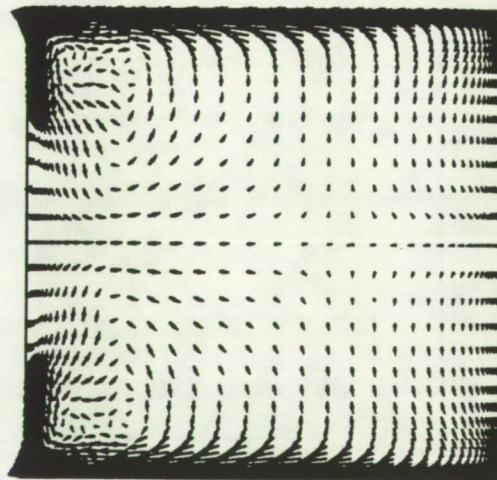


Figure 45 Secondary Flow Velocity Distribution at  $\theta=90$  degs in the Square Curved Duct

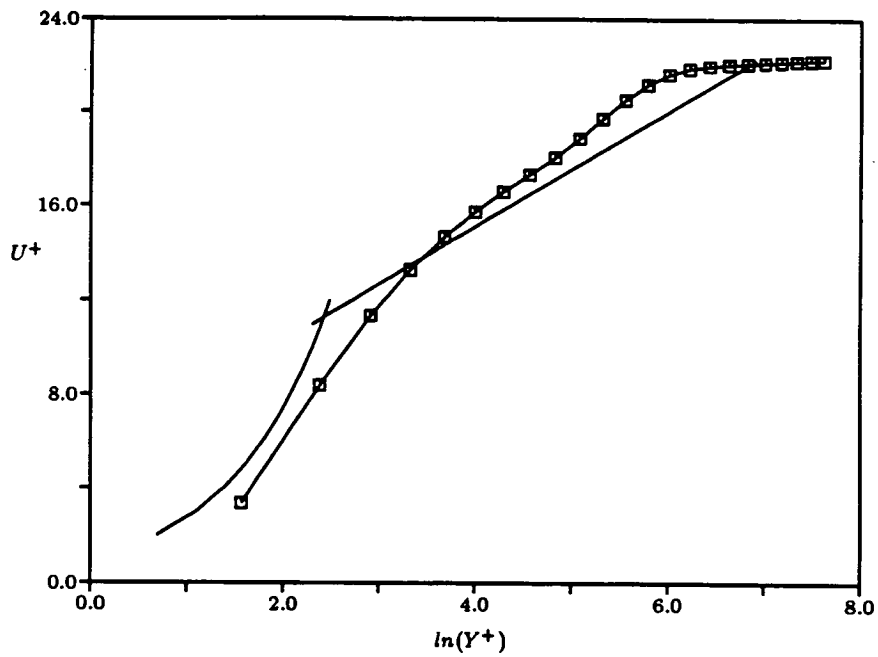


Figure 46. Calculated Universal Profile at  $\theta=90$  degs in the Square Curved Duct

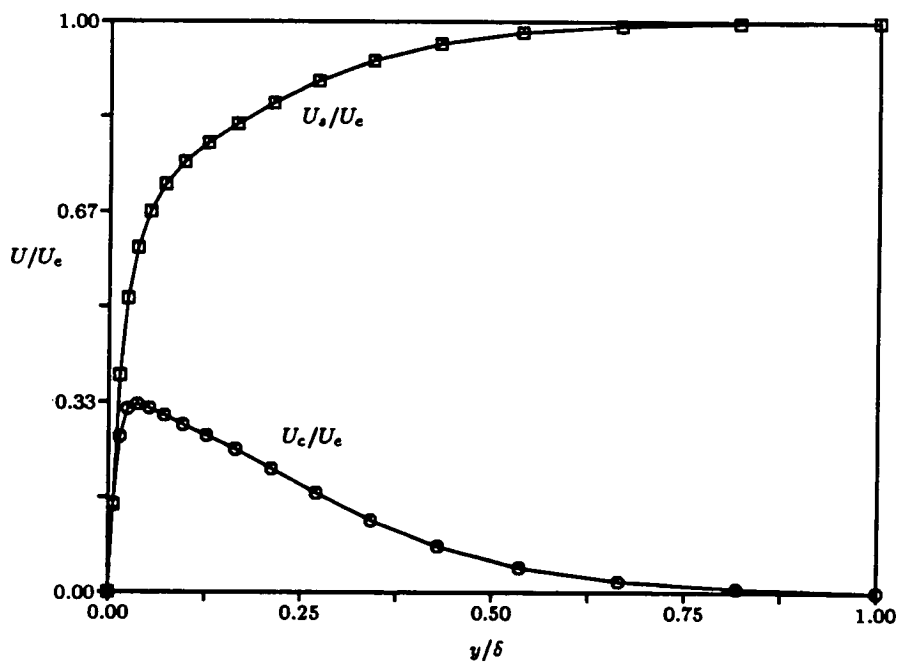


Figure 47. Streamwise and Crossflow Velocity at  $\theta=90$  degs in the Square Curved Duct

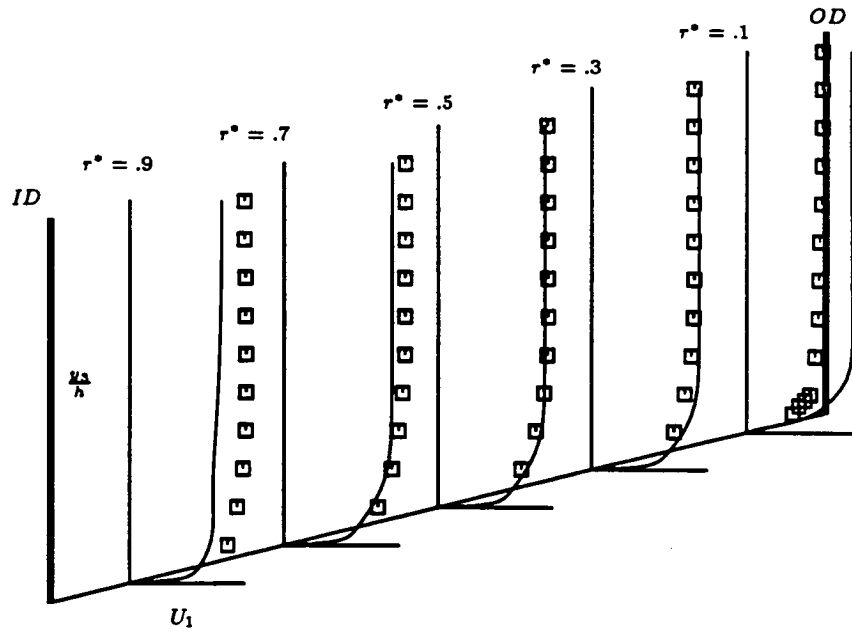


Figure 48 Streamwise Velocity Distribution  $\theta=30$  degs in the Square Curved Duct

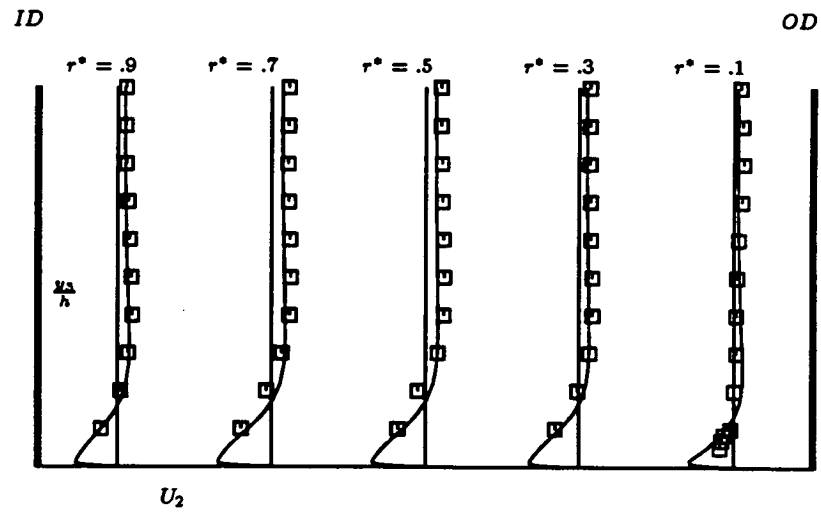


Figure 49 Crosswise Velocity Distribution  $\theta=30$  degs in the Square Curved Duct

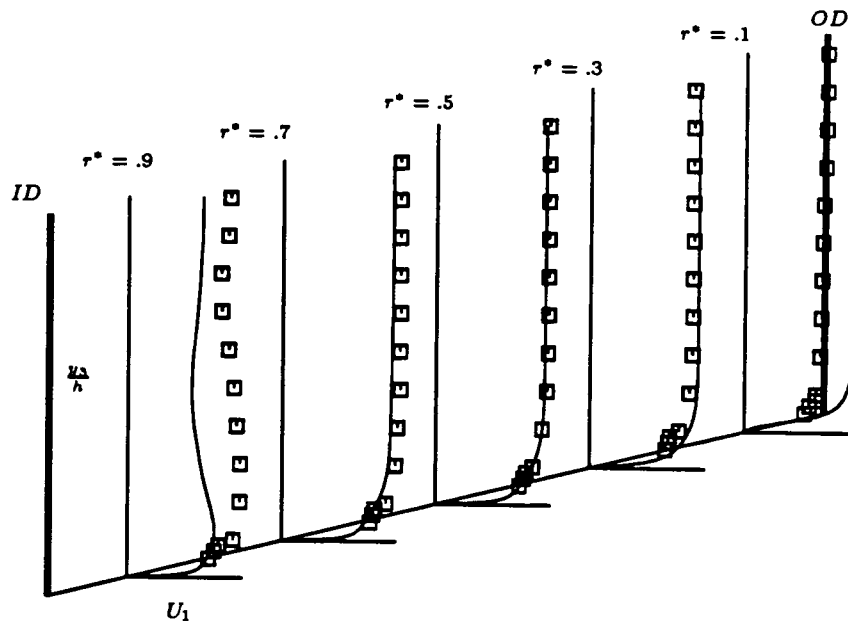


Figure 50 Streamwise Velocity Distribution  $\theta=60$  degs in the Square Curved Duct

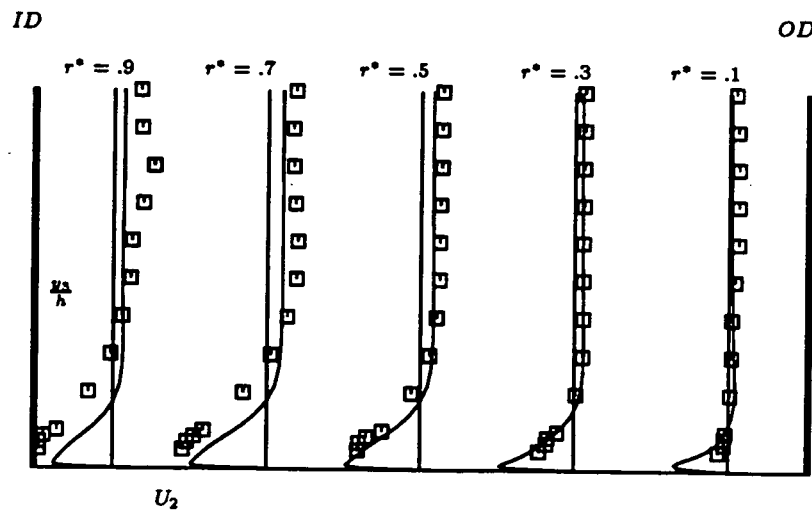


Figure 51 Crosswise Velocity Distribution  $\theta=60$  degs in the Square Curved Duct

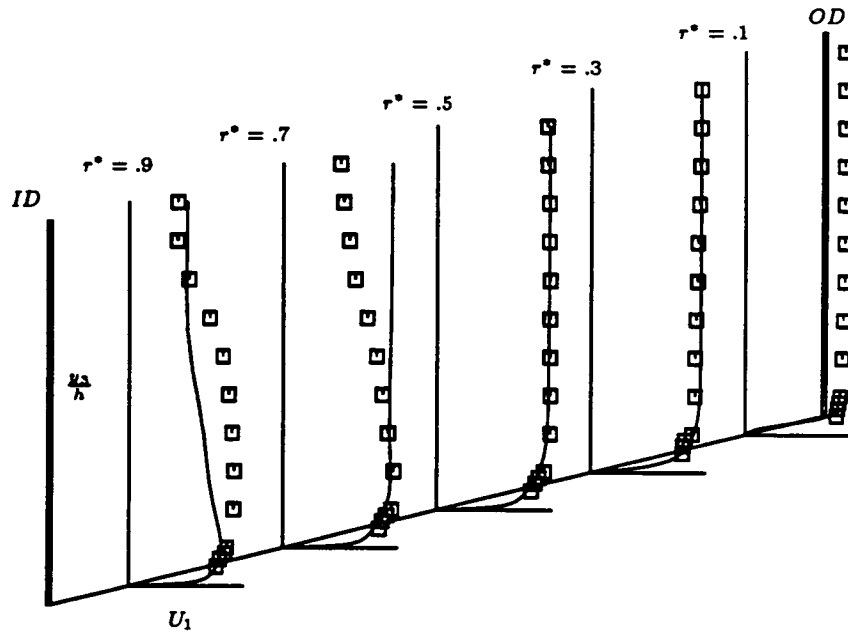


Figure 52 Streamwise Velocity Distribution  $\theta=90$  degs in the Square Curved Duct

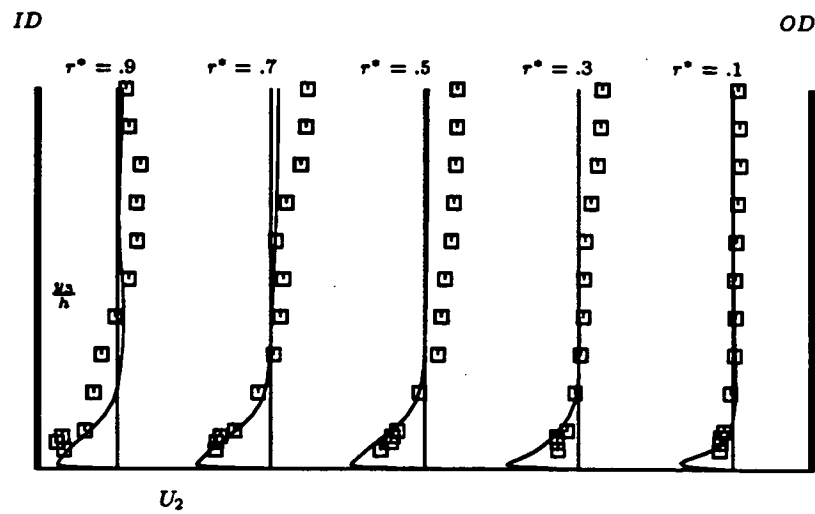


Figure 53 Crosswise Velocity Distribution  $\theta=90$  degs in the Square Curved Duct

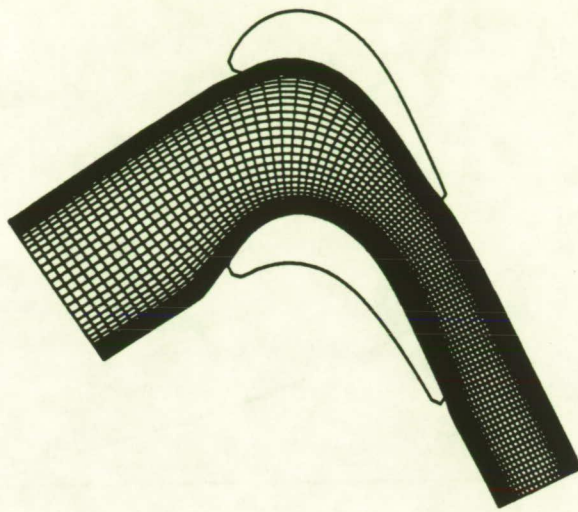


Figure 54 Coordinate Grid for LSRR Gas Turbine Cascade at Mid Span

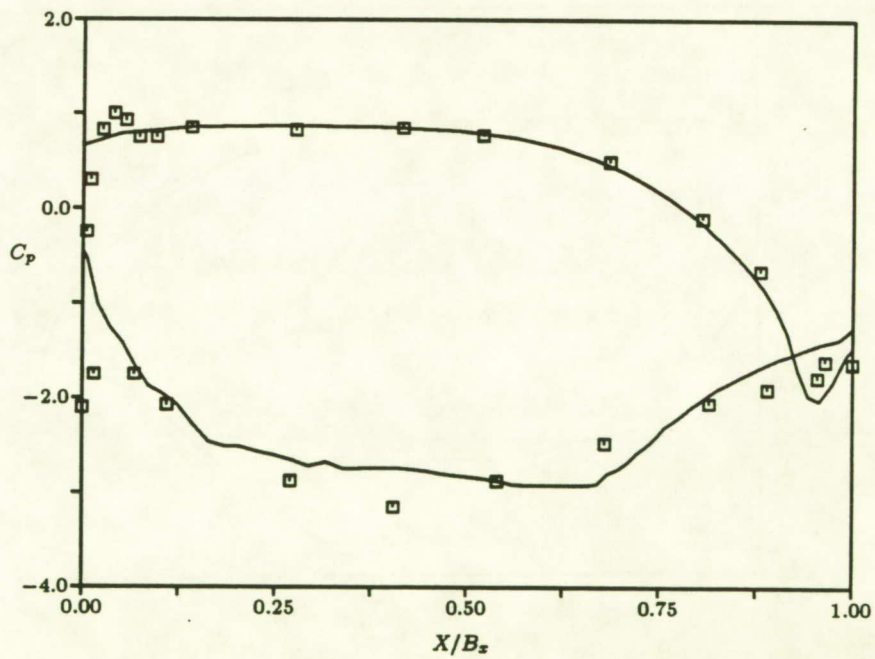


Figure 55 Calculated Mid Span Inviscid Static Pressure Distribution Compared to Experimental Data for LSRR Gas Turbine Cascade

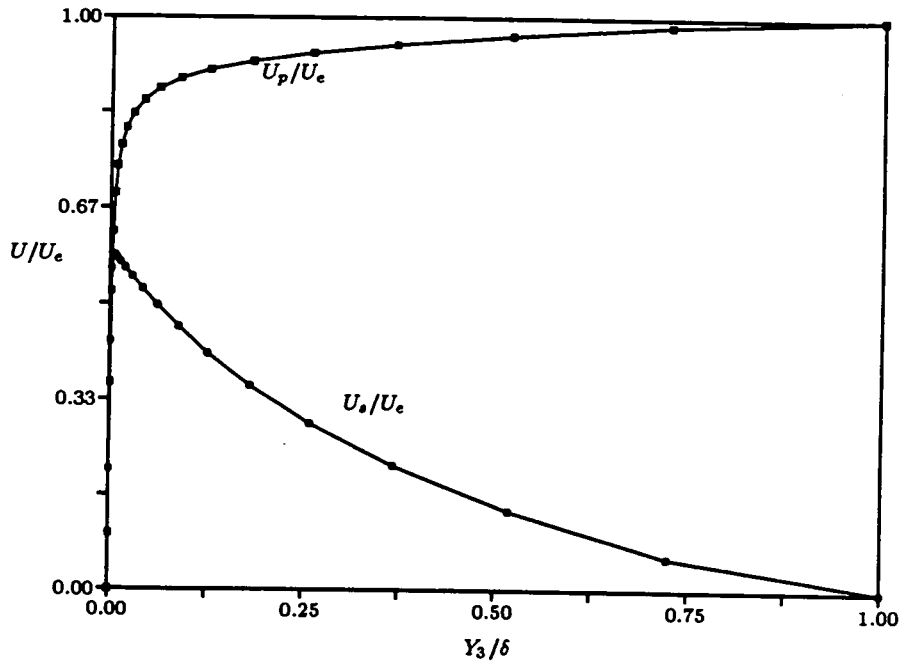


Figure 56 Detail of End Wall Boundary Layer at i-40 in LSRR Gas Turbine Cascade

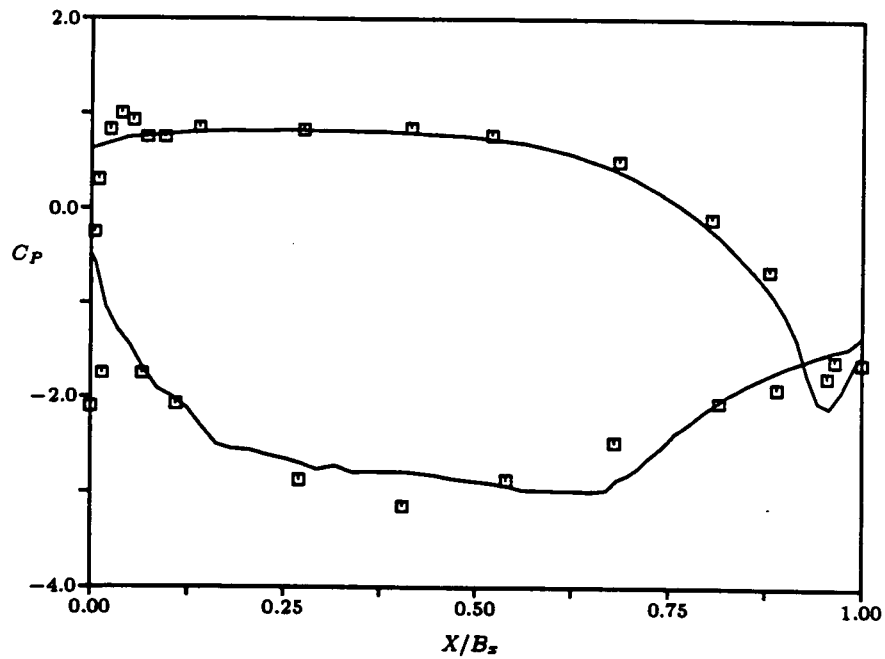
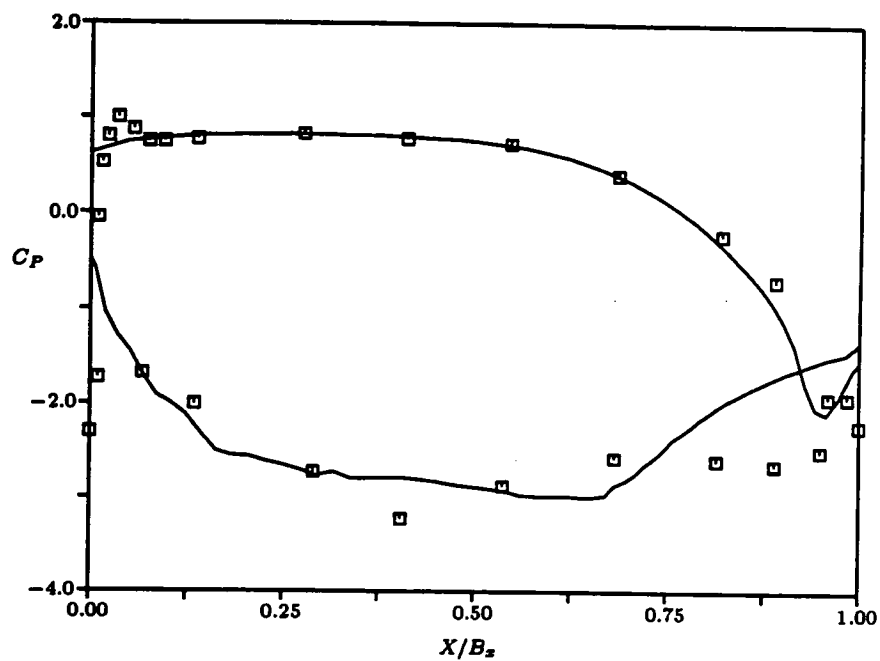
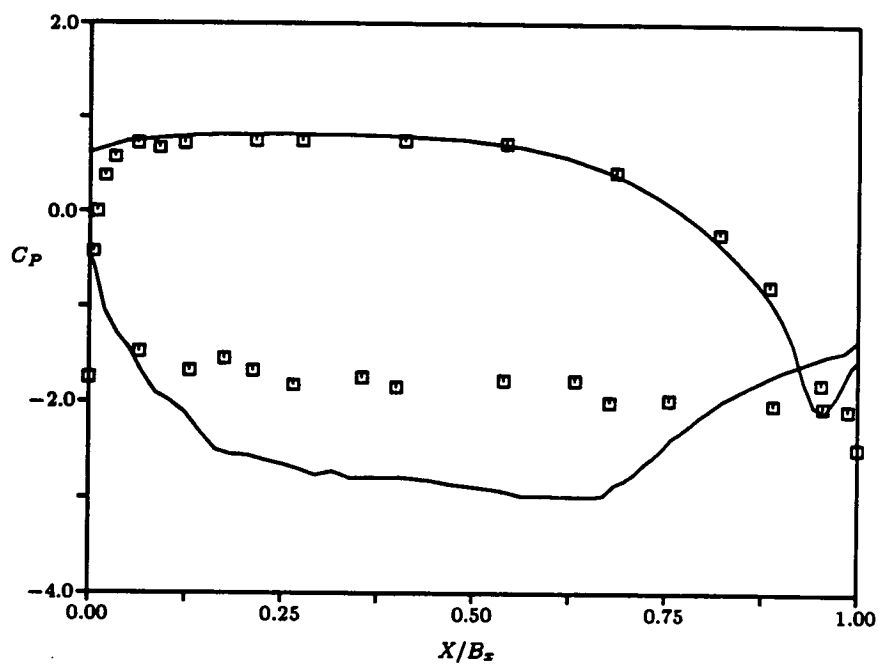


Figure 57 Comparison of Calculated and Measured Static Pressure Distribution at Mid Span for LSRR Gas Turbine Cascade



**Figure 58 Comparison of Calculated and Measured Static Pressure Distribution at Quarter Span for LSRR Gas Turbine Cascade**



**Figure 59 Comparison of Calculated and Measured Static Pressure Distribution at Hub Span for LSRR Gas Turbine Cascade**

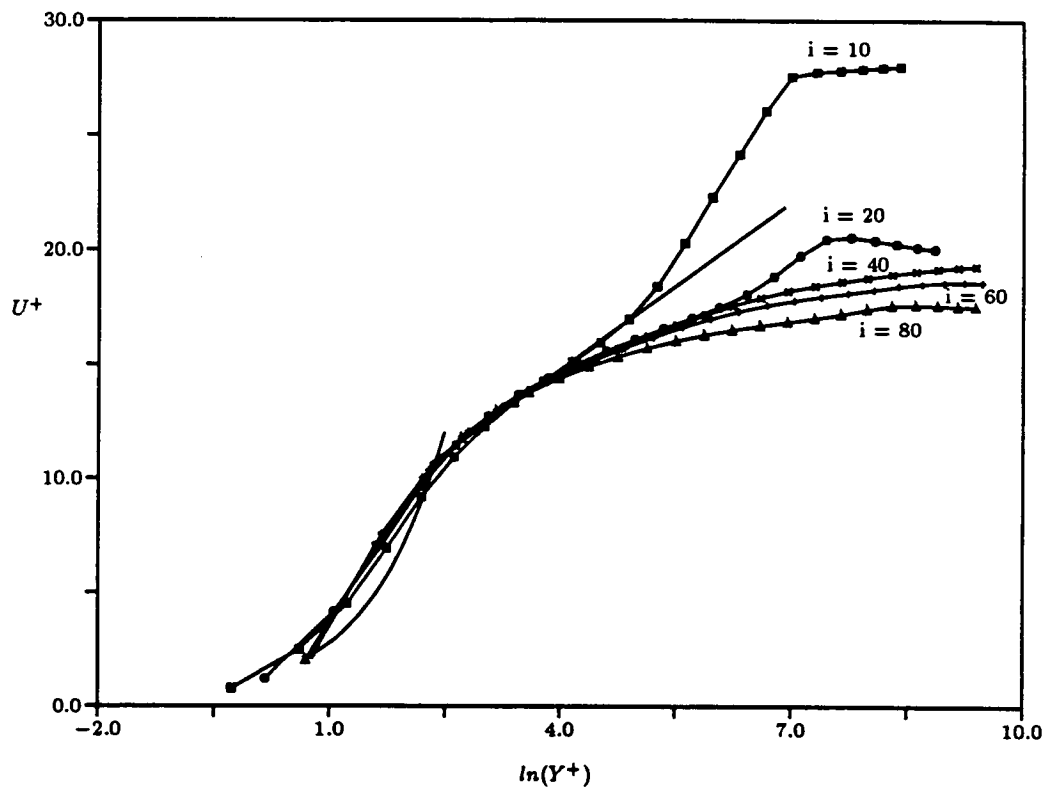


**Figure 60** Development of End Wall Boundary Layer in Universal Coordinates at Mid Gap in LSRR Gas Turbine Cascade

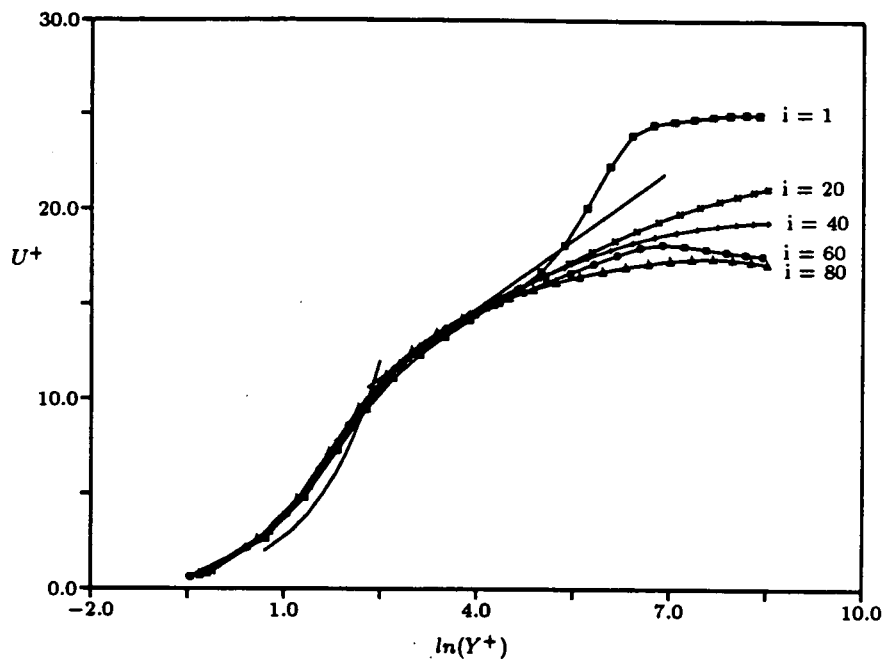


Figure 61 Development of Suction Surface Boundary Layer in Universal Coordinates at Mid Span in LSRR Gas Turbine Cascade

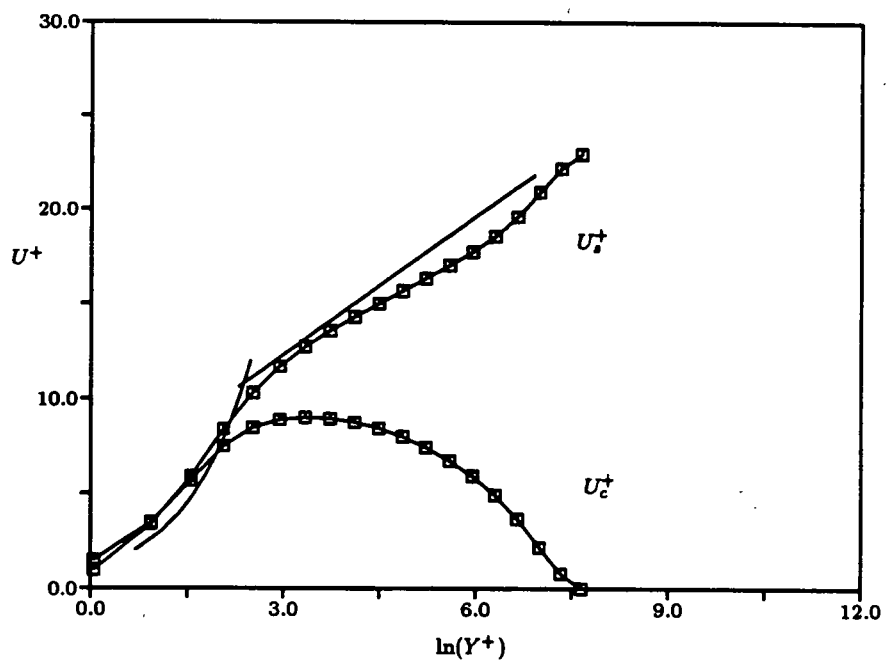
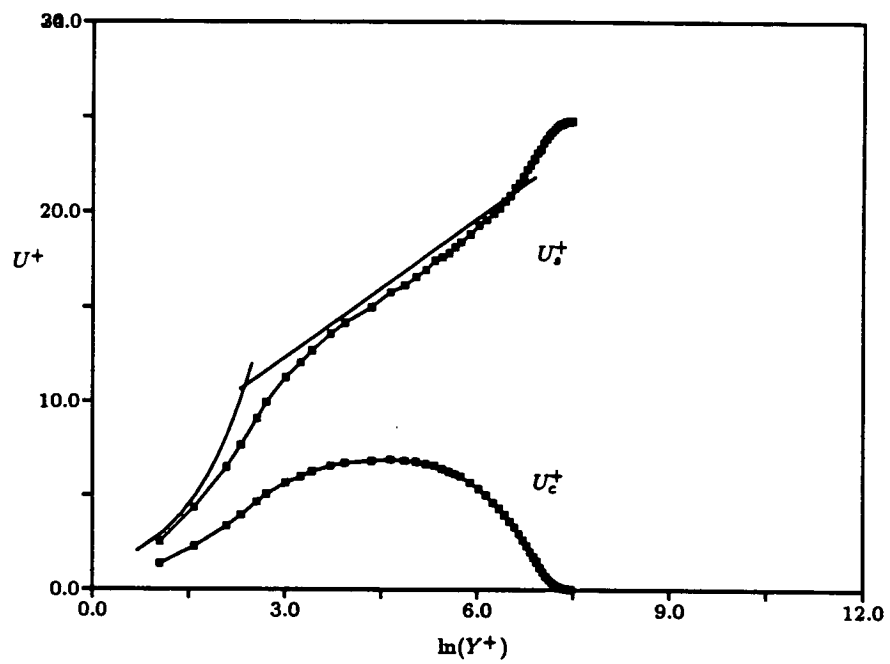
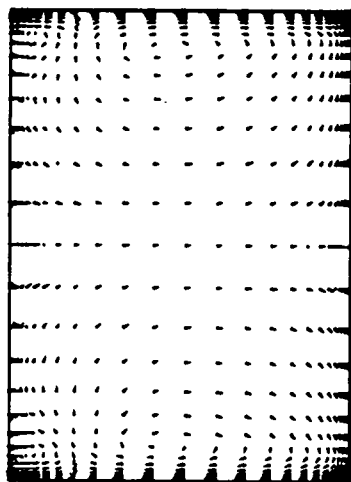


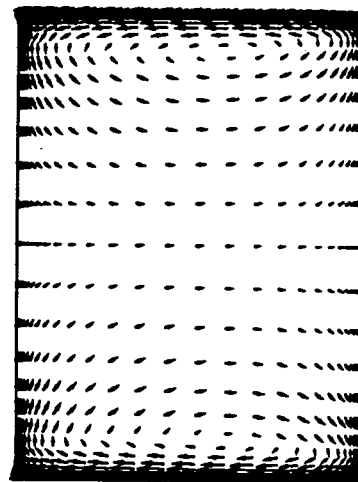
Figure 62 Calculated Streamwise and Crossflow Boundary Layer Velocity Distributions on End Wall in Universal Coordinates in the LSRR Gas Turbine Cascade



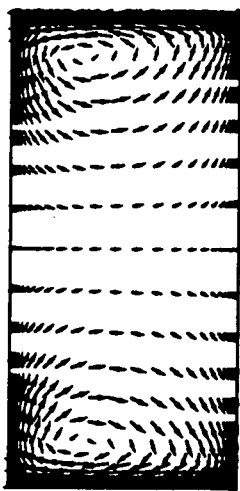
**Figure 63 Measured Streamwise and Crossflow Boundary Layer Velocity Distributions on End Wall in Universal Coordinates in the Vermeulen Duct**



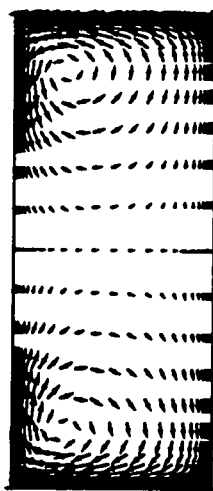
at  $i = 20$



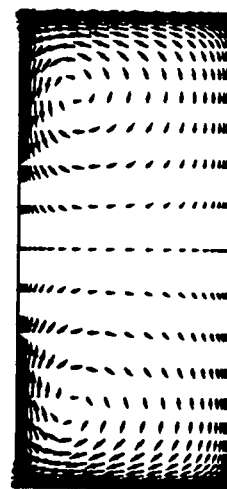
at  $i = 30$



at  $i = 40$



at  $i = 60$



at  $i = 90$

Figure 64. Development of Secondary Flow in LSRR Gas Turbine Cascade

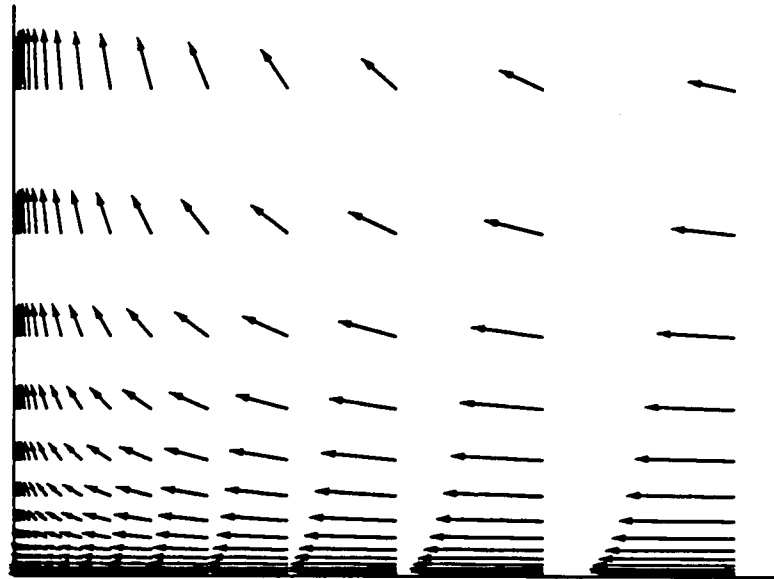


Figure 65 Detail of Corner Flow at  $i=60$  in LSRR Gas Turbine Cascade

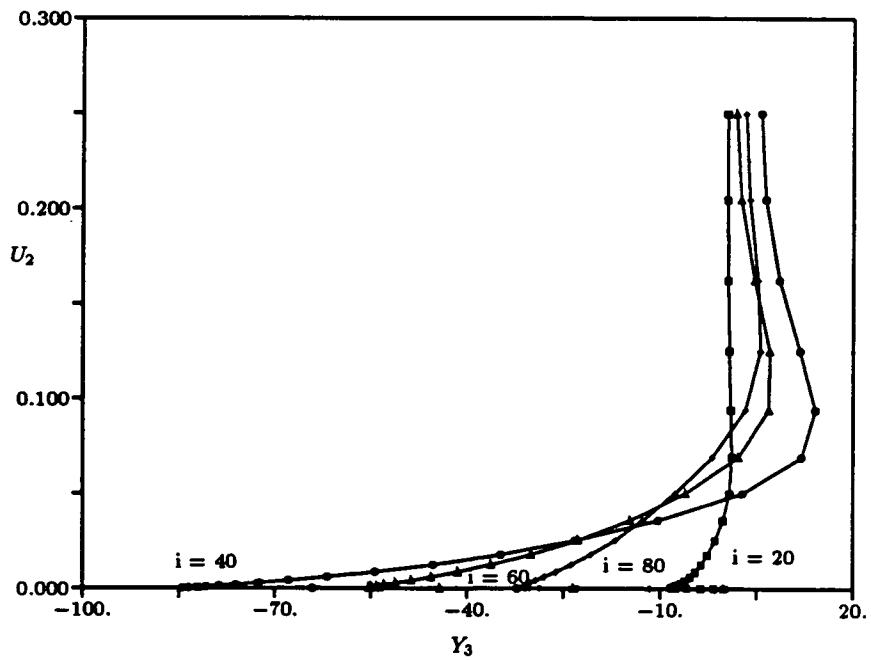
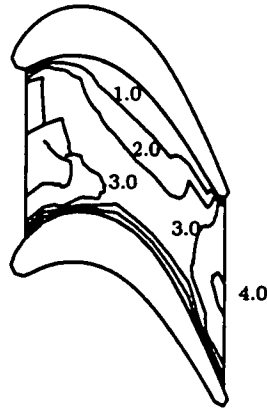
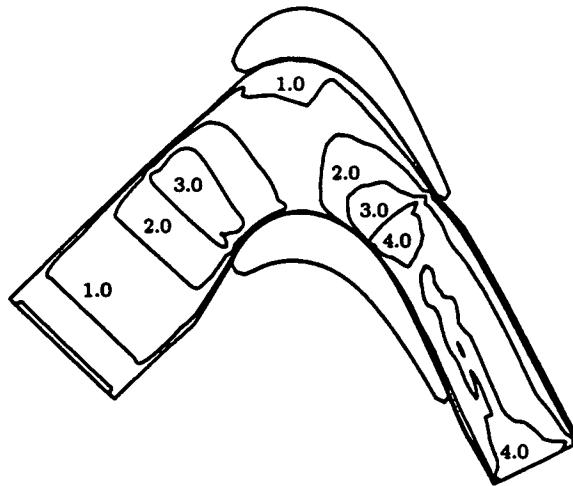


Figure 66 Development of Cross Flow Velocity on End Wall in LSRR Gas Turbine Cascade





**Figure 69 Experimental End Wall St Distribution in  
Graziani (1980) Cascade -  $St \times 10^3$**



**Figure 70 Calculated End Wall St Distribution in  
LSRR Gas Turbine Cascade -  $St \times 10^3$**

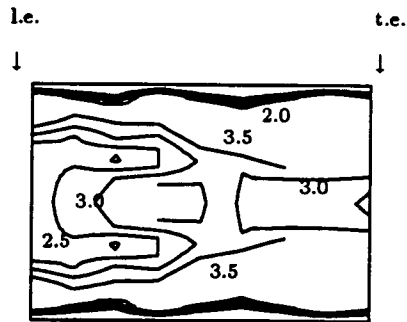


Figure 71 Experimental Suction Surface  $St$  Distribution in Graziani (1980) Cascade -  $Stx10^3$

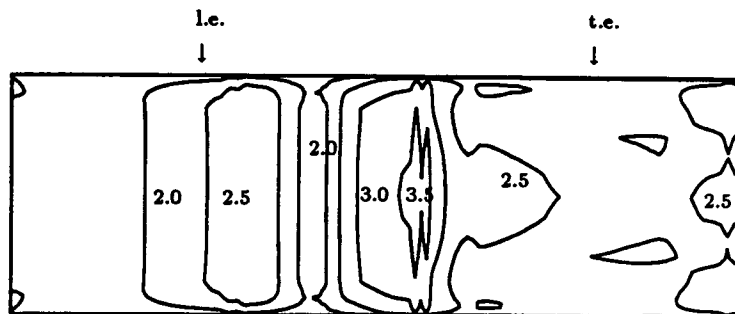
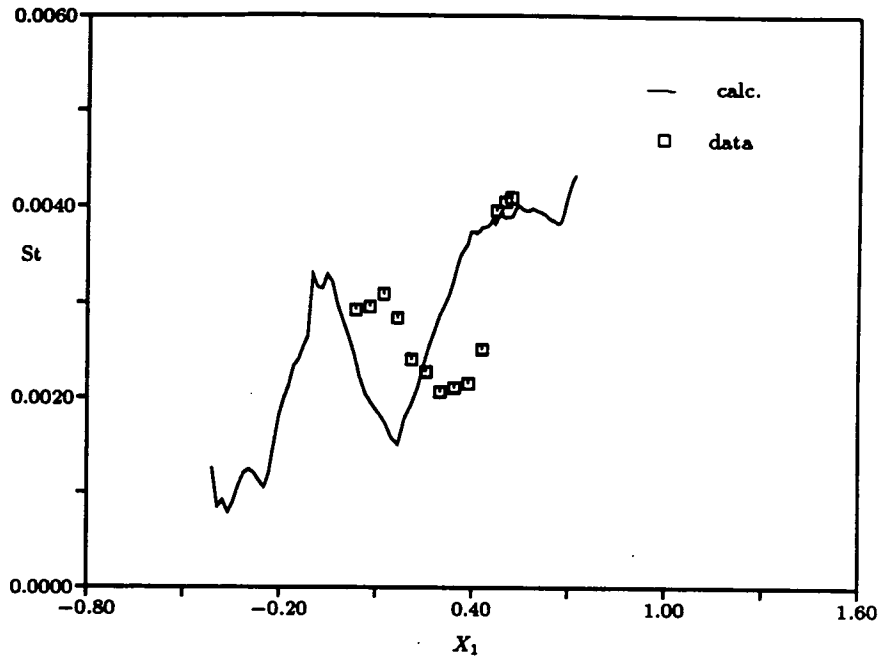
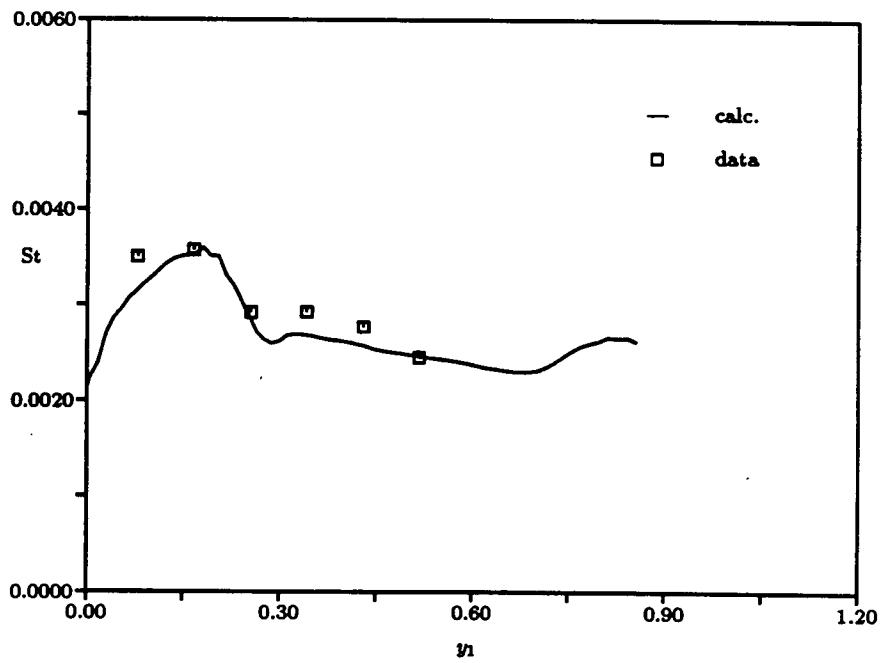


Figure 72 Calculated Suction Surface  $St$  Distribution in LSRR Gas Turbine Cascade -  $Stx10^3$



**Figure 73 Comparison of Calculated and Measured St Distribution in Graziani (1980) Cascade End Wall at Mid Gap**



**Figure 74 Comparison of Calculated and Measured St Distribution in Graziani (1980) Cascade Suction Surface at Mid Span**

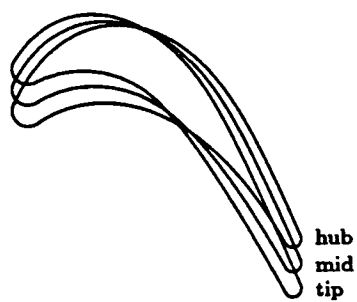


**Figure 75 LSRR Gas Turbine Rotor Blade Sections**

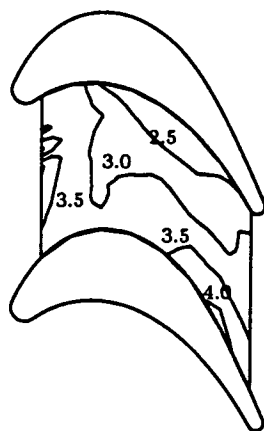


**Figure 76** Experimental LSRR Gas Turbine Rotor End Wall St Distribution -  $Stx10^3$  (See Fig. 34c)

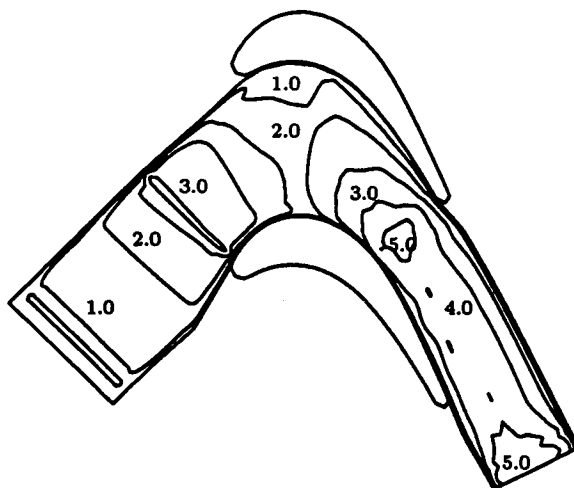


**Figure 77** Calculated LSRR Gas Turbine Rotor End Wall St Distribution -  $Stx10^3$

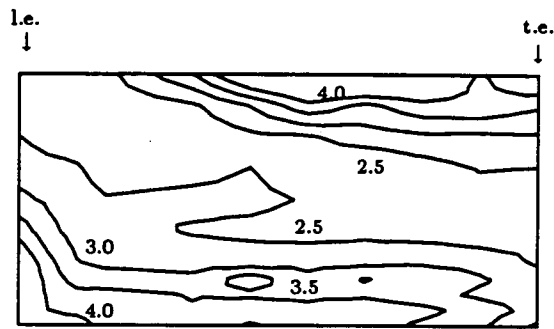


**Figure 78** Experimental LSRR Gas Turbine Rotor Suction Surface  $St$  Distribution -  $Stx10^3$  (See Fig. 34b)

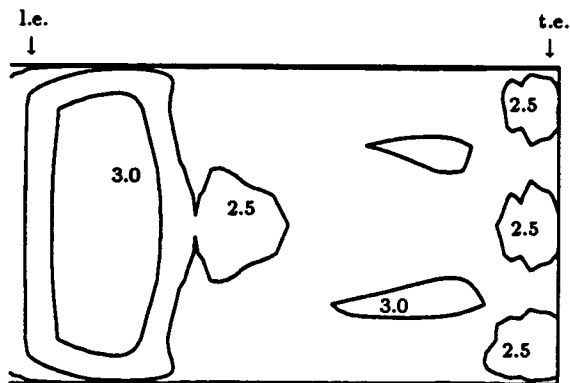


**Figure 79** Calculated LSRR Gas Turbine Rotor Suction Surface  $St$  Distribution -  $Stx10^3$

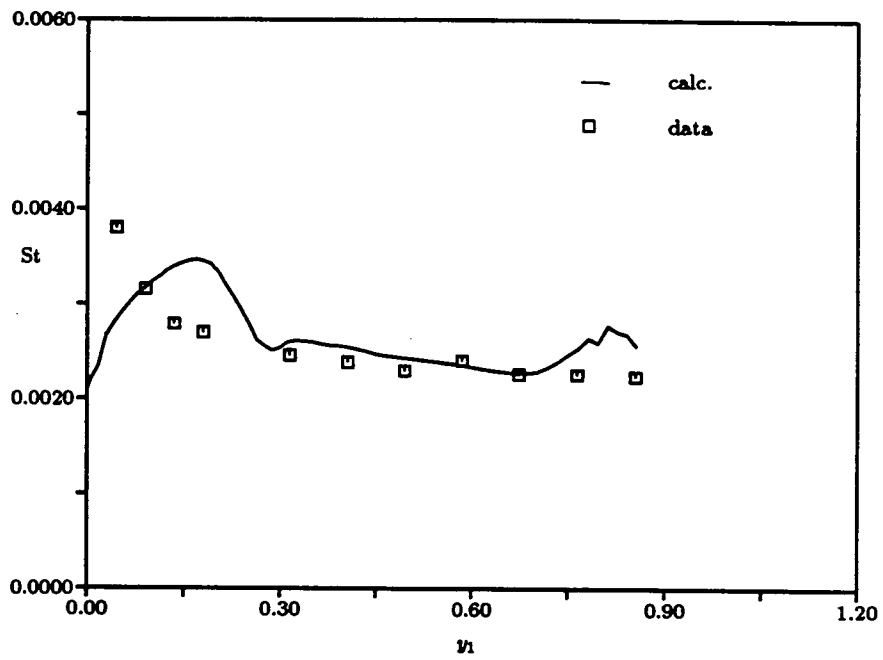
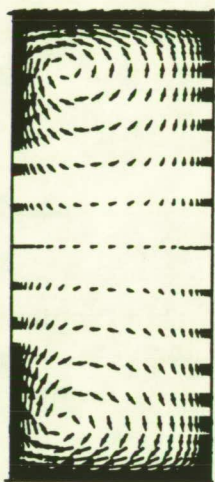
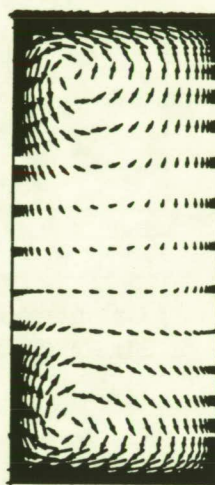


**Figure 80 Comparison of Calculated and Measured St Distribution on LSRR Gas Turbine Rotor Suction Surface at Mid Span**



Stator



Rotor

Figure 81 Comparison of Stator/Rotor Secondary Flow Near the Trailing Edge

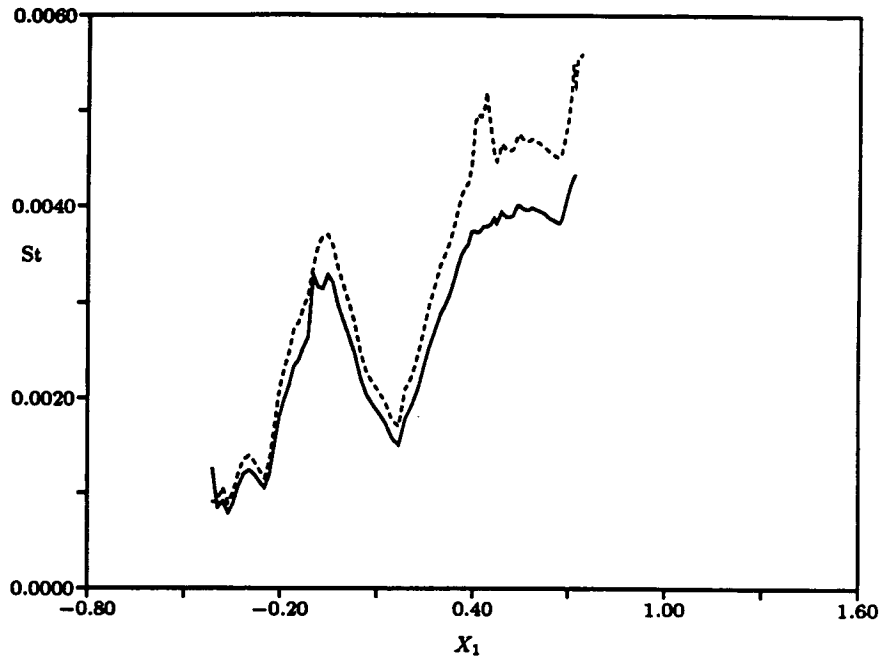


Figure 82 Calculated Stator/Rotor End Wall St Distribution at the Mid Gap  $Stx10^3$  (Solid-Stator, Dotted-Rotor)

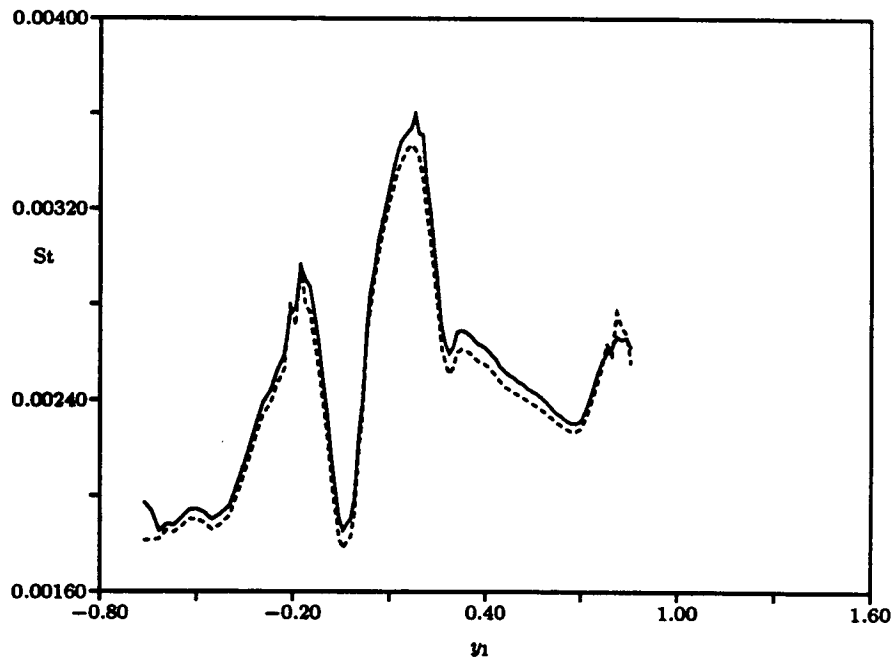


Figure 83 Experimental Stator/Rotor Suction Surface St Distribution at the Mid Span  $Stx10^3$  (Solid-Stator, Dotted-Rotor)

1. Report No.		2. Government Accession No.		3. Recipient's Catalog No.	
4. Title and Subtitle The Effects of Reynolds Number, Rotor Incidence Angle and Surface Roughness on the Heat Transfer Distribution in a Large-Scale Turbine Rotor Passage				5. Report Date November 1989	
7. Author(s) M. F. Blair and O. L. Anderson				8. Performing Organization Report No. UTRC-R89-957852-24	
9. Performing Organization Name and Address United Technologies Research Center Silver Lane East Hartford, Connecticut 06108				10. Work Unit No.	
12. Sponsoring Agency Name and Address National Aeronautics and Space Administration George C. Marshall Space Flight Center Marshall Space Flight Center, AL 35812				11. Contract or Grant No. NAS8-37351	
15. Supplementary Notes Technical Contract Monitors, Helen McConnaughey and Gil Wilhold Aerophysics Division NASA Marshall Space Flight Center, AL 35812 <i>Space Shuttle Main Engine</i> — <i>High Pressure Fuel Turbopump</i>				13. Type of Report and Period Covered Contractor Report Final	
14. Sponsoring Agency Code					
16. Abstract A combined experimental and computational program was conducted to examine the heat transfer distribution in a turbine rotor passage geometrically similar to the SSME HPFTP. Heat transfer was measured and computed for both the full-span suction and pressure surfaces of the rotor airfoil as well as for the hub endwall surface. The primary objective of the program was to provide a benchmark-quality data base for the assessment of rotor passage heat transfer computational procedures. The experimental portion of the study was conducted in a large-scale, ambient temperature, rotating turbine model. Heat transfer data were obtained using thermocouple and liquid-crystal techniques to measure temperature distributions on the thin, electrically-heated skin of the rotor passage model. Test data were obtained for various combinations of Reynolds number, rotor incidence angle and model surface roughness. The data are reported in the form of contour maps of Stanton number. These heat transfer distribution maps revealed numerous local effects produced by the three-dimensional flows within the rotor passage. Of particular importance were regions of local enhancement produced on the airfoil suction surface by the main-passage and tip-leakage vortices and on the hub endwall by the leading-edge horseshoe vortex system. Comparisons between the present results and midspan results from a previous NASA-HOST funded study are included. The computational portion consisted of the application of a well-posed parabolized Navier-Stokes analysis to the calculation of the three dimensional viscous flow through ducts simulating a gas turbine passage. These cases include a 90° turning duct, a gas turbine cascade simulating a stator passage, and a gas turbine rotor passage including Coriolis forces. The calculated results have been evaluated using experimental data of the three dimensional velocity fields, wall static pressures, and wall heat transfer on the suction surface of the turbine airfoil and on the end wall. Particular attention has been paid to an accurate modeling of the passage vortex and to the development of the wall boundary layers including the crossflow. The results of this assessment indicate that the procedure has the potential to predict the aerodynamics and the heat transfer in a gas turbine passage and can be used to develop detailed three dimensional turbulence models for the prediction of skin friction and heat transfer in complex three dimensional flow passages.					
17. Key Words (Suggested by Author(s)) Heat Transfer, Turbines, Airfoils, Endwalls				18. Distribution Statement	
19. Security Classif. (of this report) Unclassified		20. Security Classif. (of this page) Unclassified		21. No. of pages	22. Price